High-Performance Nuclear-Polarized ^{3}He Targets for Electron Scattering Based on Spin-Exchange Optical Pumping

Peter Alexander McDonald Dolph

Norfolk, VA

B.S. William & Mary 2004
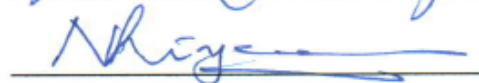
M.A. University of Virginia 2010

A Dissertation presented to the Graduate Faculty of the University of Virginia in Candidacy for the Degree of Doctor of Philosophy
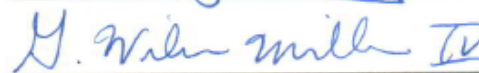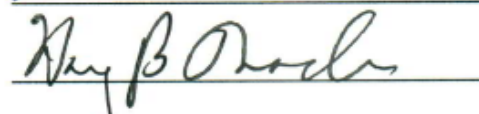
Department of Physics

University of Virginia

December 2010

Abstract

Nuclear-polarized ^{3}He targets have played an important role in electron-scattering experiments since the mid 1990's. Critical to the success and expansion of this program has been the ability to produce large amounts of polarized ^{3}He gas with relatively high polarization. This thesis describes research that has, by a convenient figure of merit, improved the performance by more than an order of magnitude.

Historically, these ^{3}He targets have been polarized through a process known as Spin-Exchange Optical Pumping (SEOP). In SEOP, polarized laser light is used to polarize an alkali metal vapor (usually, rubidium) through optical pumping. The polarized rubidium vapor transfers its polarization to ^{3}He atoms through spin-exchange collisions. Two important advances in SEOP have been the implementation of alkali-hybrid SEOP and spectrally-narrowed lasers.

In alkali-hybrid SEOP, a second species of alkali metal (usually potassium) is introduced into the cell. The potassium vapor is not optically pumped, but becomes polarized through spin-exchange collisions. The hybrid mixture more efficiently transfers its polarization to the ^{3}He gas, resulting in higher polarizations. Spectrally-narrowed lasers result in much higher optical-pumping rates. When spectrally-narrowed lasers are used to pump alkali-hybrid mixtures, tremendous gains in saturation polarization and polarization rates can be made. To implement these improvements, extensive diagnostic techniques were developed that were critical to optimization.

Although these advances have provided the enabling technology for a large number of experiments, they are alone insufficient to meet the demands of many future electron-scattering experiments. The current target design uses a two-chambered glass cell. In one chamber, known as the "pumping chamber," ^{3}He is polarized through SEOP with an alkali vapor. In the other chamber, known as the "target chamber," electron scattering occurs. The two chambers are connected by a thin transfer tube through which ^{3}He gas can diffuse. This design has worked well in

the past because, although the diffusion rates between the two chambers are slow, the rate at which ^{3}He gas is depolarized by the electron beam has been low. Future experiments, however, will need to run at much higher beam currents. In the presence of such high currents, the ^{3}He gas in the target chamber will quickly become depolarized. As part of this thesis, a new target design was developed and tested. In this design, gas is rapidly mixed between the two chambers through convection. By tagging gas inside the cell using Nuclear Magnetic Resonance (NMR) techniques, we were able to visualize the flow of gas.

Acknowledgements

First and foremost, I'd like to thank my advisor, Gordon Cates, for supporting me over the past six-and-a-half years. I learned a lot about alpacas, hay baling, sailing, and punk rock. Of course, I also learned a lot more about science and scientific writing. Your contagious enthusiasm helped to keep me motivated and I'm grateful for the time you took out of a very busy schedule to help me earn my degree.

I'd like to thank Jaideep Singh for teaching me nearly everything I know about spin-exchange optical pumping as well as ^{3}He and alkali polarimetry. I also learned a lot about the scientific method and how best to present data. I'd also like to thank Al Tobias for filling and handling nearly all cells studied in this thesis as well as his assistance with general lab operations. I learned a lot from Al, particularly the importance of good documentation and "doing things the right way."

I'd like to thank Karen Mooney, who along with Jaideep helped setup the Faraday Rotation apparatus. Together, we characterized many of the cells presented in this Thesis. Thanks is also due to Vladimir Nelyubin whose command over the temperamental Ti:Saph laser made many of the Faraday Rotation measurements possible. I'd also like to thank Wilson Miller, who along with Karen Mooney assisted with several lifetime studies. Thanks is also due to the rest of Cates Lab: Yuan Zheng, Rupesh Silwal, Yuehaw Khoo and Tom Anuniwat, as well as recent graduates Scott Rohrbaugh, James Wang, Ryan Snyder, and Michael Carl.

I'd also like to thank the members of my committee: Wilson Miller, Nilanga Liyanage, and Hank Thacker. Their feedback over the years has helped to keep me on course. I'm very grateful for the time they have given to my pursuit.

Lastly, I'd like to thank my brothers and my sister for making the holidays something I'll always look forward to; my mother-in-law for reminding me to finish my degree (and making the holidays in Utica great); my parents for encouraging me to study Physics (and paying for my education); and my wife for giving me something

to look forward to when I get home at night. I'd also like to thank my dog, Buddy, for letting me know when it's time to go home.

Contents

List of Figures

List of Tables

Chapter 1

Introduction

Nuclear-polarized ^{3}He has proven to be useful in a number of different areas of research. In electron scattering, polarized ^{3}He provides a means for studying spin-dependent interactions involving neutrons. This is because, to first approximation, a ^{3}He nucleus is comprised of a pair of protons whose spins are paired, and a single neutron that accounts for most of the nuclear spin (free neutrons aren't used because they decay with a mean lifetime of approximately 15 minutes). An important early example of the use of polarized ^{3}He in electron scattering came during the 1992 Stanford Linear Accelerator Center (SLAC) experiment, known as E142, in which the internal spin structure of the neutron was investigated [15]. More recently (and central to this thesis) were the targets used in several recent experiments performed at Jefferson Lab (JLab) in Newport News, VA . These experiments include E02-013, "Measurement of the Neutron Electric Form Factor G_E^n at High Q^2" [16] as well as several experiments investigating single-spin asymmetries such as E06-010, E06-014, and E05-015. Other important applications of polarized ^{3}He have included being used as a neutron polarizer [17], and as a source of signal for magnetic resonance imaging [18, 19].

The targets used in E142 and other early experiments were only able to tolerate relatively modest electron-beam currents of a few microamps. Additionally, these targets were usually only able to achieve ^{3}He polarizations of about 35-40%. These experiments relied upon a technique known as Spin-Exchange Optical Pumping (SEOP) to polarize the ^{3}He atoms. In this technique, circularly-polarized laser light is used to optically pump an alkali-metal vapor (historically typically rubidium (Rb)); the polarized alkali-metal atoms transfer their polarization to the ^{3}He atoms through spin-exchange collisions involving hyperfine-like interactions. Recently, much improved target performance, including higher ^{3}He polarizations have been attained in large part because of the use of two new techniques, the study and implementation of which are central to this thesis.

The first of these techniques, known as the "alkali-hybrid SEOP," involves using a mixture of Potassium (K) and Rb to carry out spin-exchange collisions in contrast to earlier work that relied on Rb alone. Although the lasers still optically pump the Rb vapor, the K vapor becomes polarized through collisions with Rb. Both alkali metals then spin-exchange with the ^{3}He gas. The E02-013 experiment, which was the first to use alkali-hybrid mixtures in the context of electron scattering, ran with ^{3}He polarizations approaching 50%.

The second technique that has substantially improved target performance is the implementation of high-power spectrally-narrowed lasers. These lasers have narrower spectral profiles and are able to achieve much higher optical-pumping rates. During the recent single-spin asymmetry Transversity experiments (E05-015) in which spectrally-narrowed laser were used in conjunction with Hybrid SEOP, polarizations approaching 70% were observed in the presence of the electron beam. We note that these two improvements were only possible with the aid of several powerful diagnostic techniques which were implemented as part of this thesis.
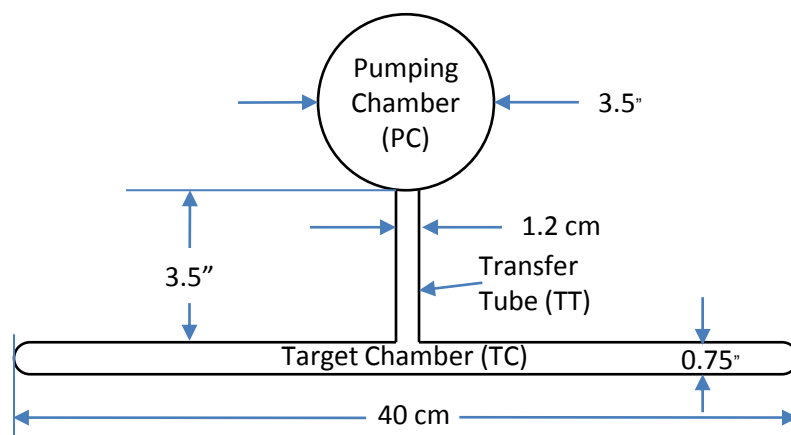
Figure 1.1: Inner Dimensions of a Large Pumping-Chamber GEN Target Cell

Although hybrid SEOP and spectrally-narrowed lasers have been employed with great success, it is likely that the next generation of electron-scattering experiments will encounter limitations unless other changes are made to the target design. His-

torically, the ^{3}He targets used in electron-scattering experiments have been two-chambered glass cells (see Fig 1.1) in which gas can freely diffuse between the "pumping chamber" (where the ^{3}He atoms are polarized) and the "target chamber" (where electron scattering occurs). As long as the time scale associated with the diffusion of gas is relatively fast compared to the time scale characterizing the depolarization of the gas, this scheme works well. However, future experiments will need to run at higher beam currents. These higher currents pose a problem as the relaxation rate of the ^{3}He gas scales with the beam current. To compensate, we've tested a prototype cell in which gas is mixed by convection. The time scales associated with convection mixing are much faster (tens of seconds instead of hours) and should be more than adequate to maintain high ^{3}He polarizations in the target chamber under demanding conditions. A new experiment to measure the aforementioned electric form factor of the neutron at momentum transfers nearly three times higher than those for which data exist has been approved to run at JLab following a major energy upgrade that is currently ongoing [20]. The experiment will require large increases in target performance, and our new convection technique will be critical to the experiment's success. Later, we will refer to this experiment as G_E^n-II.

1.1 Improvements in Effective Luminosity

Most of the electron-scattering experiments mentioned above involve spin asymmetries in which unpolarized electrons are scattered off of polarized ^{3}He atoms. From these asymmetries, physical quantites, such as G_E^n can be extracted. In such asymmetry experiments, data are acquired until a desired level of uncertainty is achieved. The amount of time it takes to achieve this uncertainty can be decreased by increasing the luminosity (defined in Eq. 1.4). In this section, we will illustrate how the improvement in ^{3}He polarization has resulted better target performance.
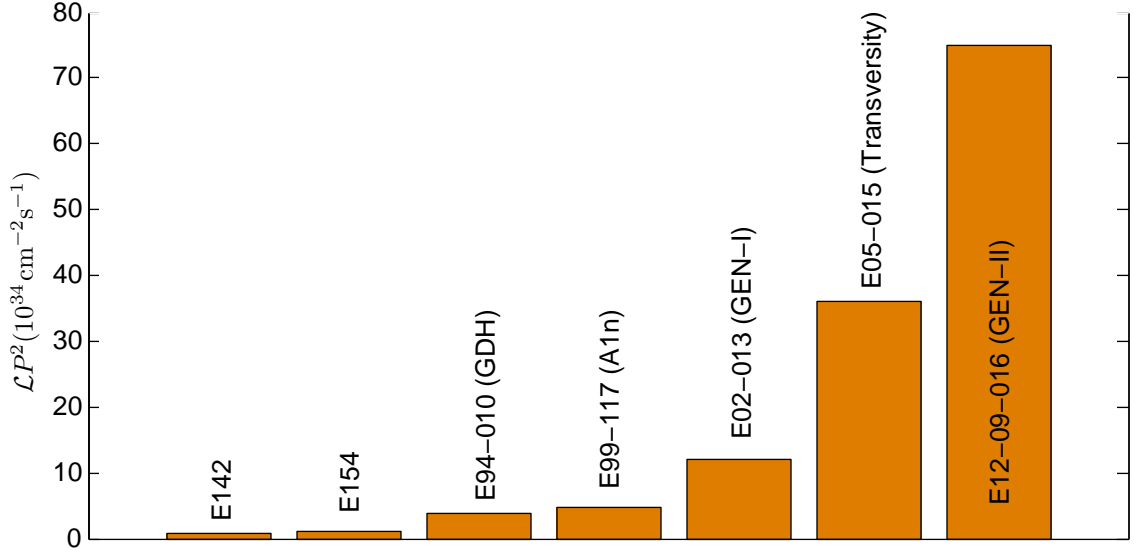
Figure 1.2: Effective Luminosity (Luminosity Weighted by ^{3}He Polarization Squared) for Some Important Electron-Scattering Experiments.

In a double-spin asymmetry experiment (in which polarized electrons are scattered of off polarized ^{3}He atoms), the measured asymmetry can be written as

$$A_{measured} = P_e P_{He} A_{physical} \tag{1.1}$$

where P_e is the electron-beam polarization, P_{He} is the polarization of the ^{3}He gas, and $A_{physical}$ is the asymmetry that characterizes the physics of interest. The fractional error in the physical uncertainty is given by Poisson statistics,

$$\frac{\delta A_{physical}}{A_{physical}} = \frac{1}{\sqrt{N} P_e P_{He}} \tag{1.2}$$

where N, the number of detected events, is proportional to the luminosity, $\mathcal{L}$, and the experiment duration, t,

$$N \propto \mathcal{L} t. \tag{1.3}$$

Here, luminosity is given by

$$\mathcal{L} = \frac{I_{beam}}{e}[\text{He}]l \tag{1.4}$$

where I_{bean} is the electron beam current, e is the charge of the electron, [He] is the density of the gas in the target chamber, and l is the length of the target chamber. Combining Eq. 1.2 and Eq. 1.3 and rearranging, we find

$$\left(\frac{\delta A_{physical}}{A_{physical}}\right)^2 \propto \frac{1}{\mathcal{L}P_{He}^2} \tag{1.5}$$

The quantity $\mathcal{L}P_{He}^2$ can be referred to as the "effective luminosity." Fig. 1.2 shows estimates for the effective luminosity for several ^{3}He electron-scattering experiments. The increase from A1n to G_E^n was due to hybrid-alkali SEOP. The increase from G_E^n to the Transversity experiments was due to the combination of hybrid-alkali SEOP and spectrally-narrowed lasers. The last entry, for G_E^n-II, shows the anticipated gains that convective mixing will allow.

1.2 Other Uses of He-3

^{3}He, a rare isotope of helium (1.37 ppm natural abundance), is produced when tritium (which itself does not exist naturally) beta decays. Tritium, an important ingredient in nuclear weapons, was produced by the U.S. Department of Energy's Savannah River Site until 1988 [21]. As a result of the Savannah River Site closing, the supply of tritium has decreased, which has resulted in a decreased supply of ^{3}He.

The isotope ^{3}He can serve as a very effective neutron detector, and is thus very useful to detect neutron emmission from fissile plutonium. Since the creation of the Department of Homeland Security in 2002, neutron detectors have been in high demand at borders and ports in the United States. Increased demand and low supply has led to a demand-to-supply ratio of roughly 10, which has caused the cost of ^{3}He

to soar from \$100 per liter to a peak of about \$2,000 per liter in recent years [22]. There is considerable pressure to use this scarce resource as efficiently as possible.

In addition to having an important role in national security, ^{3}He has important medical applications. In fact, ^{3}He Nuclear Magnetic Resonance Imaging (MRI) has been used to detect small structural damage in the lungs of people exposed to second-hand smoke [23]. Conventional MRI exploits the thermal equilibrium polarization of the hydrogen protons in water molecules in the presence of strong magnetic fields [24]. At room temperature in the presence of a 3 Tesla magnetic field, a proton is thermally polarized to 0.001%. Different tissues (fat, muscle, tumor, etc.) have different water concentrations and relaxation properties which can be identified on an MRI scanner. The lungs, however, are relatively empty. Hyperpolarized (polarized well above thermal polarization) ^{3}He provides an excellent medium for MRI studies, as the gas can be easily inhaled [25]. What the gas lacks in density (roughly 3 orders of magnitude) it easily makes up in polarization (roughly 5-6 orders of magnitude); an MRI produced with hyperpolarized ^{3}He is more detailed than one produced by a traditional MRI, inside the lungs.

It is worth noting that the techniques and improvements described in this thesis also provide capabilities for medical imaging. Recently, the author helped construct a new ^{3}He polarizer that is currently in use at UVa and utilizes these techniques. This new polarizer produces double the volume of ^{3}He gas in less than half the time of its predecessor. Moreover, the polarization of this gas has nearly doubled from about 35% to about 65%.

Chapter 2

Spin-Exchange Optical Pumping

Spin-Exchange Optical Pumping (SEOP) uses circularly-polarized laser light to polarize an alkali metal; the alkali metal in turn transfers its polarization to a noble-gas nucleus such as ^{3}He or ^{129}Xe[26]. Until recently SEOP usually employed rubidium (Rb) and broadband lasers (2.0 nm Full Width Half Maximum (FWHM)), which can achieve around 40% ^{3}He polarization in the large-volume target cells we use for electron scattering experiments (1-3 liters). Recent advances including the introduction of hybrid alkali mixtures and spectrally narrowed lasers (0.2 nm FWHM) have produced polarizations in excess of 70%.

Three basic ingredients are required for SEOP: an alkali metal (typically rubidium); a laser tuned to the D1 resonance of that particular alkali species; an appropriate noble gas (we use ^{3}He, which has one unpaired neutron). The laser is used to optically pump the alkali metal's valence electron, which in turn spin exchanges with the free neutron of the noble gas. Since the lasers are ultimately one of the limiting factors in noble gas polarization (they provide the power), maximizing the efficiencies of spin transfer and minimizing miscellaneous relaxations is crucial to making the most of the laser power available.

2.1 Polarization Review

2.1.1 General Treatment of Polarization

The spin polarization, P, of any spin 1/2 nucleus (e.g. ^{3}He) is defined by the asymmetry between the two states,

$$P = \frac{\Delta N}{\Sigma N} = \frac{N_+ - N_-}{N} \tag{2.1}$$

where $N = N_+ + N_-$ and N_+ and N_- are the number of spins in each of the two possible states.

The time evolution of polarization can be modeled by:

$$\frac{dP}{dt} = -P(\gamma + \Gamma) + \gamma, \tag{2.2}$$

where γ is the polarization rate and Γ is the the depolarization rate due to all other processes. The solution to this differential equation is

$$P(t) = Ce^{-(\gamma+\Gamma)t} + \frac{\gamma}{\gamma + \Gamma}. \tag{2.3}$$

Note that in the limit $t \to \infty$, the polarization is limited

$$P_\infty = \frac{\gamma}{\gamma + \Gamma}. \tag{2.4}$$

If we label the polarization at $t = 0$ P_0, this becomes

$$P(t) = P_0 e^{-(\gamma+\Gamma)t} + P_\infty \left(1 - e^{-(\gamma+\Gamma)t}\right). \tag{2.5}$$

2.1.2 Thermal Polarization Aside

In the absence of active polarization technique, spins in a magnetic field will be thermally polarized. The partition function, Z, is

$$Z = \sum_s e^{-E_s/k_B T} \tag{2.6}$$

where E_s is the energy of a spin in state s, $k_B = 1.38 \times 10^{-23} J/K$ is the Boltzmann constant, and T is the temperature (in Kelvin) of the system. The average energy of an ensemble of spins is

$$\langle E \rangle = \sum_s \frac{E_s e^{-E_s/k_B T}}{Z} \tag{2.7}$$

Specifically, for spins in a magnetic field where $E_s = \boldsymbol{\mu} \cdot \mathbf{B}$,

$$\langle E \rangle = -\mu B \tanh \frac{\mu B}{k_B T} \tag{2.8}$$

The thermal polarization relates the average energy of the ensemble to the energy of the upper state (the state with μ antiparallel to the applied field), $\langle E \rangle = PE$. This yields for the thermal polarization,

$$P_{thermal} = -\tanh \frac{\mu B}{k_B T}; \tag{2.9}$$

under typical operating conditions,

$$P_{thermal}^{^3He} \approx 10^{-9} \tag{2.10}$$

$$P_{thermal}^{Rb} \approx 10^{-5}. \tag{2.11}$$

2.2   Optical Pumping

2.2.1   Overview

Circularly-polarized laser light tuned to the D1 line of an alkali metal atom can induce optical pumping; in context of electron scattering experiments, rubidium (Rb) is often the alkali metal under consideration. In this process illustrated in Fig. (2.1), the angular momentum of a polarized photon is transfered to the valence electron of the Rb atom. The interaction is said to be "sudden" with respect to the nuclear spin [27]. The excited electron will enter the $5P_{\frac{1}{2}}$ orbital in the opposite spin state. Through collisions with other Rb atoms $5P_{\frac{1}{2}}$ states will "mix" and become equally populated. The excited electrons would then spontaneously decay with equal probability to either state by emitting a photon (which could then pump an S-orbital electron); however,
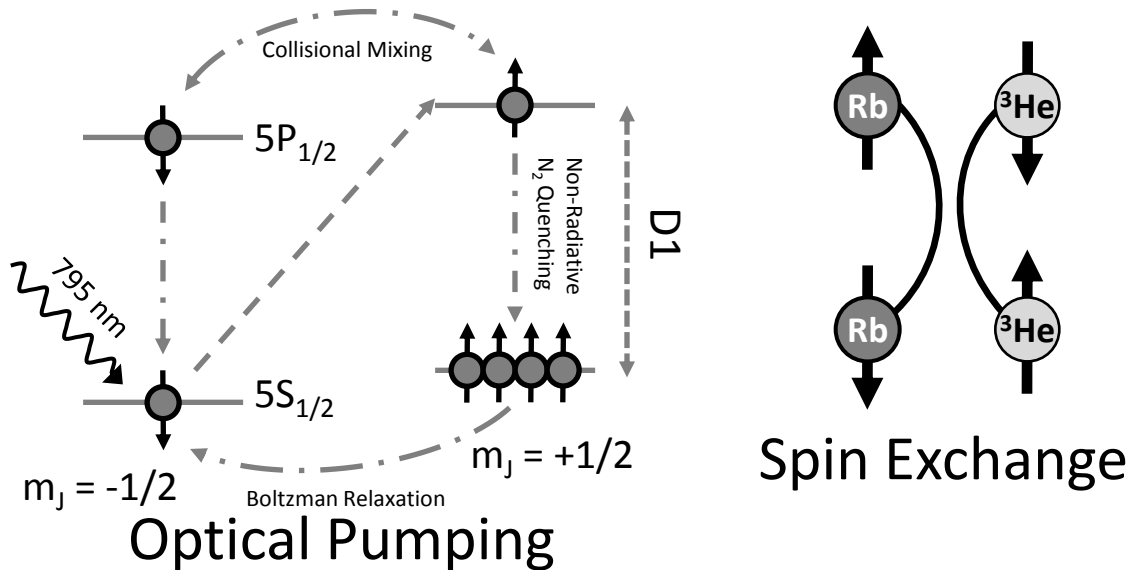
Figure 2.1: Spin-Exchange Optical Pumping of Rubidium, I = 0

a small amount of diatomic nitrogen gas is often added to non-radiatively "quench" the excited electrons through their rotational and vibration modes of oscillation [28]. In the presence of the roughly 0.1 Amagats of N_2 typical in the target cells we study, 95% of excited electrons will decay through quenching, with the remainder decaying by emitting a photon [1]. Because the alkali-alkali spin exchange rate is much faster than the spontaneous emission rate, the excited electrons will decay with equal probability to either $5S_{\frac{1}{2}}$ magnetic substate [26]. Although both ground states are being repopulated, only one of the two states is being depopulated; consequently, the Rb vapor becomes polarized. The Rb atoms become highly polarized on a time scale of milliseconds (see Sec. 2.2.6). Fig. 2.2 shows the energy level diagram of Rb-87 in the presence of a weak magnetic field. For optical pumping, Eqn.(2.4) takes the form

$$P_{Rb}(t = \infty, \vec{r}) = \frac{R_{op}(\vec{r})}{R_{op}(\vec{r}) + \Gamma_{Rb}(\vec{r})} P_{light}(\vec{r}) \cos\theta, \qquad (2.12)$$

where the polarization and direction (relative to the holding field) of the light have been introduced as limiting factors. The rates and polarizations in the above equation
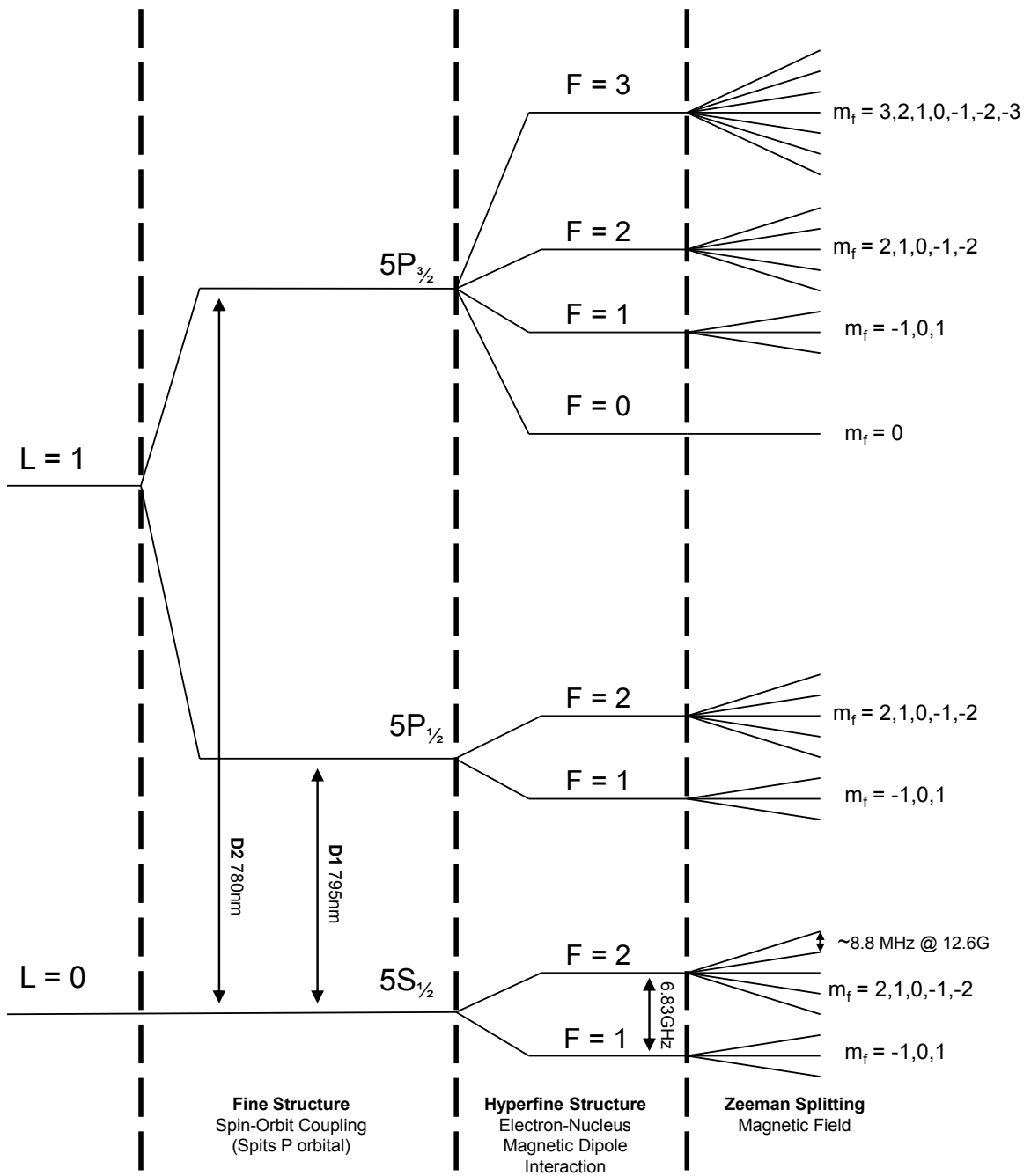
Figure 2.2: Energy-level diagram of 87-Rb, (I = 3/2, not to scale) showing full hyperfine structure

have spatial dependances – alkali atoms at the front of the cell are exposed to more intense laser light than those in the back because the atoms in the front attenuate the pump beam.

2.2.2 Alkali Metal in an External Magnetic Field

A ground state (L=0) alkali metal atom in an external magnetic field has a spin Hamiltonian

$$\mathbf{H} = A\mathbf{S} \cdot \mathbf{I} - g_e \mu_B S_z B_z - g_N \mu_N I_z B_z, \tag{2.13}$$

where A is the isotropic magnetic-dipole coupling coefficient [28]; $\mu_B = 9.274 \times 10^{-24} J/T$ and $\mu_N = 5.051 \times 10^{-27} J/T$ are the bohr and nuclear magnetons; $g_e \approx 2$ and $g_N \approx 5.59$ are the electronic and nuclear Lande g-factors; and the external magnetic field is assumed to point along the z axis. The first term is the Fermi-contact interaction between the ^{3}He nucleus and the alkali valence electron; it is responsible for spin exchange. It should be noted that the Zeeman term is dominated by the electron spin ($\mu_B \gg \mu_N$).

2.2.3 Optical Pumping Rate

Tuned D1 laser light is used to induce electric dipole transitions (see Sec. 4.2.2), which serve to polarize the alkali metal (see Fig. 2.1). The optical pumping rate for these transitions is given by

$$R = \int \Phi(\nu, \vec{r})\sigma(\nu)d\nu, \tag{2.14}$$

where $\Phi(\nu, \vec{r})$ is the photon spectral flux density and $\sigma(\nu)$ is the photon absorption cross section. It can be shown that [29]

$$\int \sigma(\nu)d\nu = \pi f r_e c, \tag{2.15}$$

where r_e is the classical electron radius and f is the oscillator strength of the transition under consideration ($f \approx \frac{1}{3}$ for the D1 transition [30]). From this result, we can assume

$$\sigma(\nu) = \pi f r_e c F(\nu, \nu_0), \qquad (2.16)$$

where $F(\nu, \nu_0)$ contains all the frequency dependance of σ. It might be desirable for

$$F(\nu, \nu_0) = \delta(v - v_0). \qquad (2.17)$$

In reality the spectral shape is a combination of a natural Lorentzian lineshape, a doppler-broadened Gaussian lineshape, and a pressure-broadened Lorentzian due to collisions with ^{3}He atoms. Under the high pressure conditions we operate under, this last effect dominates the lineshape.

$$F(\nu, \nu_0) = \frac{1}{\pi} \left(\frac{\frac{\Gamma_A}{2}}{(\nu - \nu_0)^2 + \left(\frac{\Gamma_A}{2}\right)^2} \right) \qquad (2.18)$$

whose FWHM is given by Γ_A (a quantity that depends on the helium pressure [31]). Because of this pressure broadening, the hyperfine and Zeeman states are unresolved. This gives the following for the photon-absorption cross section:

$$\sigma(\nu) = \frac{\pi r_e c}{3} \frac{1}{\pi} \left(\frac{\frac{\Gamma_A}{2}}{(\nu - \nu_0)^2 + \left(\frac{\Gamma_A}{2}\right)^2} \right). \qquad (2.19)$$

Ignoring for the moment the attenuation of the laser light, the photon spectral distribution can be expressed as the product of a spatial and a spectral Gaussian [32],

$$\Phi(\nu, \vec{r}) = \Phi_0(\vec{r}) G(\nu) \qquad (2.20)$$

$$\Phi_0(\vec{r}) = \frac{P}{h\nu} \frac{2}{w^2 \pi} e^{-2r^2/w^2} \qquad (2.21)$$

$$G(\nu) = \frac{1}{\sqrt{2\pi}\sigma_l} e^{-(\nu - \nu_l)^2 / 2\sigma_l^2}, \qquad (2.22)$$

where ν_l is the central laser frequency; σ_l is Gaussian width of the laser, related to the FWHM by $\omega_l = \gamma_l/2\sqrt{\ln 4}$; P is the power of the laser; and w is the beam waist. The absorption line width, $\Gamma_A \approx .04\text{nm/amg} \cdot [^3\text{He}]$ is ≈ 0.3nm under our operating conditions.

Eq. 2.14 can now be evaluated to give the initial optical pumping rate (the optical pumping rate at the front end of the cell)

$$R_0 = \int \phi(\nu) \cdot \sigma(\nu) d\nu \approx 20 \text{ kHz per } 20 \text{ W/31 cm}^2/2.0 \text{ nm (broadband)}, \quad (2.23)$$

$$R_0 = \int \phi(\nu) \cdot \sigma(\nu) d\nu \approx 87 \text{ kHz per } 20 \text{ W/31 cm}^2/0.2 \text{ nm (line-narrowed)}. \quad (2.24)$$

2.2.4 Pumping Chamber Temperatures

For a given laser power, an appropriate alkali density must be chosen. If the alkali density is too high, then the laser won't be able to fully penetrate the vapor and the alkali polarization will be low. Conversely, if the alkali density is too low, then much of the available laser light will pass through the cell unused. Moreover, as will be discussed in Ch. 2.3.4, the Rb-^{3}He spin-exchange rate is directly proportional to the alkali density. A balance between high alkali polarization (corresponding to low alkali density) and fast spin-exchange rates (achieved at higher alkali densities) must be found.

We achieve high alkali densities by placing the pumping chamber (pc) of our target cell in a ceramic, forced-air oven (see Fig. 2.3). The temperature of the oven, which is monitored by an RTD (resistive thermal device) attached to the pull-off of the target cell, is controlled by an Omega CN76000 temperature controller. Although this RTD is quite reliable at measuring the temperature on the outside of the cell, the temperature inside the cell can be much higher.

When the pump laser is on, the gas inside the cell is heated to significantly higher
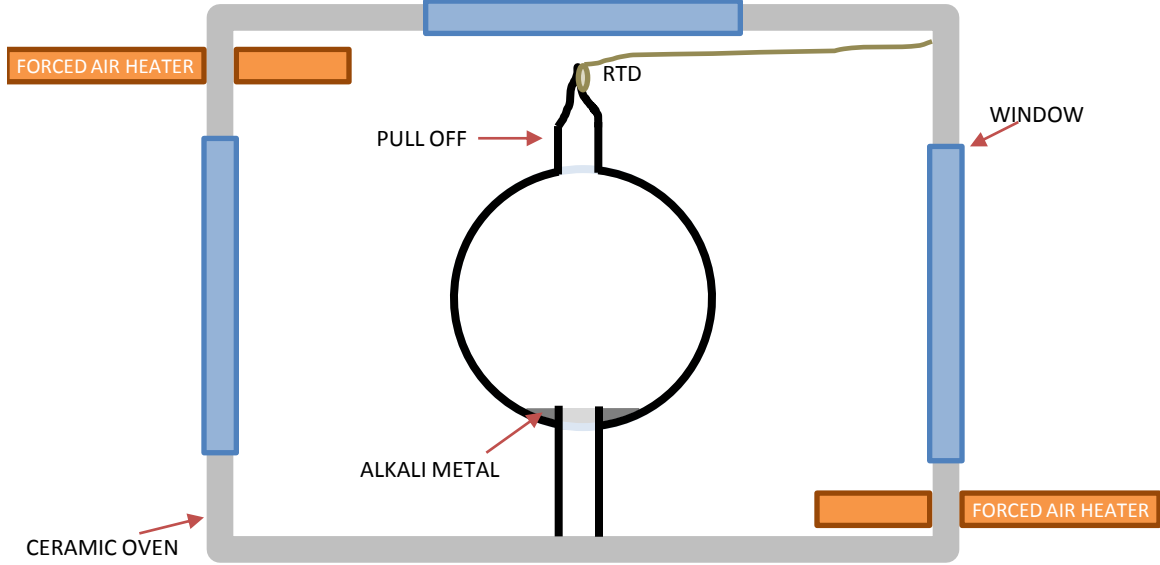
Figure 2.3: Interior of Oven (side view)

temperatures (as much as 40°C, see Ch. 3.2.5). The majority of excited Rb atoms non-radiatively decay through collisions with nitrogen molecules, effectively converting the Rb excited state energy into N_2 thermal energy. The temperature of the inside surface of the glass, however, remains much lower.

The Rb vapor pressure is in equilibrium with the pool of Rb in the cell. This pool, however is in equilibrium with the glass wall containing it. Consequently, measurements of the Rb density can be used to measure the temperature of the inner surface of the glass pc (see Ch. 4). Such measurements show that this temperature is typically about 5°C above the temperature of the pull off.

We typically operate at an oven temperature of $T = 190$°C, which corresponds to a Rb density of

$$[Rb] = 6.16 \times 10^{14} cm^3. \qquad (2.25)$$

2.2.5 Rb-X Spin Destruction Rate

Through collisions with Rb, ^{3}He, and N$_2$, the polarized rubidium atoms relax. The Rb spin destruction rate is given by

$$\Gamma_{Rb} = \Gamma_{Rb-Rb} + \Gamma_{Rb-^3He} + \Gamma_{Rb-N_2}, \tag{2.26}$$

where

$$\Gamma_{Rb-X} = k_{sd}^{Rb-X}[X]. \tag{2.27}$$

The spin-destruction rate constants have been measured by many groups; a summary of many of their results is included in Appendix A. Using the results of Appendix A.1.2,

$$k_{sd}^{Rb-3He}(T) = 55.9(9)\left(\frac{T}{473.15K}\right)^{3.31(12)} \text{Hz/amg} \tag{2.28}$$

$$k_{sd}^{Rb-N2}(T) = 290(30)\left(\frac{T}{473.15K}\right)^{2.0(25)} \text{Hz/amg} \tag{2.29}$$

$$k_{sd}^{Rb-Rb}(T) = 4.813(48) \times 10^{-13} \text{cm}^3/\text{s}. \tag{2.30}$$

Under typical operating conditions ($T_{oven} = 190°C$), the pumping chamber densities are given by

$$[^3\text{He}] \approx 7.0\,\text{amg} \tag{2.31}$$

$$[\text{N}_2] \approx 0.08\,\text{amg} \tag{2.32}$$

$$[\text{Rb}] = 6.16 \times 10^{14}\text{cm}^{-3}; \tag{2.33}$$

the target chamber densities are

$$[^3\text{He}] \approx 11.6 \, \text{amg} \tag{2.34}$$

$$[\text{N}_2] \approx 0.13 \, \text{amg} \tag{2.35}$$

$$[\text{Rb}] \approx 0 \, \text{cm}^{-3}. \tag{2.36}$$

As was mention in Ch. 1.1, our target cells have two chambers: a pumping chamber (pc) and a target chamber (tc), which are joined by a narrow transfer tube (tt) (see Fig. 1.1). The pc is kept inside of a forced air oven, which is typically heated to 190°C. At such a high temperature, a high Rb density forms, which is necessary for SEOP. The tc, however, is cooled to nearly room temperature. Because the tc is kept at a low temperature, only a negligible amount of Rb vapor is present; consequently, there is very little Rb-Rb spin-destruction in the target chamber. The approximate spin-destruction rates in the pumping chamber are:

$$\Gamma_{Rb-^3He} \approx 365 \text{Hz} \tag{2.37}$$

$$\Gamma_{Rb-N2} \approx 22 \text{Hz} \tag{2.38}$$

$$\Gamma_{Rb-Rb} \approx 293 \text{Hz} \tag{2.39}$$

$$\therefore \Gamma_{Rb} \approx 680 Hz \tag{2.40}$$

2.2.6 Alkali Polarization

Analogous to Eq. 2.5, the alkali polarization is given by

$$P_{Rb}(t) = P_0^{Rb} e^{-(R+\Gamma_{Rb})t} + P_\infty^{Rb} \left(1 - e^{-(R+\Gamma_{Rb})t}\right), \tag{2.41}$$

$$P_\infty^{Rb} = P_{light} \cos\theta \frac{R}{R+\Gamma_{Rb}} \tag{2.42}$$
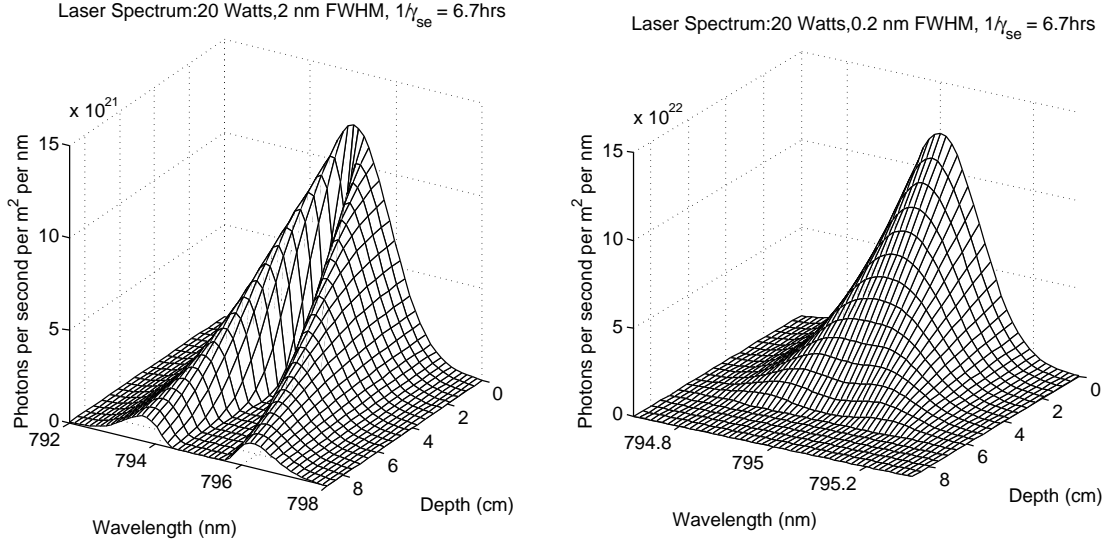
Figure 2.4: Comparison between broadband (left) and line-narrowed (right) laser spectra. The simulation was carried out on a spherical cell (9 cm diameter) with 20 W of laser light. The simulation was carried out at 190C ($1/\gamma_{se} = 6.7hrs$). Note the different Y and Z-scales.

where θ is the angle between the pump laser and the holding field for the target cell; great care is taken to make this angle as small as possible. Towards the entrance of the cell, $R + \Gamma_{Rb} \approx \mathcal{O}(10\text{'s kHz})$ causing the alkali polarization to reach its equilibrium value (P_∞) on a time scale of 100's of microseconds.

2.2.7 Spatial Variation of Optical Pumping Rate

From these equations, it may appear that the alkali polarization approaches 1; however, because the photon flux decreases as the laser light passes through the cell (by transfering its angular momentum to the alkali vapor), the optical pumping rate (see Fig. 2.4) – and therefore the alkali polarization (see Fig. 2.5)– decreases as the light passes through the cell [32],

$$\frac{1}{\Phi}\frac{\partial \Phi}{\partial z} = -(1 - P_{Rb}P_{light}\cos\theta)\sigma(\nu)[Rb]. \tag{2.43}$$

It should be noted that the attenuation is in turn dependant on the polarization of the alkali which is dependant on the polarization of the pump laser.
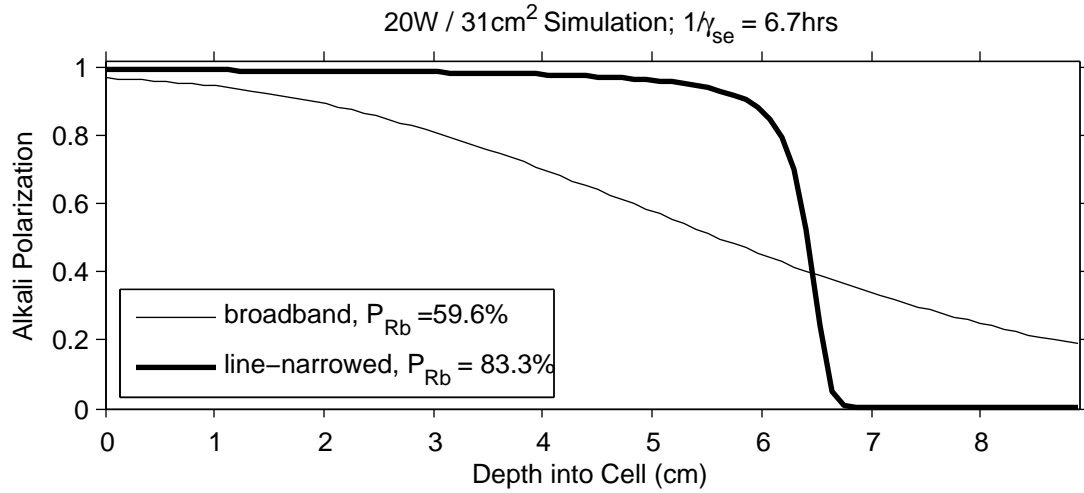
Figure 2.5: Theoretical Rb polarization for a 9cm diameter sphere at 190C. Note the sharp drop-off in alkali polarization for the line-narrowed laser. Because all of the available laser light is used (see Fig. 2.4), the line-narrowed laser is able to achieve a higher alkali polarization.

2.2.8 Improvements in Optical Pumping

The optical pumping rate (Eq. 2.23) can be increased by better matching the photon-absorption cross section of the alkali metal to the spectral width of the laser light; this can be accomplished by using line-narrowed lasers. In the past, we have used broadband Coherent FAP diode lasers with a FWHM of approximately 2.0 nm. Recently, we have acquired line-narrowed Comet lasers from Spectra-Physics, each with a FWHM of approximately 0.2 nm. These two systems each provide approximately 20 W of laser light; however, because the Comet laser spectrum is better matched to the alkali absorption cross section, the initial optical pumping rate of the Comet is about 5 times larger than the FAP's (see Eq. 2.23,2.24). When line-narrowed lasers are used in our lab, ^{3}He polarizations can increase from about 40% to about 60% in pure Rb target cells.

The plots show in Fig. 2.4, which were generated using a simulation based on the previous sections, show the difference in $\phi(\nu)$ between line-narrowed (right) and broadband lasers (left). The simulated plots show the evolution of the photon spectral

flux (photons per second per area per wavelength) as a function of wavelength and depth into a 9 cm diameter spherical cell. Although the two spectra have the same total number of photons, the light from the line-narrowed laser is more resonant (note the different Z-scale); consequently, all of the Comet light is absorbed, while the off-resonance tail ends of the FAP light exit the cell unabsorbed. Since the line-narrowed light is being used more efficiently, a higher alkali polarization can be achieved.

2.3 Spin Exchange

2.3.1 Overview

There are two ways the electron can transfer its spin. The first (and dominant mechanism) is a simple binary collision (see Fig. 2.1); the second occurs when the alkali metal and the noble gas briefly form a van der Waals molecule. The second mechanism contributes negligibly for ^{3}He SEOP [26].

2.3.2 Spin Exchange Hamiltonian

Electronic angular momentum is primarily transferred to the nucleus of ^{3}He through isotropic, fermi-contact hyperfine collisions, although some is transfered by anisotropic dipolar interactions [26]. The former can be described by the following hamiltonian,

$$H_{SE} = \alpha \mathbf{I} \cdot \mathbf{S} \tag{2.44}$$

where $\mathbf{I}$ refers to the ^{3}He nuclear spin, $\mathbf{S}$ refers to the rubidium valence electron spin, and α is the effective hyperfine coupling constant given by [33]

$$\alpha(R) = \frac{16\pi}{3} \frac{\mu_B g \mu_N}{[I]} |\Psi(R)|^2; \tag{2.45}$$

here, $\Psi(R)$ is the wavefunction of the valence electron evaluated at the nucleus of the noble gas atom. It should be noted that in order for spin exchange to successfully occur, the alkali metal valence electron has to "penetrate though the ^{3}He atom's electron cloud to the nucleus" [34].

2.3.3   Rb-Rb Collisions

The spin-exchange rate for Rb-Rb collisions is

$$\gamma_{se}^{Rb-Rb} = k_{se}^{Rb-Rb}[Rb]. \tag{2.46}$$

where $k_{se}^{Rb-Rb} = 8.4(3) \times 10^{-10}$ cm^3/s is the Rb-Rb spin-exchange rate constant (see Appendix A and Table 2.2). Under typical operating conditions ($T_{oven} = 190°C$),

$$[Rb] = 6.16 \times 10^{14} \text{cm}^{-3}, \tag{2.47}$$

which gives

$$\gamma_{se}^{Rb-Rb} \approx 500 kHz. \tag{2.48}$$

Rb-Rb spin-exchange collisions are mediated by a combination of Coulomb potential and the Pauli exclusion principle. Consequently, they're very efficient and have $\gamma_{se}^{Rb-Rb} \gg \Gamma_{Rb}$. The Rb-Rb spin-exchange efficiency, η_{Rb-Rb} is ratio of the rate at which polarization is successfully transferred between Rb atoms to the rate at which polarization is lost

$$\eta_{Rb-Rb} = \frac{\gamma_{se}^{Rb-Rb}[Rb]}{\gamma_{se}^{Rb-Rb}[Rb] + \Gamma_{Rb}[Rb]}, \tag{2.49}$$

$$= \frac{k_{se}^{Rb-Rb}[Rb]}{k_{se}^{Rb-Rb}[Rb] + \Gamma_{Rb}}. \tag{2.50}$$

Under typical operating conditions,

$$\eta_{Rb-Rb} \approx 99.9\%. \tag{2.51}$$

2.3.4 Rb-^{3}He Spin Exchange Rate

The spin exchange rate, the rate at which spin is transfered from Rb to ^{3}He, is

$$\gamma_{se} = <\sigma_{se}v>[Rb] \tag{2.52}$$

$$= k_{se}[Rb] \tag{2.53}$$

where [Rb] is the rubidium number density and $k_{se} = <\sigma_{se}v>$ is the temperature independent, velocity-averaged spin-exchange cross section (also called the spin-exchange rate constant) [35]. A summary of measured values for k_{se} is presented in Appendix A.2.1; for Rb,

$$k_{se} = 6.74(025) \times 10^{-20} \text{cm}^3/\text{s}. \tag{2.54}$$

Under typical operating conditions $(T_{oven} = 190^\circ C)$,

$$[Rb] = 6.16 \times 10^{14} \text{cm}^{-3}, \tag{2.55}$$

which gives

$$1/\gamma_{se} \approx 6.7\text{hrs} \tag{2.56}$$

for a single-chambered cell.

2.3.5 Spin Exchange Efficiency

The spin exchange efficiency, η_{Rb-He} is the ratio of the rate at which angular momentum is successfully transfered to ^{3}He to the rate at which rubidium loses angular momentum [36]. In the absence of undesirable electronic relaxation, the efficiency would be 100%.

$$\eta_{Rb-He} = \frac{\gamma_{se}[^3\text{He}]}{\gamma_{se}[^3\text{He}] + \Gamma_{Rb}[Rb]} \tag{2.57}$$

$$= \frac{k_{se}[^3\text{He}]}{k_{se}[^3\text{He}] + \Gamma_{Rb}} \tag{2.58}$$

$$= \left(1 + \frac{\Gamma_{Rb}}{k_{se}[^3\text{He}]}\right)^{-1} \tag{2.59}$$

Under typical operating conditions (Eqns. 2.31, 2.32, 2.33, 2.40),

$$\eta_{Rb-He} \approx .018; \tag{2.60}$$

thus, for these conditions it takes roughly 55 polarized rubidium atoms to polarize one ^{3}He nucleus.

2.4 Spin Exchange with (other) Alkali Metals

Historically, particularly in recent years, SEOP of ^{3}He has employed Rb to transfer laser polarization to ^{3}He. There are several other alkali candidates that outperform Rb in spin-exchange. However, as will be explained in Ch. 2.7, these other candidates are not as desirable for optical pumping.
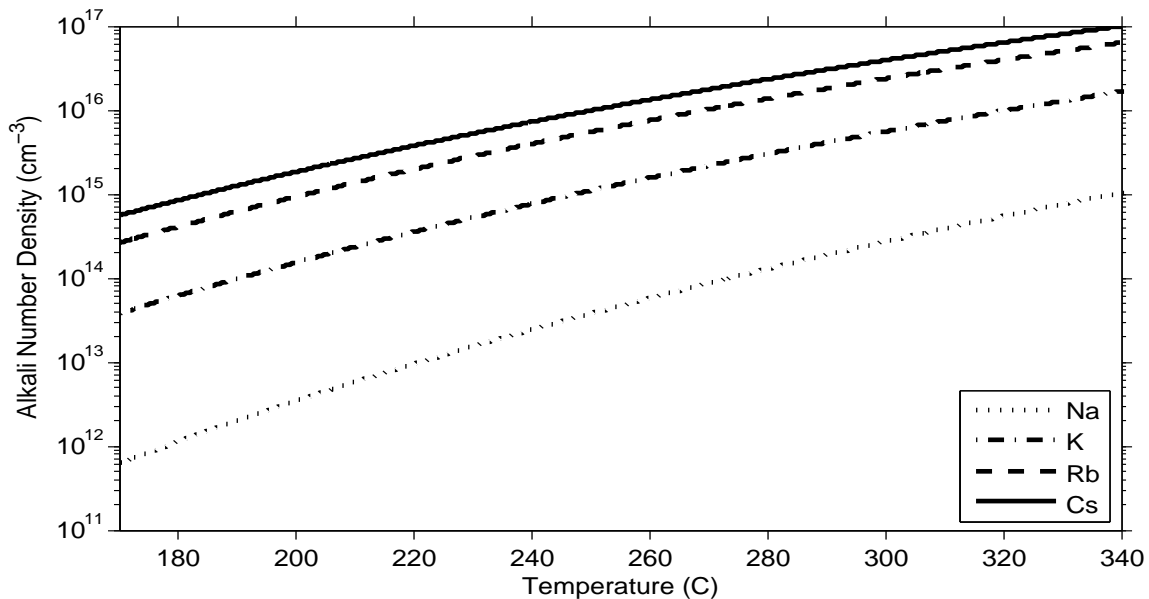
Figure 2.6: Number Density Curves

2.4.1 Vapor Pressure Curves

A liquid (or solid) in a closed system will have a small number of atoms (or molecules) evaporate. The equilibrium vapor pressure is often expressed in Pascals as

$$P = 10^{5.006 + \alpha + \frac{\beta}{T}}, \tag{2.61}$$

where α and β depend on the phase of the element under consideration (see Table 2.1) [2]. The corresponding number density is given by the ideal gas law,

Table 2.1: Alkali Molten Temperature Coefficients [2]

	Sodium	Potassium	Rubidium	Cesium
α	4.704	4.402	4.312	4.165
β	-5377	-4453	-4040	-3830

$$[A] = N/V = P/k_B T \tag{2.62}$$

$$[A] = \frac{1}{k_B T} 10^{5.006 + \alpha + \frac{\beta}{T}}, \tag{2.63}$$

where A refers to the alkali species under consideration. This number density depends on the temperature of the oven, which is in turn determined by the available lower power.

2.4.2 Alkali-X Spin Destruction and Spin-Exchange Rates

Analogous to Ch. 2.2.5, the A-X spin-destruction rate is given by

$$\Gamma_A = \Gamma_{A-A} + \Gamma_{A-^3He} + \Gamma_{A-N_2}, \tag{2.64}$$

where

$$\Gamma_{A-X} = k_{sd}^{A-X}[X]. \tag{2.65}$$

A summary of measurements of these constants can be found in Appendix A and Table 2.2. The temperature dependence of the spin-destruction rates are as follows:

$$k_{sd}^{A-3He}(T) = k_{sd473}^{A-3He}\left(\frac{T}{473.15K}\right)^{3.31(12)} \tag{2.66}$$

$$k_{sd}^{A-N2}(T) = k_{sd473}^{A-N2}\left(\frac{T}{473.15K}\right)^{2.0(25)} \tag{2.67}$$

The spin-exchange rate (see Ch. 2.3.4) for an alkali species, A is given by

$$\gamma_{se} = k_{se}^A[A]. \tag{2.68}$$

A summary of measurements of these constants (see Appendix A), is summarized in Table 2.2. The spin-exchange rate for different alkali metals are plotted (at compared to Rb) in Fig. 2.7.

Heavier metals tend to have higher spin-exchange and spin-destruction rates (see

	Spin Destruction						Spin Exchange			
	k_{sd473}^{A-3He}	Err.	k_{sd473}^{A-N2}	Err.	k_{sd473}^{A-A}	Err.	k_{se}^{A-He}	Err.	k_{se}^{A-A}	Err.
Na	0.15	33%			5.22	8%	4.74	10%	9.4	0.5%
K	4.7	6.4%	150	30%	9.16	10%	5.15	3.3%	11.3	4%
Rb	55.9	1.6%	290	10%	48.1	10%	6.74	2.5%	8.4	4%
Cs	530	5.7%	2100	9.5%	808	10%	11.1	10%	7.2	4%
units	Hz/amg		Hz/amg		10^{-14} cm^3/s		10^{-20} cm^3/s		10^{-10} cm^3/s	

Table 2.2: Spin-Destruction (at 473.15 K) and Spin-Exchange Rates from sources discussed in Appendix A. Note that all rates increase for heavier elements (except for A-A, which are all roughly the same), but spin-destruction rates increase more than spin-exchange rates.

	Spin-Relaxation Rates (Hz)				Spin-Exchange Efficiencies	
Element	Γ_{A-3He}	Γ_{A-N2}	Γ_{A-A}	Γ_{Total}	η_{A-He}	$1/\eta_{A-He}$
Na	2.4	20†	45	67	0.117	8.5
K	44	14	74	132	0.0684	15
Rb	365	22	293	680	0.0182	54
Cs	2791	141	3012	5944	0.00350	286

Table 2.3: Spin-Relaxation Rates and Spin-Exchange Efficiencies for $\gamma_{se} = 1/(6.7\text{hrs})$. The last column, $1/\eta_A$ is the number of collisions before a successful spin exchange occurs between an alkali atom and a ^{3}He atom. †Used k_{sd}^{A-N2}.

Table 2.2); however, whereas the spin-exchange rates are all approximately the same, the spin-destruction rates vary by orders of magnitude. It is for this reason that lighter alkali metals make for more desireable spin-exchange partners.

2.4.3 Spin-Exchange Efficiency

The spin-exchange efficiency (see Ch. 2.3.5) between an alkali metal A and a ^{3}He atom is defined as

$$\eta_{A-He} = \left(1 + \frac{\Gamma_A}{k_{se}^A[^3\text{He}]}\right)^{-1}. \tag{2.69}$$

If the cells are designed to give the same operating ^{3}He and N$_2$ densities (Eq. 2.31,2.32), the spin-exchange efficiency for different alkali metals can be compared for a given spin-exchange rate (which is itself determined by the available laser power). Spin-exchange efficiencies for several alkali metals are listed in Table 2.3.
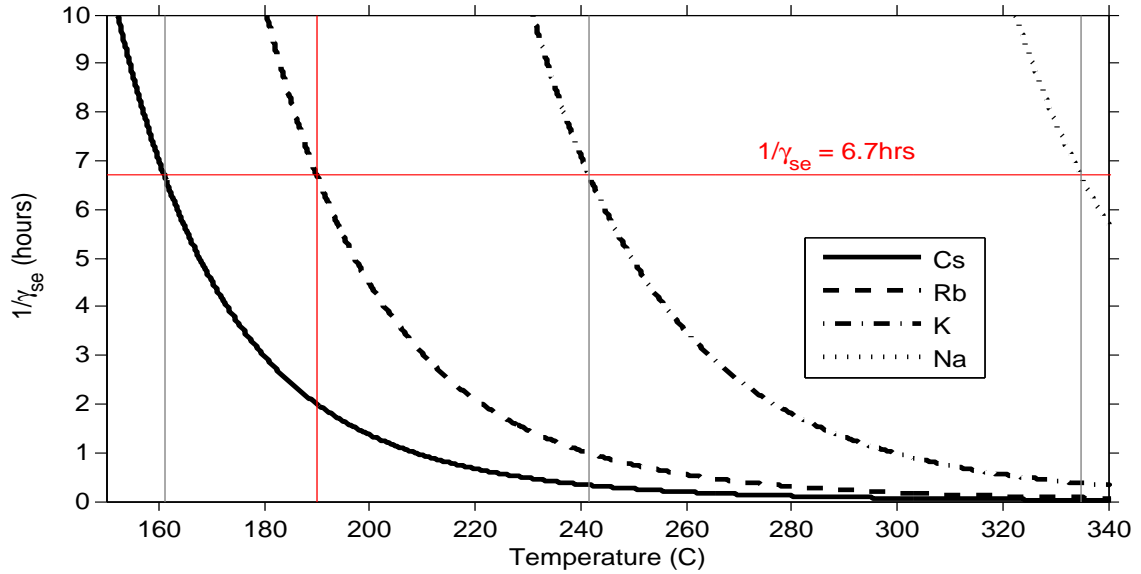
Figure 2.7: Alkali-^{3}He Spin-Exchange Rates. The red lines show a Rb-^{3}He spin-exchange rate of 1/6.7hrs at 190C. The gray lines show that the same spin-exchange rate occurs at different temperatures for different alkali metals.

2.5 ^{3}He **Spinup and Relaxation**

^{3}He polarization accumulation (spinup) is analogous to alkali polarization accumulation (see Eqn. 2.41, 2.42)

$$P_{He}(t) = P_0^{He} e^{-(\gamma_{se}+\Gamma)t} + P_\infty^{He} \left(1 - e^{-(\gamma_{se}+\Gamma)t} \right), \qquad (2.70)$$

where

$$P_\infty^{He} = P_\infty^{Rb} \frac{\gamma_{se}}{\gamma_{se}+\Gamma}, \qquad (2.71)$$

and γ_{se} is the spin-exchange rate (Eqn. 2.53) and Γ is the net ^{3}He relaxation rate.

There are many ways ^{3}He polarization can relax, including through collisions with other ^{3}He atoms [37], magnetic field inhomogeneities [38–40], and through cell wall collisions [38, 41, 42]. The net helium relaxation rate is given by the sum of these

mechanisms:

$$\Gamma = \Gamma_{dipolar} + \Gamma_{field} + \Gamma_{wall}. \tag{2.72}$$

In the presence of an electron beam, there is an additional relaxation rate, Γ_{beam}.

2.5.1 Dipolar Relaxation

When two ^{3}He atoms collide, nuclear spin (polarization) is coupled to oribital angular momentum by the magnetic dipole interaction; this coupling creates an intrinsic ^{3}He relaxation rate that is density dependant [37]. The room temperature dipolar bulk relaxation rate is given by

$$\Gamma_{dipolar} = \frac{[^3\text{He}]}{744}\text{hrs}^{-1}. \tag{2.73}$$

We typically fill cells to a uniform-temperature [He] of ≈ 8 amg, giving

$$\Gamma_{dipolar} \approx 1/(93\text{hrs}). \tag{2.74}$$

The cell-averaged (Eq. 5.72) dipolar relaxation rate is approximately the same under operating conditions (hot PC).

2.5.2 Relaxation Due To Magnetic Field Inhomogeneities

To a randomly moving ^{3}He atom, magnetic field inhomogeneities appear as a changing magnetic field. This time-dependant magnetic field can couple to the nuclear spin of the ^{3}He atom and induce relaxation [38–40],

$$\Gamma_{field} = D\frac{|\nabla B_x|^2 + |\nabla B_y|^2}{B_0^2} \tag{2.75}$$

where D is the ^{3}He self-diffusion coefficient, ∇B_x and ∇B_y are the transverse magnetic field gradients, and B_0 is the main holding field, oriented along the z-axis. The self-

diffusion coefficent of ^{3}He has been measured at 300K [43]

$$D = \frac{1440(80)\text{torr}}{P} \; cm^2/s. \tag{2.76}$$

Under typical operating conditions, $P \approx 12.5$ atm $= 9500$ torr,

$$D \approx .15 \; cm^2/s. \tag{2.77}$$

Our main holding field is established by a large ($\approx$1.5m diameter) helmholtz pair, which we run at 13 Gauss. The transverse magnetic field gradients intrinsic to the coils are $\lesssim$ 10 mG/cm [44]. This gives a negligible ^{3}He relaxation rate of

$$\Gamma_{field} \approx 1/(3600hrs). \tag{2.78}$$

2.5.3 Wall Relaxation

The target cells studied in this thesis were constructed out of reblown GE-180 (an aluminosilicate glass with low permeability [45]). Because aluminosilicate glasses are expensive, difficult to work with and are composed of atoms with heavier nuclei (unfavorable in electron scatter experiments), some groups use permeable borosilicate cells (Pyrex) that have a thin aluminosilicate (sol-gel) coating [46].

The surface physics behind ^{3}He wall relaxation is not well understood. At present, ^{3}He wall relaxation is believed to be caused by several mechanisms, including paramagnetic impurities in the glass, ^{3}He atoms becoming trapped in microfissures in the glass surface, and ferromagnetic impurities associated with the alkali metal [1, 34, 42]. It was found that reblowing the glass and following with a strong acid rinse minimized the first two mechanisms, while degaussing the cells minimizes the last one [34, 42].

Although cells have been made at the dipolar relaxation rate limit [37], our cells are typically limited by wall relaxation. We use Adiabatic Fast Passage (AFP) NMR (see

Cell Parameters		Lifetime (hrs)		
Cell Name	Fill Density (amg)	Dipolar	Wall	Total
Tigger	7.81	95.3	14.5	12.6
Samantha	7.85	94.8	28.7	22
Alex	7.93	93.8	52.6	33.7
Brady	7.87	94.5	58.1	36
Moss	7.81	95.3	71.1	40.7
Stephanie	8.02	92.8	99.5	48
Astral Weeks	8.08	92.1	104.7	49
Sosa	7.97	93.4	489.5	78.4

Table 2.4: Typical Target Cell Lifetimes

Ch. 3.1) to measure the room-temperature relaxation rate. Typical values for target cell relaxation rates ($\bar{\Gamma}$) range from $1/(10 \text{ hrs})$ to $1/(80 \text{ hrs})$. The wall contribution can be extracted using Eq. 2.72 (see Table 2.4).

Finally, we note that although wall relaxation is not well understood, it is believed to scale with the surface-to-volume ratio of the cell [26]:

$$\Gamma_{wall} \propto S/V \tag{2.79}$$

2.6 The X Factor

Until recently, it was assumed that if an infinite amount of resonant laser light was used to optically pump a very dense alkali vapor ($\gamma_{se} \gg \Gamma$), a near-unity ^{3}He polarization could be achieved (see Eq. 2.71). However, Babcock et al. recently suggested that there exists an additional surface-relaxation mechanism that appears to scale with the alkali metal density and the surface to volume ratio of the cell [47]. This cell-instrinsic relaxation rate limits the achievable ^{3}He polarization, even in the presence of infinite optical-pumping power. The equilibrium ^{3}He polarization (2.71) is now given by

$$P_\infty^{He} = P_\infty^{Rb} \frac{\gamma_{se}}{\gamma_{se}(1 + X) + \Gamma}, \tag{2.80}$$

where X appears to increase with S/V. We note that in the high spin-exchange rate limit $\gamma_{se} \gg \Gamma$,

$$P_\infty^{He} = P_\infty^{Rb} \frac{1}{1+X}. \tag{2.81}$$

Measurement techniques and results for our cells will be presented in Ch. 5.3.

2.7 Hybrid Spin Exchange

Rb-^{3}He spin exchange is a relatively inefficient process [36]: under the conditions described in Ch. 2.3.5, it takes approximately 55 polarized Rb atoms to polarize one ^{3}He atom. Spin exchange with a lighter alkali metal is more efficent: under similar conditions, it takes roughly 15 polarized potassium (K) atoms or 8 polarized sodium (Na) atoms to polarize one ^{3}He atom (see Table 2.3). This greater efficiency is because although the spin-exchange rate constants are about the same for the alkali metals, the spin-destruction rate constants are much higher for heavier alkali metals (see Ch. 2.4.2 and Tab. 2.2).

Unfortunately, optical pumping of lighter alkali metals is more difficult. Moreover, less is know about optical pumping alkali metals other than Rb. To optically pump alkali metals other than Rb, new lasers must be purchased. Such lasers currently are not as powerful and inexpensive as those for Rb optical pumping. Aside from the need to invest in new laser systems, lighter alkali metals have lower vapor pressure curves and therefore must be heated to higher temperatures to achieve a sufficiently dense vapor for spin exchange (such high temperatures are experimentally difficult). Additionally, whereas the D1-D2 fine structure splitting for Rb is 15nm, for K it's 3.4nm, and for Na it's 0.6nm (see Table 2.7). The work of Singh's Thesis [6] suggests that such small splittings lead to inefficient optical pumping even with line-narrowed lasers. The hybrid technique attempts to solve these problems [48].

The hybrid technique employs a mixture of Rb and K; the lasers optically pump
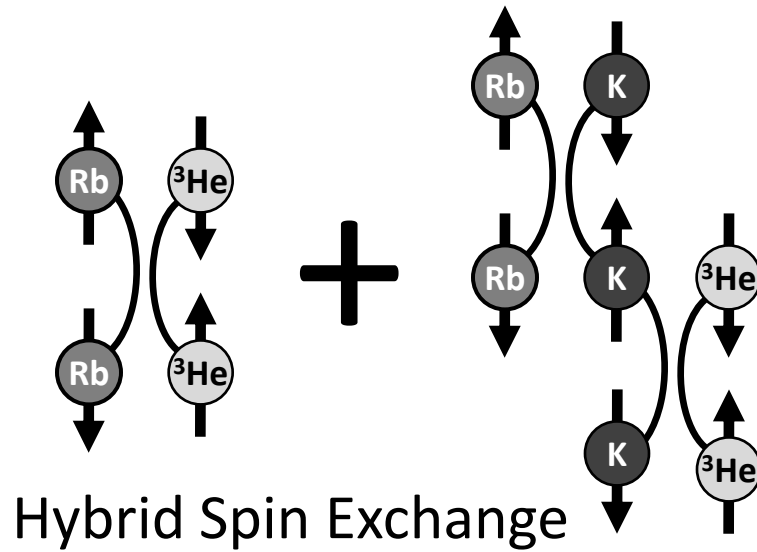
Figure 2.8: Hybrid Spin-Exchange

the former and it shares its polarization with the latter with minimal losses. Both atoms spin exchange with ^{3}He (see Fig. 2.8); however, for a fixed amount of laser light, a lower (laser-absorbing) Rb density can be used which allows the laser light to penetrate deeper into the cell. In order to compensate for the lower Rb density, the K density is increased and therefore, K carries out the majority of spin exchange. The laser polarized Rb indirectly transfers its spin more efficiently, and higher ^{3}He polarizations ($\approx 55\%$) can be attained at comparable spin-exchange rates.

	D2 (nm)	D1 (nm)	Δ (nm)	T_{melt} (C)	T_{boil} (C)	M(g/mol)
Lithium	670.776	670.791	0.015	180.54	1342	6.941
Sodium	588.9950	589.5924	.5974	97.81	882.9	22.98977
Potassium	766.49	769.896	3.4	63.25	760	39.0983
Rubidium	780.0268	794.7603	14.7335	38.89	686	85.4678
Cesium	852.113	894.347	42.234	28.40	669.3	132.90545
Francium	717.9866	816.9418	88.9552	27	677	223

Table 2.5: Alkali Metal Transistion Line [3], Phase Transition and Molar Mass [4] Data

Element	k_{sd}^{Rb-A}	Err.	k_{se}^{Rb-A}	Err.
Na	17.5	9%	7.9	1.4%
K	21.8	10%	10.1	4%
Rb	48.1	10%	8.4	4%
Cs	199.5	10%	9.8	4%
Units	$10^{-14}\text{cm}^3/\text{s}$		$10^{-10}\text{cm}^3/\text{s}$	

Table 2.6: Rb-Alkali Spin-Exchange Rate Constants (compiled from data in Appendix A). Note that the spin-exchange rate constants are all about the same, but the spin-destruction rate constants increase for heavier alkali metals.

2.7.1 Rb-A Rate Constants

Through collisions with polarized Rb, the second alkali metal (usually K) becomes polarized. The spin-exchange rate for such a collision is given by

$$\gamma_{se}^{Rb-A} = k_{se}^{Rb-A}[A] \tag{2.82}$$

where

$$k_{se}^{Rb-A} = <\sigma_{se}^{Rb-A}v> \tag{2.83}$$

$$v = \sqrt{v_{Rb}v_A}, \tag{2.84}$$

$$\sigma = \sqrt{\sigma_{Rb}\sigma_A}. \tag{2.85}$$

Such collisions can also lead to spin-destruction and have analogous equations. A summary of Rb-alkali spin-exchange (destruction) rate constants is presented in Appendix A, which is distilled in Table 2.6; it should be noted that $k_{se}^{Rb-A} \gg k_{se}^{Rb-A}$.

Alkali-Alkali collisions are very fast and efficient ($\gamma_{se}^{Rb-A} \approx 500\text{kHz}$ and $\eta_{Rb-A} \approx 99.9\%$, see Ch. 2.3.3).

2.7.2 Hybrid Alkali-³He Spin-Exchange Rate

In a hybrid cell, both alkali metals spin exchange with ^{3}He (see Fig. 2.8). The spin-exchange rate for such cells is given by the sum of the two rates,

$$\gamma_{se} = k_{se}^{Rb-He}[Rb] + k_{se}^{A-He}[A], \tag{2.86}$$

$$= k_{se}^{Rb-He}[Rb] \left(1 + D\frac{k_{se}^{A-He}}{k_{se}^{Rb-He}}\right), \tag{2.87}$$

where

$$D = [A]/[Rb] \tag{2.88}$$

is the temperature-dependant hybrid number density ratio. This temperature dependance is due to the two metals having different vapor pressure curves (see Ch. 2.4.1). In the absence of a second alkali metal (D = 0), this Eq. 2.87 reduces to Eq. 2.53. We have made cells with operating-temperature D's ranging from 2 to 20.

The same ^{3}He spin-exchange rate from a $D = 0$ (a pure Rb cell, (Eq. 2.56)) can be achieved in a hybrid cell at a lower Rb density by increasing D. The benefit to lowering the Rb density is that the same amount of laser light can penetrate deeper into the cell. A spin-exchange rate of 1/6.7 hrs (see Eqn. 2.56) with a Rb density of 1.10×10^{14}cm^{-3} (5.6 times lower than the pure Rb density (see Eq. 2.33)) can be attained in a D = 6 hybrid K/Rb cell. Such a cell would need to be operated at 237.2C to maintain an adequate alkali density. Density ratios and operating temperatures for other rubidium-alkali mixtures are summarized in Table 2.7.

2.7.3 Hybrid Alkali-³He Spin-Relaxation Rate

The effective rubidium-relaxation rate, as defined by Babcock, is [36, 49]

$$\Gamma'_{Rb} = \Gamma_{Rb} + D\left(\Gamma_K + 2k_{sd}^{Rb-A}[Rb]\right). \tag{2.89}$$

Mix	$D(T_{oven})$	$T_{oven}(C)$	f_{Rb}	Γ_A	Γ'_{Rb}	$1/\eta$	$1/\eta_{pure}$	$m_{Rb}(mg)$
Na/Rb	6.52	328.8	0.00227	$60^\dagger$	$1601^\dagger$	24	8	8.4590
K/Rb	6.0	237.2	0.0308	119	1585	23	14	69.4675
Cs/Rb	2.78	169.5	0.433	5409	16700	236	278	491.0939

Table 2.7: Hybrid Density Ratios and Operating Temperatures. The value for D was determined using a spin-exchange rate of $1/\gamma_{se} = 6.7$hrs with $[Rb] = 1.103 \times 10^{14}$cm^{-3} (see Eqn. 2.87). The last column gives the mass of Rb needed per gram of A. †Since no value for k_{sd}^{Na-N2} was available, k_{sd}^{K-N2} was used instead. This substitution probably overestimates Γ_{Na}; however, a lower bound of $\Gamma_{Na} = 40$Hz can be established if nitrogen relaxation is ignored. This gives $\Gamma'_{Rb} = 1471$Hz and $1/\eta = 22$.

We choose to use this notation as it facilitates direct comparision with pure-Rb cells.

For a hybrid cell operating at the same spin-exchange rate as a pure-Rb cell, effective Rb-relaxation rate *increases*. For D = 6 and $1/\gamma_{se} = 6.7$hrs,

$$\Gamma'_{Rb} \approx 545 + 6 \times (133 + 48)\, Hz \tag{2.90}$$

$$\approx 1630 Hz, \tag{2.91}$$

much higher than 680 Hz (see Eq. 2.40).

2.7.4 Hybrid Spin-Exchange Efficiency

The spin-exchange efficiency (see Ch. 2.3.5) for hybrid mixtures is given by

$$
\begin{aligned}
\eta_{hybrid} &= \frac{\gamma_{se}[^3\text{He}]}{\gamma_{se}[^3\text{He}] + \Gamma'_{Rb}[Rb]} \\[2mm]
&= \frac{k_{se}^{Rb-He}[Rb]\left(1 + D\frac{k_{se}^{A-He}}{k_{se}^{Rb-He}}\right)[^3\text{He}]}{k_{se}^{Rb-He}[Rb]\left(1 + D\frac{k_{se}^{A-He}}{k_{se}^{Rb-He}}\right)[^3\text{He}] + \Gamma'_{Rb}[Rb]} \\[2mm]
&= \left(1 + \frac{1}{\left(1 + D\frac{k_{se}^{A-He}}{k_{se}^{Rb-He}}\right)}\frac{\Gamma'_{Rb}}{k_{se}^{Rb-He}[^3\text{He}]}\right)^{-1} \\[2mm]
&= \left(1 + \underbrace{\frac{\Gamma'_{Rb}/\Gamma_{Rb}}{\left(1 + D\frac{k_{se}^{A-He}}{k_{se}^{Rb-He}}\right)}}_{<1} \underbrace{\frac{\Gamma_{Rb}}{k_{se}^{Rb-He}[^3\text{He}]}}_{PureRb}\right)^{-1}.
\end{aligned}
$$

(2.92)

(2.93)

(2.94)

(2.95)

Although Γ'_{Rb} is larger for a hybrid cell (than a pure Rb cell), the efficiency is higher because the Rb density is lower.

For a D = 6 K/Rb hybrid cell operating at 237.2C,

$$\eta_{hybrid} \approx 0.0427. \tag{2.96}$$

This efficiency is in-between that of a pure-Rb or pure-K cell (see Table 2.3). The efficiency can be increased up to the pure-K limit (by increasing D). Table 2.7 lists $1/\eta$ for several hybrid mixtures. Interestingly, for $1/\gamma_{se} = 6.7$hrs and $[Rb] = 1.10\times10^{14}\text{cm}^{-3}$, a K/Rb mixture performs about as well as a Na/Rb mixture (a pure Na cell would outperform a pure K cell). This is because the Rb relaxation grows very large at the high temperature necessary for Na.

Fig. 2.9 models hybrid alkali performance for different spin-exchange rates. Qualitatively, hybrid-alkali mixtures stretch out the polarization roll-off curve (a lower Rb density allows for deeper laser penetration). Line-narrowed lasers change the shape

to a sharper roll-off (the more resonant laser light is absorbed quicker). When used in conjunction, a larger cell can be more highly polarized. It should be noted however, that all four methods perform the same when either the laser power is insufficient and is thus all absorbed (bottom graph in Fig. 2.9). When the laser power is overwhelming (and is mostly transmitted), the line-narrowed methods perform the best; however, for similar laser conditions, a pure-Rb cell will actually outperform its hybrid counterpart. The size of the pumping chamber and alkali density are critical in ensuring optimal performance.

2.8 Creating Hybrid Mixtures

2.8.1 Hybrid Chemistry

Given a spin-exchange rate, γ_{se}, and a number-density ratio, D, the appropriate room-temperature masses of a hybrid alkali mixture can be calculated. Raoult's Law states that the partial vapor pressure of a component, X in a system is proportional to the vapor pressure of the pure component by mole fraction, f, of that component (see for example [50])

$$P_X = f P_0. \tag{2.97}$$

The mole fraction of a component, X is defined to be

$$f_X \equiv \frac{m_X/M_X}{\sum_i m_i/M_i}, \tag{2.98}$$

where M is a molar mass. Applying the ideal gas law to Eq. 2.97,

$$[A] = f_A [A]_0 \tag{2.99}$$
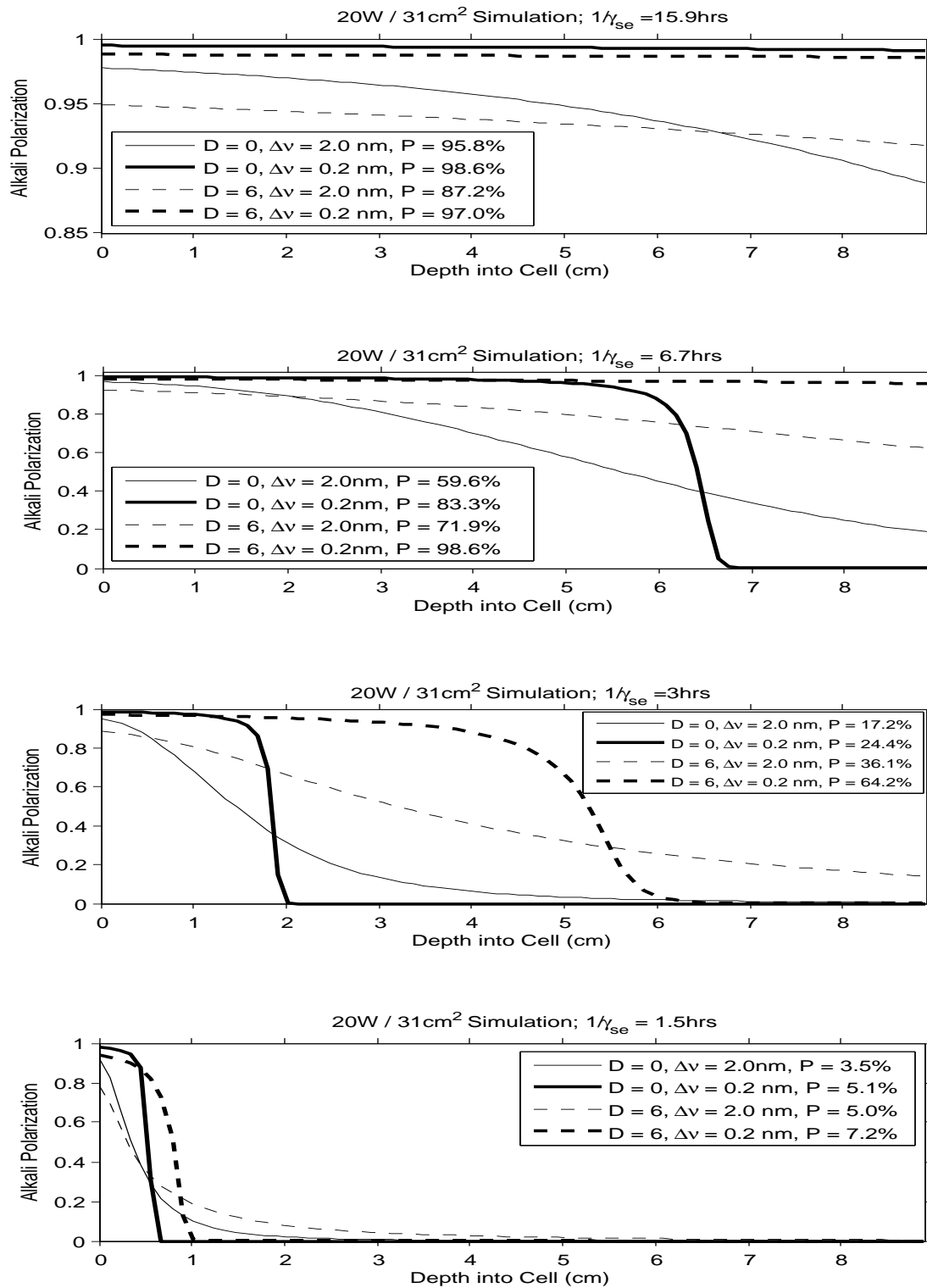
Figure 2.9: Simulation for a 3.5" K/Rb spherical cell with D = 6 (similar to Fig. 2.5). Different spin-exchange rates are plotted. In each plot, the y-axis refers to the polarization along the axis of the cell; the polarization quoted in the legend is volume-averaged. Note that for low and high spin-exchange rates, all 4 curves given roughly the same polarization. Line-narrowed lasers and hybrid cells only outperform their counterparts under certain conditions.

where A refers to the alkali metal under consideration. The temperature dependance of the number density ratio (Eqn. 2.88) can be separated

$$D(T) = \frac{f_A[A]_0}{f_{Rb}[Rb]_0} = \frac{f_A}{f_{Rb}} D_0(T), \tag{2.100}$$

where

$$D_0(T) = \frac{[A]_0}{[Rb]_0} = 10^{(\alpha_A - \alpha_{Rb} + (\beta_A - \beta_{Rb})/T)}. \tag{2.101}$$

The coefficients α and β can be found in Table 2.1. For a K/Rb mixture at 237.2C, $D_0 = 0.191$.

Since we are dealing with a two state system,

$$f_A + f_{Rb} = 1. \tag{2.102}$$

Plugging into Eq. (2.100),

$$D(T) = \frac{1 - f_{Rb}}{f_{Rb}} D_0(T). \tag{2.103}$$

For a Rb-A hybrid mixture Eq. 2.98 can be written as

$$f_{Rb} = \left(1 + \frac{m_A M_{Rb}}{m_{Rb} M_A}\right)^{-1}. \tag{2.104}$$

Values for M are summarized in Table 2.7. Finally, Eqn. 2.103 can be simplified using Eqn. 2.104.

$$D(T) = \frac{m_A M_{Rb}}{m_{Rb} M_A} D_0(T). \tag{2.105}$$

We typically work with mixtures that have 1.0g of K (or other alkali metal) and a small amount of Rb (see Table 2.7). Note that such mixtures will only have the right D at the chosen operating temperature (see Fig. 2.10).
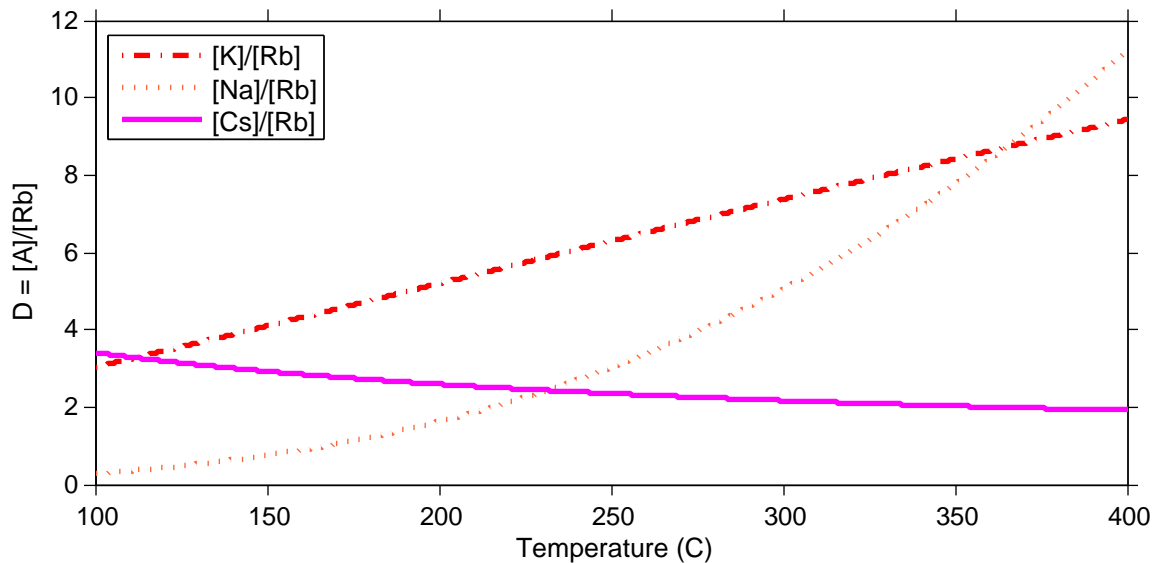
Figure 2.10: Temperature Dependance of $1/\gamma_{se} = 6.7$hrs Alkali Mixtures (see Table 2.7)

2.8.2   Mixing Alkali Metals

All alkali metals react violently with oxygen and water. Consequently, to prepare a hybrid mixture, an inert atmosphere is necessary. Our laboratory employs a glovebox, which is filled with the boil-off of a liquid nitrogen dewar; although nitrogen is not totally inert, it is economical and convenient. Because it is impossible to avoid trace amounts of oxygen and water, the gas inside the glovebox is passed continously through a regenerable purifier. The levels of moisture and oxygen can be measured with a "lightbulb test," in which the lifetime of an exposed incandescent filament is monitored. A duration of greater than 6 hours without the filament burning out corresponds to contamenant levels less than 5 ppm [51]. Alkali metal mixtures were only considered pure enough if the lightbulb lasted more than 6 hours; often, the test would suceed for several days.

Alkali-hybrid alloys are prepared by adding an appropriate amount(see Table. 2.7) of Rb to A. Approximately 1g of molten A (usually K) is poured into a prescored ampoule with a narrow neck. The K is then allowed to cool. Once cooled, m_K is
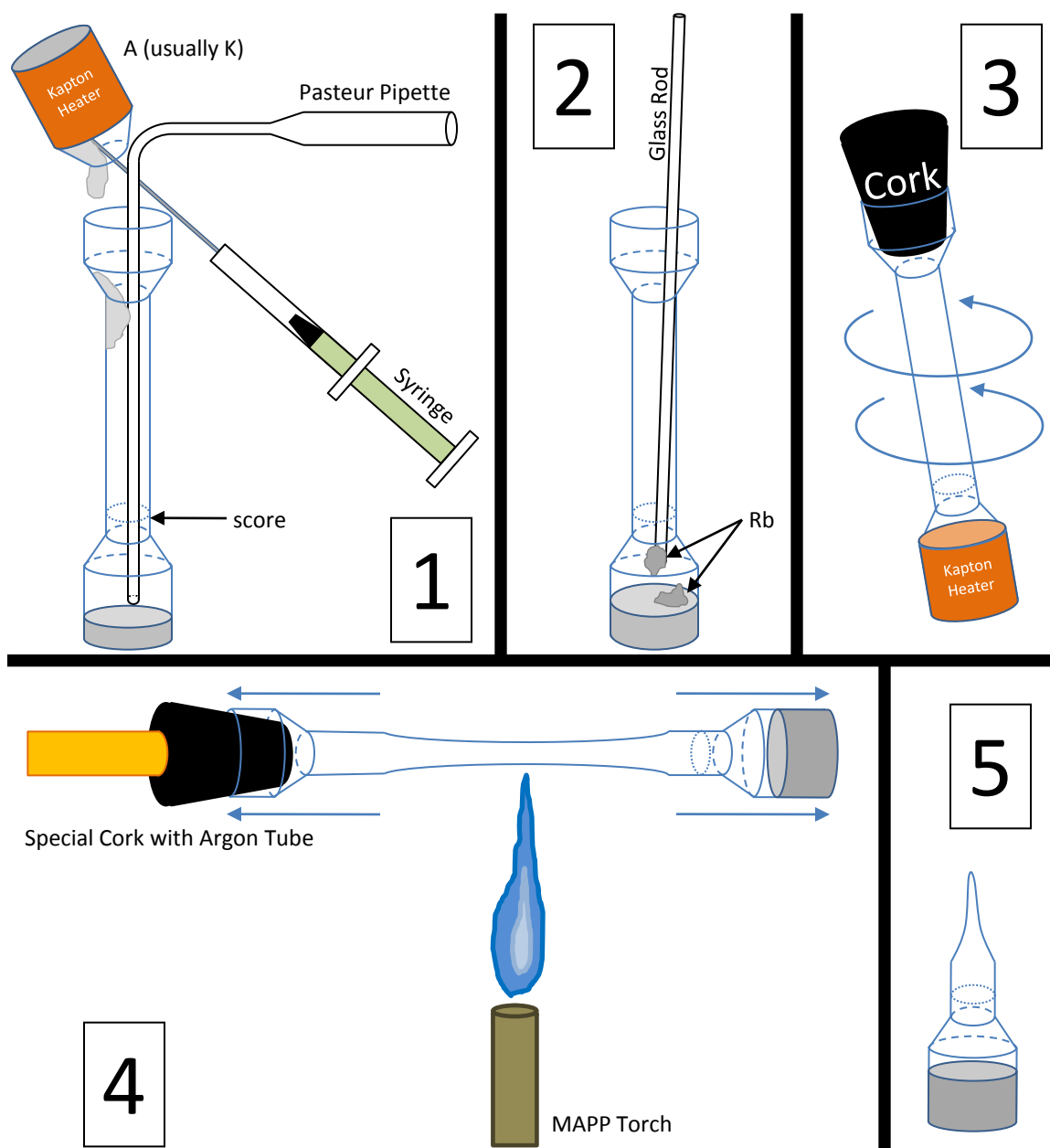
Figure 2.11: Glovebox Procedure: 1. Molten alkali (K,Na, or Cs) is forced out of its ampoule with a syringe (filled with glovebox air). The Pasteur pipette is necessary as the molten alkali forms beads wider than the neck of the ampoule (these beads would become stuck in the neck if gas from the bottom of the ampoule couldn't escape). 2. Solid Rb is lowered into the ampoule. 3. Once the desired mass ratio has been reached, the mixture is corked, heated, and swirled. 4. The ampoule is permanently sealed under argon. 5. The prescored ampoule can now be heated and agitated more thoroughly before being used in a target cell.

measured using an analytic balance. Small amounts of solid Rb (which is sticky) are lowered on the end of a glass rod into the prescored ampoule, while $m_K + m_{Rb}$ is monitored. Once the desired mass ratio has been achieved (see Eq. 2.105), the prescored ampoule is heated until the mixture melts. The molten alloy is then mixed by swirling the prescored ampoule. Finally, the mixture is corked, cooled, and removed from the glovebox. Once outside, the prescored ampoule is placed inside of an open box which has been filled with argon. The cork is removed and replaced with a special cork. The special cork has a hole drilled axially through it and is connected to tubing, which is filled with argon. The tubing is then removed from the argon bottle so there is no positive pressure inside it. Finally, the prescored ampoule is sealed along the narrow neck using a MAPP (methylacetylene-propadiene propane) torch. The sealed ampoule is then heated and thoroughly agitated. Fig. 2.11 summarizes the procedure.

Chapter 3

^{3}He Polarimetry

3.1 Nuclear Magnetic Resonance

Nuclear Magnetic Resonance (NMR) provides a method for measuring noble gas polarization that relies on the interaction of the magnetic dipole moment with an external magnetic field. The Hamiltonian for this interaction is

$$\mathcal{H} = -\boldsymbol{\mu} \cdot \mathbf{B}_0, \tag{3.1}$$

where μ is the magnetic moment of ³He. Hence, in the presence of an external magnetic field, the energy levels of ³He are split by an amount

$$U = -\boldsymbol{\mu} \cdot \mathbf{B}_0. \tag{3.2}$$

This is known as Zeeman splitting. If an oscillating magnetic field is introduced both perpendicular to the static holding field ($\mathbf{B}_0$ above) and at the frequency $\omega = U/\hbar$, resonance is achieved and transitions between the two states can occur.

For a spin-1/2 particle in a magnetic field oriented along the z-axis, Eq. (3.2) reads

$$U = -\mu_z B_0, \tag{3.3}$$

where

$$\mu_z = g\frac{q_e}{2m}S_z, \tag{3.4}$$

here, g is the Lande g-factor which has a value of 2(-1.93) for a neutron and S_z has eigenvalues $\pm\frac{\hbar}{2}$. The energy separating the two states is

$$\Delta U = g\frac{q_e}{2m}\hbar B_0 = g\mu_N B_0, \tag{3.5}$$

where μ_N is the nuclear magneton and has the value

$$\mu_N = \frac{q_e}{2m_n}\hbar \approx 5.051 \times 10^{-27} J/T. \tag{3.6}$$

These two states are separated in frequency by

$$\omega = \frac{g\mu_N B_0}{\hbar} = \gamma B_0, \tag{3.7}$$

where the gyromagnetic ratio, $\gamma/2\pi \approx 3.2434\text{kHz/Gauss}$ has been introduced. Clearly, the resonant transition frequency depends upon the size of the holding field (and vice versa). That is, NMR can be performed at either a fixed RF frequency while the holding field is swept, or a fixed holding field with the RF frequency swept. We measure the ³He magnetization using a fixed RF frequency; however we use the other technique when performing an EPR calibration measurement (see Ch. 3.2).

3.1.1 Adiabatic Fast Passage

When we perform an NMR measurement, we sweep our holding field (B_0) from below to above resonance. Specifically, we perform an Adiabatic Fast Passage (AFP) sweep [52]. The sweep is considered adiabatic if the effective field the nuclear spins feel is changed slowly enough that they can track the effective holding field (the eigenvectors of the system don't change).

$$\frac{\dot{B}}{B_1} \ll \omega \tag{3.8}$$

Under our typical operating conditions, we had

$$\dot{B} \approx 9G/6s \tag{3.9}$$

$$B_1 \approx 100mG \tag{3.10}$$

$$\omega = 56.6kHz \tag{3.11}$$

The sweep is considered fast if the time the spins are exposed to highly relaxing magnetic field inhomogeneities is minimized. In the rotating frame, the relaxation rate is given by [53]

$$\frac{1}{T_{1r}} = D\frac{|\nabla B_z|^2{}^2}{B_1} \tag{3.12}$$

Consequently, we require

$$D\frac{|\nabla B_z|^2}{B_1^2} \ll \frac{\dot{B}}{B_1} \tag{3.13}$$

Under typical operating conditions,

$$D \approx 0.15cm^2/s \tag{3.14}$$

$$\frac{|\nabla B_z|^2}{B_1^2} \approx \left(\frac{10mG}{1cm}\right)^2 \tag{3.15}$$

Combining the above equations and evaluating using typical values,

$$\underbrace{D\frac{|\nabla B_z|^2}{B_1^2}}_{1.5mHz} \ll \underbrace{\frac{\dot{B}}{B_1}}_{15Hz} \ll \underbrace{\omega}_{56.6kHz} \tag{3.16}$$

The left-most term in the above equation gives the relaxation rate of the ³He atoms during a measurement. This term can be quite large along the target chamber of the cell, whose long ends sit outside of the most uniform region of the helmholtz pair. However, because the measurements are made relatively quickly, the losses are kept to approximately 1% per measurement.

3.1.2 The Co-Rotating Frame of Reference

This section follows the work presented by A. Abragam [52]. A Nuclear spin has an angular momentum, $\mathbf{I}$ and an associated magnetic dipole moment $\mathbf{m} = \gamma\mathbf{I}$. In the presence of an external magnetic field, $\mathbf{B_0}$, the magnetic moment will experience a torque, $\mathbf{N} = \mathbf{m} \times \mathbf{B_0}$. This torque will in turn cause a change in the angular momentum of the spin,

$$\mathbf{N} = \frac{d\mathbf{I}}{dt} = \mathbf{m} \times \mathbf{B_0} \tag{3.17}$$

$$\frac{d\mathbf{m}}{dt} = \gamma\mathbf{m} \times \mathbf{B_0} \tag{3.18}$$

In the context of NMR, the most convenient frame of reference is one rotating *clockwise* ($\boldsymbol{\omega} = \omega(-\hat{\mathbf{z}})$) about the external holding field. This restricts the motion of the magnetic dipole to a plane. The coordinate transformation to a frame rotating clockwise is a simple one:

$$\hat{\mathbf{x}}' = \cos\omega t\hat{\mathbf{x}} - \sin\omega t\hat{\mathbf{y}} \tag{3.19}$$

$$\hat{\mathbf{y}}' = \sin\omega t\hat{\mathbf{x}} + \cos\omega t\hat{\mathbf{y}} \tag{3.20}$$

conversely,

$$\hat{\mathbf{x}} = \cos\omega t\hat{\mathbf{x}}' + \sin\omega t\hat{\mathbf{y}}' \tag{3.21}$$

$$\hat{\mathbf{y}} = -\sin\omega t\hat{\mathbf{x}}' + \cos\omega t\hat{\mathbf{y}}' \tag{3.22}$$

The appropriate vector transformation is given by

$$\frac{d\mathbf{x}}{dt}_{stationary} = \frac{d\mathbf{x}}{dt}_{rotating} + \boldsymbol{\omega} \times \mathbf{x}, \tag{3.23}$$

where ω is the frequency at which the frame rotates. Thus,

$$\frac{d\mathbf{m}}{dt}_{rotating} = \frac{d\mathbf{m}}{dt}_{stationary} - \boldsymbol{\omega} \times \mathbf{m} \qquad (3.24)$$

$$= \gamma\mathbf{m} \times \mathbf{B_0} + \omega(\hat{\mathbf{z}} \times \mathbf{m}) \qquad (3.25)$$

$$= \gamma\mathbf{m} \times (\mathbf{B_0} - \frac{\omega}{\gamma}\hat{\mathbf{z}}) \qquad (3.26)$$

$$= \gamma\mathbf{m} \times \mathbf{B_{eff}}. \qquad (3.27)$$

As the above equation suggests, in the rotating frame, the magnetic dipole experiences an effective field, $\mathbf{B_{eff}} = (\mathbf{B_0} - \frac{\omega}{\gamma}\hat{\mathbf{z}})$. In practice, the external field is comprised of two mutually perpendicular fields – a stationary holding field (oriented along the axis of the pump laser) and a perpendicular oscillatory RF field,

$$\mathbf{B_{eff}} = (B_0 - \frac{\omega}{\gamma})\hat{\mathbf{z}} + B_1\hat{\mathbf{y}}'. \qquad (3.28)$$

3.1.3   Formula for Polarization in Terms of Magnetization

NMR of ^{3}He produces a measurable EMF created by the interaction of the lone neutron's spin with the oscillating RF field. This EMF can be related to the magnetization of the gas, which in turn can be related to the spin polarization of the ^{3}He. The magnetization $\mathbf{M}$ of the gas is

$$\mathbf{M} = [^3He]\boldsymbol{\mu} = \gamma[^3He]\mathbf{I}. \qquad (3.29)$$

The polarization, P is

$$\mathbf{P} = \frac{\mathbf{I}}{I}. \qquad (3.30)$$

Combining the above two equations and plugging in $I = \frac{\hbar}{2}$ for I, we get

$$\mathbf{M} = \gamma/2\pi\frac{h}{2}[^3He]\mathbf{P}. \qquad (3.31)$$

The ³He number density, [³He] is measured during a cell fill. Often, a more precise value for [³He] is obtained from measurements of the pressure-broadened widths of the D1 and D2 transitions. All that remains is to measure the magnetization of the ³He ensemble.

3.1.4 Measuring the Field Created by the ³He Magnetization

Faraday's law of induction states that a change in magnetic flux will induce an EMF in a closed loop,

$$\xi = -\frac{d}{dt}\Phi = -\frac{d}{dt}\int \mathbf{B} \cdot d\mathbf{A}. \tag{3.32}$$

In the lab frame, the EMF is supplied by the changing magnetic field the ³He spins supply during an NMR measurement (their collective magnetic moment changes direction); however, in the rotating frame it is the pickup coils that are changing their orientation with respect to the ³He spins resulting in an EMF. Evaluating Eq. 3.32 is more convenient in a rotating reference frame – instead of keeping track of the direction of the nuclear magnetization, we keep track of a pickup coil that's rotating predictably. In the lab frame, the area vector of the pickup coils (that is, the one pointing along the vector normal to their two dimensional plane) is given by

$$\mathbf{A} = A\hat{\mathbf{x}}. \tag{3.33}$$

In the rotating frame, it is given by

$$\mathbf{A}_{rotating} = A(\cos\omega t\hat{\mathbf{x}}' + \sin\omega t\hat{\mathbf{y}}'). \tag{3.34}$$

Note that there is no explicit time dependence in the magnitude, only in the direction. Furthermore, if the pickup coils are sufficiently small (small enough that the magnetic field provided by the spins can be considered uniform over them), we can simplify

Eqn. (3.32)

$$\xi = -\frac{d}{dt}(\mathbf{B} \cdot \mathbf{A}) = -\frac{d\mathbf{B}}{dt} \cdot \mathbf{A} - \mathbf{B} \cdot \frac{d\mathbf{A}}{dt}, \tag{3.35}$$

where

$$\frac{d\mathbf{A}}{dt} = A\omega(-\sin\omega t\hat{\mathbf{x}}' + \cos\omega t\hat{\mathbf{y}}') \tag{3.36}$$

and $\mathbf{B}$ has yet to be determined.

3.1.5 The Magnetic Field of a Uniformly Magnetized Sphere

The pumping chambers of the cells we work with are approximately spherical. To determine the approximate magnetic field the ³He spins inside it create, it is sufficient to calculate the field of a uniformly magnetized sphere. The calculation is long, tedious, and involves even more coordinate transformations. Fortunately, it is mostly worked out in Griffith's E&M textbook [54]. The field inside a uniformly magnetized sphere is also uniform,

$$B = \frac{2}{3}\mu_0 M. \tag{3.37}$$

The field outside of a uniformly magnetized sphere is equivalent to that of a magnetic dipole whose magnetic dipole moment happens to be $\mathbf{m} = \frac{4\pi}{3}R^3\mathbf{M}$,

$$\mathbf{B_{sphere}} = \frac{\mu_0}{4\pi r^3}(3(\mathbf{m} \cdot \hat{\mathbf{r}})\hat{\mathbf{r}} - \mathbf{m}) \tag{3.38}$$

$$= \frac{\mu_0 R^3}{3r^3}(3(\mathbf{M} \cdot \hat{\mathbf{r}})\hat{\mathbf{r}} - \mathbf{M}). \tag{3.39}$$

The direction of $\hat{\mathbf{r}}$ is a little bit tricky. Clearly, we want to evaluate the magnetic field at the location of the pickup coils (this will be in the $\hat{x}'$ and $\hat{y}'$ direction – see Eq. 3.34). However, since our EMF is sensitive to the parallel components of $\mathbf{B}$ and

A, we only care about the $\hat{y}'$ component.

$$\mathbf{M} = \mathbf{M_{y'}}\hat{\mathbf{y}}' + \mathbf{M_z}\hat{\mathbf{z}} \tag{3.40}$$

$$= M(\sin\alpha\hat{\mathbf{y}}' + \cos\alpha\hat{\mathbf{z}}) \tag{3.41}$$

Combining the appropriate equations,

$$\mathbf{B_{Sphere}} \cdot \frac{d\mathbf{A}}{dt} = \frac{2\mu_0 R^3}{3r^3} AM\omega\sin\alpha\cos\omega t \tag{3.42}$$

$$\frac{d\mathbf{B_{Sphere}}}{dt} \cdot \mathbf{A} = \frac{2\mu_0 R^3}{3r^3} AM\frac{d\alpha}{dt}\cos\alpha\sin\omega t. \tag{3.43}$$

It is convenient to use the following relation

$$\frac{d\sin\alpha}{dt} = \frac{d\alpha}{dt}\cos\alpha. \tag{3.44}$$

Finally, to convert this result to a measurable EMF, we need to introduce a geometeric fudge factor, $\mho$. This factor compensates for any imperfections in our apparatus (including a non-spherical distribution of magnetization). Since we ultimately calibrate our signal using EPR, this fudge factor is only introduced for the sake of rigor.

$$\xi = -\mho\frac{2\mu_0 R^3}{3r^3} AM\left(\omega\sin\alpha\cos\omega t + \frac{d\sin\alpha}{dt}\sin\omega t\right). \tag{3.45}$$

3.1.6   Measuring The ³He Polarization

Regardless of the strength of field created by the ³He spins, if the NMR measurement is performed adiabatically, the nuclear spins will track the direction of the effective external fields (since they define its eigenvectors). Since these spins track the external

field, we can use Eqn. 3.28 to evaluate the terms dependent on α,

$$\sin \alpha = \frac{B_1}{\sqrt{B_1^2 + (B_0 - \frac{\omega}{\gamma})^2}} \tag{3.46}$$

$$\frac{d \sin \alpha}{dt} = -\frac{2(B_0 - \frac{\omega}{\gamma})\dot{B}_0 B_1}{\left(B_1^2 + (B_0 - \frac{\omega}{\gamma})^2\right)^{\frac{3}{2}}}. \tag{3.47}$$

Combining this result with Eq. 3.31, we finally arrive at a formula for the nuclear polarization,

$$\xi = -\mho \frac{\mu_0 A \gamma \hbar R^3}{3r^3} [^3He] \left(\frac{B_1 \omega}{\sqrt{B_1^2 + (B_0 - \frac{\omega}{\gamma})^2}} \cos \omega t - \frac{2(B_0 - \frac{\omega}{\gamma})\dot{B}_0 B_1}{\left[B_1^2 + (B_0 - \frac{\omega}{\gamma})^2\right]^{\frac{3}{2}}} \sin \omega t \right) P. \tag{3.48}$$

Note that the two terms are 90 degrees out of phase and that the second is proportional to the derivative of the first. Provided that the NMR measurement is swept slowly enough relative to the transition frequency ($\omega \gg \dot{B}_0$), the second term will contribute negligibly.

3.1.7 Experimental Methods

A schematic of our experimental setup is shown in Fig. 3.1, with items used for NMR measurements shown in orange. A function generator (F.G.) supplies 56.6kHZ RF frequency, which when amplified provides a B_1 field of approximately 100mG. The main holding field, B_0 is swept through resonance and pickup coils located near the pumping chamber (pc) and on target chamber (tc) measure the NMR signal. This signal is amplified using Stanford Research Systems (SRS) model 550 preamplifiers. Because the pc coils are relatively far from the pc (they're located outside the oven), they pickup a relatively smaller signal than the coils located on the tc (the tc coils touch the tc). Although both coils pickup background RF from the RF coils, making
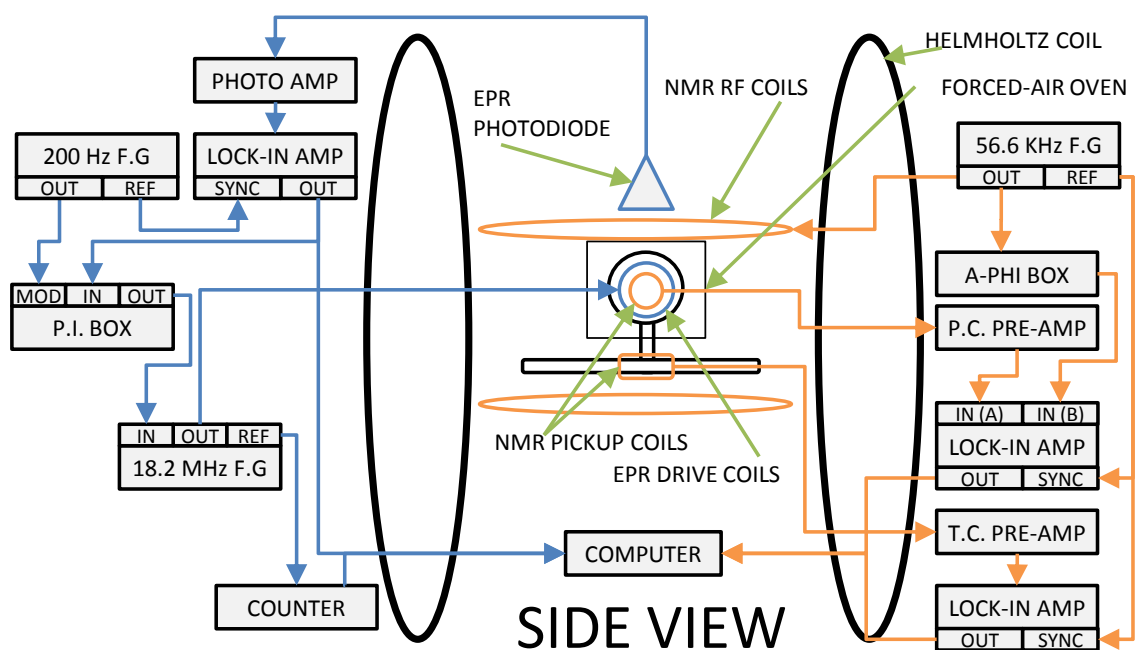
Figure 3.1: NMR (Orange) and EPR (Blue) Experimental Setup. For NMR, a 56.6kHz Function Generator (F.G.) provides the RF signal which is passed through an amplifier (not shown). Coils, oriented perpendicular to the drive coils, pickup the NMR signal, which is passed through a Stanford Research Systems (SRS)550 preamplifier. This signal provides the 'A' input for an SRS830 lockin amplifier. The raw (unamplified) signal for the F.G. is tee-d before amplification, with one branch going to the RF amplifier while the other goes through an A-ϕ box. The signal in the A-ϕ box is adjusted in the absence of an NMR signal such that its amplitude and phase match the signal measured by the pickup coils. This signal provides the 'B' input for the SRS830 lockin amplifier. The output of the amplifier is measured by a data acquisition computer. For EPR, a F.G. with voltage-controlled oscillation (VCO) is used to drive EPR coils. The VCO input of the F.G. is driven by a separate modulation F.G., whose output can be controlled by a proportional-integral (PI) feedback circuit (see Ch. 3.2.7). D2 Fluorescence is monitored by a photodiode. This signal is passed through an amplifier and measured by a lockin amplifier, locked to the modulation F.G. frequency. The output of this signal can by passed through the previously mentioned PI box, or can be sent directly to the data acquisition computer.

a sensitive measurement on the pc is much more difficult, owing to the smaller ^{3}He signal. To compensate, we use an A-ϕ box to cancel the background signal picked up by the pc coils (see Fig. 3.2). The signal from the 56.6kHZ F.G. is T-ed off; one branch goes to the RF amplifier and one branch goes to the A-ϕ box. The A-ϕ box can be used to adjust this signal until it matches the off-resonance signal picked up by the pc coils. Finally, an SR830 lockin amplifier (locked to the $\cos\omega t$ term in Eq. 3.48) subtracts this A-ϕ signal from the pc NMR signal and a precise measurement can be made (the amplified tc coil signal is sent directly to the tc lockin).

During a typical measurement, which takes about 45 seconds, the following operations are performed:

(A) Initialize Electronics

(B) Ramp RF Coils from 0 to 100mG (5 seconds)

(C) Allow RF Coils to Warm Up (5 seconds)

(D) Sweep Main Holding Field from 13 to 21 Gauss (6 seconds) and back down to 13 Gauss (6 seconds)

(E) Download Data from Memory Buffer (16 seconds)

(F) Ramp RF Coils from 100mG to 0 (5 seconds)

Fig. 3.3 shows the time-dependence of B_1, B_0, and ξ during such a measurement.

3.2 Electron Paramagnetic Resonance

Electron Paramagnetic Resonance (EPR, also Electron Spin Resonance, ESR) is a technique for probing magnetic-dipole Zeeman transitions (we typically study Potassium-39, see Fig. (3.4) or Rubidium-87 (see Fig. 2.2)). In the presence of an external magnetic field, the hyperfine structure of an alkali metal will be split into the Zeeman
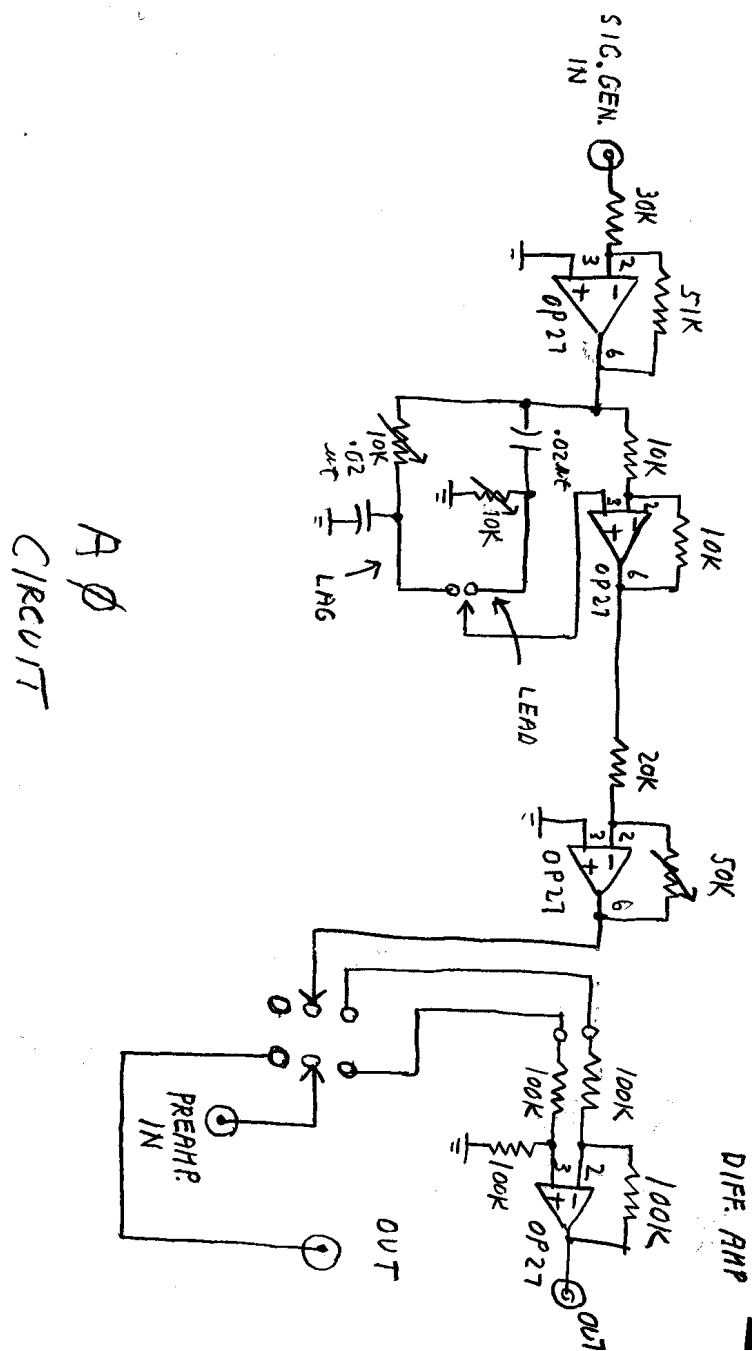
Figure 3.2: Circuit Diagram for A-φ Box
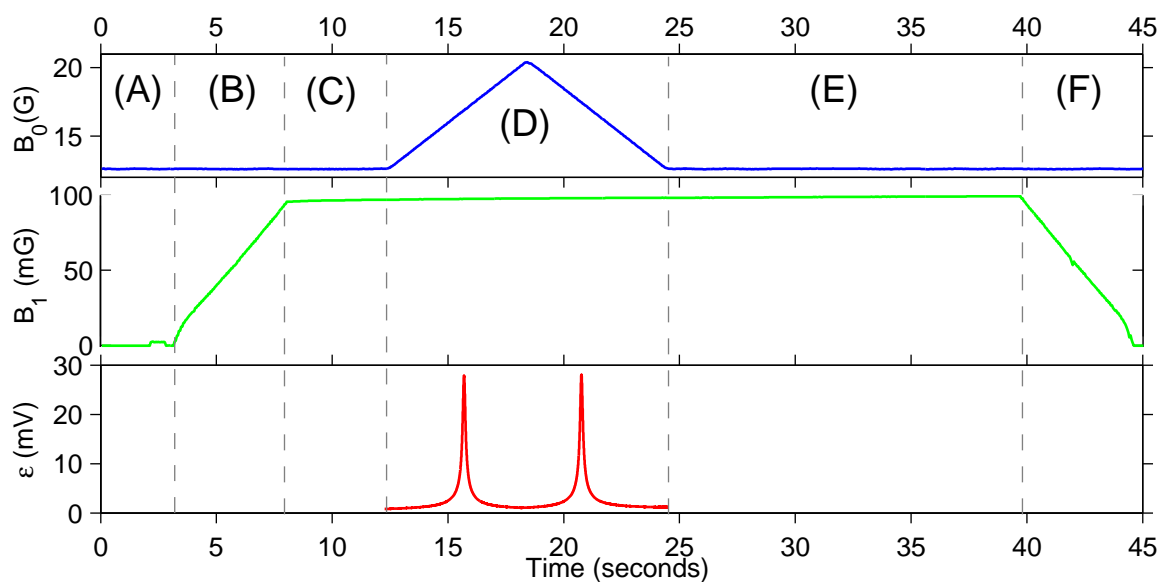
Figure 3.3: A Typical NMR Measurement (Real Data). Top: Main holding field. Middle: RF field. Bottom: NMR signal as measured by lockin amplifier

levels (see Fig. 3.4). In the low-field limit (where the hyperfine splitting is much greater than the Zeeman splitting), the Zeeman splitting is proportional to size of the external field. In addition to the main holding field ($\approx$ 13 G, see Ch. 3.1) and the Earth's field ($\approx$ 0.5 G), alkali atoms in our cells are influenced by the effective magnetic field created by the Polarized ^{3}He gas ($\approx$ 12mG). Although a small portion (roughly 1/6 for K) of this field comes from the bulk magnetization of the ^{3}He gas (see Eqn. 3.29), most of the field arises from A-^{3}He spin-exchange, fermi-contact collisions when the alkali electron and ^{3}He nucleus overlap [55, 56].

The strength of effective field created by the ^{3}He gas will depend on its polarization and density (and thus, so will the Zeeman splitting). If the ^{3}He magnetic field is isolated from all external fields and the density of the gas is well understood, a measurement of the Zeeman splitting can be used to calibrate the NMR measurement (see Ch. 3.1.5). We can isolate the field due to the noble gas by performing a frequency sweep AFP spin flip (keeping the holding field, B_0 constant). As the ^{3}He spins (and the magnetic field associated with them) change direction, the frequency of the Zeeman
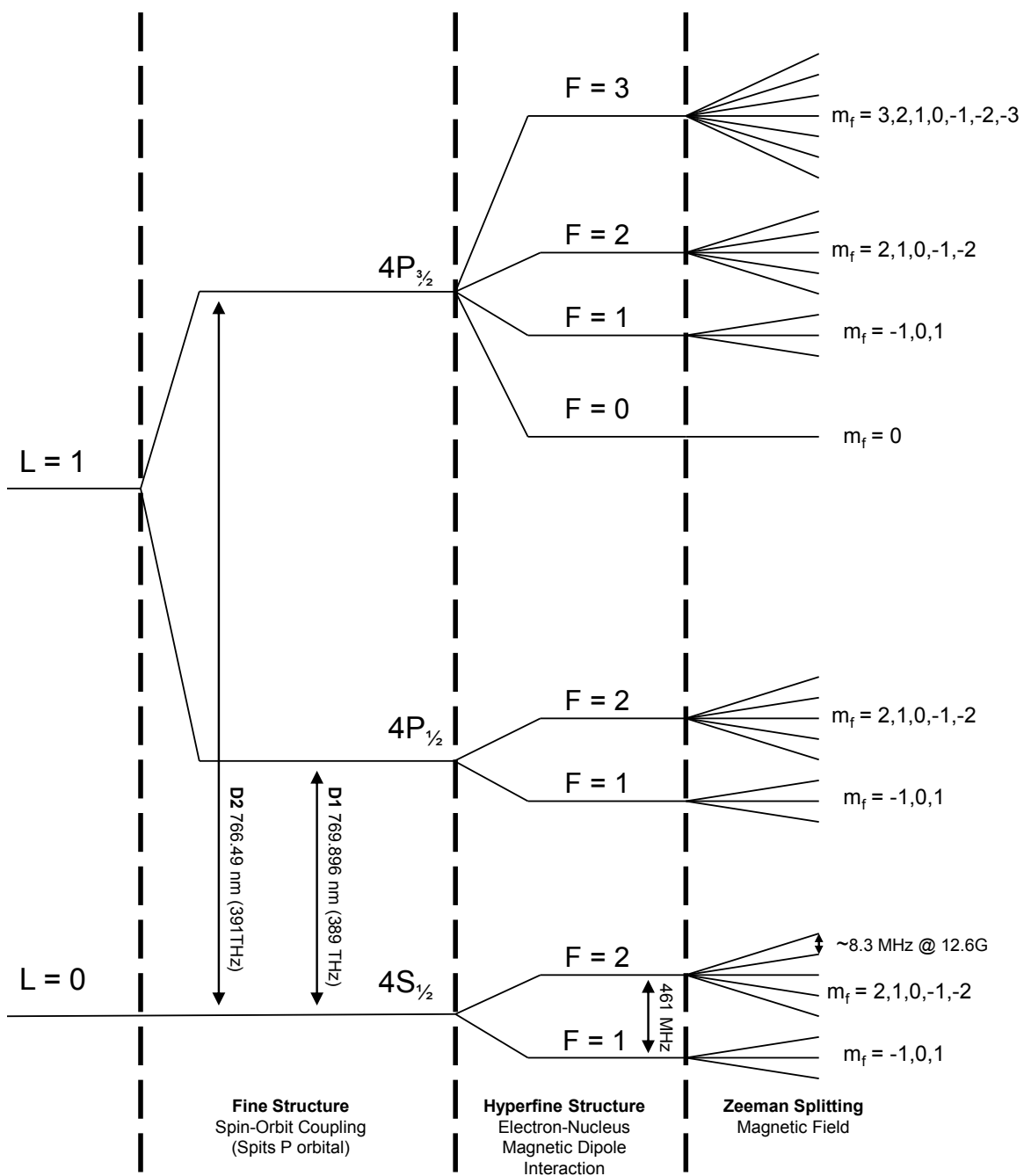
Figure 3.4: Energy-level diagram of 39-K, (I = 3/2, not to scale)

transition will change. We can use this frequency difference coupled with a knowledge of the pumping chamber ^{3}He density to extract an absolute noble gas polarization. When combined with an AFP measurement, this yields an NMR calibration.

3.2.1 The Breit-Rabi Equation and EPR Transitions

The Breit-Rabi equation, which describes the Zeeman energy levels, is

$$E(F,m) = -\frac{E_{hfs}}{2[I]} - g_I \mu_N B m \pm \frac{E_{hfs}}{2}\sqrt{1 + \frac{4m}{[I]}x + x^2}, \qquad (3.49)$$

where $\pm$ refers to the $F = I \pm J$ hyperfine manifold, E_{hfs}/h is the frequency of the hyperfine splitting, I is the nuclear spin, [I] = 2I+1, m is the azimuthal quantum number, and

$$x = (g_I \mu_N - g_S \mu_B)\frac{B}{E_{hfs}}. \qquad (3.50)$$

The EPR transition frequency between adjacent Zeeman levels is given by

$$\nu_{m \to m-1} = \frac{E(F,m) - E(F,m-1)}{h} \qquad (3.51)$$

$$= -\frac{g_I \mu_N B}{h} \pm \frac{E_{hfs}}{2h}\left(\sqrt{1 + \frac{4m}{[I]}x + x^2} - \sqrt{1 + \frac{4(m-1)}{[I]}x + x^2}\right) \qquad (3.52)$$

In the above equations, m refers to the higher state. Under our typical operating conditions, the second term in Eqn. 3.52 is much greater than the first term. As such, its sign will determine the sign of $\nu_{m \to m-1}$. I will therefore choose to make the transition frequency positive,

$$\nu_\pm = \mp\frac{g_I \mu_N B}{h} + \frac{E_{hfs}}{2h}\left(\sqrt{1 + \frac{4m}{[I]}x + x^2} - \sqrt{1 + \frac{4(m-1)}{[I]}x + x^2}\right), \qquad (3.53)$$

where $\pm$ still refers to the $F = I \pm J$ hyperfine manifold.

3.2.2 EPR Frequency Shift Due to a Small Magnetic Field

The Taylor expansion for a function is given by

$$F(x) = \sum_{i=0}^{n} \frac{d^i F(a)}{dx^i} \frac{(x-a)^i}{i!}. \tag{3.54}$$

For small deviations ($x - a \ll 1$),

$$F(x) \approx F(a) + \frac{dF(a)}{dx}(x-a) \tag{3.55}$$

$$F(x) - F(a) = \frac{dF(a)}{dx}(x-a) \tag{3.56}$$

$$\Delta F = \frac{dF(a)}{dx}\Delta x \tag{3.57}$$

Therefore, in the presence of a small external magnetic field perturbation, ΔB, an EPR transition frequency will be shifted by

$$\Delta\nu = \frac{d\nu}{dB}\Delta B, \tag{3.58}$$

where ΔB is the additional field produced by ^{3}He. As was discussed in Ch. 3.1.5, the long-range magnetic field produced by polarized ^{3}He in the pumping chamber is equivalent to the field produced by a uniformly magnetized sphere (see Eqns. 3.37, 3.31):

$$\Delta B = \frac{\mu_0(\gamma/2\pi)h}{3}P[He]. \tag{3.59}$$

There is an additional field (due to the spin-exchange interaction) that further shifts the EPR frequency. This field is traditionally treated as an enhancement to the ^{3}He magnetization [57],

$$\Delta B = \frac{\mu_0(\gamma/2\pi)h}{3}\kappa_0 P[He], \tag{3.60}$$

where κ_0 is the spin-exchange enhancement factor. The values for κ_0 and its temperature dependence have been measured by Romalis et al. [57]

$$\kappa_0^{Rb-He} = 4.52 + 0.00934\,[T(^\circ C)] \tag{3.61}$$

and more recently by Babcock et al. [55],

$$\kappa_0^{Na-He} = 4.84 + 0.00914\,[T - 200^\circ C] \tag{3.62}$$

$$\kappa_0^{K-He} = 5.99 + 0.0086\,[T - 200^\circ C] \tag{3.63}$$

$$\kappa_0^{Rb-He} = 6.39 + 0.00914\,[T - 200^\circ C] \tag{3.64}$$

Provided the ^{3}He density is known, a measurement of ΔB can be used to solve for the ^{3}He polarization. We choose to measure EPR frequency shift (instead of the EPR field shift).
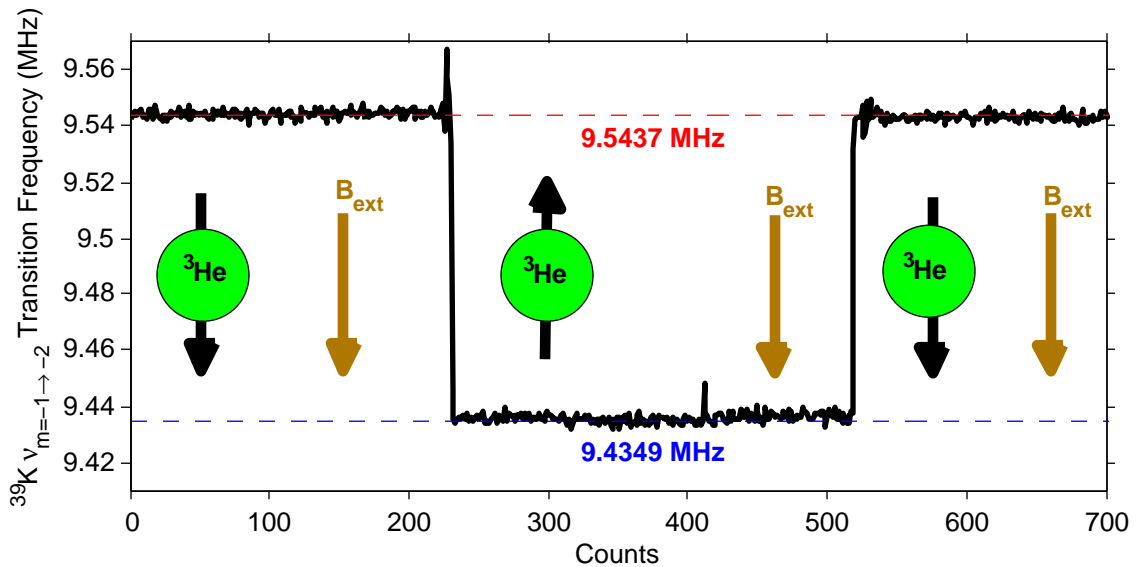
Figure 3.5: Brady 235C, 3 Comet Lasers, Low-Energy State EPR Measurement 8.15.08

When performing EPR polarimetry, we measure $\nu_\pm$ for end transitions (where an end transition is a transition involving $m = \pm m_{max}$). We're able to isolate the ^{3}He

magnetic field by using frequency-sweep AFP NMR. During the frequency sweep, the ³He spins reverse direction when resonance occurs. This change in direction will cause the magnetic field they produce to change direction as well. The alkali Zeeman transition frequencies will consequently change. The difference of those two frequency measurements is $\Delta\nu$ (see Fig. 3.5).

3.2.3 Expansion of EPR Transition Frequency

It is useful to write 3.53 as

$$\nu_\pm = \mp\frac{g_I\mu_N B}{h} + \frac{v_{hfs}}{2}\Delta, \tag{3.65}$$

where

$$\Delta = \sqrt{1+u} - \sqrt{1+u+\delta} \tag{3.66}$$

$$u = \frac{4m}{[I]}x + x^2, \tag{3.67}$$

$$\delta = -\frac{4}{[I]}x. \tag{3.68}$$

We use the EPR frequency shift to measure the ³He polarization. When Eqn. 3.65 is plugged into Eqn. 3.58, the equation for frequency shift becomes transcendental (in terms of total field, B). It is therefore customary to expand the quadratic terms using

$$\sqrt{1+u} = 1 + \frac{1}{2}u - \frac{1}{2\cdot4}u^2 + \frac{1\cdot3}{2\cdot4\cdot6}u^3 - \frac{1\cdot3\cdot5}{2\cdot4\cdot6\cdot8}u^4 + \cdots \tag{3.69}$$

The quadratic involving the lower-energy state has an additional term,

$$\sqrt{1+u+\delta} = 1 + \frac{1}{2}(u+\delta) - \frac{1}{2\cdot4}(u+\delta)^2 + \frac{1\cdot3}{2\cdot4\cdot6}(u+\delta)^3 - \frac{1\cdot3\cdot5}{2\cdot4\cdot6\cdot8}(u+\delta)^4 + \cdots$$

$$\tag{3.70}$$

The difference between these quadratics is

$$\Delta = \sqrt{1+u} - \sqrt{1+u+\delta} \tag{3.71}$$

$$= -\frac{1}{2}\delta + \frac{1}{8}(2u\delta + \delta^2) - \frac{1}{16}(3u^2\delta + 3u\delta^2 + \delta^3) + \cdots \tag{3.72}$$

We note here that the first-order Taylor expansion performed in Eq. 3.80 is valid for small perturbing fields (such as the effective field created by the polarized ^{3}He gas). The higher-order binomial expansion performed for Eq. 3.72 is an expansion of the unperturbed system in the absence of polarized ^{3}He. To calculate the EPR frequency shift $\Delta\nu$, it is necessary to plug these expansions into Eqn. 3.58,

$$\Delta\nu = \left[\mp g_I\mu_N + \frac{\nu_{hfs}}{2}\frac{d\Delta}{dB}\right]\Delta B \tag{3.73}$$

Using

$$\frac{dx}{dB} = \frac{x}{B}, \tag{3.74}$$

$$\frac{du}{dB} = \left(\frac{4m}{[I]} + 2x\right)\frac{x}{B}, \tag{3.75}$$

$$\frac{d\delta}{dB} = -\frac{4}{[I]}\frac{x}{B}, \tag{3.76}$$

$$\frac{d\Delta}{dB} = \frac{2x}{[I]}\left[1 + \underbrace{2(1-2m)\frac{x}{[I]}}_{\text{1st Order}} + \underbrace{6\left(1 - 3m + 3m^2 - \frac{[I]^2}{4}\right)\frac{x^2}{[I]^2}}_{\text{2nd Order}} + \cdots\right] \tag{3.77}$$

Under typical operating conditions, $B = 13G$ and Eqn. 3.77 only needs to be expanded to second order to agree to $< 0.1\%$ for all alkali isotopes present (see Table 3.1). Eqn. 3.77 has been expanded to 5th order by Singh [5]. Finally, if we make the

	^{39}K	^{41}K	^{85}Rb	^{87}Rb
Natural Abundance	93.26%	6.73%	72.17%	27.83 %
I	3/2	3/2	5/2	3/2
ν_{hfs} (MHz)	461.71972	254.01387	3035.73200	6834.68260
0th Ord. Pct. Err. (13G/40G)	12.6/43.3	23.9/89.4	2.02/6.31	0.80/2.49
1st Ord. Pct. Err. (13G/40G)	0.78/8.91	2.77/36.0	0.02/0.24	3E-3/0.03
2nd Ord. Pct. Err. (13G/40G)	0.01/0.60	0.09/5.50	2E-4/5E-3	3E-6/9E-5
3rd Ord. Pct. Err. (13G/40G)	2E-3/0.22	0.03/2.44	2E-7/2E-5	5E-8/4E-6
4th Ord. Pct. Err. (13G/40G)	2E-4/0.07	5E-3/1.78	2E-8/5E-6	3E-10/8E-8
5th Ord. Pct. Err. (13G/40G)	5E-6/6E-3	2E-4/0.35	3E-10/2E-7	3E-13/3E-10

Table 3.1: Alkali Data and Comparison of Expansion of Eqn. 3.77 with Actual Value. For comparison, m was chosen to be the largest value (m = [I]/2). Expansions higher than 2nd order are calculated using Singh [5]. 13G is our nominal operating field; 40G is the highest field we can create in our lab.

approximation

$$g_S\mu_B \gg g_I\mu_N, \tag{3.78}$$

$$x \approx -\frac{g_S\mu_B}{h\nu_{hfs}}B \tag{3.79}$$

and combine Eqn. 3.73 and Eqn. 3.60,

$$\Delta\nu \approx \frac{g_S\mu_B\mu_0(\gamma/2\pi)}{3[I]}\kappa_0 P[He]\left[1 - \underbrace{2(1-2m)\frac{g_S\mu_B B}{h\nu_{hfs}[I]}}_{\text{1st Order}}\right.$$

$$\left. + \underbrace{6\left(1 - 3m + 3m^2 - \frac{[I]^2}{4}\right)\left(\frac{g_S\mu_B B}{h\nu_{hfs}[I]}\right)^2}_{\text{2nd Order}} + \cdots\right]. \tag{3.80}$$

3.2.4   Low-Field Frequency Inversion

The unknowns for a given transition are B and P (see Eqn. 3.80); however a value
for B can be calculated from $\nu_\pm$ by solving Eqn. 3.65,

$$\nu_\pm = \mp \frac{g_I \mu_N B}{h} + \frac{v_{hfs}}{2}\left(-\frac{1}{2}\delta + \frac{1}{8}(2u\delta + \delta^2) - \frac{1}{16}(3u^2\delta + 3u\delta^2 + \delta^3) + \cdots\right) \quad (3.81)$$

Such an inversion is easiest when a low-field approximation is used. Dropping the
first term (recall $\mu_B \gg \mu_N$) and keeping only terms to second order in x,

$$\nu_\pm \approx \frac{v_{hfs}}{2}\left(-\frac{1}{2}\delta + \frac{1}{8}(2u\delta + \delta^2)\right) \quad (3.82)$$

$$0 \approx -\frac{v_{hfs}}{v_\pm} + \frac{x}{[I]} + (1-2m)\frac{x^2}{[I]^2}. \quad (3.83)$$

Solving the quadratic formula for x gives

$$x \approx \frac{[I]}{2(1-2m)}\left(-1 + \sqrt{1 + 4(1-2m)\frac{v_\pm}{v_{hfs}}}\right), \quad (3.84)$$

where I've chosen the root that gives physical result. Finally, with Eqn. 3.79,

$$B \approx -\frac{h\nu_{hfs}[I]}{2g_S\mu_B(1-2m)}\left(-1 + \sqrt{1 + 4(1-2m)\frac{v_\pm}{v_{hfs}}}\right). \quad (3.85)$$

This approximation agrees to $< 0.3\%$ for ³⁹K transitions at 13G.

When performing an EPR measurement (see Fig. 3.5), two frequencies are mea-
sured – the frequency when the ³He spins are aligned with the external field, and the
frequency when the ³He spins are anti-aligned with the external field. Each of these
frequencies can be inverted for a B. The value for B that is plugged into Eqn. 3.80
is calculated by taking the average of these two B's.

3.2.5 ³He Density Measurement (Temperature Test)

The EPR frequency shift depends on the ³He density (see Eq. (3.80)). Consequently, an accurate interpretation of the frequency shift requires an accurate measurement of the ³He density in the alkali metal region (that is, in the pumping chamber). We're able to make measurements of the density by comparing successive NMR measurements. In a multichambered cell, an understanding of the ³He density is analogous to an understanding of the ³He temperature by the ideal gas law. If the temperature is known everywhere in the cell, then so is the density. RTDs are attached on the pumping chamber (which in turn control the temperature of the oven) and on the target chamber. Things are further complicated in the presence of a pump laser, which heats the gas inside the pumping chamber to a temperature higher than the glass exterior where the RTD is located. The temperature inside the pumping chamber must be extracted before the density can be understood.

Assuming the gas is at the same pressure everywhere in the cell, the ideal gas law provides,

$$T_{PC} = T_{TC}\frac{[^3\text{He}]_{\text{TC}}}{[^3\text{He}]_{\text{PC}}} \tag{3.86}$$

where PC and TC refer to the pumping and target chambers, respectively. It is assumed that the gas in the target chamber is always in equilibrium with the glass cell (and therefore, that the RTD reading is representative of the gas); however, in the pumping chamber, this assumption is only made when the lasers are off.

The number of ³He atoms in the cell is the same independent of the temperature of the cell,

$$N_{PC} + N_{TC} = N_{total} \tag{3.87}$$

$$[^3\text{He}]_{\text{PC}}\text{V}_{\text{PC}} + [^3\text{He}]_{\text{TC}}\text{V}_{\text{TC}} = [^3\text{He}]_{\text{uniform}}(\text{V}_{\text{PC}} + \text{V}_{\text{TC}}) \tag{3.88}$$

where the uniform temperature ³He density is measured when the cell is being filled

and again using the pressure broadening of the alkali absorption lines.

Finally, the density can be related to an NMR signal by Eq. (3.48),

$$[^3He] = \kappa \frac{S}{P} \tag{3.89}$$

where S is the signal from the lockin, P is the ³He polarization and κ contains the constants from Eq. (3.48).

Combining Eq. (3.86) and Eq. (3.88),

$$T_{PC} = \frac{T_{TC}}{V_{TC}} \left[\frac{[^3He]_{uniform}}{[^3He]_{PC}} (V_{PC} + V_{TC}) - V_{PC} \right] \tag{3.90}$$

and using Eq. (3.89),

$$T_{PC} = \frac{T_{TC}}{V_{TC}} \frac{[^3He]_{uniform}P}{\kappa S} (V_{PC} + V_{TC}) - T_{TC} \frac{V_{PC}}{V_{TC}} \tag{3.91}$$

which can be written as

$$\underbrace{\frac{T_{TC}}{V_{TC}} \frac{[^3He]_{uniform}}{\kappa} (V_{PC} + V_{TC})}_{Constants} = \underbrace{\frac{S}{P} \left(T_{TC} \frac{V_{PC}}{V_{TC}} + T_{PC} \right)}_{DependOnLaserConditions} \tag{3.92}$$

Finally,

$$\frac{S^{ON}}{P^{ON}} \left(T_{TC} \frac{V_{PC}}{V_{TC}} + T_{PC}^{ON} \right) = \frac{S^{OFF}}{P^{OFF}} \left(T_{TC} \frac{V_{PC}}{V_{TC}} + T_{PC}^{OFF} \right) \tag{3.93}$$

and thus,

$$T_{PC}^{ON} = \frac{P^{ON} S^{OFF}}{P^{OFF} S^{ON}} \left(T_{TC} \frac{V_{PC}}{V_{TC}} + T_{PC}^{OFF} \right) - \frac{V_{PC}}{V_{TC}} T_{TC} \tag{3.94}$$

Once AFP losses have been accounted for (see Ch. 3.1.1), T_{PC}^{ON} can be calculated. Fig. 3.6 shows a typical temperature-test measurement. Values for S^{ON} and S^{OFF} are calculated by taking the average of their respective individual measurements. Typical corrections are between 20 and 40°C, depending on the laser power used. A
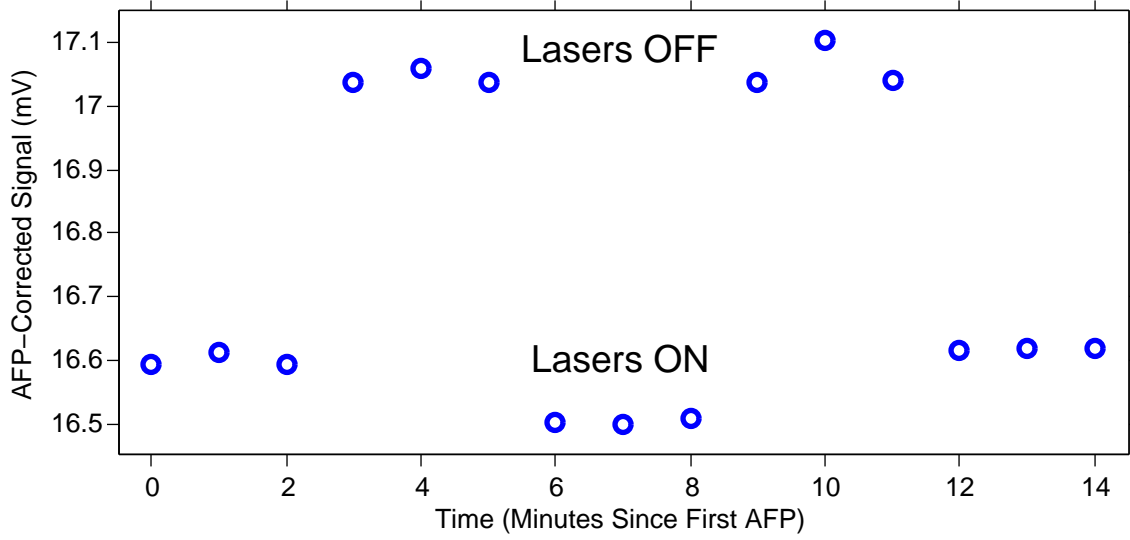
Figure 3.6: Brady 235C, 3 Comet Lasers, Pumping Chamber Coils Temperature Test. $T_{PC}^{OFF} = 235°C, T_{PC}^{ON} = (269.2 \pm 12.1)°C$

value for the temperature in the pumping chamber can also be obtained by monitoring the NMR signal in the target chamber coils,

$$T_{PC}^{ON} = V_{PC} T_{TC} \frac{1}{\frac{P^{ON} S^{OFF}}{P^{OFF} S^{ON}} \left(\left(V_{PC} \frac{T_{TC}}{T_{PC}} - 1 \right) + V_{TOT} \right) - V_{TT} - V_{TC}}$$ (3.95)

here, S and P refer to the signal and polarization in the target chamber.

3.2.6 Locating Transition Frequencies (FM Sweep)

We perform all EPR measurements by monitoring the amount of D2 flouresence from the pumping chamber (see Fig. 3.1). During optical pumping (see Ch. 2), a Rb atom can become excited to the $5P_{\frac{3}{2}}$ oribital through collisions with other Rb atoms. Although the majority of these atoms decay non-radiatively, a small fraction will relax by emitting a D2 photon. This fluorescence occurs more strongly when the alkali polarization is low. We can lower the alkali polarization by inducing Zeeman transitions. Consequently, by monitoring the D2 fluorescence, we can probe Zeeman
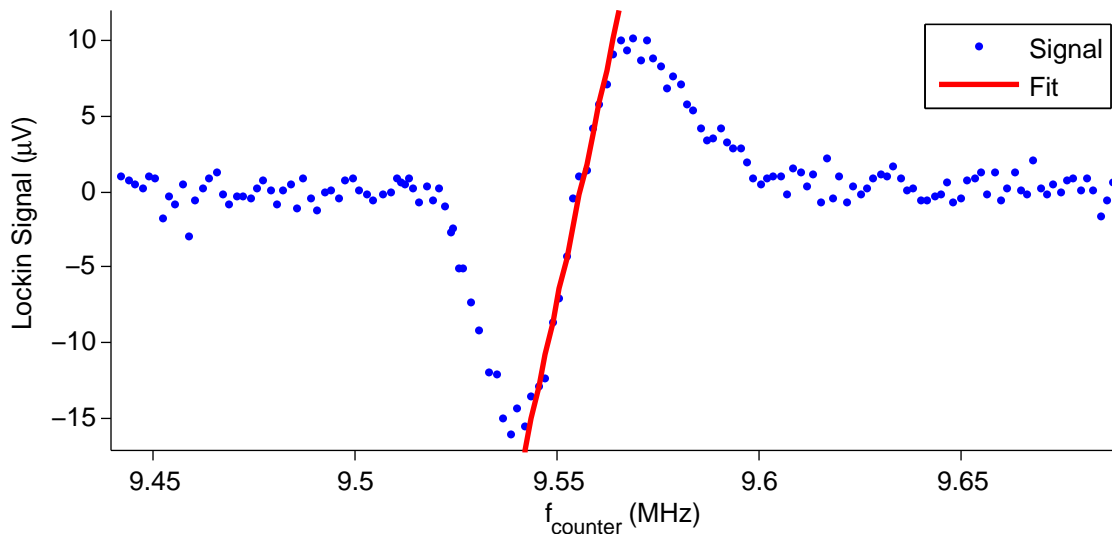
Figure 3.7: Brady 235C, 2 Comet Lasers, Low-Energy State, $f_{resonance} = 9.556MHz$

transitions.

Under operating conditions the alkali is highly polarized (typically $> 80\%$); we induce the $m_f = 2 \rightarrow m_f = 1$ (or $m_f = -2 \rightarrow m_f = -1$) ^{39}K edge transition, which depolarizes the potassium. Since the alkali-alkali spin exchange rate is so high ($\gamma_{se}^{Rb-A} \approx 500$kHz, see Ch. 2.7.1), the rubidium is also depolarized. The newly depolarized rubidium is quickly repumped to the $5P_{\frac{1}{2}}$ excited state (see Fig. (2.1)), where it collides with other alkali metal atoms. These collisions can result in further excitations (to the $5P_{\frac{3}{2}}$ level); some of those highly excited electrons will spontaneously decay emitting D2 (780 nm) light. Although these highly-excited D2 emissions are always occuring, they occur more strongly when the alkali metal is being depolarized. Hence, we observe more rubidium D2 fluorescence while inducing potassium Zeeman transitions.

The lineshape of this fluorescence is a lorentzian (see Fig. 3.7). To locate the resonance, we perform a frequency-modulated (FM) sweep; the fluorescence under such a sweep will have the lineshape of the derivative of a lorentzian; the zero-crossing of this curve corresponds to the resonance frequency of the transition [58, 59]. Once this

transition has been located, we lock to it using a proportional-integral (PI) feedback circuit. In fact, we use the same circuit used by Romalis [1]; however, we note that the diagram included in his thesis probably contains an ommission which has been included in Fig 3.8.
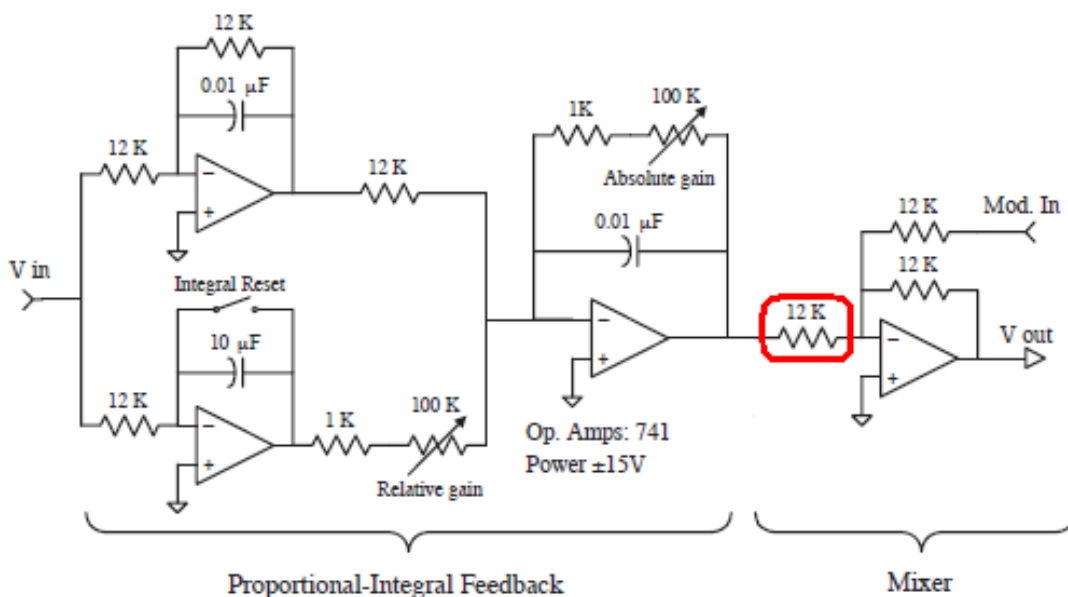
Figure 3.8: PI-Feedback Circuit from Romalis [1] with Correction in Red

3.2.7   Experimental Methods

Once the resonance has been found (and locked to), it is possible to make an EPR calibration measurement. For a diagram of the experimental setup, refer to Fig. 3.1; the components used during an EPR measurement are in blue. A Fluke 80 function generator (FG) with a voltage controlled ocillator (VCO) input is used to directly drive a pair of RF coils (no amplification). We'll refer to this FG as the main FG. Under typical operating conditions (12.6 Gauss), the main FG operates between 5 and 10 MHz (depending on which alkali isotope is being probed). The reference signal of the main FG is sent to an HP5334B universal counter to accurately monitor the frequency. The VCO of the main FG is driven by the output of the PI box. The

PI box serves to keep the frequency of the main FG locked to the Zeeman transition under consideration. Additionally, the PI box modulates the main FG signal by using a second FG which operates at 200 Hz. We'll refer to this second FG as the modulation FG. The location of the Zeeman transition is monitored by observing the intensity of D2 fluorescence as detected by a photodiode located above the oven. This intensity is monitored by a lockin amplifier which is locked to the modulation FG. When the ^{3}He spins are flipped during an EPR calibration measurement, the PI box stays locked to the appropriate Zeeman transition (corresponding to a zero signal on the lockin amplifier) by changing the VCO input of the main FG.

During a typical measurement, the following operations are performed:

A Locate resonance frequency by aquiring FM sweep spectrum (see Fig. 3.7). Note, the FM sweep is naturally performed without feedback; however, the modulation input on the PI box is used.

B Turn off EPR RF

C Perform NMR measurement (see Ch. 3.1.7)

D Turn on EPR RF and lock to transition. At this point, V_{IN} on the PI box is used; additionally, the integration is turned on.

E Begin data aquisition by monitoring the frequency of the counter

F Turn on NMR RF

G Sweep NMR RF from 56.6KHz to 30.0KHz. This will flip the ^{3}He spins, which will cause the Zeeman frequency to change.

H Turn off NMR RF

I Turn on NMR RF

J Sweep NMR RF from 30.0KHz to 56.6KHz.

K Turn off NMR RF

L Turn off EPR RF

M Perform NMR measurment.

Items **E** **t**o **K** are plotted in Fig. 3.5; the effective field created by the ³He spins in this measurement resulted in a 54.4KHz shift in the Zeeman frequency. When this information is combined with Eqs. 3.80, 3.85, information gathered from the temperature test (see Fig. 3.6), and information about the cell dimensions and uniform density, we find the external field to be 12.77G (in good agreement with our knowledge of the main holding field) and a ³He polarization of 69% is attained. This polarization can be combined with the results of the two NMR measurements (items **C** a**nd M**) to attain an NMR calibration constant. In this case, the calibration constant was 03.97%/mV.

Chapter 4

Faraday Rotation

In equilibrium, one of the factors limiting the ^{3}He polarization is the alkali polarization; which is in turn limited by the available laser power. Consequently, for a given laser power, an appropriate alkali density must be found that is sufficiently high such that $\gamma_{se} \gg \Gamma$, but appropriately low so that P_A remains high (see Eq. 2.71).

A number of the quantities presented in Ch. 2.7 depend on the *in situ* hybrid alkali density ratio, $D(T)$ (see Eqn. 2.105). The nominal operating number density ratio, $D(T_{oven})$ (which is calculated from the masses measured in the glovebox) has a relative error of about 0.6% for a $D = 5$ mixture and about 2.5% for a $D = 20$ mixture; however, due to complications that arise during cell preparation (specifically, that rubidium has a lower boiling point), proportionally more rubidium than potassium is chased into the actual cell. To appropriately fully characterize a given target cell, *in situ* measurements of $D(T)$ must be made.

Several techniques exist for determining the actual number density ratio of a completed cell. One of these techniques, which we shall refer to as "pressure broadening," monitors the passage of a tunable, weak (< 50mW) "probe" beam in the absence of "pump" lasers (pump lasers are the powerful lasers we use to optically pump our alkali vapor) [31]. In our lab, the entire cell (not just the pumping chamber) is placed in a special pressure-broadening oven. In such an oven, and in the absence of pump lasers, the temperature of the cell is very precisely known. Measurements of the relative transmission associated with the two alkali species are used to extrapolate a value for D. Although the pressure-broadening technique provides a measurement of the temperature independent molar fraction (which can be used to predict $D(T)$), it cannot do so under actual operating conditions. This is because at significantly high temperatures (those that approach operating temperatures), too much vapor is present and the probe beam is entirely absorbed. In our lab, we make measurements at temperatures as high as 140°C. Unfortunately, the vapor pressure curves for alkali metals are not known well enough to extrapolate $D(T)$ as measured by pressure

broadening to operating temperatures (typically 235°C for a hybrid cell)

Another technique for measuring $D(T)$, which we shall refer to as "Faraday Rotation", utilizes the Faraday Effect which describes how a weak ($\approx$ 1mW), linearly-polarized probe beam "rotates" in the presence of a polarized alkali vapor [60]. The amount of this rotation (the Faraday Rotation) depends on the alkali polarization as well as the amount of alkali vapor through which the probe beam passes. This "amount of alkali vapor" is the product of the alkali density with the distance that the probe beam travels through the pumping chamber (we shall refer to this distance as the "path length" of the cell). We use an apparatus based on Farady Rotation to make *in situ* measurements of the alkali polarization and density.

4.1 Faraday Rotation in Terms of Atomic Polarizability

4.1.1 The Effect of Alkali Vapor on a Polarized Probe Beam
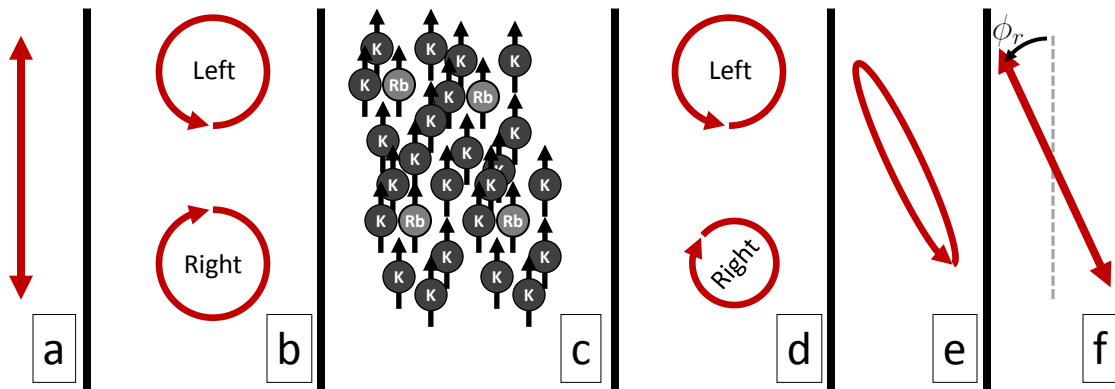
Figure 4.1: Progression of Probe Beam through a Polarized Alkali Vapor. (a) A linearly polarized beam (b) appears as the superposition of left and right circularly polarized light (c) in an alkali vapor's frame. (d) The resonant portion will be absorbed and retarded. (e) In the lab frame, eliptically polarized light will exit. (f) This roughly linearly polarized light will have rotated by an angle ϕ_r.

Fig. (4.1) shows the propagation of initially horizontally polarized light through

a hybrid alkali mixture. In Fig (4.1.a), the incident light, $\tilde{\mathbf{E}} = \mathrm{E}_0 e^{i(\mathrm{kz}-\omega\mathrm{t})}\hat{\mathbf{x}}$ can be expressed as $\mathrm{E}_0 e^{i(\mathrm{kz}-\omega\mathrm{t})}|X\rangle$, where

$$|X\rangle = \begin{pmatrix} 1 \\ 0 \end{pmatrix}$$

Similarly,

$$|Y\rangle = \begin{pmatrix} 0 \\ 1 \end{pmatrix}, |\mathcal{R}\rangle = \frac{1}{\sqrt{2}}\begin{pmatrix} 1 \\ i \end{pmatrix}, |\mathcal{L}\rangle = \frac{1}{\sqrt{2}}\begin{pmatrix} 1 \\ -i \end{pmatrix}.$$

When projected onto the atomic basis in Fig (4.1.b), the electric field can be written as

$$\vec{\mathbf{E}} = \frac{E_0}{\sqrt{2}}\left(|\mathcal{R}\rangle + |\mathcal{L}\rangle\right), \tag{4.1}$$

where the point immediately before entering the alkali vapor has been defined as the origin ($t = 0$ and $z = 0$).

The Faraday Effect relies upon two basic principles: Circular Dichroism and Circular Birefringence. Circular Birefringence occurs when a medium has different indices of refraction for the two different circular polarizations of light. Different indices of refraction will cause the two circular polarizations to travel at different speeds, resulting in a measureable phase difference (the Faraday Rotation Angle). Circular Dichroism causes different amounts of absorption for the two different circular polarizations. The net results of these two effects is that the electric field evolves differently for the two different circular polarizations. After traveling through the alkali vapor Fig (4.1.c), the fields will be

$$\vec{\mathbf{E}} = E_0 \frac{e^{-i\omega t}}{\sqrt{2}}\left(e^{i\tilde{k}_R l}|\mathcal{R}\rangle + e^{i\tilde{k}_L l}|\mathcal{L}\rangle\right), \tag{4.2}$$

where l is the distance the probe beam travels through the vapor and $\tilde{k}$ is a complex

number of the form

$$\tilde{k} = k + i\kappa. \tag{4.3}$$

Eqn. (4.2) can be factored as follows,

$$\vec{\mathbf{E}} = E_0 \frac{e^{-i\omega t}}{\sqrt{2}} e^{i\tilde{k}_R l} \left(|\mathcal{R}\rangle + e^{i\delta\tilde{k}l} |\mathcal{L}\rangle \right) \tag{4.4}$$

$$= E_0 \frac{e^{-i\omega t}}{\sqrt{2}} e^{i\tilde{k}_R l} e^{i\frac{\delta\tilde{k}l}{2}} \left(e^{-i\frac{\delta\tilde{k}l}{2}} |\mathcal{R}\rangle + e^{i\frac{\delta\tilde{k}l}{2}} |\mathcal{L}\rangle \right), \tag{4.5}$$

with

$$\delta\tilde{k} = \tilde{k}_L - \tilde{k}_R. \tag{4.6}$$

The real part of $\delta\tilde{k}l$ corresponds to the faraday rotation angle ϕ_r, while the imaginary part of $i\delta\tilde{k}l$ yields the attenuation difference. From the form of Eqn. (4.4), it should be clear that not only is the left circular component out of phase with the right circular component, but also less of it penetrates the vapor.

When projected back onto the lab frame (the $|X\rangle$, $|Y\rangle$ basis, Fig.(4.1.d)), the field is

$$\vec{\mathbf{E}} = E_0 \frac{e^{-i\omega t}}{\sqrt{2}} e^{i\tilde{k}_R l} e^{i\frac{\delta\tilde{k}l}{2}} \frac{1}{\sqrt{2}} \left(\left(e^{-i\frac{\delta\tilde{k}l}{2}} + e^{i\frac{\delta\tilde{k}l}{2}} \right) |X\rangle + i \left(e^{-i\frac{\delta\tilde{k}l}{2}} - e^{i\frac{\delta\tilde{k}l}{2}} \right) |Y\rangle \right) \tag{4.7}$$

$$= \tilde{E}' \left(\cos\left(\frac{\delta\tilde{k}l}{2} \right) |X\rangle - i\sin\left(\frac{\delta\tilde{k}l}{2} \right) |Y\rangle \right), \tag{4.8}$$

where

$$\tilde{E}' = E_0 e^{-i\omega t} e^{i\tilde{k}_R l} e^{i\frac{\delta\tilde{k}l}{2}}. \tag{4.9}$$

Using Eqn.(4.3),

$$\vec{\mathbf{E}} = \tilde{E}' \left(\cos\left(\frac{(\delta k + i\delta\kappa)l}{2} \right) |X\rangle - i\sin\left(\frac{(\delta k + i\delta\kappa)l}{2} \right) |Y\rangle \right) \tag{4.10}$$

$$= \tilde{E}_x |X\rangle - i\tilde{E}_y |Y\rangle, \tag{4.11}$$

where

$$\tilde{E}_x = \tilde{E}' \left(\cos \phi_r \cosh \beta_r - i \sin \phi_r \sinh \beta_r \right) \tag{4.12}$$

$$\tilde{E}_y = \tilde{E}' \left(\sin \phi_r \cosh \beta_r + i \cos \phi_r \sinh \beta_r \right) \tag{4.13}$$

and

$$\phi_r \equiv \frac{\delta k l}{2} \tag{4.14}$$

$$\beta_r \equiv \frac{\delta \kappa l}{2}. \tag{4.15}$$

The quantity $\frac{\kappa l}{2}$ is defined to be the faraday attenuation, β_r, while $\frac{k l}{2}$ is defined to be the faraday rotation angle, ϕ_r. Provided that the attenuation is small ($\beta_r \ll 1$), the light will be only slightly eliptical (approximately linear), Fig.(4.1.e).

4.1.2 Relationship Between Wave Number and Atomic Polarizability

For linear and isotropic media, $\vec{D} = \epsilon \vec{E} = \epsilon_0 \vec{E} + \vec{P}$ and $\mathbf{P} = [A]\mathbf{p} = [A]\alpha\vec{E}$. Here, [A] is the alkali density, $\mathbf{P}$ is the electric-dipole moment per unit volume, and α is the atomic polarizability. These can be combined:

$$\vec{D} = \epsilon_0 \left(1 + \frac{\alpha[A]}{\epsilon_0} \right) \vec{E}, \tag{4.16}$$

and

$$\frac{\epsilon}{\epsilon_0} = 1 + \frac{\alpha[A]}{\epsilon_0}. \tag{4.17}$$

The index of refraction (which can be a complex number) is defined as

$$n = \sqrt{\frac{\epsilon\mu}{\epsilon_0\mu_0}}, \tag{4.18}$$

For the targets studied in this thesis, $\mu \approx \mu_0$ and $\alpha[A]/\epsilon_0 \ll 1$. Finally, since $k = \frac{\omega}{c}n$,

$$k = \frac{\omega}{c}\sqrt{1 + \frac{\alpha[A]}{\epsilon_0}} \approx \frac{\omega}{c}\left(1 + \frac{\alpha[A]}{2\epsilon_0}\right) \tag{4.19}$$

Since α, the atomic polarizability, can be complex,

$$\tilde{k} = \frac{\omega}{c}\left(1 + \frac{\tilde{\alpha}[A]}{2\epsilon_0}\right), \tag{4.20}$$

which implies,

$$\delta\tilde{k} = \frac{\omega}{c}\frac{[A]}{2\epsilon_0}\delta\tilde{\alpha}, \tag{4.21}$$

with

$$\delta\tilde{\alpha} = \tilde{\alpha}_L - \tilde{\alpha}_R. \tag{4.22}$$

Finally,

$$\phi_r = \frac{l\omega[A]}{4c\epsilon_0}Re\left[\delta\tilde{\alpha}\right] \tag{4.23}$$

The important result is that the faraday rotation angle $\phi_r = \frac{kl}{2}$ can be expressed as a function of the laser frequency, path length, alkali number density, and the atomic polarizability.

4.2 Atomic Polarizability in Terms of Electric Dipole Interaction

In the presence of an external electric field the electron cloud surrounding an atomic nucleus will shift. This shift gives the dipole moment of the atom,

$$\mathbf{p} = \boldsymbol{\alpha} \cdot \mathbf{E}. \tag{4.24}$$

here, α is the atomic polarizability. In our case, the probe beam provides the electric field which polarizes the atomic alkali vapor (via the dipole interaction). Since the probe beam is weak (that is, the pump beam is principally responsible for the alkali polarization and hence the states of the system), it can be treated as a small perturbation.

Much of this section follows the work of Singh [6] and Wu [60].

4.2.1 Time Dependent Perturbation Theory

The time dependent Schroedinger Equation is

$$i\hbar|\dot{\Psi}(t)\rangle = \hat{H}|\Psi(t)\rangle, \tag{4.25}$$

where the Hamiltonian has an unperturbed component as well as an electromagnetic interaction term, $\hat{H} = H_0 + H_{EM}$. The Expansion Postulate states that a wavefunction can be expressed as a sum over its orthogonal fourier components,

$$|\Psi(t)\rangle = \sum_i c_i(t)e^{-iE_it/\hbar}|i\rangle. \tag{4.26}$$

Inserting the expansion postulate wavefunction into the Schroedinger equation,

$$i\hbar\sum_i\left(-\frac{iE_i}{\hbar}c_i + \dot{c}_i\right)e^{-iE_it/\hbar}|i\rangle = \hat{H}_0|\Psi\rangle + \hat{H}_{EM}\sum_i c_i e^{-iE_it/\hbar}|i\rangle. \tag{4.27}$$

$$E_i|\Psi\rangle + i\hbar\sum_i \dot{c}_i e^{-iE_it/\hbar}|i\rangle = \tag{4.28}$$

Using $\hat{H}_0|\Psi\rangle = E|\Psi\rangle$ and taking the inner product with a final state $\langle f|$,

$$i\hbar \sum_i \dot{c}_i e^{-iE_i t/\hbar} \langle f|i\rangle = \sum_i c_i e^{iE_i t/\hbar} \langle f|\hat{H}_{EM}|i\rangle \tag{4.29}$$

$$i\hbar \dot{c}_f = \sum_i c_i e^{i(E_f - E_i)t/\hbar} \langle f|\hat{H}_{EM}|i\rangle \tag{4.30}$$

$$= \sum_i c_i e^{i\omega_{fi} t} \langle f|\hat{H}_{EM}|i\rangle \tag{4.31}$$

Here, ω_{fi} is the transition frequency between the two states. This formalism works well when considering a simple two level system; however, when considering a bifurcated two level system (such as an alkali atom in a magnetic field), it is more natural to express the wavefunction as

$$|\Psi(t)\rangle = \sum_s a_s(t) e^{-iE_s t/\hbar}|s\rangle + \sum_p b_p(t) e^{-iE_p t/\hbar}|p\rangle, \tag{4.32}$$

where s and p refer to the orbital angular momentum of an alkali atom. Explicitly, there will be only two terms in the s-sum, whereas the p-sum will have six terms (two for $P_{1/2}$ and four for $P_{3/2}$). Proceding as above,

$$i\hbar \dot{a}_s = \sum_\sigma a_\sigma e^{i\omega_{s\sigma} t} \langle s|\hat{H}_{EM}|\sigma\rangle + \sum_p b_p e^{i\omega_{sp} t} \langle s|\hat{H}_{EM}|p\rangle \tag{4.33}$$

$$i\hbar \dot{b}_p = \sum_s a_s e^{i\omega_{ps} t} \langle p|\hat{H}_{EM}|s\rangle + \sum_\rho b_\rho e^{i\omega_{p\rho} t} \langle p|\hat{H}_{EM}|\rho\rangle. \tag{4.34}$$

Since we're only inducing transitions between p and s states (the D1 and D2 lines), the equations simplify

$$i\hbar \dot{a}_s = \sum_p b_p e^{i\omega_{sp} t} \langle s|\hat{H}_{EM}|p\rangle \tag{4.35}$$

$$i\hbar \dot{b}_p = \sum_s a_s e^{i\omega_{ps} t} \langle p|\hat{H}_{EM}|s\rangle. \tag{4.36}$$

Finally, a phenomenological dampening term is conventionally introduced to reflect the lifetime of the excited p states [60],

$$i\hbar \dot{a}_s = \sum_p b_p e^{i\omega_{sp}t} \langle s|\hat{H}_{EM}|p \rangle \tag{4.37}$$

$$i\hbar \dot{b}_p = \sum_s a_s e^{i\omega_{ps}t} \langle p|\hat{H}_{EM}|s \rangle - i\hbar\frac{\gamma}{2}b_p \tag{4.38}$$

4.2.2 The Dipole Interaction

The probe beam interacts with the alkali metal via the electric dipole interaction,

$$H_{EM} = -\boldsymbol{p} \cdot Re[\boldsymbol{E}] \tag{4.39}$$

$$H_{EM} = e\boldsymbol{r} \cdot Re[\boldsymbol{E}], \tag{4.40}$$

where **r** is the position operator and the real part of **E** is the physical field (the probe beam). The real part of any complex number, E can be expressed as

$$Re[E] = \frac{E + E^*}{2}. \tag{4.41}$$

Using these results with Eqn.(4.38),

$$\dot{b}_p + \frac{\gamma}{2}b_p = \frac{e}{2i\hbar}\sum_s a_s e^{i\omega_{ps}t}\left[e^{-i\omega t}\langle p|\mathbf{r} \cdot \mathbf{E}|s\rangle + e^{i\omega t}\langle p|\mathbf{r} \cdot \mathbf{E}^*|s\rangle\right] \tag{4.42}$$

where ω is the frequency of the probe laser. The solution to this first-order, linear differential equation [61] is

$$b_p = \frac{e}{2i\hbar}\left[\frac{\sum_s a_s e^{i(\omega_{ps}-\omega)t}\langle p|\mathbf{r} \cdot \mathbf{E}|s\rangle}{\frac{\gamma}{2} + i(\omega_{ps} - \omega)} + \frac{\sum_s a_s^* e^{i(\omega_{ps}+\omega)t}\langle p|\mathbf{r} \cdot \mathbf{E}^*|s\rangle}{\frac{\gamma}{2} + i(\omega_{ps} + \omega)}\right]. \tag{4.43}$$

If the probe beam is tuned near to a transition frequency ($\omega_{ps} - \omega \approx 0$), the second term can be ignored; this is the Rotating Wave Approximation.

$$b_p = \frac{e}{2\hbar} \left[\frac{\sum_s a_s e^{i(\omega_{ps}-\omega)t} \langle p|\mathbf{r} \cdot \mathbf{E}|s \rangle}{\omega - \omega_{ps} + i\frac{\gamma}{2}} \right]. \tag{4.44}$$

Eqn.(4.32) can now be expressed in terms of the probability coefficients, P_s of just the $S_{1/2}$ states. That is, since $|a_s|^2 = P_s$, we can now start to talk about the alkali polarization. The alkali polarization, P is defined as

$$P = P_+ - P_-. \tag{4.45}$$

Because the P_s coefficients are normalized, there is no need to divide by their sum,

$$1 = P_+ + P_-. \tag{4.46}$$

Linear combinations of these two equations are useful

$$P_+ = \frac{1+P}{2} \tag{4.47}$$

$$P_- = \frac{1-P}{2}. \tag{4.48}$$

4.2.3 Atomic Polarizability, Revisited

The atomic polarizability, α, was introduced in section 4.1.2, but can be defined more generally as

$$\mathbf{p} = \boldsymbol{\alpha} \cdot Re[\mathbf{E}]. \tag{4.49}$$

To solve for the atomic polarizability, we need to evaluate the expectation value of the dipole moment

$$
\begin{aligned}
\langle \mathbf{p} \rangle &= \langle \psi | - e\mathbf{r} | \psi \rangle \\
&= -e \left[\sum_\sigma a_\sigma e^{i\omega_\sigma t} \langle \sigma | + \sum_\rho b_\rho e^{i\omega_\rho t} \langle \rho | \right] |\mathbf{r}| \left[\sum_s a_s e^{-i\omega_s t} | s \rangle + \sum_p b_p e^{-i\omega_p t} | p \rangle \right]
\end{aligned}
$$

where σ and ρ refer to the initial variables (analogous to s and p states). Electric dipole transitions must conserve parity. This means that

$$
\langle \sigma | \mathbf{r} | s \rangle = \langle \rho | \mathbf{r} | p \rangle = 0 \tag{4.50}
$$

With the aid of Eqn.(4.44),

$$
\langle \mathbf{p} \rangle = -\frac{e^2}{2\hbar} \sum_{\sigma,p,s} \left[\frac{a_\sigma^* a_s e^{i(\omega_{\sigma p}+\omega_{ps}-\omega)t}}{\omega - \omega_{ps} + i\frac{\gamma_p}{2}} \langle \sigma | \mathbf{r} | p \rangle \langle p | \mathbf{r} \cdot \mathbf{E} | s \rangle + C.C. \right] \tag{4.51}
$$

where $C.C.$ refers to the complex conjugate of the first term. By orthonormality,

$$
a_\sigma^* a_s = \delta_{\sigma,s} P_s. \tag{4.52}
$$

This means that

$$
\begin{aligned}
\langle \mathbf{p} \rangle &= -\frac{e^2}{2\hbar} \sum_{p,s} \left[P_s e^{i(\omega_{sp}+\omega_{ps}-\omega)t} \frac{\langle s | \mathbf{r} | p \rangle \langle p | \mathbf{r} \cdot \mathbf{E} | s \rangle}{\omega - \omega_{ps} + i\frac{\gamma_p}{2}} + C.C. \right] \tag{4.53} \\
&= \frac{e^2}{2\hbar} \sum_{p,s} \left[P_s e^{-i\omega t} \frac{\langle s | \mathbf{r} | p \rangle \langle p | \mathbf{r} \cdot \mathbf{E} | s \rangle}{\omega_{ps} - \omega + i\frac{\gamma_p}{2}} + C.C. \right] \tag{4.54}
\end{aligned}
$$

Finally, with the aid of Eqn.(4.49) and Eqn.(4.41),

$$\tilde{\alpha} = \frac{e^2}{\hbar} \sum_{p,s} P_s \frac{\langle s|\mathbf{r}|p\rangle \langle p|\mathbf{r}|s\rangle}{\omega_{ps} - \omega + i\frac{\gamma_p}{2}} \tag{4.55}$$

$$= \frac{e^2}{\hbar} \sum_{p,s} P_s \frac{|\langle s|\mathbf{r}|p\rangle|^2}{\omega_{ps} - \omega + i\frac{\gamma_p}{2}} \tag{4.56}$$

The matrix elements in the sum can be evaluated using the Wigner-Eckart Theorem

(see Appendix B)

$$|\langle s|\mathbf{r}|p\rangle|^2 = |\langle s||r||p\rangle|^2 \frac{|\langle \frac{1}{2}m_f|1q,p\rangle|^2}{2} \tag{4.57}$$

where q refers to the azimuthal state of $\mathbf{r}$. The relevant terms are

$$|\langle\frac{1}{2}\frac{1}{2}|\mathbf{R}|\frac{1}{2}-\frac{1}{2}\rangle|^2 = |\langle\frac{1}{2}||r||\frac{1}{2}\rangle|^2 \frac{|\langle\frac{1}{2}\frac{1}{2}|11,\frac{1}{2}-\frac{1}{2}\rangle|^2}{2} = \frac{1}{3}|\langle\frac{1}{2}||r||\frac{1}{2}\rangle|^2 \tag{4.58}$$

$$|\langle\frac{1}{2}-\frac{1}{2}|\mathbf{L}|\frac{1}{2}\frac{1}{2}\rangle|^2 = \frac{1}{3}|\langle\frac{1}{2}||r||\frac{1}{2}\rangle|^2 \tag{4.59}$$

$$|\langle\frac{1}{2}-\frac{1}{2}|\mathbf{R}|\frac{3}{2}\frac{3}{2}\rangle|^2 = \frac{1}{4}|\langle\frac{1}{2}||r||\frac{3}{2}\rangle|^2 \tag{4.60}$$

$$|\langle\frac{1}{2}\frac{1}{2}|\mathbf{R}|\frac{3}{2}-\frac{1}{2}\rangle|^2 = \frac{1}{12}|\langle\frac{1}{2}||r||\frac{3}{2}\rangle|^2 \tag{4.61}$$

$$|\langle\frac{1}{2}-\frac{1}{2}|\mathbf{L}|\frac{3}{2}\frac{1}{2}\rangle|^2 = \frac{1}{12}|\langle\frac{1}{2}||r||\frac{3}{2}\rangle|^2 \tag{4.62}$$

$$|\langle\frac{1}{2}\frac{1}{2}|\mathbf{L}|\frac{3}{2}\frac{3}{2}\rangle|^2 = \frac{1}{4}|\langle\frac{1}{2}||r||\frac{3}{2}\rangle|^2 \tag{4.63}$$

where $\mathbf{R}$ and $\mathbf{L}$ refer to the different atomic polarizabilities, α_R and α_L.

4.2.4 Formula for Faraday Rotation Angle

The Faraday Rotation Angle, Eq. 4.23, is

$$\phi_r = \frac{l\omega[A]}{4c\epsilon_0} Re\left[\tilde{\alpha}_L - \tilde{\alpha}_R\right] \tag{4.64}$$

where

$$Re[\tilde{\alpha}] = \frac{e^2}{\hbar} \sum_{p,s} P_s |\langle s|\mathbf{r}|p\rangle|^2 \frac{\omega_{ps} - \omega}{(\omega_{ps} - \omega)^2 + \frac{\gamma_p^2}{4}}. \tag{4.65}$$

Using the results of Ch. 4.2.2 and Ch. 4.2.3, we can write

$$\tilde{\alpha}_L = \frac{e^2}{6\hbar}\left[\left(\frac{2+P}{2}\right)\frac{|\langle\frac{1}{2}||r||\frac{3}{2}\rangle|^2}{\Delta_{D2}+i\frac{\gamma_{D2}}{2}} + (1-P)\frac{|\langle\frac{1}{2}||r||\frac{1}{2}\rangle|^2}{\Delta_{D1}+i\frac{\gamma_{D1}}{2}}\right] \tag{4.66}$$

$$= \frac{e^2}{6m}\left[\frac{2+P}{\omega_{D2}}\frac{1}{\Delta_{D2}+i\frac{\gamma_{D2}}{2}} + \frac{1-P}{\omega_{D1}}\frac{1}{\Delta_{D1}+i\frac{\gamma_{D1}}{2}}\right] \tag{4.67}$$

$$\tilde{\alpha}_R = \frac{e^2}{6m}\left[\frac{2-P}{\omega_{D2}}\frac{1}{\Delta_{D2}+i\frac{\gamma_{D2}}{2}} + \frac{1+P}{\omega_{D1}}\frac{1}{\Delta_{D1}+i\frac{\gamma_{D1}}{2}}\right] \tag{4.68}$$

$$\delta\tilde{\alpha} = \frac{Pe^2}{3m}\left[\frac{1}{\omega_{D2}}\frac{1}{\Delta_{D2}+i\frac{\gamma_{D2}}{2}} - \frac{1}{\omega_{D1}}\frac{1}{\Delta_{D1}+i\frac{\gamma_{D1}}{2}}\right] \tag{4.69}$$

$$Re[\delta\tilde{\alpha}] = -\frac{Pe^2}{3m}\left[\frac{1}{\omega_{D2}}\frac{\Delta_{D2}}{\Delta_{D2}^2+\frac{\gamma_{D2}^2}{4}} - \frac{1}{\omega_{D1}}\frac{\Delta_{D1}}{\Delta_{D1}^2+\frac{\gamma_{D1}^2}{4}}\right] \tag{4.70}$$

where

$$\Delta_D = \omega - \omega_D \tag{4.71}$$

is the detuning of the probe laser from a particular transition, D. The faraday rotation for a single alkali metal angle is therefore

$$\phi_r = -\left(\frac{e^2}{12mc\epsilon_0}\right)P[A]l\omega\left[\frac{1}{\omega_{D2}}\frac{\Delta_{D2}}{\Delta_{D2}^2+\frac{\gamma_{D2}^2}{4}} - \frac{1}{\omega_{D1}}\frac{\Delta_{D1}}{\Delta_{D1}^2+\frac{\gamma_{D1}^2}{4}}\right] \tag{4.72}$$

In a hybrid cell,

$$\phi_r^{total} = \phi_r^{Rb} + \phi_r^K \tag{4.73}$$

4.2.5 Formula Faraday Attenuation

The faraday attenuation is the imaginary counterpart of the faraday rotation.

$$\beta_r = \frac{l\omega[A]}{4c\epsilon_0}Im\left[\delta\tilde{\alpha}\right]. \tag{4.74}$$

From the form of Eq. 4.56, it follows that

$$Im[\alpha] = \frac{e^2}{\hbar} \sum_{p,s} P_s |\langle s|\mathbf{r}|p\rangle|^2 \frac{\frac{\gamma_p}{2}}{(\omega_{ps} - \omega)^2 + \frac{\gamma_p^2}{4}}. \tag{4.75}$$

The derivation of the previous chapter is sufficient to derive the faraday attenutation, under the substitution $(\omega_{ps} - \omega) \rightarrow \frac{\gamma_p}{2}$ for terms in the numerator. Hence,

$$\beta_r = \left(\frac{e^2}{24mc\epsilon_0}\right) P[A]l\omega \left[\frac{1}{\omega_{D2}} \frac{\gamma_{D2}}{\Delta_{D2}^2 + \frac{\gamma_{D2}^2}{4}} - \frac{1}{\omega_{D1}} \frac{\gamma_{D1}}{\Delta_{D1}^2 + \frac{\gamma_{D1}^2}{4}}\right]. \tag{4.76}$$

If the laser is tuned close to one particular resonance,

$$\beta_r \approx -\frac{\gamma}{2\Delta}\phi_r. \tag{4.77}$$

Typically, we don't study β_r; however, we try to minimize Eq. 4.77 so the attenuation in small.

4.3 Alkali Polarimetry

The faraday rotation angle, ϕ_r (Eq. 4.72) and the saturation ^{3}He polarization, P_∞^{He} (Eq. 2.71) both depend on the alkali polarization, P_A. To fully understand either, measurements of P_A must be made.

Alkali polarization measurements can be made by probing Zeeman-transition populations [62]. Under our operating conditions, the populations of these sublevels are well modeled by the spin-temperature distribution [63]. We make *in situ* measurements of the alkali polarization by monitoring the faraday rotation angle while Zeeman transitions are induced [64]. Such transitions depolarize the alkali metal and consequently decrease the faraday rotation angle. During a measurement (see Fig. 4.2) at 18.2MHz, the main holding field is swept through the different Zeeman transitions

and a spectrum of Lorentzian resonances is produced (see Fig. 4.6). A value for the alkali polarization is extracted by comparing the areas of successive peaks.

The area under a particular peak is given by

$$A(F, m_F) = A_0 \left(F(F+1) - m_F(m_F - 1) \right) e^{m_F \beta} (1 - e^{-\beta}) \qquad (4.78)$$

where F is the total quantum number, m_F is the azimuthal component, A_0 is a proportionality constant that is independant of F, m_F, and β, and β is the spin temperature, given by

$$\beta = \ln \frac{1 + P_A}{1 - P_A} \qquad (4.79)$$

Under our operating conditions, transitions in the same F manifold are well resolved; however, transitions involving the same m_F are unresolved between the F and $F - 1$ manifolds. Such transitions are called twin transitions.

m_F Transition	P (I = 5/2)	P (I = 3/2)
$\frac{3 \to 2}{2 \to 1}$	$\frac{R-3/7}{R+3/7}$	
$\frac{2 \to 1}{1 \to 0}$	$\frac{R-7/9}{R+7/9}$	$\frac{R-1/2}{R+1/2}$
$\frac{1 \to 0}{0 \to -1}$	$\frac{R-1}{R+1}$	$\frac{R-1}{R+1}$
$\frac{0 \to -1}{-1 \to -2}$	$\frac{R-9/7}{R+9/7}$	$\frac{R-2}{R+2}$
$\frac{-1 \to -2}{-2 \to -3}$	$\frac{R-7/3}{R+7/3}$	

Table 4.1: Equations for alkali polarization using the ratio of areas of adjacent Zeeman transitions

To extract a value for P_A, we compare adjacent areas,

$$R = \frac{A(F, m_F) + A(F - 1, m_F)}{A(F, m_{F-1}) + A(F - 1, m_{F-1})} \qquad (4.80)$$

Note that because we can't resolve the twin transitions, we add their areas together. Finally, a value for P_A can attained by combining Eqs. 4.78-4.80. Table 4.3 gives values of P_A for different transitions.

4.4 Experimental Methods
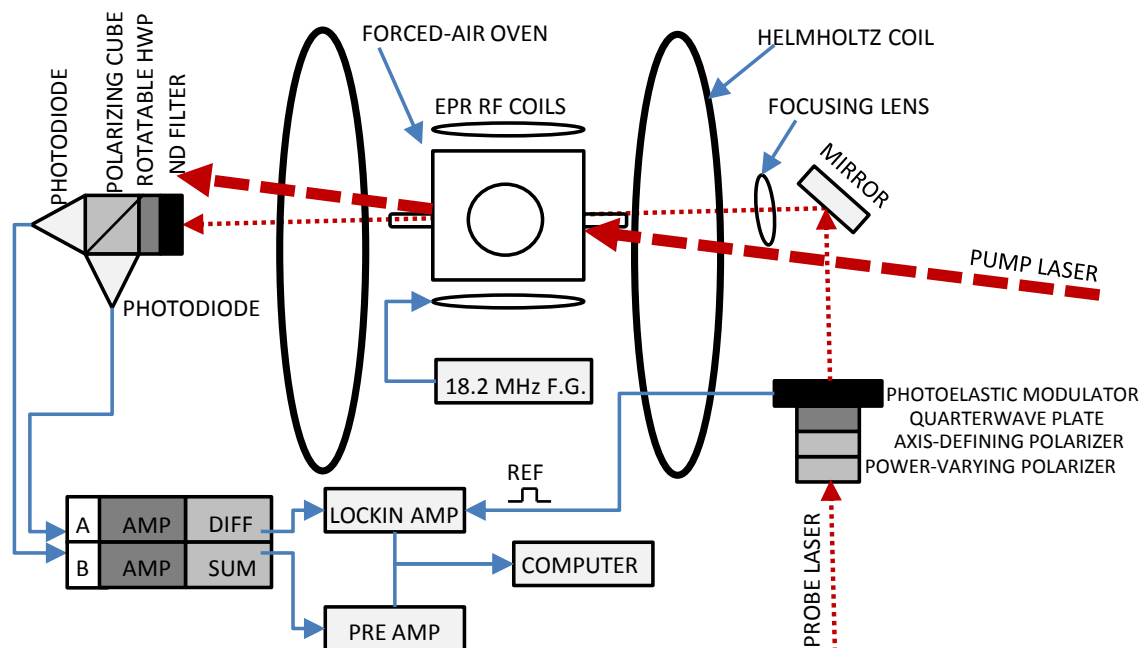
Figure 4.2: Experimental Setup (Top View). The pump laser has been drawn at an angle relative to the helmholtz field. This was only done to make the graphic more readable. In reality, the pump beam is nearly parallel to the helmholtz field.

A schematic of the experimental setup is shown in Fig. 4.2. The probe beam first passes through two polarizing cubes; the first is used to control its power (typically 1 mW), the second to define the linear axis of the beam. The linearly-polarized beam then passes through a quarter wave plate (QWP) and a 50 kHz photoelastic modulator (PEM) – the QWP and PEM are used in conjunction with a lock-in amplifier to isolate relatively weak signals. After the probe beam exits the cell, it passes through a neutral density (ND) filter, a rotatable halfwave plate (HWP), and a polarizing beam-splitting cube before being detected in two photodiodes. The ND filter is used to block out room light and minimize background from the pump laser. A polarizing cube is used to separate the linear polarization into its horizontal and vertical components. The photodiode signals are amplified before being added and subtracted from each other. A detailed discussion of experimental techniques is

presented in the following sections.

4.4.1 Measuring Angles with a Polarizing Beam Splitting Cube

The faraday rotation angle can be measured by using a polarizing beam splitting cube. The cube will pass (reflect) the horizontal (vertical) linear components of the probe beam (hence, it will separate the light into its $|X\rangle$ and $|Y\rangle$ components). The light, once separated, can then be detected by photodiodes. Since the photodiodes make a power measurement, we calculate $|\tilde{E}_x|^2$ and $|\tilde{E}_y|^2$ using Eqs. 4.12 and 4.13,

$$|\tilde{E}_x|^2 = \tilde{E}' \left(\cos^2 \phi_r \cosh^2 \beta_r + \sin^2 \phi_r \sinh^2 \beta_r \right) \tag{4.81}$$

$$|\tilde{E}_y|^2 = \tilde{E}' \left(\sin^2 \phi_r \cosh^2 \beta_r + \cos^2 \phi_r \sinh^2 \beta_r \right). \tag{4.82}$$

To eliminate common factors that depend on absolute laser power ($\tilde{E}'$), a ratio of the difference to the sum of the components can be made:

$$\frac{\Delta}{\Sigma} = \frac{|\tilde{E}_x|^2 - |\tilde{E}_y|^2}{|\tilde{E}_x|^2 + |\tilde{E}_y|^2} \tag{4.83}$$

$$= \frac{\left(\cosh^2 \beta_r - \sinh^2 \beta_r \right) \left(\cos^2 \phi_r - \sin^2 \phi_r \right)}{\left(\cosh^2 \beta_r + \sinh^2 \beta_r \right) \left(\cos^2 \phi_r + \sin^2 \phi_r \right)} \tag{4.84}$$

$$= \frac{\cos \left(2\phi_r \right)}{\cosh \left(2\beta_r \right)}. \tag{4.85}$$

It is important to note that the angle measured by the photodiodes is twice the actual rotation angle.

4.4.2 Using a Half-Wave Plate to Cancel Unwanted Rotation

Every optic along the path of the probe beam distorts the beam by a small amount. This distortion can both change the degree of linear/circular polarization and add

a small amount of rotation. We label the sum of this miscellaneous rotation ϕ_{misc}.
Consequently, even in the absence of an alkali vapor, an initially horizontally-polarized
probe beam will have a small vertical component when it arrives at the detector cube.
To compensate for this additional rotation, a rotatable half-wave plate is introduced
immediately before the polarizing beam splitting cube (see Appendix C.2). With
the addition of a HWP, Eq. 4.85 becomes

$$\frac{\Delta}{\Sigma} = \frac{\cos 2\Phi}{\cosh(2\beta_r)}. \tag{4.86}$$

where

$$\Phi = 2\phi_h - \phi_{misc} - \phi_r. \tag{4.87}$$

and ϕ_h is the angle the fast axis of the HWP makes with respect to the linear polar-
ization of the probe beam. The HWP can be used to "null" the difference signal in
the absence of polarized alkali vapor ($\phi_r = 0$). To ensure $\Delta = 0$ ($\Phi = 45°$), the fast
axis of the HWP must be set to

$$\phi_h = \frac{1}{2}\left(45° + \phi_{misc}\right). \tag{4.88}$$

At this angle,

$$\frac{\Delta}{\Sigma} = \frac{\cos\left(90° - 2\phi_r\right)}{\cosh(2\beta_r)} \tag{4.89}$$

$$= -\frac{\sin(2\phi_r)}{\cosh(2\beta_r)} \tag{4.90}$$

4.4.3 Using a Photoelastic Modulator

Although great care is taken to minimize the amount of background leaked into the
detector, measured signals tend to be rather noisy. To manage this unfavorable signal-
to-noise, we use a Photoelastic Modulator (PEM, see Appendix C.3) to modulate the

polarization of the probe beam. When used in conjunction with a lockin amplifier, very sensitive measurements can be made.

After passing through two linear polarizers (Fig. 4.2), the horizontally-polarized probe beam travels through a quarter-wave plate (see Appendix C.1), which is oriented at 45° with respect to the polarizing cube. This setup typically yields circular polarizations in excess of 99% (even after passing through the rest of the optics and the cell, the polarization is still greater than 95%). Next the circularly polarized light travels through a PEM, which has its fast axis horizontal (and hence at 45° to the QWP's fast axis). The evolution of the probe beam through these additional optics is described in detail in Appendix C.3.

With the addition of a PEM, Eq. 4.88 becomes

$$\frac{\Delta}{\Sigma} = \frac{P \sin \Gamma(t) \cos 2\Phi}{\cosh 2\beta + \cos \Gamma(t) \sinh 2\beta}. \tag{4.91}$$

where $\Gamma(t)$ is the retardance of the PEM (see Appendix C.1) and P, the degree of circular polarization immediately before the PEM has been introduced. Note that for $\Gamma = -\frac{\pi}{2}$ (A QWP at $-45°$), this reduces to Eq. 4.85. Using $\Gamma(t) = \Gamma_0 \sin(\gamma t)$, where for us Γ_0 is in the range of $.013(2\pi)$ to $.65(2\pi)$, the PEM terms can be expanded in terms of bessel functions (J_i),

$$\sin(\Gamma_0 \sin(\gamma t)) = 2 \left[J_1(\Gamma_0) \sin(\gamma t) + J_3(\Gamma_0) \sin(3\gamma t) + ... \right] \tag{4.92}$$

$$\cos(\Gamma_0 \sin(\gamma t)) = J_0(\Gamma_0) + 2 \left[J_2(\Gamma_0) \cos(2\gamma t) + J_4(\Gamma_0) \cos(4\gamma t) + ... \right] \tag{4.93}$$

where, γ is the modulation frequency of the PEM (50kHz for us).

A lockin amplifier can be used to select different frequency terms in the bessel function expansion. For the difference signal, if the lockin is referenced at 50 kHz, only the first term in Eq. 4.92 needs to be considered. For the sum signal, the 100 kHz and higher terms in Eq. 4.93 can simply be ignored if a 1ms lowpass filter is

employed ($V_{out} \approx .001 V_{in}$). Eq. 4.91 now reads:

$$\frac{\Delta}{\Sigma} = \frac{2PJ_1(\Gamma_0)\cos 2\Phi}{\cosh 2\beta + J_0(\Gamma_0)\sinh 2\beta}.$$

(4.94)

Note that the term isolated by the lockin amplified, $\sin\gamma t$ has been removed from the numerator. To maximize the detected signal for Eq. 4.94, we choose $\Gamma_0 = 0.3 \times 2\pi$, which is very close to the maximum value of J_1.

4.4.4 The Normalization

Under typical operating conditions (corresponding to sufficiently detuned light), $\beta \approx 0$ and the denominator in Eq. 4.94 can be set to 1 (see Eq. 4.77). However, instead of ignoring the denominator, we rewrite Eq. 4.94 as

$$\frac{\Delta}{\Sigma} = N \times \cos 2\Phi.$$

(4.95)

where we have introduced the normalization, $N(\beta, \Gamma_0)$. The normalization can be measured (using a lockin amplifier) by simply rotating the HWP (recall $2\Phi = 4\phi_h - 2\phi_{misc} - 2\phi_r$). Such measurements also yield important information about ϕ_r. As an example, consider Fig. 4.3.

The data in Fig. 4.3 is atypical (often, the second sin-wave is not visible). The double-sin form of the data is due to the fact that our achromatic HWP is neither fully achromatic nor fully half-wave. The retardance of our HWP is actually closer to 0.47 waves, but varies depending on the wavelength of the probe beam. To compensate for this imperfaction, instead of fitting normalizations to Eq. 4.95, we fit to

$$\frac{\Delta}{\Sigma} = N \times \cos(4\phi_H - 2\phi) + M \times \cos(2\phi_H + a) + b$$

(4.96)

where ϕ_H is the angle measured on the HWP relative to its mount (note, this is not
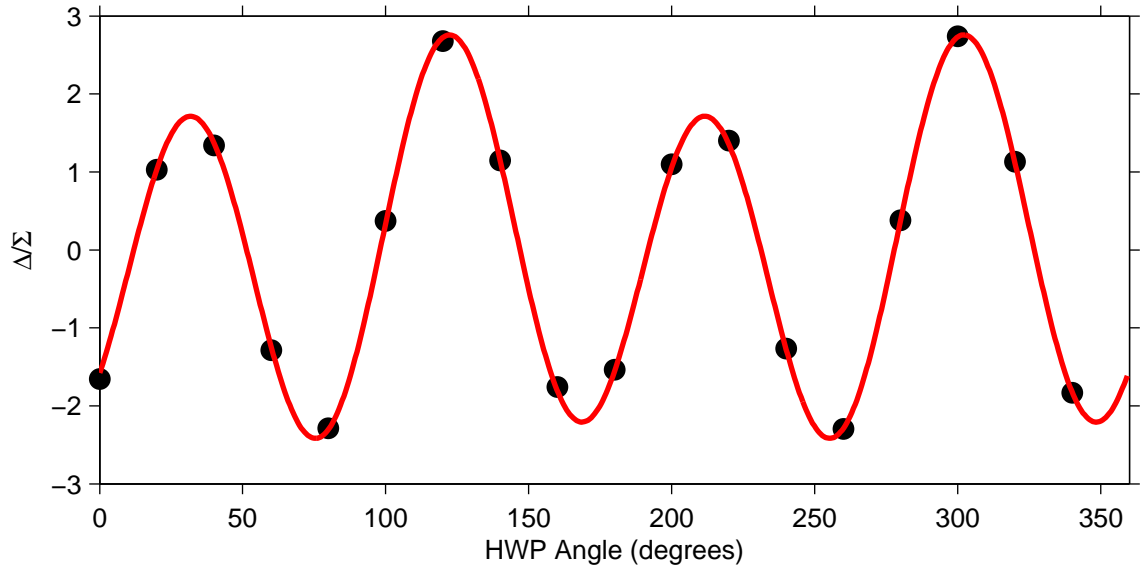
Figure 4.3: Normalization Measurement for Target Cell Alex. $\lambda = 772.028$nm, $T_{oven} = 235°$C, Lasers OFF

necessarily relative to the HWP fast axis) and

$$\phi = \phi_{misc} + \phi_r + 2\phi_{offset}, \tag{4.97}$$

where ϕ_{offset} is the angle between the fast-axis of the HWP and the angle corresponding to 0 on the mount. We note that, ϕ_{misc} has a wavelength dependance.

4.4.5   Measuring Faraday Rotation Angles

We measure Faraday Rotation angles using the setup illustrated in Fig. 4.2. To start, we heat our cell to a desired set temperature (usually 235°C for a hybrid cell) and allow the oven temperature to stabilize with the pump lasers off. A normalization measurement is performed at a particular probe wavelength as described in Ch. 4.4.4. This gives a measurement of the phase, which we shall refer to as $\phi_{lasers\ off}$. The detected difference signal, Δ is then zeroed by rotating the HWP (see Ch. 4.4.2).

At this point, we note that although we're interested in ϕ_r, what we actually

measure is sin of the rotation angle (Eq. 4.96 when properly nulled). Consequently, for $\phi_r > 45°$, care must be taken to ensure the domain is well understood. To understand the domain, we perform a "rampup," in which we slowly turn on the pump lasers while monitoring the difference (Δ) and sum (Σ) signals. As the laser power increases, so does the alkali polarization and consequently the faraday rotation angle. By monitoring the zero-crossings (when $\Delta = 0$) and the maxima of Δ, the domain can be understood. A typical rampup is shown in Fig. 4.4.

An undesirable consequence of the increased laser power is that the alkali density will also increase, corresponding to an increase in temperature of about 5°C in equilibrium (for a discussion on pumping chamber temperatures, see Ch. 2.2.4. It is interesting to note that at the same time, the temperature of the ^{3}He gas in the pumping chamber was measured to be 269°C (see Fig. 3.6)). Because the lasers are now heating the cell, it will take some time for the feedback circuit controlling the oven to stabilize again. While the oven is stabilizing, the alkali density and polarization will change (as the density increases, the polarization often drops as the pump laser becomes attenuated). An added consequence of the increased alkali density is that the probe laser attenuation will increase, causing a decrease in the normalization, N of the measurement. This explains why the third flip in Fig. 4.4 occurs at a lower Δ/Σ than the first flip.

From rampup measurements like the one in Fig. 4.4, rough estimates of the faraday rotation angle can be made. After stabilizing, this particular measurement appears to have $2\phi_r < -540°$ (corresponding to the third zero-crossing); however, it's not clear if this measurement had a fourth flip (which would give $2\phi_r < -630°$). This difficulty arises because extracting ϕ_r from a measurement of Δ/Σ requires us to take the arcsin of Δ/Σ:

$$2\phi_r \approx -\sin^{-1} \frac{1}{N} \frac{\Delta}{\Sigma} \qquad (4.98)$$

here, we have ignored the full double-sin form of the normalization (see Ch. 4.4.4).
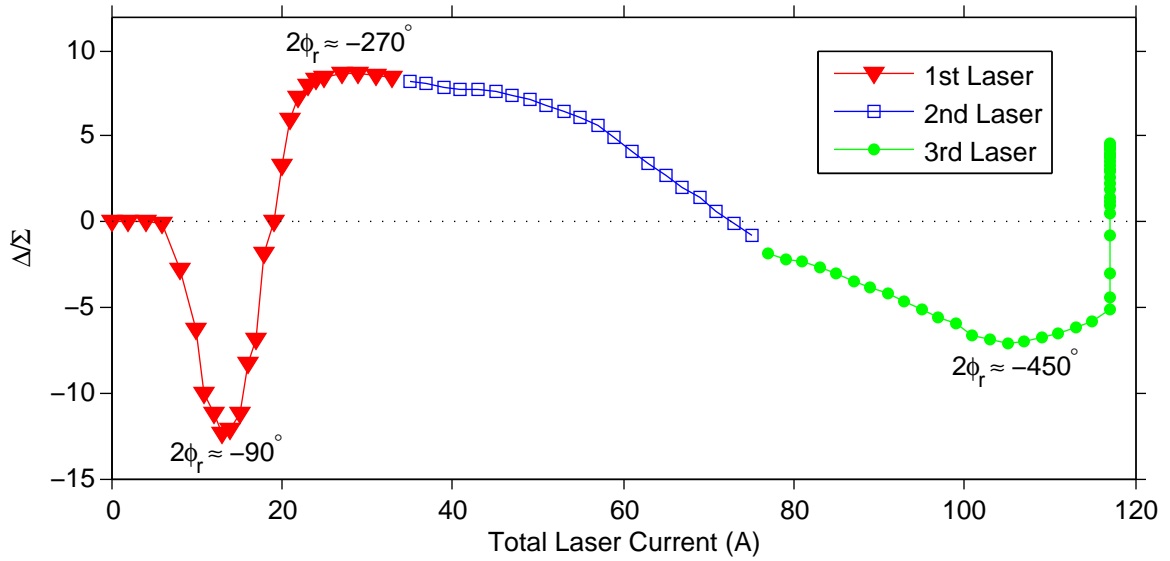
Figure 4.4: Laser Rampup Scan for Target Cell Brady. $\lambda = 782.5nm$, $T_{oven} = 235°C$. Three lasers are slowly ramped up producing 3 distinct flips and 3 zero crossings, giving $2\phi_r > 540°C$. The irregular shape is created because the lasers heat up the cell, whose temperature is controlled by a feedback circuit.

The domain of $\sin^{-1}$ is only 180°, implying that ϕ_r has a 90° domain (corresponding to the space between a maximum and minimum). A better way to determine the domain and rotation angle is to compare normalization measurements

Reliable measurements of $2\phi_r$ can be made by comparing normalization with and without the pump lasers. Once the oven has stabilized with the pump lasers on, a second normalization measured is made. The normalization technique described in Ch. 4.4.4 gives a direct measurement of $2\phi_r$ that doesn't require $\sin^{-1}$ to be calculated. Rather, a normalization measurement gives a value for 2ϕ in the phase of the sin-wave (see Eq. 4.96; also, note that ϕ, not ϕ_r is being measured, see Eq. 4.97). The domain of a sin-wave is 360°, implying that ϕ has a 180° domain (this elimates ambiguity around extrema like the one in Fig. 4.4).

Before a value for ϕ_r can be extracted from the normalization technique, a rough guess for the rotation angle is needed. Fortunately, rampups like the one in Fig. 4.4 provide this. For example, in this measurement, the rotation angle is somewhere

between $-720° < 2\phi < -360°$. Thus, we need to adjust our 2ϕ value from the normalization fit by $360°$. The normalization measured before the lasers were ramped on had a phase of $2\phi_{off} = 313.8°$. The normalization measured after the lasers were ramped on had a phase of $2\phi_{on} = 79.9°$; this number needs to be adjusted by $360°$ to account for the new domain attained: $2\phi_{on,adj} = -280.1°$. Finally,

$$\phi_r = \phi_{on} - \phi_{off} \tag{4.99}$$

$$= -270.0° \tag{4.100}$$

4.4.6   Extracting Number Density Ratios

The equation for the faraday rotation angle of a single alkali species (Eq.4.72) can be written as

$$\phi_r = -\left(\frac{e^2}{12mc\epsilon_0}\right) P[A]l\omega \left[f_1 - f_2\right] \tag{4.101}$$

where

$$f_1 = \frac{1}{\omega_{D2}} \frac{\Delta_{D2}}{\Delta_{D2}^2 + \frac{\gamma_{D2}^2}{4}} \tag{4.102}$$

$$f_2 = \frac{1}{\omega_{D1}} \frac{\Delta_{D1}}{\Delta_{D1}^2 + \frac{\gamma_{D1}^2}{4}} \tag{4.103}$$

For a Rb/K hybrid mixture, Eq. 4.101 becomes

$$\phi_r = -\left(\frac{e^2}{12mc\epsilon_0}\right) Pl\omega \left([Rb]\left[f_1^{Rb} - f_2^{Rb}\right] + [K]\left[f_1^K - f_2^K\right]\right) \tag{4.104}$$

which we chose to write as

$$\phi_r = -\left(\frac{e^2}{12mc\epsilon_0}\right) P[K]l\omega \left(\left[f_1^{Rb} - f_2^{Rb}\right]/D + \left[f_1^K - f_2^K\right]\right) \tag{4.105}$$

where $D = [K]/[Rb]$ is the K/Rb number density ratio (Eq. 2.88). To extract a value for $[D]$ and $P_A[K]l$, we perform several faraday rotation angle measurements (see Ch. 4.4.5) and fit the resulting angles to Eq. 4.105. Typically, we introduce a third fit parameter, $\delta\lambda$ to account for any offset between our wavemeter and the NIST resonances (see Tab. 2.7).
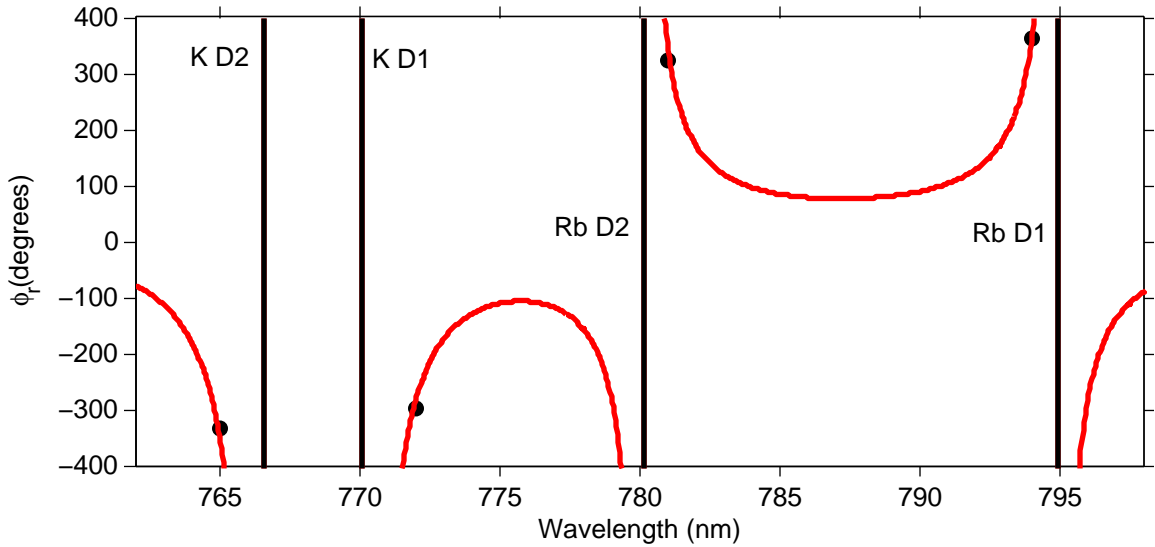
Figure 4.5: Faraday Rotation measurement of Brady at 235C with 3 Comets. D=2.60(19)

Fig. 4.5 shows a typical measurement. For this particular measurement, target cell Brady was pumped at an oven set temperature of 235C with three line-narrowed Comet lasers. The resulting fit gave $D = 2.60(19)$, $P_Al[K] = (48.6 \pm 2.8)\text{cm}/\text{cm}^3$, and $\delta\lambda = (1 \pm 43) \times 10^{-3}\text{nm}$. The quoted errors have been rescaled to give a reduced chi-squared of 1.

4.4.7 Measuring Alkali Polarizations

We note that the alkali polarization measurement (see Ch. 4.3) introduces an additional alkali-relaxation mechanism; in equilibrium, the alkali polarization is given

by

$$P_A(\Gamma_{rf}) = \frac{R}{R + \Gamma_A + \Gamma_{rf}} \tag{4.106}$$

where R is the optical pumping rate, Γ_{rf} is the EPR RF depolarization rate, and Γ_A is the total alkali relaxation rate in the absence of EPR RF. Eq. 4.106 can be rewriten as

$$\frac{1}{P_A} = \frac{1}{P_0} + \frac{\Gamma_{rf}}{R} \tag{4.107}$$

where

$$P_0 = \frac{R}{R + \Gamma_A} \tag{4.108}$$

$$\Gamma_{rf} \propto B_{rf}^2 \propto I^2 \tag{4.109}$$

here, B_{rf} is the magnetic field of the RF and I is the current in the EPR RF coils. Finally, we write

$$\frac{1}{P_A} = \frac{1}{P_0} + mI^2 \tag{4.110}$$

where m is a slope that is inversely proportional to the optical pumping rate.

We extrapolate to P_0, the alkali polarization corresponding to $\Gamma_{rf} = 0$, by performing several sweeps with different RF field amplitudes. Fig. 4.6 shows the result of a typical alkali polarization scan, which we performed at an off-resonance probe wavelength of 785nm with 1 comet laser on target cell Brady. Under these conditions, 4 peaks are clearly visible: 2 corresponding to ^{39}K, the most abundant isotope present, and 1 each for ^{41}K and ^{87}Rb. However, whereas the potassium peaks correspond to single transitions (or the twin transition for the higher field ^{39}K peak), the ^{87}Rb peak contains all the transitions of that isotope. The field separation between zeeman sublevels (see Eq. 3.85) is much smaller for rubidium because $\nu_{hfs}^{Rb} \gg \nu_{hfs}^{K}$ (see Tab. 3.1).

To extrapolate to P_0, each polarization scan in Fig. 4.6 is fit to a lorentzian.
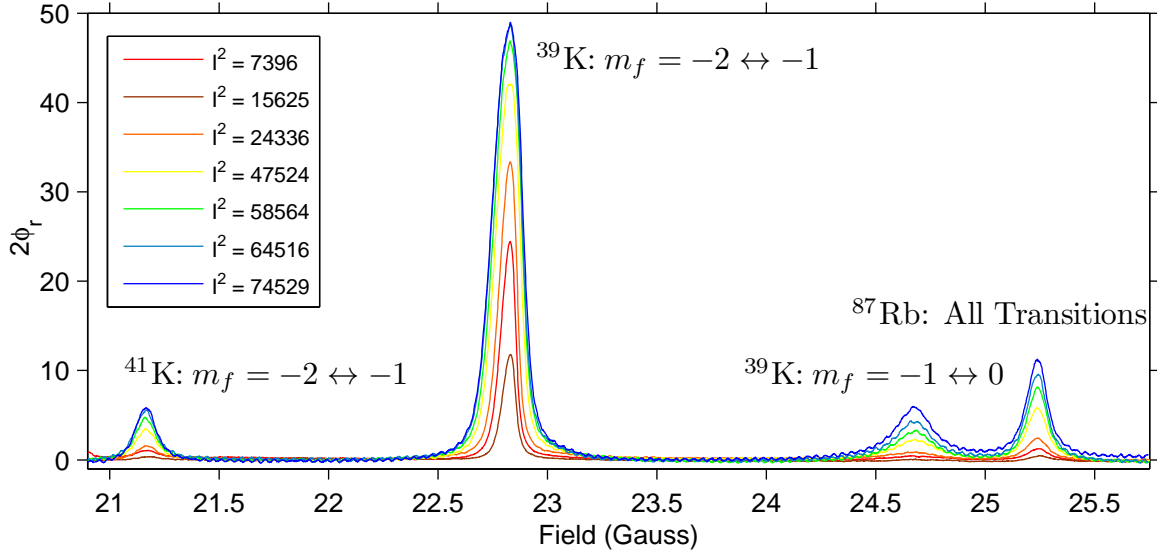
Figure 4.6: Alkali Polarization Scan for Target Cell Brady at Probe Wavelength 785nm with 1 Comet Laser.

The ratio of the two ^{39}K peaks is calculated. The polarization of each scan can be extracted from the ratio by using Tab. 4.3. The inverse of these polarizations are plotted as a function of I^2 (here, I refers to the current of the EPR RF coil) and fit to Eq. 4.110; we refer to these plots as P_0 plots.

Fig. 4.7 shows two P_0 plots. The top line (red) shows the same data that were plotted in Fig. 4.6; the bottom line (blue) shows data that were taken with two line-narrowed comet lasers. In both cases, the errorbars were attained by forcing the reduced chi-squared to equal 1. In addition to a higher P_0 being attained with more laser power ($99 \pm 1\%$ vs. $95 \pm 1\%$), we note that the slope, m is smaller. The decrease in the slope is because m is inversely proportional to the optical pumping rate, R. We note here that we also attempted to perform alkali polarization measurements with 3 line-narrowed comet lasers. However, the alkali polarization and optical pumping rate were so high under those conditions that we were unable to see a second ^{39}K peak.

Using the data from Ch. 4.4.6, which were performed using all 3 line-narrowed comet lasers, and combining with a conservative alkali polarization of $99 \pm 1\%$, we

find $[K]l = (49.1 \pm 2.9) \times 10^{14} \mathrm{cm/cm^3}$.
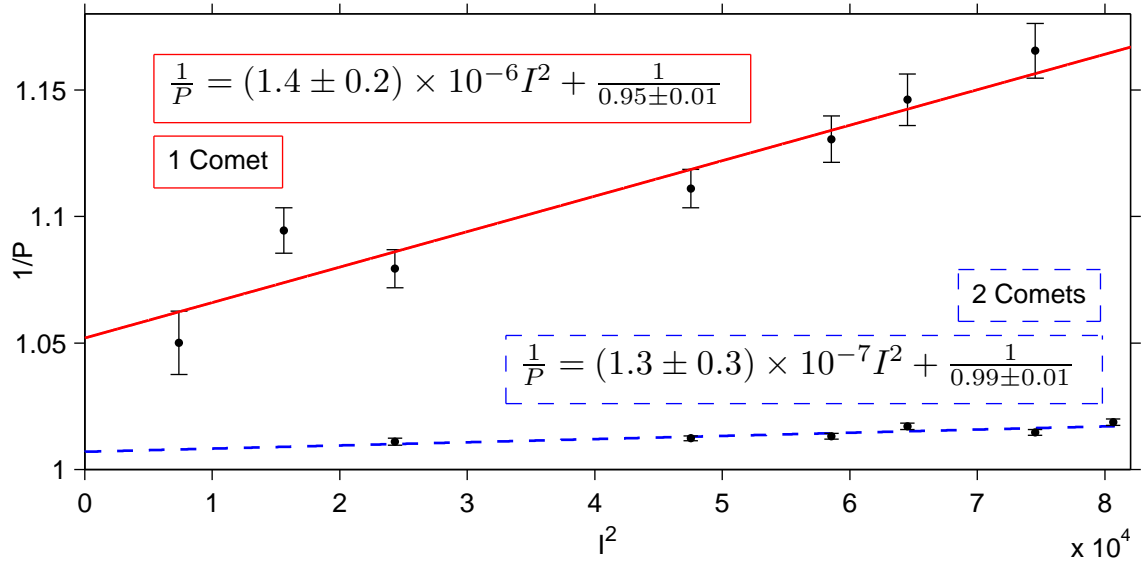
Figure 4.7: P_0 Plot for Target Cell Brady at Probe Wavelength 785nm. Several alkali polarization measurements are made at different EPR RF amplitudes. The alkali polarization in the absence of any RF can be extrapolated by fitting the data to Eq. 4.110

4.4.8 Path Length Determination

The path length of the probe laser inside the cell can be very difficult to measure. Although measurements of the outer diameter of the pumping chamber are trivial to obtain, our cells are hand blown and consequently have large variations in the thickness of the glass. We measure the inner diameter of the glass spheres by taking calibrated images with a CCD camera (see Fig. 4.8, left). The calibration is performed by calculating the ratio of actual size (cm) to image size (pixels) of an object at various distances from the camera (ranging from about 15 cm to just over a meter),

$$c_i = \alpha(d_i + d) \tag{4.111}$$

where c_i is the calibration constant for measurement i, d_i is the distance from the front of the camera to the plane of the measurement, α is geometric proportionality

constant, and d is an unknown offset that corresponds to the distance between the front of the camera and the CCD sensor. Several measurements of c_i are fit to a line, which yields values for d and α. Finally, a value for c_y, the calibration constant at the location of the probe beam can be attained. The path length image (see Fig. 4.8, right), which is attained at modest alkali densities (and in the absense of the pump laser), is acquired using a D2 filter with the probe laser tuned slightly off the D2 resonance. The path length of the probe beam for target cell Brady was found to be 6.59 ± 0.25cm. Using the information from Sec. 4.4.5, 4.3, this gives $[K] = (7.45 \pm 0.52) \times 10^{14}$cm^{-3}. This density can be used to calculate the temperature of the inside of the glass pumping chamber, which is in equilibrium with the alkali metal puddle (see Ch. 2.2.4).

Because we have a two-component system, the density measured by faraday rotation cannot be directly compared to the vapor pressure curves presented in Ch. 2.4.1 without also knowing f_{Rb}, or equivalently, D. However, this density can be combined with D to extract a temperature for the pool of molten alkali metal. To do this, we rewrite Eq. 2.103 as

$$f_{Rb} = \frac{D_0(T)}{D_0(T) + D(T)} \tag{4.112}$$

where D_0 is the ratio of densities given by pure vapor pressure curves. Because $f_{Rb} + f_K = 1$,

$$f_K = \frac{D(T)}{D_0(T) + D(T)} \tag{4.113}$$

Using Eq. 2.99, this gives

$$[K]_{pure} = \frac{[K]_{farrot}}{f_K} \tag{4.114}$$

$$= \left(1 + \frac{D_0(T)}{D(T)}\right) [K]_{farrot} \tag{4.115}$$

This equation is transcendental for (T) and must be solved numerically. When this

is done, we find $[K]_{pure} = (8.00 \pm 0.56) \times 10^{14} \mathrm{cm}^{-3}$ corresponding to a temperature of 241.4°C. This temperature is very close to the oven set temperature of 235°C.
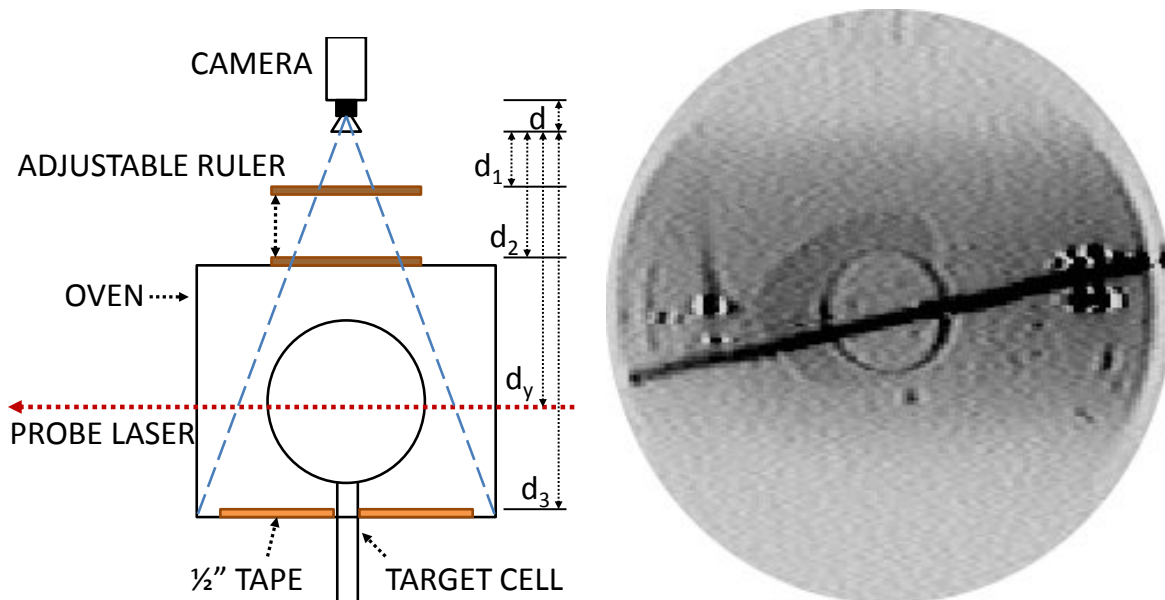
Figure 4.8: Path Length Measurement. (Left) Schematic showing calibration procedure. (Right) CCD image showing path length of probe laser.

4.5 Comparison Between Faraday Rotation and Pressure Broadening Data

In addition to measuring D using Faraday Rotation, measurements of the molar fractions f_{Rb} and f_K are made using the pressure-broadening technique, described at the beginning of Ch. 4. Such measurements can be extrapolated to operating conditions using Eq. 2.100. A comparison showing good agreement between the two techniques is presented in Table 4.2.

Cell	T_{pc}^{set}	D_{fr}	D_{pb}
Alex	235	1.37(08)	1.19(07)
Stephanie	235	1.39(11)	1.50(10)
Brady	235	2.60(02)	2.36(24)
Samantha	235	4.37(10)	4.34(23)
Astral Weeks	235	7.09(55)	6.21(56)

Table 4.2: Comarison between Faraday-Rotation and Pressure-Broadening Data. Pressure-broadening ratios, D_{pb}, were attained at a temperature 5°C above the temperature measured in the oven (for more on oven temperatures, see Ch. 2.2.4).

Chapter 5

Hybrid Results

In this Chapter, we present results showing the dramatic performance that can be achieved when line-narrowed lasers are used to pump hybrid cells. Additionally, we show how recently-implemented alkali polarimetry has allowed us to better characterize and understand these results. The improvements in ^{3}He polarization have resulted in much higher effective luminosities in recent electron-scattering experiments (see Fig. 1.2 and Ch. 1.1). Such improvements in effective luminosity have made experiments in new energy ranges possible. Additionally, the time it takes for an experiment to achieve a desired level of uncertainty has decreased.

In this chapter, we first present a theory explaining the dynamics of SEOP in a two-chambered target cell. We then present results showing the dramatic improvement in ^{3}He polarization. Finally, we present a discussion about how to extract X factors from these cells.

5.1 Diffusion in a Two-Chambered Target Cell

So far, this thesis has only alluded to the difficulties of working with two-chambered target cells. In this section, we'll present a theory of diffusion in a two-chambered target cell.

5.1.1 The Single-Chambered Cell

It is straightforward to describe both the buildup and decay of polarization in a target cell such as that shown in Fig. 1.1 in terms of various parameters, many of which are easily measured and understood. We begin by considering the simpler example of a single-chambered cell, where the equation describing the time evolution of the polarization is given by:

$$\dot{P} = \gamma_{se}P_A - (\gamma_{se} + \Gamma)P, \tag{5.1}$$

where P is the ^{3}He polarization, P_A is the polarization of the alkali vapor, γ_{se} is the rate at which the ^{3}He is polarized due to spin exchange, and Γ is the spin-relaxation rate of the ^{3}He due to all other processes. The solution to Eq. 5.1 is given by

$$P(t) = P_0 e^{-(\gamma_{se}+\Gamma)t} + P_A \frac{\gamma_{se}}{\gamma_{se}+\Gamma}(1 - e^{-(\gamma_{se}+\Gamma)t}) \qquad (5.2)$$

where P_0 is the ^{3}He polarization at $t = 0$.

5.1.2 The Double-Chambered Cell

In electron-scattering experiments, target cells have been employed that have two chambers: a pumping chamber (pc), where SEOP occurs, and a target chamber (tc), through which the electron beam passes (see Fig. 1.1). This design has several practical advantages, including the fact that ionization due to the electron beam does not affect the polarization of the alkali vapor. The two chambers are connected by a short, narrow transfer tube (tt). Polarized gas from the pc diffuses into the tc where it interacts with the electron beam. The polarization build up in such a cell can be described by the coupled differential equations

$$\dot{P}_{pc} = \gamma(P_A - P_{pc}) - \Gamma_{pc}P_{pc} - d_{pc}(P_{pc} - P_{tc}) \qquad (5.3)$$

$$\dot{P}_{tc} = -\Gamma_{tc}P_{tc} + d_{tc}(P_{pc} - P_{tc}) \qquad (5.4)$$

where d_{pc} (d_{tc}) is the diffusion rate out of the pumping (target) chamber [65]. The diffusion rates are related by $f_{pc}d_{pc} = f_{tc}d_{tc}$ where $f_{pc}(f_{tc})$ is the fraction of atoms in the pc(tc) and $f_{pc} + f_{tc} = 1$. Using the ideal gas law, $PV = Nk_BT$ and assuming the pc and tc are at the same pressure, we can write

$$f_{pc}\frac{T_{pc}}{V_{pc}} = f_{tc}\frac{T_{tc}}{V_{tc}}, \qquad (5.5)$$

which can be rewritten as

$$f_{pc} = \frac{V_{pc}/V_{tc}}{V_{pc}/V_{tc} + T_{pc}/T_{tc}} \tag{5.6}$$

It is convenient to write the rate equations as

$$\dot{P}_{pc} = aP_{pc} + bP_{tc} + B \tag{5.7}$$

$$\dot{P}_{tc} = cP_{pc} + dP_{tc} \tag{5.8}$$

where

$$a = -(\gamma_{se} + \Gamma_{pc} + d_{pc}) \tag{5.9}$$

$$b = d_{pc} \tag{5.10}$$

$$c = d_{tc} \tag{5.11}$$

$$d = -(\Gamma_{tc} + d_{tc}) \tag{5.12}$$

$$B = \gamma_{se}P_A \tag{5.13}$$

The easiest way to solve these coupled differential equations is to decouple them:

$$\dot{P}_{pc} = aP_{pc} + bP_{tc} + B \tag{5.14}$$

$$\ddot{P}_{pc} = a\dot{P}_{pc} + b\dot{P}_{tc} + \dot{B} \tag{5.15}$$

$$\ddot{P}_{pc} = a\dot{P}_{pc} + b(cP_{pc} + dP_{tc}) \tag{5.16}$$

We can eliminate P_{tc} by solving Eq. 5.14 for P_{tc}:

$$bP_{tc} = \dot{P}_{pc} - aP_{pc} - B \tag{5.17}$$

This gives

$$\ddot{P}_{pc} = a\dot{P}_{pc} + bcP_{pc} + d\dot{P}_{pc} - adP_{pc} - Bd \tag{5.18}$$

Finally,

$$\ddot{P}_{pc} - (a + d)\dot{P}_{pc} - (bc - ad)P_{pc} = -Bd \tag{5.19}$$

The solution to Eq. 5.19 is given by

$$P_{pc}(t) = P_{pc}^g(t) + P_{pc}^p(t) \tag{5.20}$$

where $P_{pc}^g(t)$ is the general solution and $P_{pc}^p(t)$ is the particular solution. The general solution is found by solving

$$\ddot{P}_{pc} - (a + d)\dot{P}_{pc} - (bc - ad)P_{pc} = 0. \tag{5.21}$$

The general solution is

$$P_{pc}^g(t) = c_{pc}^+ e^{\lambda^+ t} + c_{pc}^- e^{\lambda^- t} \tag{5.22}$$

where the eigenvalues, $\lambda^\pm$ are given by

$$\lambda^\pm = \frac{1}{2}\left[(a + d) \pm \sqrt{(a + d)^2 + 4(bc - ad)}\right] \tag{5.23}$$

$$= \frac{1}{2}(a + d)\left[1 \pm \sqrt{1 + \frac{4(bc - ad)}{(a + d)^2}}\right]. \tag{5.24}$$

These eigenvalues correspond to physical rates according to the following relationship

$$\Gamma_s = -\lambda^- \tag{5.25}$$

$$\Gamma_f = -\lambda^+ \tag{5.26}$$

where s refers to slow and f refers to fast.

The particular solution is easy to guess:

$$P_{pc}^p(t) = \frac{Bd}{bc - ad} \tag{5.27}$$

The solution to Eq. 5.19 is therefore

$$P_{pc}(t) = c_{pc}^+ e^{-\Gamma_f t} + c_{pc}^- e^{\Gamma_s t} + \frac{Bd}{bc - ad} \tag{5.28}$$

This can be simplified by defining some constraints

$$P_{pc}(t = \infty) = P_{pc}^\infty \tag{5.29}$$

$$P_{pc}(t = 0) = P_{pc}^0 \tag{5.30}$$

Eq. 5.30 is the particular solution,

$$P_{pc}^\infty = \frac{Bd}{bc - ad} \tag{5.31}$$

Eq. 5.30 gives

$$C_{pc} \equiv c_{pc}^+ = P_{pc}^0 - P_{pc}^\infty - c_{pc}^- \tag{5.32}$$

Finally,

$$P_{pc}(t) = C_{pc} e^{-\Gamma_f t} + (P_{pc}^0 - P_{pc}^\infty - C_{pc}) e^{-\Gamma_s t} + P_{pc}^\infty \tag{5.33}$$

The target chamber solution is found similarly (and has the same characteristic rates, Γ_s and Γ_f),

$$P_{tc}(t) = C_{tc} e^{-\Gamma_f t} + (P_{tc}^0 - P_{tc}^\infty - C_{tc}) e^{-\Gamma_s t} + P_{tc}^\infty \tag{5.34}$$

where

$$P_{tc}^\infty = -\frac{Bc}{bc - ad} = -\frac{c}{d} P_{pc}^\infty \tag{5.35}$$

Finally, C_{pc} can be obtained by using Eq. 5.33 to solve Eq. 5.14 at $t = 0$

$$C_{pc} + (P_{pc}^0 - P_{pc}^\infty - C_{pc}) + P_{pc}^\infty = a P_{pc}^0 + b P_{tc}^0 + B \tag{5.36}$$

$$C_{pc} = \frac{\Gamma_s(P_{pc}^\infty - P_{pc}^0) - aP_{pc}^0 - bP_{tc}^0 - B}{\Gamma_f - \Gamma_s} \tag{5.37}$$

Similarly,

$$C_{tc} = \frac{\Gamma_s(P_{tc}^\infty - P_{tc}^0) - cP_{pc}^0 - dP_{tc}^0}{\Gamma_f - \Gamma_s} \tag{5.38}$$

It is useful to introduce the quantity $\delta\Gamma$ and to express the slow time constant as

$$\Gamma_s = \langle\gamma_{se}\rangle + \langle\Gamma\rangle - \delta\Gamma \tag{5.39}$$

where $\langle\gamma_{se}\rangle = f_{pc}\gamma_{se}$ is the spin-exchange rate averaged throughout the double-chambered cell (since the spin exchange rate is zero in the target chamber, and γ_{se} in the pumping chamber), and $\langle\Gamma\rangle = f_{pc}\Gamma_{pc} + f_{tc}\Gamma_{tc}$ is the spin-relaxation rate averaged throughout the cell. Comparing Eq. 5.39 with Eq. 5.2, we see that $\delta\Gamma$ is the difference between Γ_s and the rate $(\gamma_{se} + \Gamma)$ that governs the time evolution of a single-chambered cell. Given Eq. 5.39, we find that

$$\delta\Gamma = \frac{d_{pc} + d_{tc}}{2}\left[\sqrt{1 - 2u\delta f + u^2} - 1 + u\delta f\right] \tag{5.40}$$

where $\delta f = f_{pc} - f_{tc}$ and

$$u = \frac{\gamma_{se} + \Gamma_{pc} - \Gamma_{tc}}{d_{pc} + d_{tc}} \quad . \tag{5.41}$$

For most of the situations we have considered, the quantity u is fairly small. This is due to two things. First, the spin-exchange rate γ_{se} is usually fairly slow compared to the sum of the two diffusion rates d_{pc} and d_{tc}. Also, the spin-relaxation rates in the pumping and target chambers, Γ_{pc} and Γ_{tc}, are generally of the same order as one another, ensuring that their difference is fairly small. Also, if they are unequal, it is usually the case that Γ_{tc} is larger than Γ_{pc}. It is thus reasonable to expand $\delta\Gamma$

in terms of u finding that

$$\delta\Gamma \approx f_{pc}f_{tc}(d_{pc} + d_{tc})u^2 \quad .\tag{5.42}$$

We also note that as $u \to 0$, as will be the case if the diffusion rates are extremely fast, $\Gamma_s \to \langle\gamma_{se}\rangle + \langle\Gamma\rangle$, which is equivalent to the form that appears in Eq. 5.2.

Lastly, we consider the fast root of Eq. 5.24 and its corresponding rate. To start, we take a difference between the rates:

$$\Gamma_f - \Gamma_s \;=\; -(\lambda^+ - \lambda^-)\tag{5.43}$$

$$=\; -(a + d)\tag{5.44}$$

$$=\; (d_{pc} + d_{tc})\gamma_{se} + \Gamma_{pc} + \Gamma_{tc}\tag{5.45}$$

solving for Γ_f and using the result of Eq. 5.39, we find

$$\Gamma_f = (d_{pc} + d_{tc}) + (\gamma_{se} - \langle\gamma_{se}\rangle) + (\Gamma_{pc} + \Gamma_{tc} - \langle\Gamma\rangle) + \delta\Gamma \quad .\tag{5.46}$$

In the fast-diffusion limit, $\Gamma_f \to \infty$; under these conditions, Eqs. 5.33 and 5.34 reduce to the form of Eq. 5.2.

A plot of the polarization as a function of time in a target cell is often referred to as a "spinup curve". In Fig. 5.1a, we show data illustrating a spinup for both the pumping chamber and the target chamber for the target cell, "Brady", a typical target cell of the geometry shown in Fig. 1.1. NMR measurements were made using the technique of adiabatic fast passage (AFP) [52] every three minutes. Also shown on Fig. 5.1, but obscured beneath the many data points, is a fit to the data using double-exponential functions of the form given in Eqs. 5.33 and 5.34. The fit clearly describes the data well.

5.1.3 Initial Polarization Evolution

Some of the parameters discussed earlier can be readily determined by studying spinup curves of the sort shown in Fig. 5.1. To extract values for the diffusion rates d_{pc} and d_{tc}, it is particularly valuable to examine the spinup curves during the initial time period during which the polarization is growing. For small values of the time t, it is readily apparent from Fig. 5.1 that the nature of the time evolution in the two chambers is quite different. Under the assumption that the time $t \ll 1/\Gamma_f$, we can expand Eqs. 5.33 and 5.34 in a Taylor series to second order obtaining

$$P_{pc}(t) = P_{pc}^0 + m_{pc}t + \frac{1}{2}q_{pc}t^2 \tag{5.47}$$

$$P_{tc}(t) = P_{tc}^0 + m_{tc}t + \frac{1}{2}q_{tc}t^2 \tag{5.48}$$

where

$$m_{pc} = \gamma_{se}P_A + d_{pc}(P_{tc}^0 - P_{pc}^0) - P_{pc}^0(\gamma_{se} + \Gamma_{pc})$$

$$m_{tc} = d_{tc}(P_{pc}^0 - P_{tc}^0) - P_{tc}^0\Gamma_{tc}$$

$$q_{pc} = \Gamma_S\Gamma_F(P_{pc}^\infty - P_{pc}^0) - (\Gamma_F + \Gamma_S)\left[d_{pc}(P_{tc}^0 - P_{pc}^0) - P_{pc}^0\Gamma_{pc} + \gamma_{se}(P_A - P_{pc}^0)\right]$$

$$q_{tc} = \Gamma_S\Gamma_F(P_{tc}^\infty - P_{tc}^0) - (\Gamma_F + \Gamma_S)\left[d_{tc}(P_{pc}^0 - P_{tc}^0) - P_{tc}^0\Gamma_{tc}\right] \tag{5.49}$$

If the cell starts with $P_{pc}^0 = P_{tc}^0 = 0$, then

$$P_{pc}(t) = \gamma_{se}P_At - \frac{1}{2}\gamma_{se}P_A(\gamma_{se} + \Gamma_{pc} + d_{pc})t^2 \tag{5.50}$$

$$P_{tc}(t) = \frac{1}{2}\gamma_{se}P_Ad_{tc}t^2 \, . \tag{5.51}$$

Looking again at Fig. 5.1, the initial shape of spinup curve appears to be linear in the pumping chamber and quadratic in the target chamber, in agreement with Eqs. 5.50
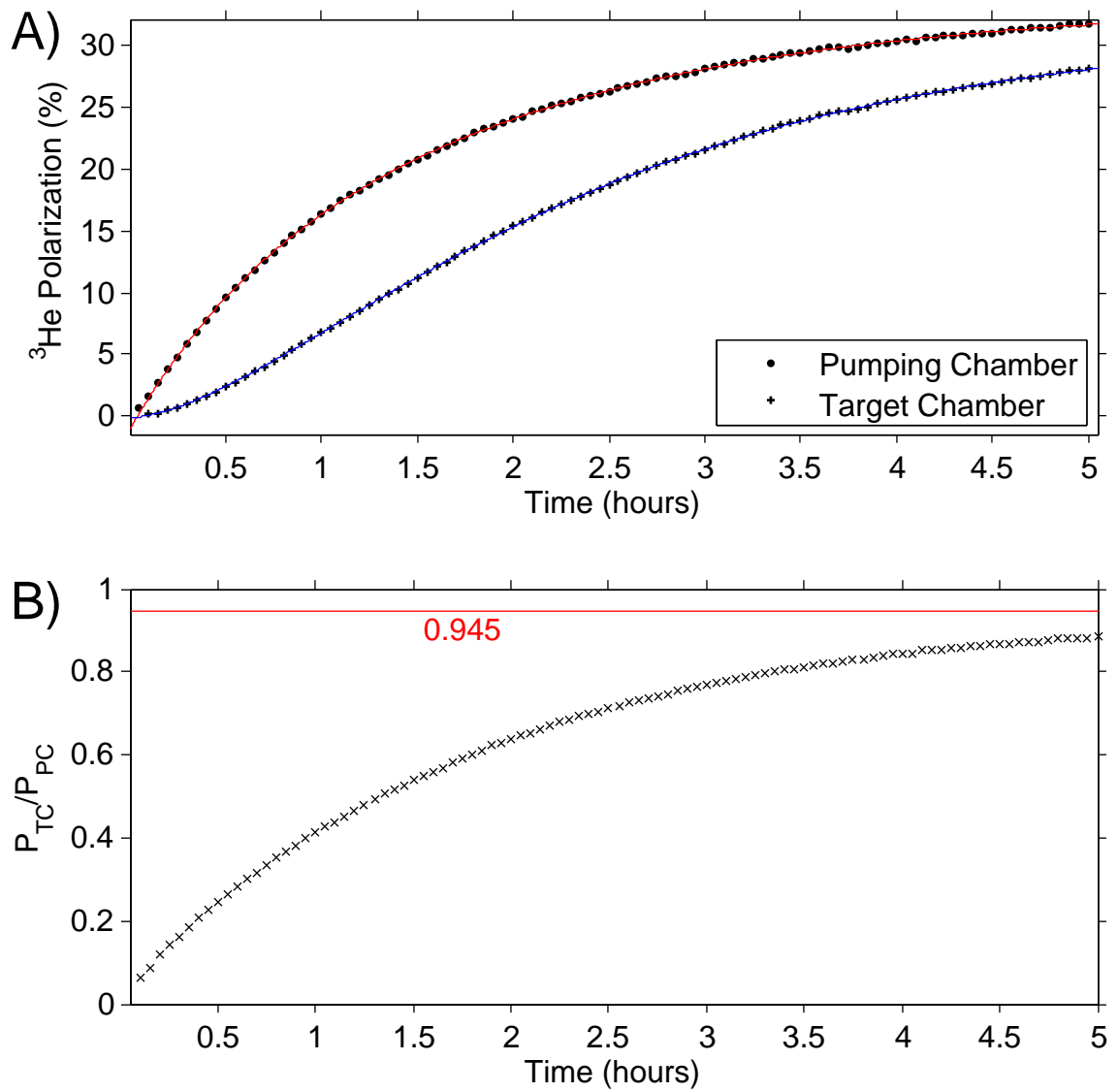
Figure 5.1: Top: A diffusion-style spinup for the target cell Brady. The lasers are turned on immediately before data taking. AFP measurements are made rapidly (every 3 minutes). Bottom: During a typical spinup, the target chamber polarization lags behind the pumping chamber polarization. The target-chamber polarization was calibrated using an estimate based on cell dimensions.

and 5.51.

Measurements of the early time behavior of the polarization buildup can provide valuable information that translates into a better understanding of the difference in polarization between the pumping and target chambers under operating conditions. The slope of the polarization buildup in the pumping chamber is $m_{pc} = P_A \gamma_{se}$; measured values for m_{pc} in several target cells are presented in Table E in Appendix E. Given sufficient diagnostics, P_A is relatively straightforward to measure (see Ch. 4.4.7). For the data shown in Figs. 5.1,5.2, $P_A = 0.99(01)$. Using this value and the slope of the polarization buildup in the pumping chamber, we find that $\gamma_{se} = (0.25 \pm 0.025)\text{hrs}^{-1}$. With this number in hand, we can fit the coefficient of the quadratic buildup of polarization in the target chamber, finding $d_{tc} = (0.72 \pm 0.10)\text{hrs}^{-1}$. As will be discussed in the next subsection, a value for d_{tc} can also be computed from first principles given the dimensions of the cell. The comparison of this value with that resulting from the fits described above provides insight into the degree to which we understand the diffusion process taking place in our cells.

5.1.4 The Diffusion Rates

Using gas kinetic theory, the dimensions of the target cell, the fill density of ^{3}He when the cell was constructed, the average temperatures of the pumping and target cells and the assumption that the temperature gradient along the transfer tube is linear, it possible to compute d_{pc} and d_{tc} from first principles.

In the absence of spin exchange and spin relaxation, Eqs. 5.3,5.4 simplify

$$\dot{P}_{pc} = -d_{pc}(P_{pc} - P_{tc}) \tag{5.52}$$

$$\dot{P}_{tc} = -d_{tc}(P_{pc} - P_{tc}) \tag{5.53}$$

The diffusion rates can be solved for using the diffusion flux. To start, we consider one-dimensional diffusion of a single-component gas exposed to a temperature gradient, given by Fick's first law,

$$J = -D(T)\frac{dC}{dz} \tag{5.54}$$

where J is the diffusion flux, $D(T)$ is the diffusion coefficient, and $C(z)$ is the concentration. The temperature dependence of the diffusion coefficient is given by [1, 6]

$$D(T) = D_0 \frac{n_0}{n}\left(\frac{T}{T_0}\right)^{m-1} \tag{5.55}$$

where n is the density of the gas and n_0, D_0, and T_0 are empirically measured. The flux of atoms traveling in the transfer tube from the target chamber to the pumping chamber is given by [6]

$$J_{tt} = J_+ - J_- \tag{5.56}$$

where $J_+(J_-)$ refers to the flux of spin-up (spin-down) particles. The concentration of spin-up (spin-down) particles is given by [65]

$$C_\pm = n\frac{1 \pm P}{2} \tag{5.57}$$

where P is the polarization. Combining the above equations and simplifying,

$$J_{tt} = -D_0 n_0 \left(\frac{T(z)}{T_0}\right)^{m-1}\frac{dP}{dz} \tag{5.58}$$

If we further assume that the polarization gradient is linear [1, 6, 65], we can solve the above differential equation,

$$J_{tt} = -D_0 n_0 \frac{2-m}{T_0^{m-1}}\frac{T_{pc} - T_{tc}}{T_{pc}^{2-m} - T_{tc}^{2-m}}\frac{P_{pc} - P_{tc}}{L_{tt}}. \tag{5.59}$$

Eq. 5.59 gives the total rate per area per time. The rate per atom is given by

multiplying Eq. 5.59 by the cross-sectional area of the transfer tube and dividing by the product of the target chamber volume and density. Comparing Eqs. 5.52,5.53 with Eq. 5.59, we can extract the diffusion rates

$$d_{pc} = \frac{A_{tt}}{V_{pc}L_{tt}}D_0\frac{n_0}{n_{pc}}\frac{2-m}{T_0^{m-1}}\frac{T_{pc}-T_{tc}}{T_{pc}^{2-m}-T_{tc}^{2-m}} \tag{5.60}$$

$$d_{tc} = \frac{A_{tt}}{V_{tc}L_{tt}}D_0\frac{n_0}{n_{tc}}\frac{2-m}{T_0^{m-1}}\frac{T_{pc}-T_{tc}}{T_{pc}^{2-m}-T_{tc}^{2-m}} \tag{5.61}$$

where A_{tt} and L_{tt} are the cross-sectional area and length of the transfer tube. Values for D_0, T_0, n_0, and m are given by [66, 67]:

$$D_0 = 2.789 \; cm^2/s \tag{5.62}$$

$$T_0 = 353.14 \; K \tag{5.63}$$

$$n_0 = 0.7733 \; amg \tag{5.64}$$

$$m = 1.705 \tag{5.65}$$

Using this, it is convenient to write Eq. 5.61 in terms of typical dimensions,

$$d_{tc} = 0.80 \; hrs^{-1} \cdot \frac{A_{tt}}{0.5 \; cm^2} \cdot \frac{6 \; cm}{L_{tt}} \cdot \frac{90 \; cm^3}{V_{tc}} \cdot \frac{10 \; amg}{n_{tc}} \cdot \frac{\Upsilon}{4/3} \tag{5.66}$$

where

$$\Upsilon(T_{pc}, T_{tc}) = \frac{2-m}{273.15^{m-1}}\frac{T_{pc}-T_{tc}}{T_{pc}^{2-m}-T_{tc}^{2-m}} \tag{5.67}$$

Putting in the dimensions for Brady which are $A_{tt} = 0.667$cm^2, $L_{tt} = 9.07$cm, $V_{tc} = 74.6$cm^3, $n_{tc} = 10.5$ amg, and $\Upsilon = 1.34$ (with $T_{tc} = 24$C and $T_{pc} = 270$C), we find, for the conditions shown in Fig. 2, that $d_{tc} = 0.82$hrs^{-1}, within 13% of the values found from fitting the polarization buildup curves.
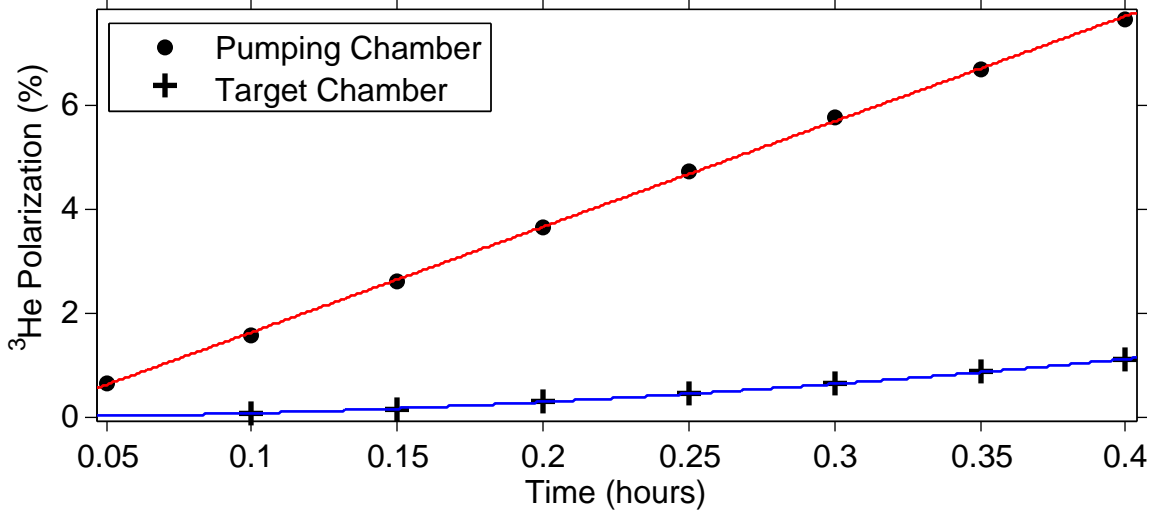
Figure 5.2: Early-Time Behavior of Brady Spinup

5.1.5 Polarization Gradients

As discussed in the introduction, and as is clear from the preceding discussion in section 5.1.2, there is generally a difference in polarization between the pumping and target chambers. Given the values for the equilibrium polarizations P_{pc}^∞ and P_{tc}^∞ determined earlier, we find that their ratio is given by

$$\frac{P_{tc}^\infty}{P_{pc}^\infty} = -\frac{c}{d} = \frac{1}{1 + \Gamma_{tc}/d_{tc}}. \tag{5.68}$$

We define the polarization gradient as

$$\Delta \equiv 1 - \frac{P_{tc}^\infty}{P_{pc}^\infty} = \frac{1}{1 + d_{tc}/\Gamma_{tc}} \tag{5.69}$$

The gradient approaches 0 for cells with long lifetimes and fast diffusion. In the absence of beam depolarization, it is not unreasonable to assume that Γ_{tc} is of the same order as Γ_{pc} (later, however, we'll assume that because the two chambers have different surface-to-volume ratios, they have different relaxation rates). Assuming

that $\Gamma_{tc} = 1/30$ hrs^{-1}, a relaxation rate fairly typical for a target cell, and $d_{tc} = 0.80$ hrs^{-1}, we would thus have

$$\Delta = 0.04 \quad , \tag{5.70}$$

or a 4% relative difference in polarization between the pumping and target chambers. The gradient becomes worse in the presence of an electron beam. In this case $\Gamma_{tc} = \Gamma_{tc}^0 + \Gamma_{beam}$, where Γ_{tc}^0 is the relaxation rate without beam depolarization. For example, with a target cell typical of those used recently at JLab and a beam current of 10μ A, we would have a beam-induced relaxation rate of $\approx 1/40$hrs^{-1} resulting in a polarization gradient

$$\Delta = 0.068 \quad . \tag{5.71}$$

A relative difference, under operating conditions, of 6-7% in the polarization between the pumping and target chambers is certainly significant. Since the running time required to reach a given statistical accuracy is inversely proportional to the polarization squared, a polarization gradient of this size increases running time by something like 12-14%. Depending on the precise means of calibration for polarimetry, such a polarization gradient also contributes to normalization errors. The negative impacts of polarization gradients become even worse as the beam current is increased. If instead of $10\,\mu$A of beam current, we had $100\,\mu$A, the same cell that previously yielded $\Delta \approx 0.07$ would have a gradient $\Delta \approx 0.26$. Clearly, diffusion is not a satisfactory mechanism for transferring polarized gas from the pumping chamber to the target chamber at significantly higher luminosities. It is thus necessary to establish a faster transfer mechanism, and such a mechanism, based on convection, is presented next in section 6.1.

5.1.6 Rates in a Two-Chambered Cell

Under operating conditions, the pumping chamber in a two-chambered cell is heated to form a dense alkali vapor. The target chamber, however, is cooled to room temperature to minimize the amount of alkali vapor present. These two distinct temperature regions will have correspondingly different densities. Consequently, when discussing relaxation and spin-exchange rates, we must consider cell-averaged rates. The volume-averaged relaxation rate of a two-chambered cell is given by

$$\langle \Gamma \rangle = f_{pc}\Gamma_{pc} + f_{tc}\Gamma_{tc}, \tag{5.72}$$

where f_{pc} is the fraction of atoms in the pumping chamber (see Eq. 5.6) and Γ_{pc} and Γ_{tc} are the total ^{3}He relaxation rates in the pumping and target chambers. The volume-averaged spin-exchange rate is

$$\langle \gamma_{se} \rangle = f_{pc}\gamma_{pc} + f_{tc}\gamma_{tc} \tag{5.73}$$

$$= f_{pc}\gamma_{pc} \tag{5.74}$$

since the alkali density in the target chamber is essentially zero.

We typically measure the room-temperature relaxation rate (the inverse, $1/\Gamma$ is often called the "lifetime" of the cell) by performing a "spindown." At the beginning of such a measurement, 5 NMR measurements are made rapidly (every 3 minutes). Provided the lifetime of the cell is much longer than 3 minutes, we can fit the 5 measurements to a line and extract a value for the loss-per-measurement (see Fig. 5.3). After these loss measurements have been made, we increase the NMR interval to 3 hours and monitor the decay of ^{3}He polarization (see Fig. 5.4). Provided the lifetime of the cell is much longer than the diffusion time scale, the ^{3}He polarization evolution
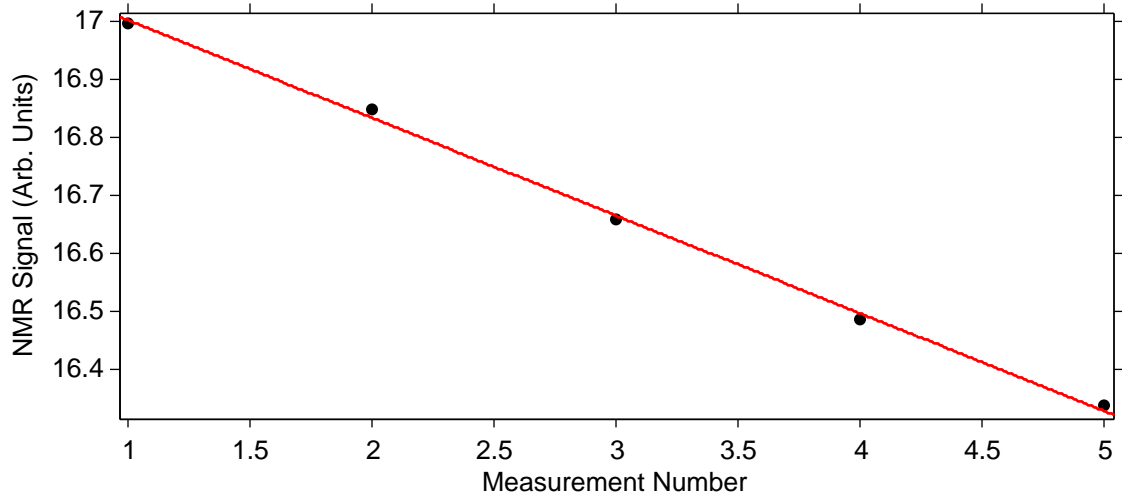
Figure 5.3: NMR Loss Measurement for Target Cell Brady. These data have a loss of $\alpha = 0.0101$

in the absence of optical pumping is given by

$$P(t) = P_0 e^{-t/\tau^{raw}} \tag{5.75}$$

where τ^{raw} is the raw lifetime of the cell. For the data shown in Fig. 5.4, $\tau^{raw} =$ 30.1 hours. The lifetime of the cell in the absence of NMR measurements can be attained by correcting the data for losses. We correct the data point-by-point using the following equation

$$V_i^{cor} = \frac{V_i^{raw}}{(1 - \alpha)^i} \tag{5.76}$$

where V_i^{cor} is the loss-corrected NMR amplitude for measurement i, V_i^{raw} is the ith raw NMR amplitude, and α is the NMR loss-per-measurement. When corrected for NMR losses, the data shown in Fig 5.4 has a corrected lifetime of $\tau^{cor} = 33.5$hours.

Provided the interval between NMR measurements is regular, the effective loss lifetime for a given spindown can be calculated by comparing the raw lifetime, τ^{raw}
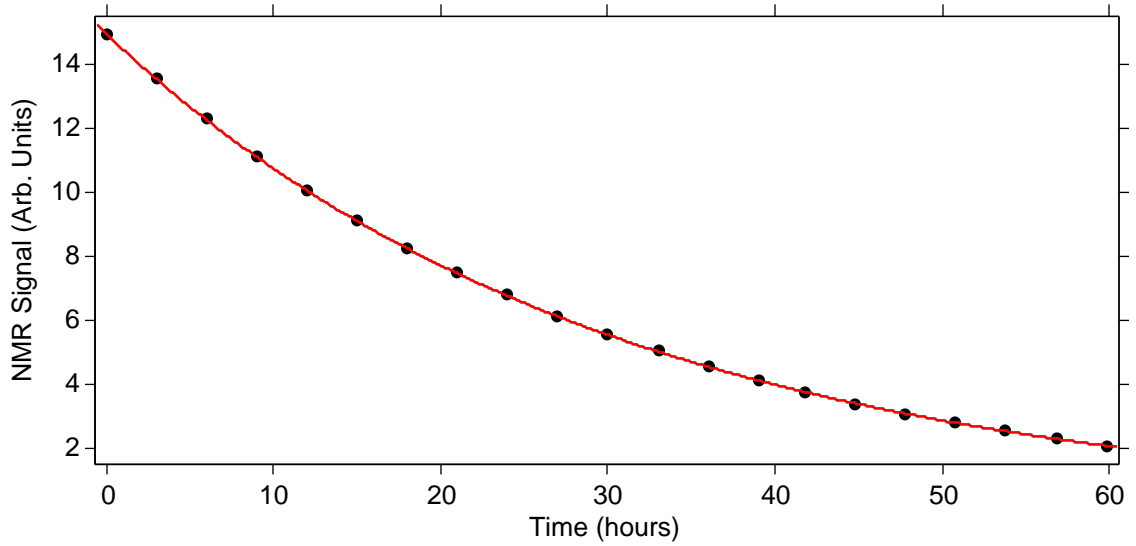
Figure 5.4: Spindown for Target Cell Brady. These data give a raw lifetime of 30.1 hours. When corrected for NMR losses, the lifetime increase so 33.5 hours.

with the loss-corrected lifetime, τ^{cor}:

$$1/\tau^{raw} = 1/\tau^{cor} + 1/\tau^{loss} \tag{5.77}$$

For the data in Fig. 5.4, $\tau^{loss} \approx 297$ hours.

During a typical spinup, NMR measurements are made every 2 hours. Often, it is useful to adjust the lifetime of cell as though NMR measurements during a spindown had been made every 2 hours. This can be accomplished by increasing the NMR-loss rate by a factor of $3/2$. The effective two-hour raw lifetime for the data in Fig. 5.4 is 28.6 hours.

Finally, a subtle consequence of two-chambered cell dynamics is that the lifetime of the cell depends on the temperature of the two chambers, even in the absence of an alkali vapor. When the cell is hot, gas is pushed out of the pumping chamber and into the target chamber, causing f_{pc} to decrease (see Eq. 5.6). The target chamber, which has a higher surface-to-volume ratio, may have a higher wall-relaxation rate (see Ch. 2.5.3). Additionally, the dipolar-relaxation rate, $\Gamma_{dipolar}$, has a density

dependance (see Eq. 2.73). Consequently, $\langle \Gamma \rangle$ will increase when the cell is hot.

To account for these effects, we first assume that the surface of the glass in the two chambers has the same relaxation rate; however because the surface-to-volume ratio, S/V is higher in the target chamber, the relaxation rate in the target chamber must be higher by the ratio of surface-to-volume ratios:

$$\Gamma_{tc}^{wall} = \frac{\text{S/V}_{tc}}{\text{S/V}_{pc}} \Gamma_{pc}^{wall} \tag{5.78}$$

For the cells studied for this thesis, the ratio of surface-to-volume ratios was between 2 and 4.

For the second effect, we write Eq. 2.73 as

$$\langle \Gamma_{dipolar} \rangle = \frac{1}{744\text{hrs}^{-1} \cdot \text{amg}} \left(f_{pc}[^3\text{He}]_{pc} + f_{tc}[^3\text{He}]_{tc} \right) \tag{5.79}$$

where

$$[^3\text{He}]_{pc} = f_{pc}[^3\text{He}]_{uniform} \frac{V_{pc} + V_{tc}}{V_{pc}} \tag{5.80}$$

$$[^3\text{He}]_{tc} = f_{tc}[^3\text{He}]_{uniform} \frac{V_{pc} + V_{tc}}{V_{tc}}. \tag{5.81}$$

Here, $[^3\text{He}]_{uniform}$ is the uniform-temperature density in the cell in amagats. With these results, we can write

$$\langle \Gamma \rangle = \Gamma_{pc}^{wall} \left(f_{pc} + f_{tc} \frac{\text{S/V}_{tc}}{\text{S/V}_{pc}} \right) + \frac{[^3\text{He}]_{uniform}(V_{pc} + V_{tc})}{744} \left(\frac{f_{pc}^2}{V_{pc}} + \frac{f_{tc}^2}{V_{tc}} \right) \tag{5.82}$$

If the cell dimensions are well known, Eq. 5.82 can be solved for Γ_{pc}^{wall} at a uniform temperature (the conditions of a spindown). Using knowledge about the temperature of the cell under operating conditions, this value for Γ_{pc}^{wall} can then be used in Eq. 5.82

to find a value for $\langle \Gamma \rangle$ under operating conditions:

$$\langle \Gamma \rangle = \frac{f_{pc} + f_{tc}\frac{\mathrm{S/V_{tc}}}{\mathrm{S/V_{pc}}}}{f_{pc}^u + f_{tc}^u \frac{\mathrm{S/V_{tc}}}{\mathrm{S/V_{pc}}}} \left(\langle \Gamma^u \rangle - \frac{[^3\mathrm{He}]^u}{744} \right) + \frac{[^3\mathrm{He}]^u (V_{pc} + V_{tc})}{744} \left(\frac{f_{pc}^2}{V_{pc}} + \frac{f_{tc}^2}{V_{tc}} \right) \qquad (5.83)$$

where terms with the superscript u refer to values for uniform temperature throughout the cell.

We note here that because we currently have no to way to test if this theory is correct, we assign values for $\langle \Gamma \rangle$ (equivalently $1/\tau$) by taking the average between the value given by Eq. 5.83 and $\langle \Gamma_u \rangle$ (where $\langle \Gamma_u \rangle$ has been adjusted for 2 hour intervals). The uncertainty is given by half the difference. A summary of values for $\langle \Gamma \rangle^{-1}$ computed in this fashion can be found in Table 5.1.

5.2   Cell Performance

Electron-scattering experiments using polarized ^{3}He targets have seen a more-than-tenfold increase in effective luminosity over the past 20 years (effective luminosity is defined here as luminosity weighted by ^{3}He polarization-squared). This increase (see Ch. 1.1 and Fig. 1.2) has enabled experimentalists to study new energy regimes by dramatically decreasing the amount of time it takes to achieve a given statistical error. We are able to increase the beam current because γ_{se} is bigger, a direct consequence of the improvements in laser technology and hybrid spin exchange. These improvements have led to a dramatic increase in ^{3}He polarization (from below 40% before GEN to nearly 70% after GEN).

Two major advances in Spin-Exchange Optical Pumping (SEOP) have enabled the dramatic increases in performance. The combination of line-narrowed lasers with hybrid-alkali mixtures has resulted in significantly higher ^{3}He polarizations in large two-chambered target cells. Hybrid-alkali mixtures are perhaps the easiest advance

| Cell | Lasers | | T_{pc}^{set} | P_{He}^∞ | Γ_s^{-1} | $\langle\Gamma\rangle^{-1}$ | P_A | D_{pb} |
	Type	I_0	°C		hrs	hrs		
Proteus	3F	3.8	180	0.46	27	74	-	0
Priapus	3F	3.8	180	0.44	21	56	-	0
Penelope	3F	3.8	180	0.39	18	46	-	0
Powell	3F	3.8	180	0.38	13	25	-	0
Prasch	3F	3.8	180	0.33	13	33	-	0
Edna	3F	2.4	235	0.56(04)	5.71(02)	23.7(1.5)	-	3.63(20)
Al	2.5F	3.2	235	0.53(04)	7.86(08)	24.1(1.1)	-	4.53(25)
	5F	6.1	235	0.54(04)	6.73(21)	24.0(1.1)	-	4.53(25)
Barbara	2.5F	1.6	235	0.37(03)	5.5(08)	38.1(2.3)	-	4.80(25)
	5F	3.1	235	0.57(04)	4.76(63)	38.1(2.3)	-	4.80(25)
Gloria	3F	1.7	235	0.60(04)	6.13(06)	31.4(1.7)	-	7.20(40)
Anna	1F	0.6	235	0.33(02)	5.60(36)	9.50(71)	-	9.64(57)
	1.5F	1.0	235	0.39(02)	5.37(16)	9.50(66)	-	9.50(71)
Dexter	1.5F	1.5	235	0.47(04)	7.58(17)	16.4(8)	-	20*
	5F	6.1	235	0.49(04)	6.63(13)	16.4(8)	-	20*
Dolly	3F	1.0	235	0.43(03)	6.16(07)	30.0(1.8)	-	20(1.3)
	1C1F	1.4	235	0.62(03)	5.79(07)	29.9(1.8)	-	20(1.3)
Simone	2C1F	3.8	215	0.32(02)	14.6(3)	18.3(7)	0.91(05)	8.89(45)
	2C1F	3.8	255	0.58(03)	6.05(13)	18.2(8)	0.92(05)	10.3(52)
Sosa	2C1F	1.9	160	0.57(03)	16.7(09)	55.7(1.8)	1.00(03)	0
	2C1F	1.9	170	0.61(03)	11.7(03)	55.5(2.0)	0.98(03)	0
	2C1F	1.9	180	0.55(03)	8.79(09)	55.2(2.2)	0.97(03)	0
	2C1F	1.9	190	0.40(02)	6.39(22)	55.1(2.3)	-	0
	2C1F	1.9	200	0.26(01)	5.40(17)	55.4(2.1)	0.83(17)	0
Boris	3F	1.8	235	0.42(03)	6.25(06)	21.1(1.2)	?	2.45(23)
Samantha	3F	1.8	235	0.50(03)	6.30(13)	20.8(1.2)	-	4.34(23)
	3C	2.6	235	0.68(03)	4.63(03)	17.1(1.1)	0.99(03)	4.34(23)
Alex	2C1F	2.6	235	0.59(03)	4.81(03)	26.8(2.0)	0.99(03)	1.19(07)
Moss	1C1F	1.8	235	0.62(03)	5.35(04)	24.5(1.6)	0.95(09)	2.40(13)
Tigger	1C1F	1.8	235	0.51(03)	4.89(05)	12.1(9)	0.95(09)	5*
Astral Weeks	2C1F	2.6	235	0.69(03)	6.57(12)	35.3(1.9)	0.99(03)	6.21(56)
Stephanie	3C	2.6	235	0.71(04)	4.55(09)	37.0(2.3)	0.99(03)	1.50(10)
Brady	1C	0.9	235	0.62(03)	4.8(1.1)	26.8(1.6)	0.95(03)	2.36(24)
	2C	1.8	235	0.68(03)	5.52(70)	26.8(1.7)	0.99(03)	2.36(24)
	3C	2.6	235	0.70(03)	5.30(01)	26.9(1.7)	0.99(03)	2.36(24)
Maureen	3C	2.6	235	0.66(03)	5.42(12)	23.4(1.4)	0.97(09)	4.42(55)

Table 5.1: Cell Performance for experiments before GEN (top), GEN (middle), and after GEN (bottom). Values for experiments before GEN were taking from Singh [6]. Within each experiment grouping, data is sorted by type of laser used. *Indicates nominal value for D_{pb}.

for an established lab to make as they require very little financial investment. Line-narrowed lasers, which cost about the same as their broadband counterparts, are now the clear choice for a lab looking to purchase new lasers for SEOP with ^{3}He (for a discussion on using line-narrowed lasers for SEOP with both ^{3}He and ^{129}Xe, see Appendix D).

5.2.1 Effect of Hybrid Mixtures

The hybrid technique (see Ch. 2.7) typically employs a small amount of Rb and a large amount of K. As with a pure-Rb cell, lasers optically pump the Rb. However, in addition to spin exchange with ^{3}He atoms, these Rb atoms can now exchange spin with K atoms (K-Rb spin exchange is very rapid and efficient). Potassium more efficiently transfers its spin to ^{3}He atoms resulting in significantly lower laser-power requirements. Thus, for a given laser power, a hybrid cell can achieve a higher ^{3}He polarization with a fast spin-exchange rate, γ_{se}.

To understand the impact of hybrid technology, we consider Eq. 2.80,

$$P_\infty^{He} = P_\infty^{Rb} \frac{\gamma_{se}}{\gamma_{se}(1+X) + \Gamma},$$ (5.84)

where P^{Rb} is given by Eq. 2.12,

$$P^{Rb} = P_{light} \frac{R}{R + \Gamma'_{Rb}}$$ (5.85)

here, Γ'_{Rb} is the effective rubidium relaxation rate (see Eq. 2.89), R is the optical pumping rate, P_{light} is the circular polarization of the pump laser, Γ is the room-temperature relaxation rate of the cell, X is the X factor of the cell, and γ_{se} is the spin-exchange rate, given by Eq. 2.87,

$$\gamma_{se} = k_{se}^{Rb-He}[Rb] \left(1 + D\frac{k_{se}^{A-He}}{k_{se}^{Rb-He}}\right).$$ (5.86)

In the above equation, k_{se} is the spin-exchange rate constant (see Tab. 2.2), $D = [K]/[Rb]$ is the hybrid number density ratio, and $[Rb]$ is the Rb number density.

As was discussed in Ch. 2.7.2, we prepare our hybrid mixtures so that they will give the same spin-exchange rate that a pure-Rb cell would have at 190°C ($1/\gamma_{se} = 6.7$hrs). We've found great success with a density ratio of $D = 6$. Such a cell would need to be heated to 237.2°C and would have a Rb number density that is about 5.6 times lower than a pure-Rb cell heated to 190°C. *This lower light-absorbing Rb density allows the laser light to penetrate deeper into the cell while maintaining a high intensity.* To understand this, consider Eq. 2.43 for fully-polarized, parallel laser light,

$$\frac{1}{\Phi(z)}\frac{\partial \Phi(z)}{\partial z} = -\left(1 - P_{Rb}(z)\right)\sigma(\nu)[Rb]. \tag{5.87}$$

In this equation, which describes the attenuation of the laser light, Φ is the photon flux, z is the depth into the cell, P_{Rb} is the Rb polarization at that depth, and σ is the photon-absorption cross section. By decreasing the Rb density (while maintaining high alkali density), fewer photons are absorbed at a given depth and the laser light is able to penetrate deeper into the cell. Consequently, the optical pumping rate at a given depth (given Eq. 2.14) increases

$$R(z) = \int \Phi(\nu, \vec{r}, z)\sigma(\nu)d\nu. \tag{5.88}$$

We note that for the conditions described, the effective-Rb relaxation rate is higher for hybrid cells – about 2.4 times higher. We also note that for these conditions, the attenuation of the laser light, $\left(1 - P_{Rb}(z)\right)\sigma(\nu)[Rb]$, is lower for hybrid cells – about 5.6 times lower when the alkali polarizations are the same and even lower deep into the cell when the hybrid performance starts to kick in (see Fig. 2.5, which shows how the alkali polarization drops off slower in a hybrid cell). Because the hybrid cell has a lower laser attenuation, the optical pumping rate is higher. Although the alkali

relaxation rate is higher for hybrid cells, the total optical pumping rate is also higher (and by a greater amount). Consequently, the alkali polarization will be higher in a hybrid cell.

Figure 5.5: Maximum Achieved He-3 Polarization as a Function of D for 14 Target Cells. The data were acquired over a ten-year period using broadband lasers, with different cell geometries, available laser power, and hybrid density ratios. For Pure Rb cells (triangles), the oven was set to 180°C; for hybrid cells, the oven was set to 235°C. Hybrid cells outperform pure rubidium cells. The values for D in this table were extracted from pressure-broadening data, as more cells were measured this way.

The impact of alkali-hybrid mixtures is illustrated in Fig. 5.5, which shows data for 14 Target cells acquired over the span of a decade, all of which were pumped using broadband laser light. In this figure, the saturation ^{3}He polarization is plotted as a function of number density ratio, $D = [K]/[Rb]$, as determined by the pressure-broadening technique (see Ch. 4). The triangles show pure-Rb cells, which naturally have $D = 0$. From hybrid data (circles), it appears as though the ideal number density ratio is somewhere between 3 and 9. Outside of this range, there is either too much K (some of which is inefficiently pumped by off-resonance light), or there is too little K (and thus spin-exchange is no longer dominated by K).

The main advantage of the hybrid technique is that the available laser power is used more efficiently. For example, consider Fig. 5.6, which plots P_{He}^∞ as a function of
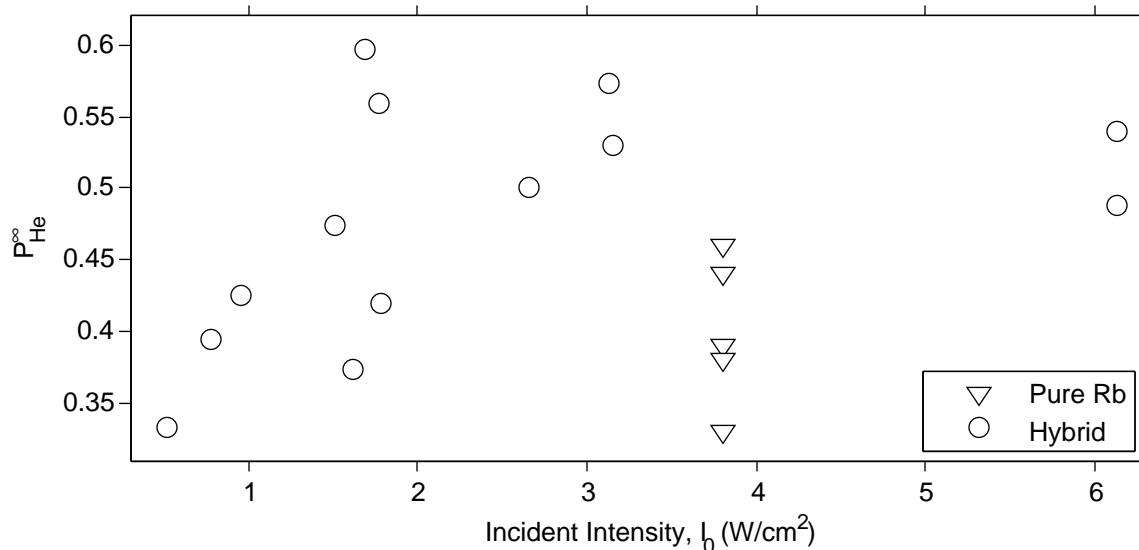
Figure 5.6: Maximum Achieved He-3 Polarization as a Function of Laser Intensity for 18 Target Cells. The data were acquired over a ten-year period, with different hybrid density ratios. For Pure Rb cells (triangles), the oven was set to 180°C; for hybrid cells, the oven was set to 235°C.

incident laser intensity. This plot shows that hybrid cells are able to achieve higher ^{3}He polarizations than pure-Rb cells when pumped with comparable laser intensity. Additionally, hybrid cells achieved comparable or higher ^{3}He polarization even when pumped with significantly less laser intensity. As a specific example, consider the hybrid target cell with the highest saturation polarization, Gloria. For this cell, which had a pumping-chamber diameter of 3.5 inches, 3 broadband lasers were used and $P_{He}^{\infty} = 0.60$. For comparison, consider the best performing pure-Rb target cell in Fig. 5.6, Proteus. Proteus had a 2.5-inch-diameter pumping chamber and was also pumped with 3 broadband lasers. In spite of the fact that the laser intensity was nearly double for Proteus, a lower saturation ^{3}He polarization, $P_{He}^{\infty} = 0.46$, was measured. Moreover, Gloria achieved this significantly higher ^{3}He polarization despite having a room-temperature lifetime that was less than half that of Proteus (31.4 vs. 74 hrs).

5.2.2   Impact of Narrowband Lasers
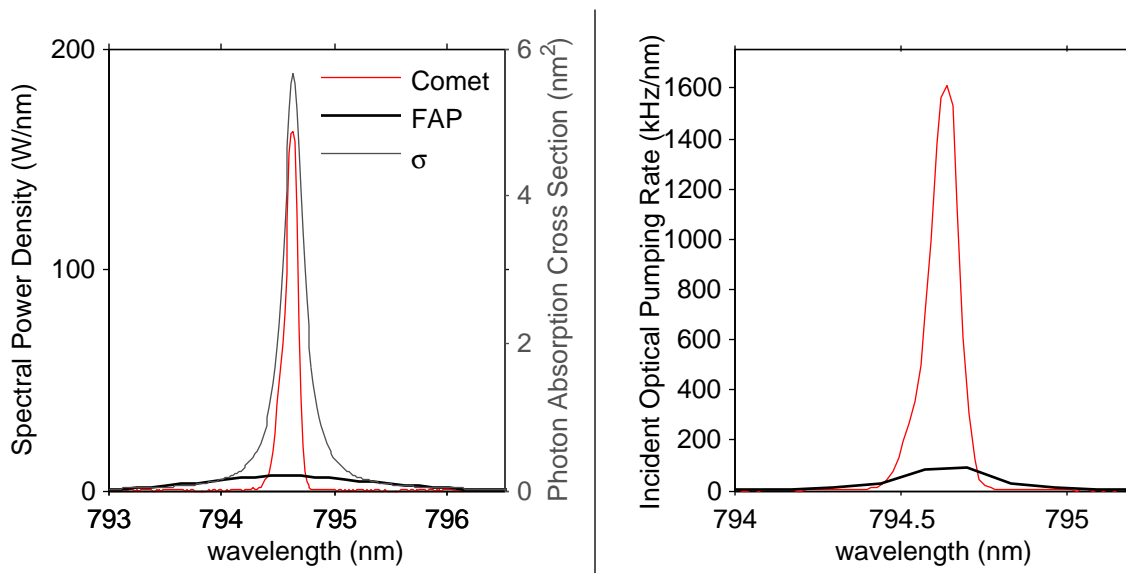
Figure 5.7: LEFT: Actual Laser Spectra of a Broadband FAP laser and a Narrowband Comet Laser. Also plotted is a theoretical photon-absorption cross section. The two lasers have approximately the same total power; however, the Comet laser has a spectral width that is 1/10th that of the FAP laser. RIGHT: Theoretical Incident Optical Pumping Rate Using Actual Spectra. The Comet laser (24.8W) has a total incident optical-pumping rate of 189kHz; the FAP laser (22.1W) has a total incident optical-pumping rate of 33.9kHz. When normalized for power, the Comet has an incident optical-pumping rate that is approximately 5 times higher than FAP's.

Using line-narrowed lasers to pump rubidium and hybrid cells has resulted in much higher ^{3}He polarizations in large two-chambered target cells. These lasers (see Ch. 2.2.8) have spectral profiles that more closely match the Rb D1 absorption line shapes in our high-pressure cells than their broadband counterparts. This more resonant laser light results in higher optical pumping rates (see Eq. 5.88). These higher optical pumping rates in turn lead to higher alkali polarizations and thus higher ^{3}He polarizations (see Eq. 5.85 and Eq. 5.84).

To illustrate the advantage of narrowband lasers, we present data acquired from actual laser spectra in Fig. 5.7. The left portion of the figure shows two typical laser spectra – one from a broadband FAP laser and one from a line-narrowed Comet laser. The left figure also shows a theoretical photon-absorption cross section, σ, typical for

our high-pressure target cells. The right portion of the figure shows an inferred (at the front end of the cell) optical-pumping rate calculated using the real spectra and theoretical photon-absorption cross section. When normalized for power, the comet laser has an inferred maximum optical-pumping rate that is approximately 5 times greater than the FAP's.
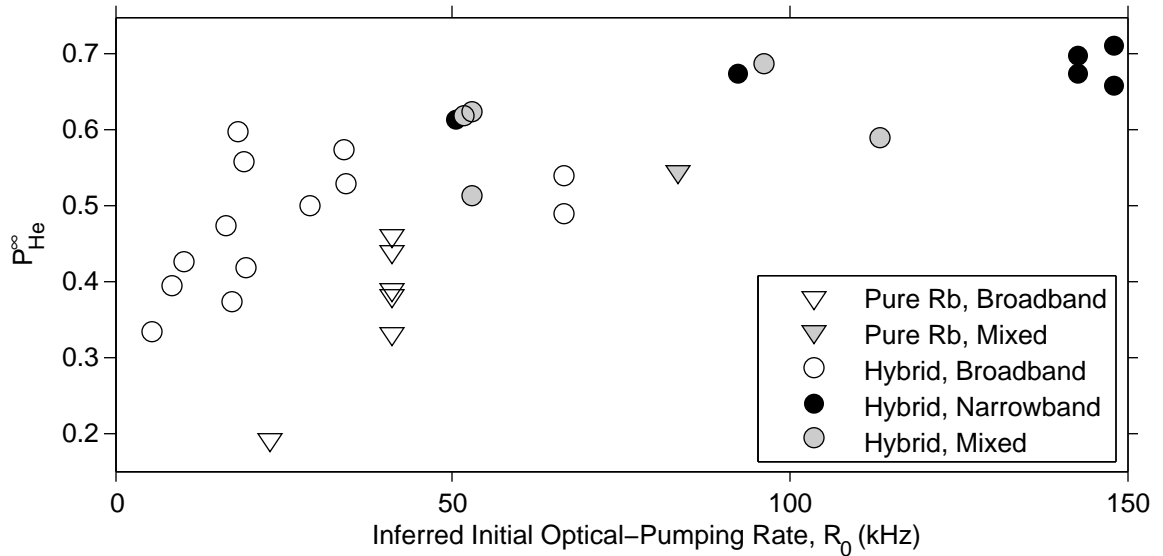
Figure 5.8: Maximum Achieved He-3 Polarization as a Function of Inferred Maximum Optical-Pumping Rate for 20 Target Cells. The data were acquired over a ten-year period, with different hybrid density ratios. For Pure Rb cells (triangles), the oven was set to 180°C; for hybrid cells, the oven was set to 235°C. This inferred plot shows the tremendous advantage of line-narrowed lasers, particularly when used in conjunction with hybrid-alkali technology.

Finally, we present the impact of narrowband lasers in Fig. 5.8, which plots P_{He}^{∞} as a function of inferred maximum optical-pumping rate. This plot clearly illustrates the tremendous improvements in P_{He}^{∞} that can be achieved when narrowband lasers are used to pump hybrid cells.

5.2.3 Cumulative Effects

When line-narrowed lasers are used in conjunction with hybrid technology, very high
^{3}He polarizations can be attained in large two-chambered target cells. Moreover,

with the implementation of the alkali-polarimetry techniques discussed in Ch. 4.4, we are able to better understand the limitations to the saturation ^{3}He polarization. In particular, by measuring the alkali polarization, we're able to adjust the alkali density to match the available laser power. So long as the alkali polarization remains high (near 1), we can continue to increase P_∞^{He} by increasing the spin-exchange rate (which can be accomplished by increasing the oven temperature). By increasing the spin-exchange rate, we are able to approach the X-factor limit,

$$P_\infty^{He} = P_A \frac{\gamma_{se}}{\gamma_{se}(1+X) + \Gamma} \Rightarrow \frac{1}{1+X} \qquad (5.89)$$

This substantial increase in ^{3}He polarization (accomplished by increasing the spin-exchange rate) is only possible if the alkali polarization remains high, however. Fortunately, by implementing alkali-hybrid mixtures and line-narrowed lasers, we're able to keep alkali polarizations high. These high alkali polarizations finally allow us to increase the spin-exchange rate. To study this, we present Fig. 5.9, which plots saturation ^{3}He polarization as a function of characteristic spinup time ($1/\Gamma_s$, see Eq. 5.39).

Several trends are clear in Fig. 5.9. We note that pure-Rb cells pumped with broadband lasers tend to only achieve high ^{3}He polarizations when $1/\Gamma_s$ is slow; this is because under these conditions, the alkali polarization is high only when the spin-exchange rate is low. Additionally, when pure-Rb cells are pumped with narrowband laser light, high ^{3}He polarizations can be attained; however, these higher polarizations are only possible at modest $1/\Gamma_s$. Hybrid cells, however, have excellent performance at high spin-exchange rates, particularly when pumped with narrowband laser light.

We note that although tremendous gains in saturation ^{3}He polarization have been made, we believe further gains in the current design are possible. The cells studied in this thesis were tested in preparation for several Jefferson Lab experiments, including E02-013 (GEN-I) and E05-015 (Transversity). An emphasis was placed on broadly
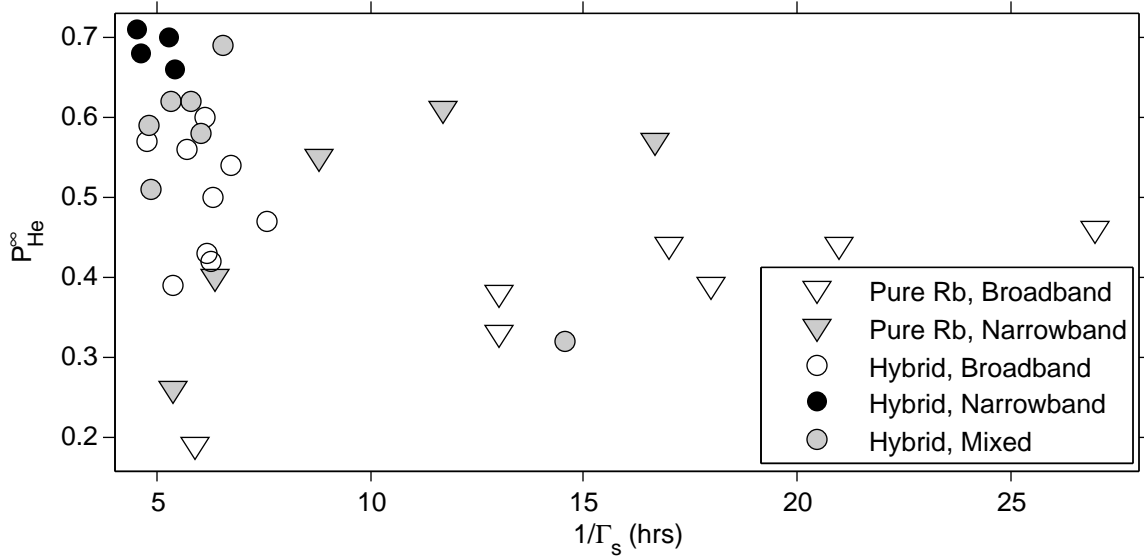
Figure 5.9: Maximum Achieved He-3 Polarization as a function of $1/\Gamma_s$ for over 20 Target Cells. The data were acquired over a ten-year period, with different cell geometries and varying available laser power (several cells were measured at multiple spin-exchange rates); however, several trends are evident. Narrowband lasers outperform broadband lasers in the limit $\Gamma_s \to 0$. Additionally, hybrid mixtures are able to attain higher polarizations in the same limit.

characterizing as many cells as possible. Due to time constraints (and concerns about our cells exploding), only limited effort was made in optimizing the alkali-^{3}He spin-exchange rate. We believe that many of our cells could have been run harder (at higher temperatures) and still maintained Rb polarizations near 100%. However, due to the very real risk of cells exploding at high temperatures, we refrained from pushing these cells too hard. We believe that with enough line-narrowed lasers, a hybrid target cell could achieve its X-factor limited polarization (higher than 80% for many of the cells studied).

Finally, we present Fig. 5.10, which plots P_∞^{He} as a function of D (identical to Fig. 5.5, except with narrowband data included). The data presented in Fig. 5.10 were acquired under similar spin-exchange conditions (the pure-Rb cells were pumped at 180°C, while the hybrid cells were pumped at 235°C). As with Fig. 5.5, the data suggest that pure Rb cells that are pumped by broadband lasers cannot do as well as their hybrid counterparts when pumped with the same lasers; however, when narrow-
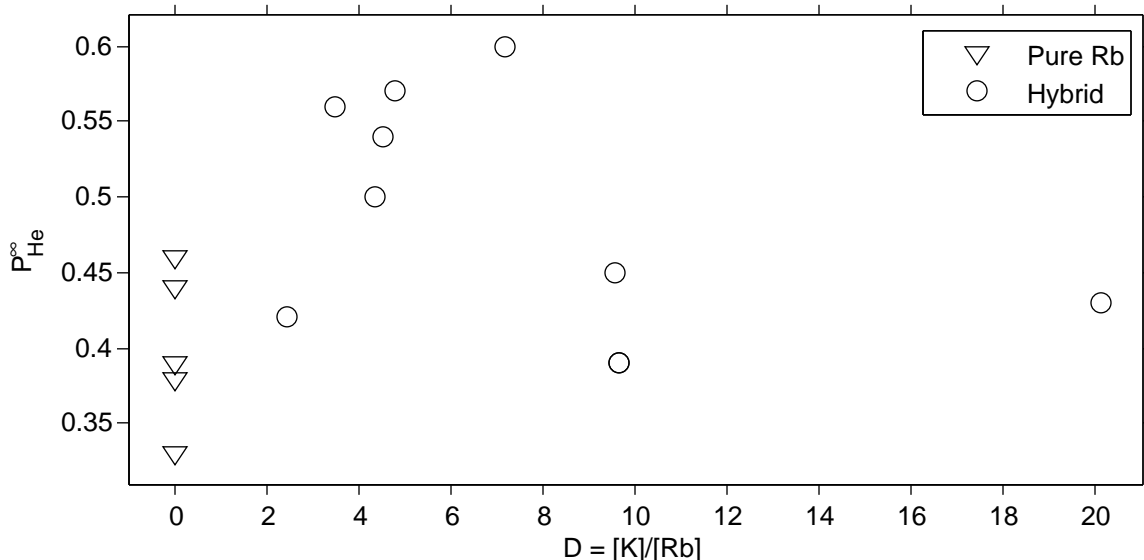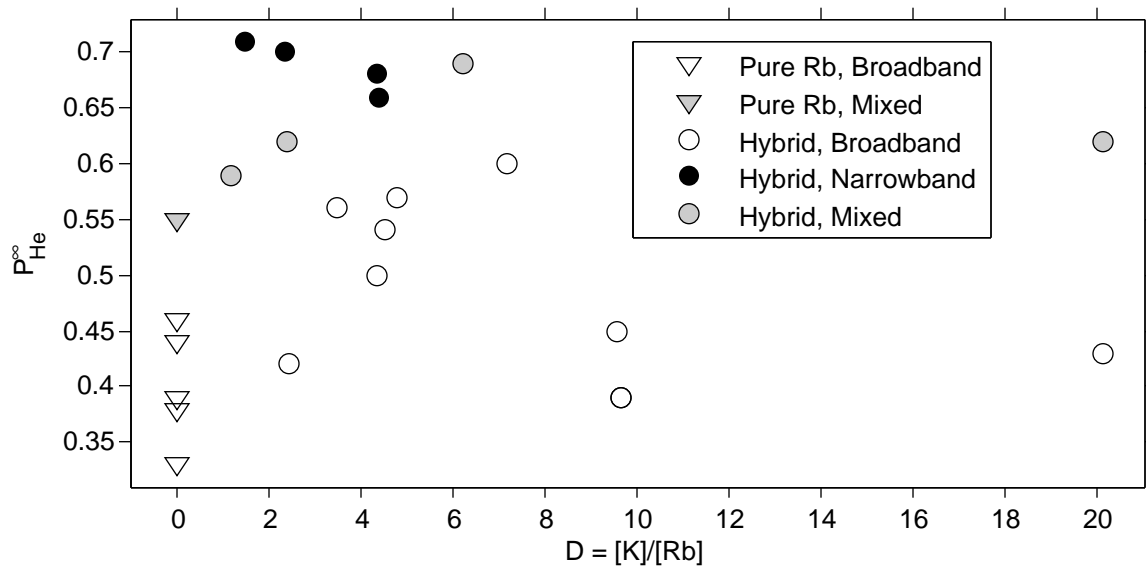
Figure 5.10: Maximum Achieved He-3 Polarization as a Function of D for 20 Target Cells. The data were acquired over a ten-year period, with different cell geometries, available laser power, and hybrid density ratios. For Pure Rb cells (triangles), the oven was set to 180°C; for hybrid cells, the oven was set to 235°C. Line-narrowed lasers outperform broadband lasers and hybrid cells outperform pure rubidium cells. When used in conjunction very high ^{3}He polarizations can be attained. The values for D in this table were extracted from pressure-broadening data, as more cells were measured this way.

band lasers are used, the range of acceptable D's appears to increase. Additionally, regardless of density ratio, line-narrowed lasers outperform broadband lasers. When used in conjunction, very high polarizations can be achieved in target cells. A summary of measured quantities can be found in Table 5.1 and Table E in Appendix E.

5.3 The X Factor, revisited

In the past, it was believed that at sufficiently high alkali densities (such that $\gamma_{se} \gg \langle \Gamma \rangle$) and with sufficiently high laser power (such that $P_A \approx 1$), ^{3}He polarizations approaching 1 could be achieved. Indeed, many of the cells measured during this thesis came close to satisfying these conditions (see Table E); however, at best, ^{3}He polarizations of around 0.7 were measured. This anamolous behavior is explained by the X factor.

The X factor, which was briefly discussed in Ch. 2.6, is believed to be a surface-relaxation mechanism that appears to scale with alkali density [47]. For a double-chambered hybrid target cell in the fast-diffusion limit ($d_{tc} \to \infty$), this additional relaxation mechanism limits the maximum achievable ^{3}He polarization to

$$P_\infty^{He} = P_\infty^A \frac{\langle \gamma_{se} \rangle}{\langle \gamma_{se} \rangle (1 + X) + \langle \Gamma \rangle}. \tag{5.90}$$

In the high spin-exchange rate limit, $\langle \gamma_{se} \rangle \gg \langle \Gamma \rangle$, Eq. 5.90 becomes

$$P_{He}^\infty = P_\infty^A \frac{1}{1 + X}, \tag{5.91}$$

which can be written as

$$X_{max} = \frac{P_\infty^A}{P_\infty^{He}} - 1 \tag{5.92}$$

where we've introduced X_{max}, which is an upper bound on the X factor, found in the high spin-exchange rate limit.

Measurements of X and an understanding of the physics behind it are critical to further increasing P_{He}.

5.3.1 Measuring X

We extract values for X using four different methods. Each method requires us to write Eqn. 5.90 as

$$P_\infty^{He} = P_\infty^A \frac{\langle \gamma_{se} \rangle}{\Gamma_s} \tag{5.93}$$

where we approximate Γ_s (see Eq. 5.39) as

$$\Gamma_s = \langle \gamma_{se} \rangle (1 + X) + \langle \Gamma \rangle. \tag{5.94}$$

Under this approximation, we assume $\delta\Gamma \approx 0$, which is true under typical operating conditions.

The first and simplest method for measuring X, which we label as X_1, requires measurements of P_A, P_∞^{He}, Γ, and Γ_s (although a limit can be established if P_A is unknown). We write Eq. 5.94 as

$$\langle \gamma_{se} \rangle = \frac{\Gamma_s - \langle \Gamma \rangle}{1 + X} \tag{5.95}$$

and evalue Eq. 5.93 using this result. We then solve for X_1:

$$X_1 = \frac{P_\infty^A}{P_\infty^{He}} \left(1 - \frac{\langle \Gamma \rangle}{\Gamma_s} \right) - 1 \tag{5.96}$$

We note that if a measurement of P_A is not available, an upper limit on X_1 can be made by setting $P_A = 1$:

$$X_1 \leq \frac{1}{P_\infty^{He}} \left(1 - \frac{\langle \Gamma \rangle}{\Gamma_s} \right) - 1 \tag{5.97}$$

The second method, which we label X_2 requires measurements of Γ, Γ_s, [Rb], and

D. We write Eq. 5.94 as

$$X = \frac{\Gamma_s - \langle \Gamma \rangle}{\langle \gamma_{se} \rangle} - 1 \tag{5.98}$$

where $\langle \gamma_{se} \rangle$ is evaluated using Eq. 2.87 and Eq. 5.74

$$\langle \gamma_{se} \rangle = f_{pc} k_{se}^{Rb-He} [Rb] \left(1 + D \frac{k_{se}^{A-He}}{k_{se}^{Rb-He}} \right) \tag{5.99}$$

values for k_{se} are summarized in Tab. 2.2. Finally,

$$X_2 = \frac{\Gamma_s - \langle \Gamma \rangle}{f_{pc} k_{se}^{Rb-He} [Rb] \left(1 + D \frac{k_{se}^{A-He}}{k_{se}^{Rb-He}} \right)} - 1 \tag{5.100}$$

The third method, which gives X_3, is very similar to the second method and requires measurements of P_A, Γ, Γ_s, and m_{pc}. We start with Eq. 5.98, but evaluate γ_{se} using Eq. 5.50 and Eq. 5.74:

$$\langle \gamma_{se} \rangle = f_{pc} m_{pc} P_A^\infty \tag{5.101}$$

This gives

$$X_3 = P_A \frac{\Gamma_s - \langle \Gamma \rangle}{f_{pc} m_{pc}} \tag{5.102}$$

Again, if P_A is unknown, an upper limit can be established

$$X_3 \leq \frac{\Gamma_s - \langle \Gamma \rangle}{f_{pc} m_{pc}} \tag{5.103}$$

The fourth method, which gives X_4, requires measurements of P_A, P_∞^{He}, Γ, and m_{pc}. We start by plugging Eq. 5.94 into Eq. 5.93 and then solving for X

$$X = \frac{P_\infty^A}{P_\infty^{He}} - \frac{\langle \Gamma \rangle}{\langle \gamma_{se} \rangle} - 1 \tag{5.104}$$

Making use of Eq. 5.101,

$$X_4 = \frac{P_\infty^A}{P_\infty^{He}} - \frac{P_\infty^A \langle \Gamma \rangle}{f_{pc} m_{pc}} - 1 \tag{5.105}$$

Again, if P_A is unknown, an upper limit can be established

$$X_4 \leq \frac{1}{P_\infty^{He}} - \frac{\langle \Gamma \rangle}{f_{pc} m_{pc}} - 1 \tag{5.106}$$

5.3.2 Comparison Between Faraday-Rotation and Diffusion-Spinup Slopes

In addition to extracting m_{pc} from a spinups like those described in Ch. 5.1.3, it is possible to extract an independant value for m_{pc} from Faraday Rotation data using

$$m_{pc} = P_A \gamma_{se} \tag{5.107}$$

$$= P_A [K] k_{se}^K \left(1 + \frac{k_{se}^{Rb}}{k_{se}^K} \frac{1}{D} \right) \tag{5.108}$$

$$= \frac{P_A [K] l}{l} k_{se}^K \left(1 + \frac{k_{se}^{Rb}}{k_{se}^K} \frac{1}{D} \right) \tag{5.109}$$

We choose to make a comparison between the two techniques to aid in our understanding of the uncertainty associated with each measurement. Although great care is taken to fully understand the uncertainties associated with each technique, a comparison between techniques can be used to check for consistency. Important quantities and their associated uncertainties, such as the X factor (see Ch. 2.6), are calculated using these values.

The quantity $P_A [K] l$ is a fit parameter in Eq. 4.105, as described in Ch. 4.4.6; consequently, a value for m_{pc} can be attained without measuring the alkali polarization. Values and uncertainties for the spin-exchange rate constants, k_{se}^{Rb-He} and k_{se}^{K-He} can be found in Appendix A.

In Fig. 5.11, the ratio of the two slopes, $m_{pc}^{farrot} / m_{tc}^{spinup}$ is plotted for six different

pairs of data (the full set for which we have data). The average was taken and the errors on the ratio were rescaled to give $\chi^2/\text{degree-of-freedom} = 1$. To rescale the errors on the ratio, the errors on $P_A[K]l$ and l were increased. The error on m_{pc}^{spinup} was left at 10% relative; the error on D was left unchanged as the ratio was less sensitive to changes in it. Values for the quanties used in the plot can be found in Table E in Appendix E.
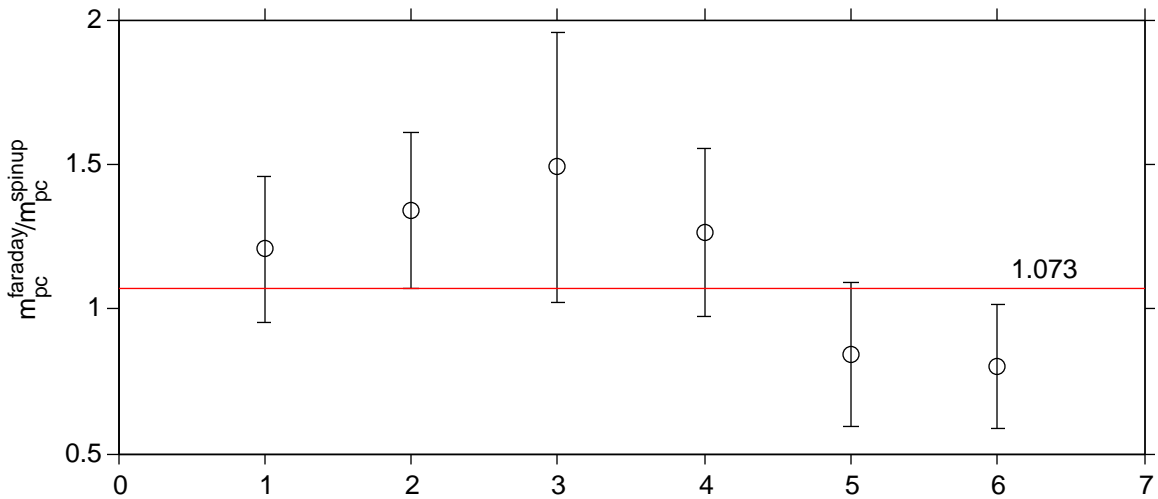
Figure 5.11: Ratio of m_{pc} as Extracted from Faraday Rotation and Diffusion Spinups. The errors on $P_A[K]l$ and l were rescaled to give $\chi^2 = 6 - 1$; the error on D was left unchanged as it propagates weakly.

5.3.3   X Factor Results

Calculations of X, as described in Ch. 5.3.1, were performed using the data presented in Table E in Appendix E. A summary of X factors is presented is presented in Table 5.2.

We note that many of the cells measured in Table 5.2 have X-factor limited ^{3}He polarizations above 0.80. With sufficient laser power, it should be possible to measure previously unattained ^{3}He polarizations in large target cells. However, an interesting

Cell	Lasers	T_{pc}^{set}	X_1	X_2	X_3	X_4	X_{avg}	χ^2_{red}
	2C1F	160	0.22(07)	0.23(29)	0.48(17)	0.11(12)	0.23(06)	1.05
	2C1F	170	0.26(07)	-	-	-	-	-
Sosa	2C1F	180	0.49(09)	0.32(28)	0.76(20)	0.44(11)	0.49(06)	0.80
	2C1F	190	-	-	-	-	-	-
	2C1F	200	1.86(59)	1.14(1.04)	2.19(73)	1.83(58)	1.84(34)	0.23
Alex	2C1F	235	0.37(08)	0.46(33)	0.85(21)	0.27(11)	0.38(06)	2.0
Stephanie	3C	235	0.22(07)	0.40(46)	-	-	-	-
	3C	235	0.14(07)	0.32(38)	0.11(13)	0.14(09)	0.14(05)	0.09
Brady	2C	235	0.17(08)	-	-	-	-	-
	1C	235	0.27(10)	-	-	-	-	-
Moss	1C1F	235	0.19(12)	-	-	-	-	-
Tigger	1C1F	235	0.10(13)	-	-	-	-	-
Samantha	3C	235	0.07(07)	0.46(18)	-	-	-	-
Maureen	3C	235	0.13(12)	-	-	-	-	-
Astral Weeks	2C1F	235	0.17(07)	0.53(31)	0.23(14)	0.16(09)	0.18(05)	0.48

Table 5.2: X-Factor Results. For X_{avg}, a weighted mean was taken assuming uncorrelated errors. χ^2_{red} is the reduced χ^2 (χ^2 per degree-of-freedom)

behavior appears for the pure-Rb target cell, Sosa, which has an X-factor that appears to increase with temperature. A temperature-dependence to X would disagree with the results of Babcock et. al. [47]. It may be, however, that this is a systematic effect that is not yet identified.

5.3.4   Understanding X-Factor Errors

To better understand the error propogation that was used to assign errors to the various values of X, we present the following discussion. Each value of X had several input parameters ($1/\langle\Gamma\rangle$, for example). The error in X due to an uncertainty in an input parameter, y, can be written as

$$\delta X_y = \frac{dX}{dy}\delta y \tag{5.110}$$

The relative error in X due to an uncertainty in y is

$$\frac{\delta X_y}{X} = \frac{\frac{dX}{dy}\delta y}{X} \tag{5.111}$$

	$1/\langle\Gamma\rangle$	$1/\Gamma_s$	P_∞^A	P_∞^{He}	f_{pc}	m_{pc}	[Rb]	D	k_{se}^{Rb-He}	k_{se}^{K-He}
X1	2.01	-2.01	8.21	-8.21	-	-	-	-	-	-
X2	1.00	-5.10	-	-	-4.10	-	-4.10	-2.72	-1.37	-2.72
X3	2.41	-12.2	9.83	-	-9.83	-2.17	-	-	-	-
X4	1.89	-	7.90	-9.79	1.89	1.89	-	-	-	-

Table 5.3: Slopes for Target Cell Brady, Pumped with 3 Narrowband Comets

The relative error in X due to a relative uncertainty in y is

$$\frac{\delta X_y}{X} = \frac{\frac{dX}{dy}}{X}\frac{\delta y}{y}y \tag{5.112}$$

This can be written as

$$\frac{\delta X_y}{X} = a\frac{\delta y}{y} \tag{5.113}$$

where

$$a \equiv \frac{dX}{dy}\frac{y}{X} \tag{5.114}$$

will be referred to here as a "slope." This slope is important in understanding how sensitive X is to its input uncertainties. As an example, consider Table 5.3, which lists various slopes for the target cell Brady (pumped with 3 line-narrowed lasers). X_4 is relatively insensitive to relative uncertainties in f_{pc} (slope of 1.89); however, X_3 is very sensitive to relative uncertainties in f_{pc} (slope of -9.83). This means that a 10% uncertainty in f_{pc} would result in a roughly 100% uncertainty in X_4.

Finally, we note that our treatment of X-factors is not yet complete. Much of the data deserves more analysis, however, the analysis that has been presented provides some insight into the rough size of X.

Chapter 6

Towards A Next Generation

Target Cell

While polarized ^{3}He targets based on SEOP have been used quite effectively in electron-scattering studies, it is likely that the next generation of experiments will encounter limitations unless there are changes to the basic designs employed. As has been described earlier, such targets typically utilize a sealed glass cell with two distinct chambers: a "pumping chamber" in which the gas is polarized, and a "target chamber" through which the electron beam passes (see Fig. 1.1). The two chambers are connected by a "transfer tube". In this design, gas that is polarized in the pumping chamber migrates into the target chamber largely by diffusion (see Ch. 5.1). As long as the time scales associated with diffusion are reasonably short in comparison with the time scales associated with the depolarization of the gas, this is a very effective scheme. For example, in the E142 experiment at SLAC [15], the time constants with which the gas was internally depolarized were on the order of 50 hours without beam and around 40 hours in the presence of a $2\,\mu$A electron beam [68]. The time scale over which diffusion caused mixing was much shorter, on the order of 0.5-1 hour. With the time scale for the mixing of the gas being considerably faster than the other relevant time scales, the polarization gradient was only 1–2% (the polarization gradient describes the difference between pumping-chamber and target-chamber polarization, see Ch. 5.1.5, particularly Eq. 5.69). In more recent experiments, targets have been subjected to currents as high as $15\,\mu$A. In these cases the polarization gradient was more like $5 - 8\%$. Future experiments anticipate using electron beam currents of 60–80 μA [20]; in the absence of a new approach, the polarization gradients would be unacceptably high, as much of tens of percent absolute.

It should be noted that at the time of the work described in reference [15], regardless of the time constants characterizing diffusion, it would have been impractical to achieve high polarizations in SEOP-based ^{3}He targets at high electron-beam currents because of limits in the rate at which the ^{3}He nuclei could be polarized. By incorporating line-narrowed lasers and hybrid-alkali mixtures into the target design,

the characteristic polarization time has drastically decreased (see Ch. 5). In a single-chambered cell, the time constant for polarizing the gas can fairly easily be of the order of two hours, whereas in the mid 1990's a typical number would have been 10-20 hours. With these two advances, it is reasonable to hope to achieve target polarizations of 60% or more, even in the presence of an electron beam of $60 - 80\,\mu\mathrm{A}$. This can only be done, however, if the aforementioned problem of polarization gradients can be addressed.

We report here on a new design for high-density targets based on SEOP for use in electron scattering experiments. While similar in many respects to those used in [15, 20][GEN,Transversity], the design incorporates the ability to circulate the gas between the pumping chamber and the target chamber using convection instead of diffusion. As will be discussed below, the convection is achieved by maintaining a temperature differential between different parts of the target cell, and does not involve pumps or other moving parts. We have built a simple prototype to demonstrate the circulation concept, and have shown that the velocity of the gas moving through the target chamber can be varied between 5–80 cm/min in a simple, controllable manner. The advent of a means to circulate a polarized noble gas in a sealed vessel without the use of pumps has great potential for high-luminosity polarized ^{3}He targets. The simplicity of the approach has advantages from the perspective of reliability and reduces concerns about spin-relaxation from the introduction of new materials. It makes it possible to greatly increase the electron beam current without causing a polarization gradient, and it also makes it possible to physically separate the pumping chamber and the target chamber by much larger distances than was previously possible.

6.1 Convection Driven Cells

6.1.1 Experimental Setup

We describe here a variant of the target cell geometry that is depicted in Fig. 1.1. There are still two chambers, a pumping chamber and a target chamber. Unlike the geometry of the cell in Fig. 1.1, however, the two chambers are connected by two transfer tubes instead of one, as shown in Fig. 6.1. With this design, it is possible to induce convection, thus causing rapid transfer of gas between the two chambers. Furthermore, all that is required to induce convection is to maintain a temperature differential between the vertical segments of the two transfer tubes. By controlling the temperature differential, the speed of the convection can be adjusted. With rapid mixing of gas between the two chambers, the aforementioned polarization gradients can be made negligible.
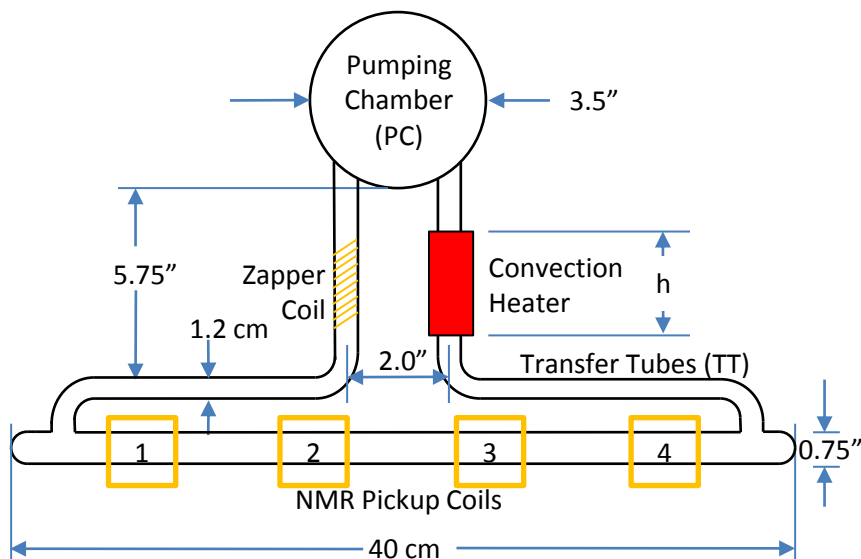
Figure 6.1: All-Glass Convection Test Cell. The pumping chamber is placed inside of an optical pumping oven. The right transfer tube is heated while the left transfer tube is cooled. The two transfer tubes have different densities which creates a counter-clockwise convection current in the cell. The zapper coil is used to depolarize a slug of gas. This slug is then monitored as it travels through the pickup coils on the target chamber.

We have constructed a prototype target cell of the geometry shown in Fig. 6.1. A

small heater was used to maintain a temperature differential. With a portion of one of the transfer tubes at an elevated temperature, the gas contained therein had a lower density than the corresponding gas in the other transfer tube, and thus experienced a small buoyant force that drove convection. We were thus able to demonstrate that it was quite straightforward to drive convection in a reproducible and well-controlled manner.

To visualize the convection, the gas within a small section of one of the transfer tubes was "tagged" by depolarizing it with a pulse of RF tuned to the Larmor frequency of the ^{3}He nuclei. This was accomplished by sending the RF to a small coil wrapped around the transfer tube (labeled in Fig. 6.1 as the "zapper coil"). NMR signals were then detected at each of four locations along the target chamber using "pickup coils" comprising small coils of wire wrapped around the target chamber. NMR signals were obtained once every 2.5 seconds, and are plotted on Fig. 6.2 as a function of time for each of the four pickup coils. Time zero in this plot corresponds to the moment when a slug of gas was tagged.
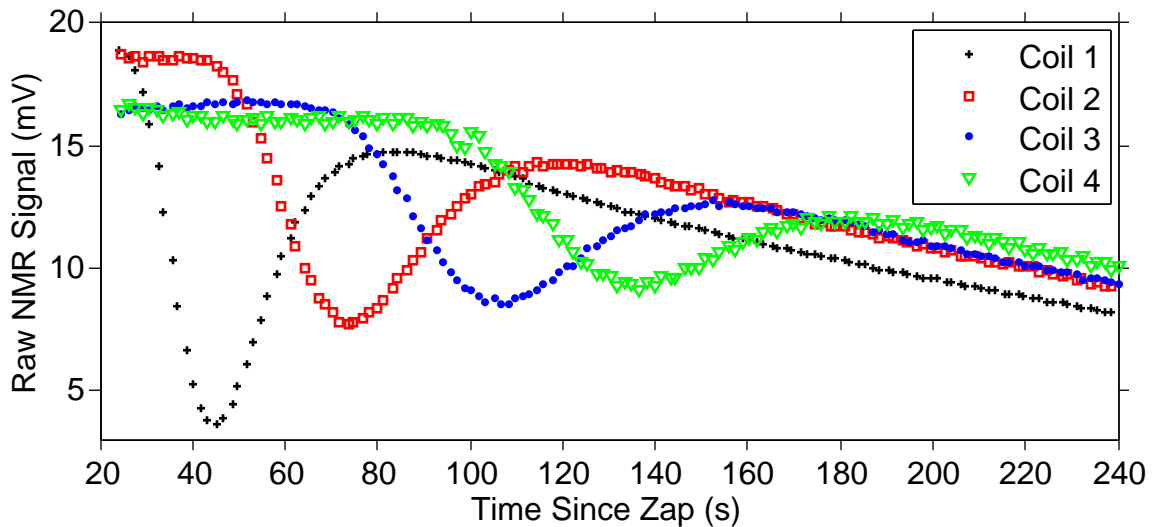
Figure 6.2: Raw Convection Data: Oven at 215°C, Transfer Tubes at 50°C, 24°C. This particular measurement had a velocity of 20cm/min in the target chamber

It is readily apparent from Fig. 6.2 that a transient dip occurs in the signal from each pickup coil. This dip corresponds to the passage of the depolarized slug of gas. The difference of the position (in time) of the dip for each of the four pickup coils provides a measure of the speed with which the tagged slug of gas was moving. Given the known spacing of the four pickup coils, the measurement illustrated in Fig. 6.2 corresponds to a gas velocity of 20 cm/minute.

Also apparent from Fig. 6.2 is the fact that each successive dip becomes wider and more shallow. This is largely because of diffusion, but also because the gas follows the classic parabolic Hagen-Pouiselle velocity distribution. That is, the velocity as a function of the distance r from the middle of the tube has the functional form $v(r) = v_{max}(1 - r^2/R^2)$, where R is the radius of the tube. Hence, the slug of gas, which is initially fairly localized to the region around the "zapper coil", becomes increasingly spread out as it moves through the target chamber. We also note that the NMR signal decreases as a function of time. This is largely due to the buildup of small AFP losses intrinsic to our system, particularly for rapid frequency with which the AFP measurements were made for this measurement (during a typical spinup or spindown, AFP measurements are made once every two or three hours; for this particular measurement, AFPs were performed every 2.5 seconds).

The velocity of the gas can be controlled by changing the temperature of the heater on the hot transfer tube. The measured velocity is expected to be proportional to the difference between the gas densities in the two transfer-tubes, and since the density scales inversely with temperature, we should expect that the to velocity scale as

$$v(T) = \alpha \times \left(\frac{1}{T_{cold}} - \frac{1}{T} \right) \tag{6.1}$$

where T is the temperature of the heated transfer tube in degrees Kelvin. In Fig. 6.3, the velocity of the gas, measured using data such as those in Fig. 6.2, is plotted as a

function of T. The data are also fit to a function of the form of Eq. 6.1. The quality of the fit is clearly quite good, and yields $T_{cold} = 24.5(3)°C$ and $\alpha = 7.82(04) \times 10^4 K \cdot cm/min$. An RTD placed on the cold transfer tube read $T_{cold} = 24°C$, which is in good agreement with value from the fit.
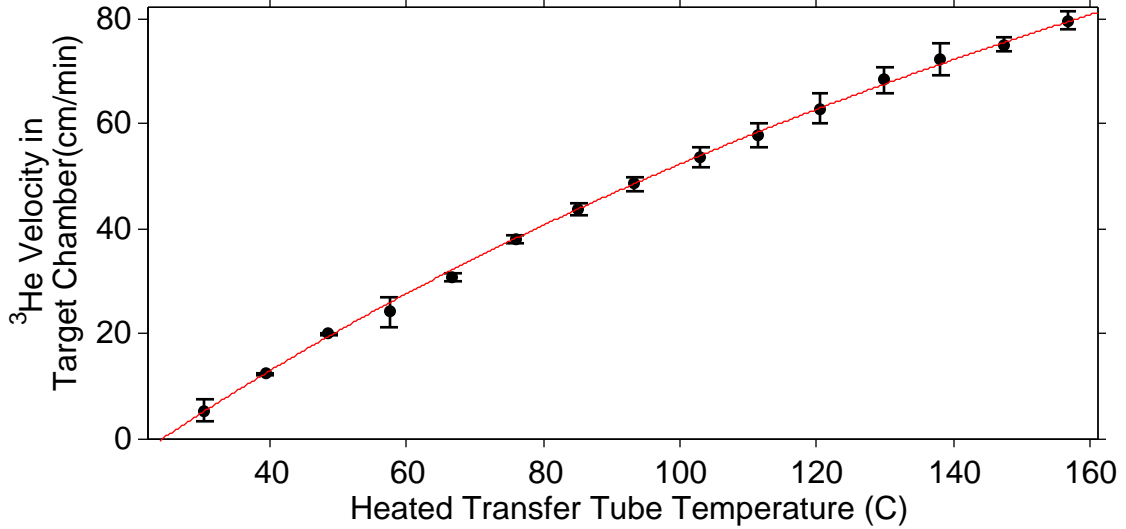
Figure 6.3: Convection Data: Oven at 215C, Transfer Tubes at T, 24C

Ultimately, the value of a convection-driven target cell is measured by the degree to which polarization gradients can be avoided between the pumping chamber and the target chamber. It is critical that, as gas is depolarized by an electron beam, freshly polarized gas is delivered from the pumping chamber. Ideally, one would like the ratio of the polarizations of the two chambers to be as close to unity as possible. In Fig. 5.1b, the ratio of the pumping chamber polarization to the target chamber polarization is plotted as a function of time. (The pumping chamber polarizations were calibrated using EPR (see Ch. 3.2). The target chamber polarizations were attained by first calibrating the response of the pickup coils under different temperature conditions. Next, EPR-calibrated pumping chamber data was compared with uniform cell-temperature spindown data (during a spindown, it is believed that the polarization gradient is minimized). Finally, these two results are combined to get a

value for target-chamber polarization during a spinup.) The ratio begins at zero, and gradually climbs to a value less than 1, reflecting a substantial polarization gradient. In Fig. 6.4, we plot the same ratio for a convection-driven cell for three different operating conditions. In all cases, the temperature of the oven was held at 215°C. The three curves correspond to different temperatures for the transfer tube that is outfitted with a heater. For the data shown with the open squares, the transfer-tube set temperature was 24°C, the same as the other (unheated) transfer tube. This case corresponds to no driven convection, and the data are similar to that shown in Fig. 1.1b. For the data shown with the filled triangles, the set temperature was 50°C, and for the data shown with the filled circles, the set temperature was 100°C. These last two conditions corresponded to gas velocities of approximately 19.9 cm/min and 48.5 cm/min. In both of these cases, the ratio of the polarizations of the target chamber and the pumping chamber quickly reached a value close to 1. It is notable that there is very little difference between these last two curves despite substantially different gas velocities. In short, as soon as convection rather than diffusion is responsible for the gas transfer between the two chambers, polarization is relatively uniform throughout the cell.

6.2   Theory Explaining Gas Velocity

From a practical perspective, it is already quite apparent, from Fig. 6.3 that the velocity of the gas can be well controlled by adjusting the heater on one of the transfer tubes. It is quite useful, however, to establish that the magnitude of the velocity is reasonably well understood from first principles. For one thing, when designing target cells beyond our initial prototype, we would like to know in advance the size of the temperature gradients that will be necessary to achieve gas flow of a certain rate. In fact, at the level of roughly 20% or so, it is straightforward to
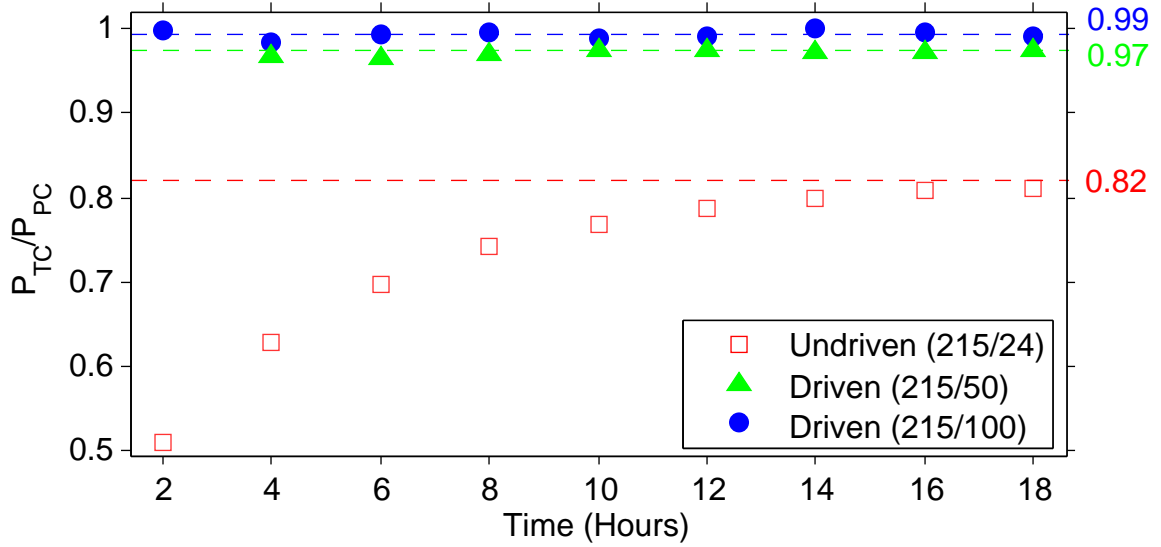
Figure 6.4: Comparison of 3 Spinups. The polarization ratio between chambers is smallest in the undriven spinup. Additionally, it takes longer for the polarization ratio to equilibriate. When the cell is driven, the polarization ratio diminishes and equilibrium is achieved rapidly. We note that the equilibrium-polarization ratio in the undriven case is very low because the transfer tubes are much longer than in normal target cells (see Fig. 5.1.b)

understand quantitatively the behavior shown in Fig. 6.3.

6.2.1   Hagen-Pouiselle Flow

The convective motion of the gas inside the cell depicted in Fig. 6.1 can be described as Hagen-Pouiselle flow [69, 70]. This occurs when a pressure differential between two ends of a pipe causes the laminar flow of a viscous gas or fluid. In equilibrium, the driving force (from the pressure differential) must equal the retarding force from the viscosity, that is:

$$F_{driving} = F_{retarding}   . \tag{6.2}$$

If the pipe is circular in cross section, and Eq. 6.2 is to be satisfied, each annular ring of fluid of thickness dr must obey the relation

$$\Delta P 2\pi r dr = -2\pi\eta l \frac{d}{dr}\left(r\frac{dv}{dr}\right) dr   , \tag{6.3}$$

where ΔP is the pressure differential, η is the viscosity of the fluid and l is the length of the pipe. With the boundry condition that the velocity of flow must go to zero at the perimeter of the pipe, the solution to this differential equation is

$$v(r) = \frac{1}{4}\frac{\Delta P(r^2 - R^2)}{\eta l} \tag{6.4}$$

where R is the radius of the pipe. This is sometimes referred to as the Hagen-Pouiselle equation.

6.2.2 Viscosity and Laminar Flow

Since our temperatures are in the classical regime $(T \gg 3K)$, the viscosity of ^{3}He can be calculated from the ^{4}He viscosity, using [71].

$$\eta_{\text{He3}} = \sqrt{\frac{m_{\text{He3}}}{m_{\text{He4}}}}\eta_{\text{He4}} \tag{6.5}$$

$$= 0.8681\ \eta_{\text{He4}} \tag{6.6}$$

We parameterize the ^{4}He viscosity in the range of $0 - 300°C$ using Kestin et al. [72]

$$\eta_{\text{He4}} = A + B \times T + C \times T^2 \tag{6.7}$$

where T has units of $°C$ and

$$A = 18.82(2)\ \mu\text{Pa} \cdot \text{s} \tag{6.8}$$

$$B = 0.0456(2)\ \mu\text{Pa} \cdot \text{s}/°\text{C} \tag{6.9}$$

$$C = -13.8(6)p\text{Pa} \cdot \text{s}/(°\text{C})^2 \tag{6.10}$$

At $20°C$, $\eta_{\text{He3}} = 17.12\mu$Pa·s. The flow in a pipe is Laminar if the Reynold's

number is below 2320 [73]. The Reynolds number is defined as

$$Re = \frac{2R\rho v}{\eta},$$ (6.11)

where ρ is the density of the fluid and R is the radius of the pipe.

A pipe 1.2cm wide that is filled with 8 amagats ^{3}He at $20°C$ ($\rho \approx 1\text{kg}/\text{m}^3$) will have laminar flow provided $v \ll 20000$ cm/min.

6.2.3 Flow in the Convection Cell

The flow in the convection cell arises from a forced density difference between the two transfer tubes – one tube is maintained at room temperature while the other is heated (see Fig. 6.1). Eqn. 6.3 now reads

$$\Delta\rho gh 2\pi r dr = -2\pi \sum_i^5 \eta_i l_i \frac{d}{dr_i}\left(r_i \frac{dv_i}{dr_i}\right) dr_i$$ (6.12)

where h is the vertical length of transfer tube at a different temperature (see Fig. 6.5).

We approximate the pumping chamber as a cylinder with transfer tubes entering axially. In this configuration Fig. (6.5), there are 5 distinct regions in the cell (3 temperatures: $T_1 = T_4$, T_2, and $T_3 = T_5$ and 3 radii: $R_1 = R_2 = R_3$, R_4, and R_5). The density of the gas and its viscosity are temperature dependant. The continuity equation, $\rho_j A_j v_j = \rho_i A_i v_i$ and some distance rescaling provide further simplification,

$$v_i = \frac{\rho_1 R_1^2}{\rho_i R_i^2} v_1$$ (6.13)

$$r_i = \frac{R_i}{R_1} r_1$$ (6.14)

$$\frac{d}{dr_i} = \frac{R_1}{R_i} \frac{d}{dr_i}$$ (6.15)

Since v_i and r_i have been expressed interms of v_1 and r_1, we'll drop their subscripts.
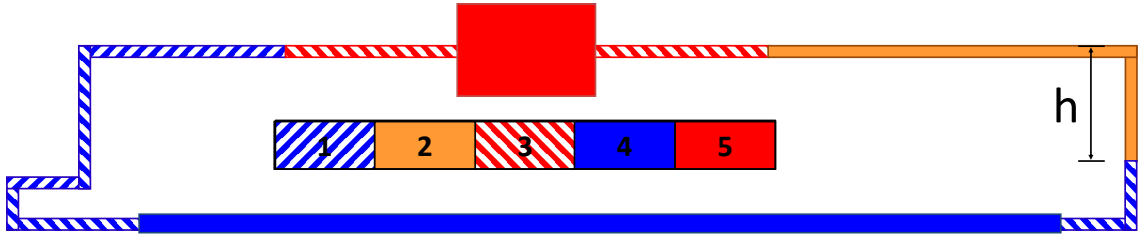
Figure 6.5: Convection Cell Cylindrical Approximation

The solution to Eq. 6.12 is

$$v(r) = \frac{1}{4} \frac{\Delta\rho g h r^2}{\eta_1 \left(l_1 + l_4 \frac{R_1^2}{R_4^2}\right) + \eta_2 l_2 \frac{\rho_1 R_1^2}{\rho_2 R_2^2} + \eta_3 \frac{\rho_1}{\rho_3} \left(l_3 \frac{R_1^2}{R_3^3} + l_5 \frac{R_1^2}{R_5^2}\right)} + C \ln r + D \qquad (6.16)$$

Applying appropriate boundary conditions $(v(0) \neq \infty \ \& \ v(R_1) = 0)$,

$$v(r) = \frac{1}{4} \frac{\Delta\rho g h \left(r^2 - R_1^2\right)}{\eta_1 \left(l_1 + l_4 \frac{R_1^2}{R_4^2}\right) + \eta_2 l_2 \frac{\rho_1 R_1^2}{\rho_2 R_2^2} + \eta_3 \frac{\rho_1}{\rho_3} \left(l_3 \frac{R_1^2}{R_3^3} + l_5 \frac{R_1^2}{R_5^2}\right)} \qquad (6.17)$$

Eqn. (6.17) assumes that there are no "minor losses" in the system, where a minor loss represents a pressure drop due to a sudden change in flow from a pipe fitting or a pipe expansion/contraction. Our use of the term 'minor loss' refers to a loss that is small relative to the overall length of pipe under consideration [69, 74]. In our case, due to the relatively short length of the cell, the minor losses are actually significant. The actual cell, Fig. (6.1) consists of four elbow bends, two tees, and four expansions/contractions. The retarding forces these losses exert on the gas can be approximated by considering instead an equivalent length of straight pipe.

The expansions/contractions have a relatively small loss, which is approximated to be equivalent in magnitude to the loss that would be incurred passing through a pipe of length [74]

$$L_{equivalent} = \frac{2RK}{f}, \qquad (6.18)$$

where R is the tube radius, f is the friction factor ($f = 64/Re$ for laminar flow) and K is the fluid-independent resistance coefficient. For sudden expansions/contractions,

$$K_{expansion} = \left(1 - \frac{r_{small}^2}{r_{large}^2}\right)^2 \tag{6.19}$$

$$K_{contraction} = \frac{1}{2}\left(1 - \frac{r_{small}^2}{r_{large}^2}\right)^2 \tag{6.20}$$

Gas flowing through the transfer tube/target chamber junction has $K_{contraction} \approx 0.18$, $K_{expansion} \approx 0.35$. At $v = 60$cm/min ($Re \approx 10$), this gives a negligibe $L_{equivalent} \approx 0.1$cm – gas flowing between the pumping chamber and the transfer tube will have an even smaller $L_{equivalent}$.

The losses in the bends, however, are much greater. We model the loss coefficient in the bends using the 3-K method of Darby [75],

$$K = \frac{K_1}{R_e} + K_i\left(1 + \frac{K_d}{D^{0.3}}\right) \tag{6.21}$$

where D is the diameter of the pipe (in inches) and K_1, K_i, K_d are geometry-dependent loss coefficients. We approximate our glass bends as flanged, welded bends with $r_b/D = 2$ (here, r_b is the radius of the bend); such bends have $K_1 = 800, K_i = 0.056, K_d = 3.9$. For lamiar flow, the 3-K method gives

$$L_{equivalent} = \frac{2R}{64}\left[K_1 + ReK_i\left(1 + \frac{K_d}{D^{0.3}}\right)\right] \tag{6.22}$$

We treat the transfer tube/target chamber tee junctions as elbows (effectively ignoring the dead-end branch of the tee – an open tee has an $L_{equivalent}$ that is approximately double). The system therefor has five bends in temperature-region 1 (which have a total equivalent length of approximately 63cm) and one bend in temperature-region 2 (which has an equivalent length of approximately 13cm).

Finally, using the ideal gas law to evaluate $\Delta\rho$ in terms of T, we get

$$v(r) = \frac{m_{^3He} P g h \left(r^2 - R_1^2\right)/4k_B \left(\frac{1}{T_{cold_{tt}}} - \frac{1}{T_{hot_{tt}}}\right)}{\eta_1 \left(l'_1 + l_4 \frac{R_1^2}{R_4^2}\right) + \eta_2 l'_2 \frac{\rho_1 R_1^2}{\rho_2 R_2^2} + \eta_3 \frac{T_3}{T_1}\left(l_3 \frac{R_1^2}{R_3^3} + l_5 \frac{R_1^2}{R_5^2}\right)} \tag{6.23}$$

where

$$l'_1 = l_1 + 5 \times \frac{2R_1}{64}\left[K_1 + Re_1 K_i \left(1 + \frac{K_d}{D_1^{0.3}}\right)\right] \tag{6.24}$$

$$l'_2 = l_2 + \frac{2R_2}{64}\left[K_1 + Re_2 K_i \left(1 + \frac{K_d}{D_2^{0.3}}\right)\right] \tag{6.25}$$

Note that the Reynold's number is dependent on the velocity of the gas.

The pressure in Eqn. 6.23 can be calculated in terms of the pressure corresponding to a cell, all of the parts of which are at the same temperature,

$$P = \frac{P_{uniform}}{T_{uniform}}\left(\frac{V_I}{T_I V_{total}} + \frac{V_{II}}{T_{II} V_{total}} + \frac{V_{III}}{T_{III} V_{total}}\right)^{-1} \tag{6.26}$$

This pressure varies less than 0.5% over the temperature range we studied.

Table 6.1 lists values for R and l. Measurements of R (which is the inner diameter of the tube) require a knowledge of the thickness of the glass tube. We measured the thickness of the glass by observing interference patterns using a scannable single-frequency laser.

R1	R2	R3	R4	R5	h	l1	l2	l3	l4	l5
.498	.521	.502	.806	4.034	4.76	24.99	20.87	15.18	40.32	5.6

Table 6.1: Alkali-^{3}He Best Guesses for Cell Dimensions (cm)

6.2.4   Evolution of a Cylindrical Slug

As was described in Ch. 6.1.1, we use a 'zapper' coil to tag a small slug of gas. In the absense of diffusion, this slug, which starts out at $t = 0$ as a cylinder, evolves parabolically according to Hagen-Pouiselle flow. The slug can then be monitored (see Fig. 6.2) as it passes through the pickup coils located on the target chamber (see Fig. 6.1). In this section, we present a theory describing the signal measured by the pickup coils in the target chamber. For this discussion, we'll ignore diffusion and consider a zapper coil that is located along the target chamber (instead of along the transfer tube).

The initially-cylindrical slug will evolve under Hagen-Pouiselle flow into a paraboloid (see the left portion of Fig. 6.6). The front and back surfaces of this slug are described by

$$
\begin{aligned}
z(r, t)^{front} &= v_{max}\left(1 - \frac{r^2}{R^2}\right)t & (6.27) \\
z(r, t)^{back} &= z(r, t)^{front} - \mathcal{Z} & (6.28)
\end{aligned}
$$

where $\mathcal{Z}$ is the length of the zapper coil. The volume between these two surfaces is conserved and is given by

$$
\begin{aligned}
V &= \frac{\pi R^2}{v_{max}t}\left(\int_0^{v_{max}t} z\,dz - \int_0^{v_{max}t}(z - \mathcal{Z})dz\right) & (6.29) \\
&= \pi R^2 \mathcal{Z} & (6.30)
\end{aligned}
$$

We'll approximate the signal inside of the pickup coil as being proportional to the volume of the slug that is directly inside of the pickup coil (in reality, the pickup coils are sensitive to gas that is outside of the pickup coils as well). Under this approximation, the first pickup coil won't see any signal until after $t = Z_0/v_{max}$, where Z_0 is the distance between the front edge of the zapper coil and the back end
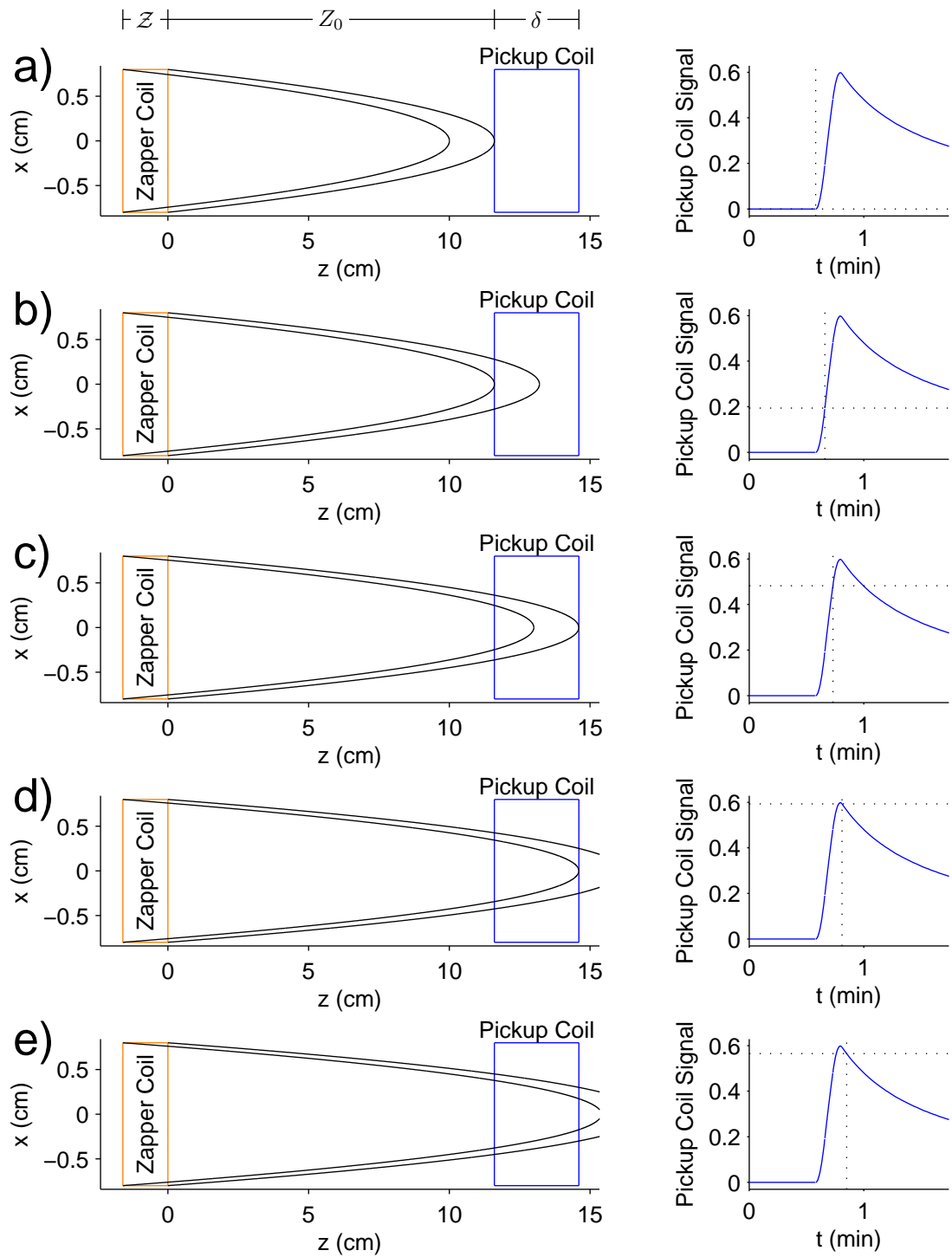
Figure 6.6: Progress of Parabolic Slug along Target Chamber. LEFT: Side view of the slug. RIGHT: Volume of the slug that is inside of the pickup coil as a function of time.

of the pickup coil. We'll refer to the region where $t \leq Z_0/v_{max}$ as region 'a' (see Fig. 6.6.a). When $Z_0/v_{max} \leq t \leq (Z_0 + \mathcal{Z})/v_{max}$, the volume of gas inside of the pickup coil is

$$V_b \;=\; \frac{\pi R^2}{v_{max}t} \left(\int_0^{v_{max}t-Z_0} z\,dz \right) \tag{6.31}$$

$$\;=\; \frac{1}{2}\pi R^2 v_{max}t \left(1 - \frac{Z_0}{v_{max}t} \right) \tag{6.32}$$

We'll refer to this region as region 'b' (see Fig. 6.6.b). Region 'c' begins when the fastest part of the back end of the slug enters the pickup coil and ends when the fastest part of the front end of the slug exits the pickup coil (see Fig. 6.6.c). This corresponds to $(Z_0 + \mathcal{Z})/v_{max} \leq t \leq (Z_0 + \delta)/v_{max}$, where δ is the length of the pickup coil. In region 'c,' the volume of gas inside of the pickup coil is

$$V_c \;=\; \frac{\pi R^2}{v_{max}t} \left(\int_0^{v_{max}t-Z_0} z\,dz - \int_0^{v_{max}t-Z_0-\mathcal{Z}} z\,dz \right) \tag{6.33}$$

$$\;=\; \frac{1}{2}\pi R^2 \mathcal{Z} \left(2 - \frac{2Z_0}{v_{max}t} - \frac{\mathcal{Z}}{v_{max}t} \right) \tag{6.34}$$

The next region, region 'd' (see Fig. 6.6.d), is defined for $(Z_0 + \delta)/v_{max} \leq t \leq (Z_0 + \delta + \mathcal{Z})/v_{max}$ has a volume of

$$V_d \;=\; \frac{\pi R^2}{v_{max}t} \left(\int_{v_{max}t-Z_0-\delta}^{v_{max}t-Z_0} z\,dz - \int_0^{v_{max}t-Z_0-\mathcal{Z}} z\,dz \right) \tag{6.35}$$

$$\;=\; \frac{1}{2}\pi R^2 v_{max}t \left[\left(1 - \frac{Z_0}{v_{max}t} \right)^2 - \left(1 - \frac{Z_0+\delta}{v_{max}t} \right)^2 - \left(1 - \frac{Z_0+\mathcal{Z}}{v_{max}t} \right)^2 \right] \tag{6.36}$$

The signal in the pickup coil reaches its maximum value in region 'd' at time

$$t_{max} \;=\; \frac{Z_0}{v_{max}} \sqrt{ 1 + \frac{2(\mathcal{Z}+\delta)}{Z_0} + \frac{\delta^2 + \mathcal{Z}^2}{Z_0^2} } \tag{6.37}$$

Region 'e' occurs when the fastest part of the back-end of the slug exits the pickup

coil. This corresponds to $\leq (Z_0 + \delta + \mathcal{Z})/v_{max} \leq t$ and has a volume of

$$V_e = \frac{\pi R^2}{v_{max}t} \left(\int_{v_{max}t-Z_0-\delta}^{v_{max}t-Z_0} zdz - \int_{v_{max}t-Z_0-\delta}^{v_{max}t-Z_0} (z - \mathcal{Z})dz \right) \tag{6.38}$$

$$= \frac{1}{2}\pi R^2 v_{max} t \left(2\mathcal{Z}\delta \right) \tag{6.39}$$

We note some differences between real data (Fig. 6.2) and the simulated data (Fig. 6.6, Right). For the real data, a slug of negatively-polarized gas passed through a cell that had positively-polarized gas. For the simulation, a slug of fully polarized gas passed through an otherwise unpolarized cell. For this reason, the data in Fig. 6.2 starts out with a high signal and then dips down (while the simulated data starts with no signal and then increases). Another difference is that the real data had AFP losses, which make the signal decrease long after the slug has exited. Additionally, diffusion was present in the real data, which allowed the different streamlines to mix.

As was described in Ch. 6.1.1, we estimate the velocity of a slug of gas by measuring the signal in target chamber coils (see Fig. 6.2). Specifically, we compare the time at which extrema occur and obtain a velocity by knowing the coil separation. However, it's not clear from this method whether the measured velocity corresponds to the maximum velocity of the slug, the average velocity of the slug, or some combination of the two. To better understand this, we present Fig. 6.7, which simulates the passage of a slug through two pickup coils. Using Eq. 6.37 with $v_{max} = 20$cm/min, $Z_0 = 11.6$cm, $\mathcal{Z} = 1.6$cm, $\delta = 3$cm, and $\Delta = 10$cm, we find maxima at $t = 0.795$min and $t = 1.301$min. This gives a velocity of 19.8 cm/min, which agrees with v_{max} at the 1% level.

To better understand this, we rewrite Eq. 6.37 as

$$t = \frac{Z_0 + \delta + \mathcal{Z}}{v_{max}} \sqrt{1 - \frac{2\delta\mathcal{Z}}{(Z_0 + \delta + \mathcal{Z})^2}} \tag{6.40}$$
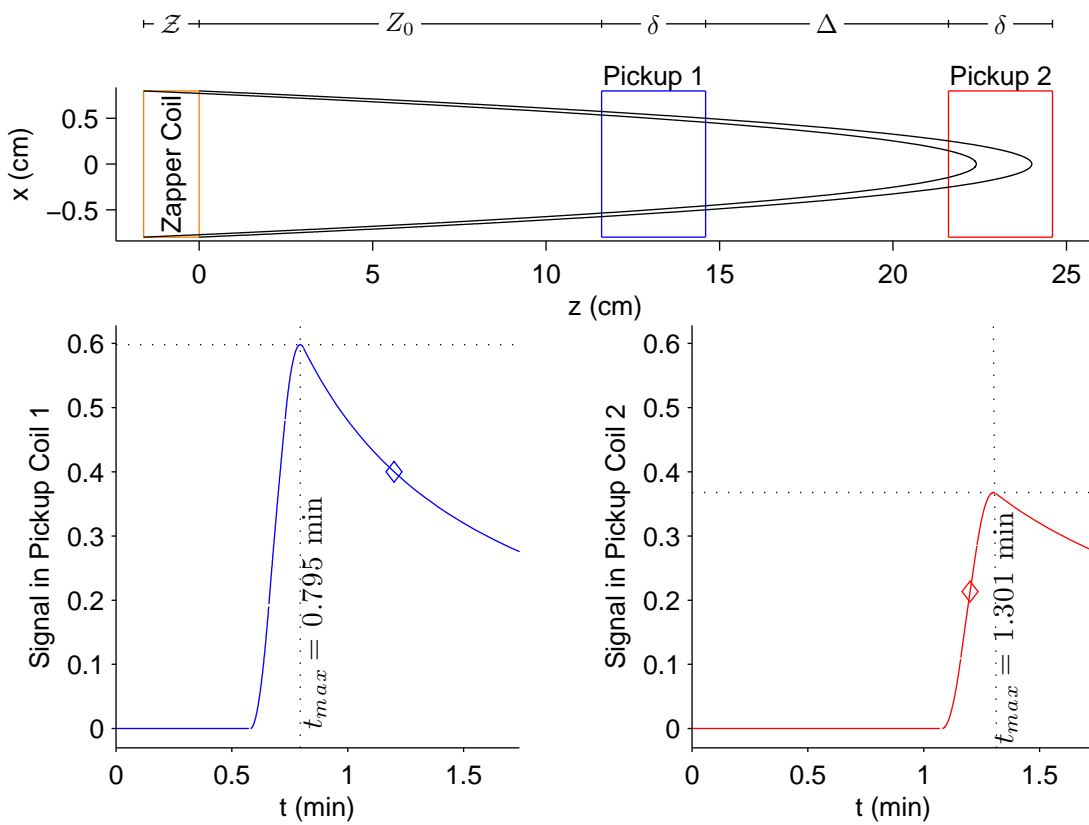
Figure 6.7: Progress of Parabolic Slug along Target Chamber. LEFT: Side view of the slug. RIGHT: Volume of the slug that is inside of the pickup coil as a function of time.

Provided $2\delta\mathcal{Z}/(Z_0 + \delta + \mathcal{Z})^2 \ll 1$, we can approximate Eq. 6.40 to first order using a Taylor expansion

$$t \approx \frac{1}{v_{max}} \left(Z_0 + \delta + \mathcal{Z} - \frac{\delta\mathcal{Z}}{(Z_0 + \delta + \mathcal{Z})} \right) \tag{6.41}$$

The time interval between two coils a distance Δ apart is therefore

$$\Delta t \approx \frac{\Delta}{v_{max}} (1 + G) \tag{6.42}$$

where

$$G = \frac{\delta\mathcal{Z}}{(Z_0 + \delta + \mathcal{Z})(Z_0 + \Delta + \delta + \mathcal{Z})} \tag{6.43}$$

Under typical operating conditions, $G \approx 0$, which implies

$$v_{max} \approx \frac{\Delta}{\Delta t} \tag{6.44}$$

This implies that the velocites measured in Ch. 6.1.1 are maximum velocities.

6.2.5   Comparison between Theory and Experiment

With the results of the preceeding sections, we're finally in a position to compare our theory with actual experimental results. To make a comparison with Eq. 6.1, we rewrite Eq. 6.23 as

$$v_{max} = \frac{\mathcal{A} \left(\frac{1}{T_{cold_{tt}}} - \frac{1}{T_{hot_{tt}}} \right)}{1 + \beta(T)} \tag{6.45}$$

where

$$v_{max} = v(r = 0) \tag{6.46}$$

$$\mathcal{A} = \frac{mPghR^2}{4k_B}\gamma \tag{6.47}$$

$$\beta(T) = \left(\beta_1\Delta T + \beta_2(\Delta T)^2 + \beta_3(\Delta T)^3\right)\gamma \tag{6.48}$$

$$\gamma = \frac{1}{\eta_1(l_1' + l_4\frac{R_1^2}{R_4^2} + l_2'\frac{R_1^2}{R_2^2}) + \eta_3\frac{T_3}{T_1}(l_3\frac{R_1^2}{R_3^2} + l_5\frac{R_1^2}{R_5^2})} \tag{6.49}$$

$$\Delta T = T_2 - T_1 \tag{6.50}$$

$$\beta_1 = l_2'\frac{R_1^2}{R_2^2}\left[\frac{\eta_1}{T_1} + 0.8681\left(B + 2C(T_1 - 273)\right)\right] \tag{6.51}$$

$$\beta_2 = 0.8681l_2'\frac{R_1^2}{R_2^2}\left[\frac{B + 2C(T_1 - 273)}{T_1} + C\right] \tag{6.52}$$

$$\beta_3 = 0.8681l_2'\frac{R_1^2}{R_2^2}\left[\frac{C}{T_1}\right] \tag{6.53}$$

In the above equations, all temperatures are in kelvin. Also, we have chosen to ignore the small temperature-dependence of the pressure in α.

Evaluating the above equations in terms of our best guesses for cell dimensions and temperatures, with $T_{cold} = 24.5°C$ gives $\mathcal{A} = 9.14 \times 10^4$K·cm/min, $\beta_1 = 1.03 \times 10^{-3}, \beta_2 = 1.26 \times 10^{-6}$, and $\beta_3 = -4.26 \times 10^{-10}$. When data generated using this formalism are fit to Eq. 6.1, we find $\alpha = 7.96(03) \times 10^4$K·cm/min and $T_{cold} = 22.0(2)°C$. These values are surprisingly close to the measured values ($\alpha = 7.82(04) \times 10^4$K·cm/min and $T_{cold} = 24.5(3)°C$).

If this simulated data is instead fit to a formalism that is first order in ΔT,

$$v_{max} = \frac{\mathcal{A}\left(\frac{1}{T_{cold_{tt}}} - \frac{1}{T_{hot_{tt}}}\right)}{1 + \beta_1\Delta T}, \tag{6.54}$$

we find $\mathcal{A} = 9.18(01) \times 10^4$K·cm/min, $T_{cold} = 24.6(01)$, and $\beta_1 = 1.15(004) \times 10^{-3}$, in excellent agreement with the input parameters of the simulation. For comparison, we also fit the real data to Eq. 6.54; we find $\mathcal{A} = 7.47(22) \times 10^4$K·cm/min, $T_{cold} = 24.3(8)$,

and $\beta_1 = -0.2(2) \times 10^{-3}$. In this case, we note that the fit appears to be worse (including a non-physical negative value for β_1). We suspect this is because the error intrinsic to our measurements is greater in size than the effect of β_1.

Chapter 7

Conclusion

The implementation and optimization of hybrid-alkali SEOP and line-narrowed lasers in high-luminosity polarized-^{3}He targets have been instrumental in the success of several recent high-profile electron-scattering experiments at Jefferson Lab. These enabling technologies have resulted in unprecedented ^{3}He polarizations in large, two-chambered target cells. Moreover, the time scale characterizing ^{3}He polarization accumulation has decreased. Despite these improvements, these technologies alone will not be enough to meet the needs of future experiments, which will need to run at higher beam currents. In the presence of such high beam currents, the gas in the target chamber will become quickly depolarized. To compensate for this large polarization gradient, we propose a convection-driven target cell, a prototype of which was successfully tested as part of this thesis.

Prior to the work presented in this thesis, target cells were characterized by their saturation ^{3}He polarization and room-temperature lifetime. Although these parameters are important for target performance, it is very difficult to optimize cell performance without more information. As part of this thesis, several important diagnostic techniques were designed and implemented. These techniques have allowed a greater understanding of ^{3}He polarimetry and diffusion. Moreover, targets can now be characterized in terms of their alkali polarization, alkali density, and X-factor. Knowledge of these parameters can be used to optimize target performance. For example, we know that a K/Rb density ratio of $3 <$[K]/[Rb]< 9 appears to give the best performance in hybrid cells. Additionally, Line-narrowed lasers increase alkali polarization. There is strong evidence that a hybrid-alkali cell pumped by line-narrowed lasers should be able to maintain a high alkali polarization at high temperatures. Under such conditions, it should be possible to achieve the X-factor limited ^{3}He polarization, which should be above 80% for some of the cells studied in this thesis.

Although considerable gains have been made in the current ^{3}He target design, without further changes, the design will be inadequate to handle the next generation

of electron-scattering experiments. These experiments, which will necessarily run at higher beam currents, will create large polarization gradients between the pumping chamber (where SEOP occurs) and the target chamber (where electron scattering occurs). In the current design, gas mixes between the two chambers largely by diffusion. Provided the mixing rate is much faster than the relaxation rate, this design works well; however, this design works poorly when the relaxation rate in the target chamber is very high (as will be the case in future experiments). To solve this problem, we propose a new target design that mixes the gas by convection. We successfully tested such a design and demonstrated an ability to control the mixing rate.

Appendices

Appendix A

Spin-Exchange & Spin Destruction Rate Constants

This section is identical to the Tech Note by the same name [76]

A.1 Alkali-Alkali Collisions

A.1.1 Spin Exchange

The alkali-alkali spin exchange rate constants are estimated by:

$$A_{\text{se}}^{ab} = \bar{v}\sqrt{\sigma_{\text{se}}^a \sigma_{\text{se}}^b} = \left[\frac{1\text{ MHz}}{10^{15}/\text{cm}^3}\right]\sqrt{\left[\frac{\sigma_{\text{se}}^a}{100\text{Å}^2}\right]\left[\frac{\sigma_{\text{se}}^b}{100\text{Å}^2}\right]\left[\frac{10\text{ g/mol}}{M_a} + \frac{10\text{ g/mol}}{M_b}\right]} \quad (A.1)$$

where σ_{se} is the alkali-alkali spin exchange cross section and $\bar{v}$ is the relative mean thermal velocity of the alkali-alkali pair, and M_a & M_b are the molecular weights of the two alkali atoms involved in the collision. The A-A spin exchange rate constant is assumed to be independent of temperature just as e^--A spin exchange [77]. Therefore the cross section must have a $1/\sqrt{T}$ temperature dependence.

	$\langle\sigma_{se}\rangle$	err.	$\langle\sigma_{exp}\rangle$	exp. err.	$\langle\sigma_A/\sigma_{Rb}\rangle_{th}$	std. dev. (5)
Na	**100.7**	0.5	100.7	0.5 (2)	0.568	0.104
K	**158.3**	6.3	171.2	21.8 (2)	0.906	0.019
Rb	**173.5**	6.6	173.5	6.6 (5)	-	-
Cs	**186.2**	8.0	183.3	9.7 (3)	1.108	0.062
	Å^2	Å^2	Å^2	Å^2		

Table A.1: Alkali-Alkali Spin Exchange Cross Section in Å^2 at $T = 200\,^{\circ}\text{C} = 473.15\,\text{K}$. All values are averaged and scaled from [7] with the addition of a new measurement for Rb from [8]. The number in parenthesis refers to the numbers of values used to calculate the each weighted average. The uncertainties on the experimental values are those originally quoted by the authors. The final column is the standard deviation of the ratios from theoretical calculations.

A.1.2 Spin Destruction

The alkali-alkali spin destruction rate constants are estimated by:

$$A_{sd}^{ab} = \bar{v}\sqrt{\sigma_{sd}^a \sigma_{sd}^b} = \left[\frac{1\text{ kHz}}{10^{15}/\text{cm}^3}\right]\sqrt{\left[\frac{\sigma_{se}^a}{0.1\text{Å}^2}\right]\left[\frac{\sigma_{se}^b}{0.1\text{Å}^2}\right]\left[\frac{10\text{ g/mol}}{M_a} + \frac{10\text{ g/mol}}{M_b}\right]} \quad (A.2)$$

where σ_{se} is the alkali-alkali spin exchange cross section and $\bar{v}$ is the relative mean thermal velocity of the alkali-alkali pair, and M_a & M_b are the molecular weights of the two alkali atoms involved in the collision. The A-A spin destruction rate constant is assumed to be independent of temperature. All measurements have observed a (mostly) linear increase in relaxation rate with respect to the alkali density. Therefore the cross section must have a $1/\sqrt{T}$ temperature dependence.

The observed alkali-alkali spin destruction rate is written as [13]

$$k_{obs} = k_{sd}/s = k_a + \left(\frac{k_b^0}{1 + B/B_D}\right)\left(\frac{[A]}{10^{15}\text{ cm}^{-3}}\right)^n \quad (A.3)$$

where k_a is the magnetic field independent part due to binary collisions, k_b is the field dependent part that is due to singlet and triplet alkali dimers, B_D is the magnetic decoupling width, n is a small next to leading order alkali power dependence, and $[A]$ is the alkali number density.

	k_a	k_b^0	B_D	n	$[A]_{\text{max}}$	$\langle k_b \rangle$	s	$s\,(k_a + \langle k_b \rangle)$	ref.
K	7.5E-15	8.2E-15	230	1/4	2.0	7.80E-15	6	9.18E-14	[13]
Rb	1.5E-14	2.6E-14	1150	1/4	2.5	2.62E-14	10.8	4.45E-13	[13]
Rb	1.50E-14	2.88E-14	1150	0	2.5	2.88E-14	10.8	4.74E-13	[78]
Cs	1.9E-13	1.8E-13	2900	0	0.78	1.80E-13	22	8.14E-12	[13]
	cm^3/s	cm^3/s	gauss		$10^{15}\ \text{cm}^{-3}$	cm^3/s		cm^3/s	

Table A.2: Kadlecek Measurements of Alkali-Alkali Spin Destruction Magnetic Decoupling Parameters.

For $B \ll 230$ Gauss, the spin destruction cross section is obtained by

$$\sigma_{\text{sd}} = k_{\text{sd}}/\bar{v} = s(k_a + k_b)/\bar{v} \tag{A.4}$$

where s is the nuclear slowing down factor and $\bar{v}$ is the mean relative velocity:

$$\bar{v} = \sqrt{\frac{8RT}{\pi}\left(\frac{1}{M_a} + \frac{1}{M_b}\right)} \tag{A.5}$$

where $R = 8.314472$ J/mol/K is the ideal gas constant, T is the temperature in Kelvin, and $M_{a,(b)}$ are the molecular weights in kg/mol. For k_b values from [13], we average over [A] and multiply by k_B^0 to get an effective k_b:

$$\langle k_b \rangle = k_b^0 \frac{([A]_{\text{max}}/10^{15}\ \text{cm}^{-3})^n}{1 + n} \tag{A.6}$$

A.2 Alkali-Buffer Gas Collisions

A.2.1 Spin Exchange with He-3 Nuclei

The ^{3}He polarization evolution is given as:

$$P_{\text{He}}(t) = P_A k_{\text{se}}[A]\tau\left(1 - \exp(-t/\tau)\right) \tag{A.7}$$

	Mass (amu)	**Abd.**	I	μ (μ_N)	g_I	$\epsilon(I,P_A)$ $P_A=0$	$\epsilon(I,P_A)$ $P_A=1$	$s=1+\epsilon$ $P_A=0$	$s=1+\epsilon$ $P_A=1$
Li	6.941					4.823	2.924	5.823	3.924
^{6}Li	6.0151223	0.0759	1	+0.822056	+0.822056	8/3	2	11/3	3
^{7}Li	7.0160040	0.9241	3/2	+3.25644	+2.17096	5	3	6	4
Na	22.989770					5	3	6	4
^{23}Na	22.9897697	1.0	3/2	+2.21752	+1.47835	5	3	6	4
K	39.0983					5.003	3.001	6.003	4.001
^{39}K	38.9637069	0.93258	3/2	+0.39146	+0.26097	5	3	6	4
^{40}K	39.9639987	0.000117	4	−1.298	−0.3245	80/3	8	83/3	9
^{41}K	40.9618260	0.06730	3/2	+0.21487	+0.14325	5	3	6	4
Rb	85.4678					9.811	4.443	10.81	5.443
^{85}Rb	84.911789	0.7217	5/2	+1.35302	+0.541208	35/3	5	38/3	6
^{87}Rb	86.909184	0.2783	3/2	+2.7512	+1.8341	5	3	6	4
Cs	132.90545					21	7	22	8
^{133}Cs	132.905447	1.0	7/2	+2.579	+0.7369	21	7	22	8

Table A.3: Alkali Isotopic & Nuclear Data. $\epsilon(I, P_A)$ is the paramagnetic coefficient and s is the nuclear slowing down factor. For $P_A = 0$, $\epsilon = 4I(I+1)/3$ and for $P_A = 1$, $\epsilon = 2I$.

	$\langle\sigma_{sd}\rangle$	σ_{sd}	measurement	value	rel. err.	reference
Na	**0.00557**	0.0056	k_{sd}	5.2E-14	0.08	[79]
K	**0.0128**	0.0128	k_a, k_b	(7.5,8.2)E-15	0.10	[13]
		0.0112	σ_{rms} (500 K)	1.00E-18	0.10	[14], *superseded by* [13]
		0.0255	$\bar{\sigma}$ (533 K)	2.4E-18	0.08	[9], *no density measurement*
Rb	**0.0994**	0.0919	k_a, k_b	(1.5,2.6)E-14	0.10	[13]
		0.0978	k_a, k_b	(1.50,2.88)E-14	0.10	[78], *superseded by* [13]
		0.0871	k_{sd}/s	3.9E-14	0.10	[35]
		0.1675	k_{sd}	8.11E-13	0.04	[80]
		0.1714	k_{sd}	8.3E-13	0.07	[10], *large* Rb-^{3}He *contribution*
		0.1583	$\bar{\sigma}$ (463 K)	1.6E-17	0.13	[9], *no density measurement*
Cs	**2.08**	2.0965	k_a, k_b	(1.9,1.8)E-13	0.10	[13]
		2.0300	$\bar{\sigma}$ (473 K)	2.03E-16	0.20	[81]
	Å^2	Å^2	k in cm^3/s, σ in cm^2			

Table A.4: Alkali-Alkali Spin Destruction Cross Section in Å^2 at $T = 200\,°C = 473.15\,K$. The relative uncertainties are those originally quoted by the authors. All values, except those in *italics*, are used in the weighted mean. The final uncertainty for each value is about 10%. Only measurements where the alkali density was measured independently was used, thereby ruling out [9]. Measurement [10] is not included because the large temperature dependent Rb-^{3}He spin relaxation rate was not accounted for and could lead to error as large as 50%.

where P_A is the volume average alkali polarization, k_{se} is the spin exchange rate constant, $[A]$ is the alkali number density, and τ^{-1} is the total ^{3}He relaxation rate. These are related to the isotropic spin exchange k_{iso} and anisotropic spin exchange k_{ani} rate constants as:

$$k_{se} = k_{iso} - k_{ani}/2 \tag{A.8}$$

$$1/\tau = 1/\tau_0 + k_{se}[A](1 + X) \tag{A.9}$$

where $1/\tau_0$ is the ^{3}He relaxation rate that is independent of the alkali density and X accounts for an extra alkali density/temperature dependent relaxation mechanism. If X was completely due to anisotropic spin exchange, then it is given by:

$$X_{ani} = \frac{3k_{ani}/(2k_{iso})}{1 - k_{ani}/(2k_{iso})} \tag{A.10}$$

When the laser is turned off, the alkali polarization reaches approaches a new equilibrium due to spin exchange with ^{3}He given by:

$$P_A(t) = P_{He}(t)k_{se}[^3He]\tau_A/s\,(1 - \exp(-t/\tau_A)) \tag{A.11}$$

where $[^3He]$ is the ^{3}He number density, τ_A^{-1} is the observed A relaxation rate, and s is the nuclear slowing down factor. The rate constants can be obtained by:

$$k_{rate} = \frac{P_{He}^\infty}{P_A[A]\tau} = \frac{(dP_{He}/dt|_{t=0})}{P_A[A]} = k_{se} \tag{A.12}$$

$$k_{repol} = \frac{sP_A^\infty}{P_{He}[^3He]\tau_A} = \sqrt{\frac{s\,(dP_A/dt|_{t=0})}{[^3He][A]P_A\tau_A}} = k_{se} \tag{A.13}$$

$$k_{relax} = \frac{1 - \tau/\tau_0}{[A]\tau} = k_{se}(1 + X) \tag{A.14}$$

The rate constant is been found to be temperature independent [35, 64, 79].

	k_{se}	$1/\langle k_{se}\rangle$	$\langle k_{se}\rangle$	rel. err.	$\langle k_{exp}\rangle$	rel. err.	$\langle k_{th}\rangle$	std. dev.
Na	**4.74**	5.86	1.27	0.1	6.10	0.10	3.76	0.13
K	**5.15**	5.39	1.38	0.031	5.04	0.033	6.27	0.08
Rb	**6.74**	4.12	1.81	0.025	6.74	0.025		
Cs	**11.1**	2.51	2.97	0.1	13.6	0.10	9.18	0.12
	$10^{-20}\,\mathrm{cm^3/s}$	$\mathrm{hrs\cdot10^{15}/cm^3}$	Hz/amg		$10^{-20}\,\mathrm{cm^3/s}$		$10^{-20}\,\mathrm{cm^3/s}$	

Table A.5: Alkali-^{3}He Spin Exchange Rate Constant. The experimental values are the weighted average from Tab. A.7. The theoretical values are obtained from the theoretical ratio to Rb from Tab. (A.6) and the experimental value for Rb.

	$\langle k^{A}_{iso}/k^{Rb}_{iso}\rangle$	$\bar{\sigma}_{iso}\times10^8$	$k_{iso}\times10^{20}$	$k_{iso}\times10^{20}$	k_{ani}/k_{iso}	X_{ani}	$k_{iso}\times10^{20}$
Na	0.56	1.2	21	2.3	0.100	0.158	6.7
K	0.93	2.1	35	4.9	0.037	0.057	9.0
Rb		2.1	35	5.6	0.030	0.046	10
Cs	1.36	2.7	44	8.1	0.017	0.026	
		$\mathrm{\AA^2}$	$\mathrm{cm^3/s}$	$\mathrm{cm^3/s}$			$\mathrm{cm^3/s}$
		[82] (100 °C)		[83] (190 °C)			[11] (200 °C)

Table A.6: Alkali-^{3}He Spin Exchange Rate Constant Parameters from Theory. The rate constants from [11] were scaled to $473.15\,\mathrm{K}$ by $T^{1.275}$ using a parameterization of the temperature dependence based on their calculations.

	k_{se}	err.	ref.	method
Na	6.1	0.6	[79]	repolarization
K	5.5	0.2	[49]	rate/repolarization
K	*6.1*	0.4	[36]	*superseded by* [49]
K	4.0	0.3	[84]	relaxation
Rb	6.5	0.4	[84]	relaxation
Rb	6.8	0.2	[64]	rate/repolarization
Rb	6.7	0.6	[35]	repolarization
Rb	*6.1*	0.2	[10]	*relaxation*
Rb	*12.0*	2.0	[17]	*relaxation*
Cs	13.6	1.3	[84]	relaxation
	$10^{-20}\,\mathrm{cm^3/s}$			

Table A.7: Measurements of Alkali-^{3}He Spin Exchange Rate Constant. All values, except those in *italics,* are used in the weighted mean. There are three general methods for extraction the spin exchange rate: "Repolarization" refers to measuring the alkali polarization due to spin exchange with ^{3}He with no optical pumping; "Rate" refers to measuring the equilibrium ^{3}He polarization, A polarization, and ^{3}He spin up time constant; "Relaxation" refers to measuring the ^{3}He relaxation when the cell is hot and with the lasers off. In all cases, the A density is needed to extract the rate constant. The first two methods measure k_{se} while the last method measures $k_{se}(1+X)$. For this reason, older relaxation method measurements are not included in the final average.

	k_{473}	err.	quantity	value	temp.	notes
Na	**0.15**	**0.05**				
	0.23	0.13	$k_{se} + k_{sd}$	$(8 \pm 1) \times 10^{-20}\,\mathrm{cm^3/s}$	600	[79]
	0.11	0.01	k_{se}^{Na}/k_{se}^{Rb}	0.0020 ± 0.0002	473.15	Tab. A.9
K	**4.7**	**0.3**				
	12	1	$k_{sd}/\bar{v}$	$(8.0 \pm 0.8) \times 10^{-25}\,\mathrm{cm^2}$	325	for ^{4}He, [85]
	3.5	0.3	k_{sd}	$(8.9 \pm 0.9) \times 10^{-20}\,\mathrm{cm^3}/s$	423	rescaled from ^{4}He, [86]
	4.9	0.5	k_{se}^{K}/k_{se}^{Rb}	0.088 ± 0.009	473.15	Tab. A.9
Rb	**55.9**	**0.9**				fit to Tab. A.10
Cs	**530**	**30**				
	490	50	$k_{sd}/\bar{v}$	$(2.43 \pm 0.24) \times 10^{-23}\,\mathrm{cm^2}$	288	for ^{4}He, [87]
	550	50	$k_{sd}/\bar{v}$	$(2.8 \pm 0.3) \times 10^{-23}\,\mathrm{cm^2}$	290	for ^{4}He, [88]
	560	60	k_{se}^{Cs}/k_{se}^{Rb}	10 ± 1	473.15	Tab. A.9
	Hz/amg					

Table A.8: Alkali-^{3}He Spin Destruction Rate Constant. For measurements made on ^{4}He, the rate constants are rescaled by the square root of the ratio of reduced masses. All values are rescaled to 473.15 K using the Rb temperature scaling of $T^{3.31}$. Values from theoretical calculations are scaled relative to the experimental value for Rb.

A.2.2 Spin Destruction Due to He Atoms

The spin destruction rate constant for A-^{3}He collisions has a temperature dependence given by:

$$k_{sd}(T) = k_{473} \left(\frac{T}{473.15\,\mathrm{K}} \right)^n \tag{A.15}$$

From a fit of world data (Tab. A.10) for Rb-^{3}He collisions, we find $k_{473} = (55.9 \pm 0.9)$ Hz/amg and $n = 3.31 \pm 0.12$. We'll assume that the rate constants for all other alkali have the same temperature dependence.

A.2.3 Spin Destruction Due to Nitrogen Molecules

The spin destruction rate constant for A-N$_2$ collisions has a temperature dependence given by:

$$k_{sd}(T) = k_{473} \left(\frac{T}{473.15\,\mathrm{K}} \right)^n \tag{A.16}$$

	T	$\bar{\sigma}_{\mathrm{sd}}$	k_{sd} (at 473.15)	$k_{\mathrm{sd}}^{\mathrm{A}}/k_{\mathrm{sd}}^{\mathrm{Rb}}$
Na	428.15	1.2	0.083	0.0020
K	459.15	65	3.6	0.088
Rb	459.15	750	41	
Cs	423.15	6000	406	10
	K	$10^{-10}\,\text{Å}^2$	Hz/amg	

Table A.9: Theoretical Estimate for Spin Destruction in A-^{3}He Pairs Due to the Spin-Rotation Interaction. Calculations are from [12]. Based on the experimental data for K, Rb, and Cs, the uncertainty is estimated to be about 10%. The rate constant is rescaled to 473.15 K using the Rb temperature scaling of $T^{3.31}$.

T	k_{sd}	quantity	value	notes
305	12.40	$k_{\mathrm{sd}}/\bar{v}$	3.1E-24 cm^2	for ^{4}He, [89]
363	22.80	$\Gamma_{\mathrm{sd}} + \Gamma_{\mathrm{se}}$	278 Hz	[^{3}He] = 11.3 amg, [90]
378	24.03	$k_{\mathrm{sd}} + k_{\mathrm{se}}$	0.96E-18 cm^3/s	[35]
383	28.02	$\Gamma_{\mathrm{sd}} + \Gamma_{\mathrm{se}}$	337 Hz	[^{3}He] = 11.3 amg, [90]
383	22.90	$k_{\mathrm{sd}} + k_{\mathrm{se}}$	0.92E-18 cm^3/s	[35]
393	28.81	$k_{\mathrm{sd}} + k_{\mathrm{se}}$	1.14E-18 cm^3/s	[35]
403	33.24	$\Gamma_{\mathrm{sd}} + \Gamma_{\mathrm{se}}$	396 Hz	[^{3}He] = 11.3 amg, [90]
403	33.06	$k_{\mathrm{sd}} + k_{\mathrm{se}}$	1.30E-18 cm^3/s	[35]
413	36.03	$k_{\mathrm{sd}} + k_{\mathrm{se}}$	1.41E-18 cm^3/s	[35]
418	36.53	$k_{\mathrm{sd}} + k_{\mathrm{se}}$	1.43E-18 cm^3/s	[35]
423	38.47	$\Gamma_{\mathrm{sd}} + \Gamma_{\mathrm{se}}$	455 Hz	[^{3}He] = 11.3 amg, [90]
423	41.58	$k_{\mathrm{sd}} + k_{\mathrm{se}}$	1.61E-18 cm^3/s	[35]
428	40.15	$k_{\mathrm{sd}} + k_{\mathrm{se}}$	1.56E-18 cm^3/s	[35]
433	43.61	$k_{\mathrm{sd}} + k_{\mathrm{se}}$	1.69E-18 cm^3/s	[35]
438	44.99	$k_{\mathrm{sd}} + k_{\mathrm{se}}$	1.74E-18 cm^3/s	[35]
443	48.81	$k_{\mathrm{sd}} + k_{\mathrm{se}}$	1.88E-18 cm^3/s	[35]
520	73.90	$k_{\mathrm{sd}}/v_{\mathrm{rms}}$	1.3E-13 cm^2	for ^{4}He, [13]
K	Hz/amg			

Table A.10: Rb-^{3}He Spin Destruction Rate Constant vs. Temperature. Each measurement has an uncertainty of about 10%.
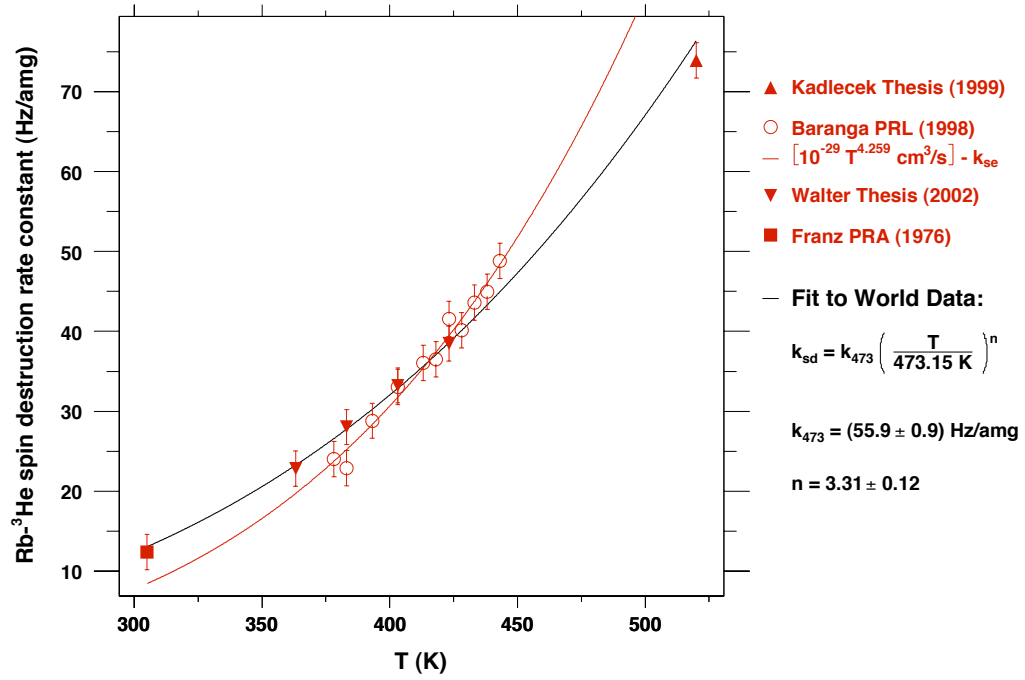
Figure A.1: Fit to Rb-^{3}He Spin Destruction Rate Constant World Data.

From a weighted mean of the two fits of the world data (Tab. A.12) for Rb-N$_2$ collisions, we find $k_{473} = (290 \pm 30)$ Hz/amg and $n = 2.00 \pm 0.25$. We'll assume that the rate constants for all other alkali have the same temperature dependence.

	k_{473}	err.	quantity	value	temp.	notes
Na	**150?**					no data, set to K value
K	**150**	**50**				
	200	20	$k_{\rm sd}/v_{\rm rms}$	$(7.9 \pm 0.8) \times 10^{-23}\,{\rm cm}^2$	437	[14]
Rb	**290**	**30**	$(n = 2.00 \pm 0.25)$			
	266	3	$(n = 1.74 \pm 0.06)$			fit to Tab. A.12 w/o [13]
	390	40	$(n = 3.29 \pm 2.00)$			fit to [13] data in Tab. A.12
Cs	**2100**	**200**				
	2050	110	$k_{\rm sd}/\bar{v}$	$(5.52 \pm 0.55) \times 10^{-22}\,{\rm cm}^2$	288	[87]
	2210	110	$k_{\rm sd}/\bar{v}$	$(6.00 \pm 0.44) \times 10^{-22}\,{\rm cm}^2$	290	[88]
	Hz/amg					

Table A.11: Alkali-N_2 Spin Destruction Rate Constant. The Rb mean values come from weighted average of the two fits weighted by the number of distinct temperature points for each set. All values are rescaled to 473.15 K using the Rb temperature scaling of T^2. The Rb values from [13] are significantly larger that the data. Since the K value is from [14] which is a similar measurement of the Rb values from [13], the K value is rescaled to the mean Rb value.

T	$k_{\rm sd}$	quantity	value	notes
300	118.06	$k_{\rm sd}/\bar{v}$	8.0E-23 cm^2	[91]
305	123.41	$k_{\rm sd}/\bar{v}$	8.3E-23 cm^2	[89]
363	173.08	$\Gamma_{\rm sd}$	703 Hz	[N_2] = 4.07 amg, [90]
363	162.31	$\Gamma_{\rm sd}$	1244 Hz	[N_2] = 7.68 amg, [90]
383	185.01	$\Gamma_{\rm sd}$	1418 Hz	[N_2] = 7.68 amg, [90]
393	196.47	$\Gamma_{\rm sd}$	798 Hz	[N_2] = 4.07 amg, [90]
403	203.02	$\Gamma_{\rm sd}$	1556 Hz	[N_2] = 7.68 amg, [90]
423	220.60	$\Gamma_{\rm sd}$	896 Hz	[N_2] = 4.07 amg, [90]
423	221.94	$\Gamma_{\rm sd}$	1701 Hz	[N_2] = 7.68 amg, [90]
463	252.04	$k_{\rm sd}$	(9.38 ± 0.22)E-18 cm^3/s	[80]
480	404.90	$k_{\rm sd}/v_{\rm vrms}$	2.0E-22 cm^2	[13]
500	*419.50*	$\Gamma_{\rm sd}/s$	(21.2 ± 0.1) Hz	$p_{N_2} = 760\ torr,\ [78],\ superseded\ by\ [13]$
520	526.80	$k_{\rm sd}/v_{\rm vrms}$	2.5E-22 cm^2	[13]
K	Hz/amg			

Table A.12: Alkali-N_2 Spin Destruction Rate Constant. All values have a 10% uncertainty unless otherwise noted.
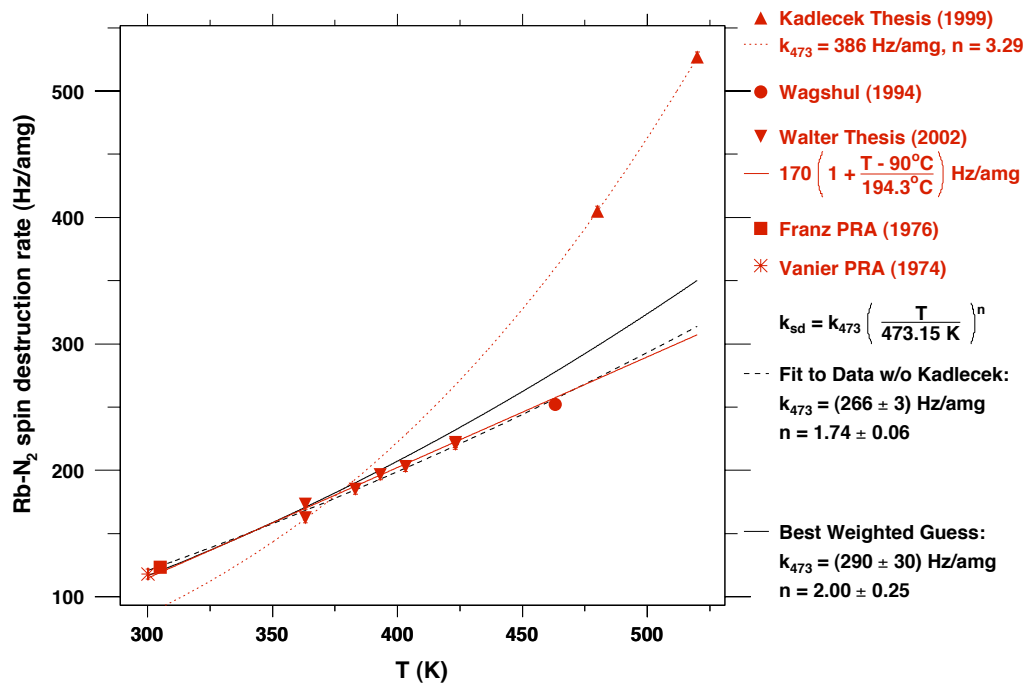
Figure A.2: Fit to Rb-N$_2$ Spin Destruction Rate Constant World Data.

Appendix B

Wigner-Eckart Theorem

Fig. (B.1) shows the six nonvanishing matrix elements in Eqn.(4.56). The Wigner-
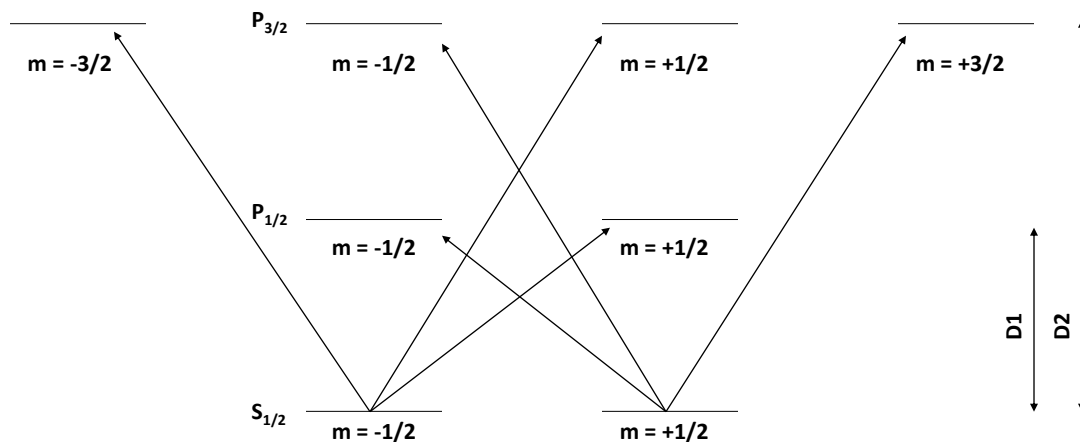
Figure B.1: Dipole Transitions Allowed by Selection Rules

Eckart Theorem separates the radial dependence of a matrix element from its azimuthal component. It can be used to evaluate the six matrix elements,

$$\langle n_f j_f m_f | T_k^q | n_i j_i m_i \rangle = \langle n_f j_f || T_k || n_i j_i \rangle \frac{\langle j_f m_f | k q, j_i m_i \rangle}{\sqrt{2j_f + 1}} \tag{B.1}$$

The first term (the so called double barred term) can be evaluated in terms of the empirically measured Einstein A coefficient. The second term is a Clebsch-Gordan

coefficient. For us, the irreducible spherical vector tensor, T_k^q comes from $Re[\delta\alpha]$ (see Eqn.(4.23) and Eqn.(4.56)). Since $\delta\alpha = \alpha_L - \alpha_R$, our spherical vector will have the form

$$T_k^q \approx T_1^{-1} - T_1^1. \tag{B.2}$$

B.1   Clebsch Gordan Coefficients

The notation $\langle j_f m_f | kq, j_i m_i \rangle$ can be somewhat confusing. It can be interpreted as a system with total angular momentum j_f, azimuthal state m_f, which is composed of a linear combination of angular momentum states. One of these constituent states happens to be the state $|kq, j_i m_i\rangle$ or, as I prefer to write it, $|kq\rangle|j_i m_i\rangle$. As an example, consider a system which is composed of a spin one particle and a spin one half particle. Their normalized highest state will be

$$|\frac{3}{2}\frac{3}{2}\rangle = |11\rangle|\frac{1}{2}\frac{1}{2}\rangle. \tag{B.3}$$

If we apply the angular momentum lowering operator J_-,

$$J_-|j, m\rangle = \hbar\sqrt{j(j+1) - m(m-1)}|j, m-1\rangle \tag{B.4}$$

$$\hbar\sqrt{3}|\frac{3}{2}\frac{1}{2}\rangle = \hbar\sqrt{2}|10\rangle|\frac{1}{2}\frac{1}{2}\rangle + \hbar|11\rangle|\frac{1}{2} - \frac{1}{2}\rangle \tag{B.5}$$

$$|\frac{3}{2}\frac{1}{2}\rangle = \underbrace{\sqrt{\frac{2}{3}}}_{C_1}|10\rangle|\frac{1}{2}\frac{1}{2}\rangle + \underbrace{\frac{1}{\sqrt{3}}}_{C_2}|11\rangle|\frac{1}{2} - \frac{1}{2}\rangle \tag{B.6}$$

we get our first set of non-trivial Clebsch Gordon (CG) coefficients. Explicitly,

$$C_1 = \sqrt{\frac{2}{3}} = \langle\frac{3}{2}\frac{1}{2}|10, \frac{1}{2}\frac{1}{2}\rangle. \tag{B.7}$$

Next, since states with different j's are orthogonal ($\langle\frac{3}{2}\frac{1}{2}|\frac{1}{2}\frac{1}{2}\rangle = 0$), we can find the $|\frac{1}{2}\frac{1}{2}\rangle$ states.

$$|\frac{1}{2}\frac{1}{2}\rangle = A|10\rangle|\frac{1}{2}\frac{1}{2}\rangle + B|11\rangle|\frac{1}{2} - \frac{1}{2}\rangle \tag{B.8}$$

$$\langle\frac{3}{2}\frac{1}{2}|\frac{1}{2}\frac{1}{2}\rangle = 0 \tag{B.9}$$

$$\frac{1}{\sqrt{3}}A + \sqrt{\frac{2}{3}}B = \tag{B.10}$$

$$A = -\sqrt{2}B \tag{B.11}$$

Second, we'll normalize the coefficients.

$$|A|^2 + |B|^2 = 1 \tag{B.12}$$

$$B = \pm\frac{1}{\sqrt{3}} \tag{B.13}$$

Since A is the coefficient of the state with highest azimuthal quantum number of the highest total angular momentum (that is, since it has the state $|11\rangle$), we'll follow the Condon-Shortley convention and force it positive (that is, we'll pick the *negative* root for B). Finally,

$$|\frac{1}{2}\frac{1}{2}\rangle = \underbrace{-\sqrt{\frac{1}{3}}}_{C_3}|10\rangle|\frac{1}{2}\frac{1}{2}\rangle + \underbrace{\frac{2}{\sqrt{3}}}_{C_4}|11\rangle|\frac{1}{2} - \frac{1}{2}\rangle \tag{B.14}$$

C_4 is the C-G coefficient that drives the left circularly polarized (α_L) D1 transition. The six relevant C-G coefficients are

$$\langle \frac{1}{2}\frac{1}{2}|11, \frac{1}{2} - \frac{1}{2}\rangle = \sqrt{\frac{2}{3}} \tag{B.15}$$

$$\langle \frac{1}{2} - \frac{1}{2}|1 - 1, \frac{1}{2}\frac{1}{2}\rangle = -\sqrt{\frac{2}{3}} \tag{B.16}$$

$$\langle \frac{1}{2}\frac{1}{2}|1 - 1, \frac{3}{2}\frac{3}{2}\rangle = \frac{1}{\sqrt{2}} \tag{B.17}$$

$$\langle \frac{1}{2}\frac{1}{2}|11, \frac{3}{2} - \frac{1}{2}\rangle = \frac{1}{\sqrt{6}} \tag{B.18}$$

$$\langle \frac{1}{2} - \frac{1}{2}|11, \frac{3}{2} - \frac{3}{2}\rangle = \frac{1}{\sqrt{2}} \tag{B.19}$$

$$\langle \frac{1}{2} - \frac{1}{2}|1 - 1, \frac{3}{2}\frac{1}{2}\rangle = \frac{1}{\sqrt{6}}. \tag{B.20}$$

The top two coefficients are D1 transitions; the bottom four are D2. Other coefficients that will be useful in evaluating the double barred matrix element are

$$\langle \frac{1}{2}\frac{1}{2}|10, \frac{1}{2}\frac{1}{2}\rangle = -\frac{1}{\sqrt{3}} \tag{B.21}$$

$$\langle \frac{1}{2} - \frac{1}{2}|10, \frac{1}{2} - \frac{1}{2}\rangle = \frac{1}{\sqrt{3}} \tag{B.22}$$

$$\langle \frac{1}{2}\frac{1}{2}|10, \frac{3}{2}\frac{1}{2}\rangle = -\frac{1}{\sqrt{3}} \tag{B.23}$$

$$\langle \frac{1}{2} - \frac{1}{2}|10, \frac{3}{2} - \frac{1}{2}\rangle = -\frac{1}{\sqrt{3}} \tag{B.24}$$

B.2 Evaluating the Double Barred Matrix Element

The radial integral is difficult to calculate exactly for a hydrogen atom and much harder for a heavy alkali atom. As such, it is typically inferred from empirical data on decay rates (specifically the Einstein A coefficient).

$$A_{j_f,j_i} = \frac{e^2}{3\pi\epsilon_0\hbar c^3} \frac{\omega_{fi}^3}{2j_f + 1} \sum_{m_f,m_i} |\langle j_f m_f|r|j_i m_i\rangle|^2. \tag{B.25}$$

These rates can in turn be related to the quantum mechanical oscillator strength,

$$f_{j_f,j_i} = -\frac{2m}{3\hbar}\frac{\omega_{fi}}{2j_f+1}\sum_{m_f,m_i}|\langle j_f m_f|r|j_i m_i\rangle|^2 \tag{B.26}$$

$$f_{j_i,j_f} = \frac{2m}{3\hbar}\frac{\omega_{fi}}{2j_i+1}\sum_{m_f,m_i}|\langle j_f m_f|r|j_i m_i\rangle|^2. \tag{B.27}$$

(For a full derivation, see Atomic and Laser Spectroscopy by Alan Corney [92]). The top equation gives the oscillator strength for spontaneous decay, while the bottom equation is for optical pumping. The values for the relevant oscillator strengths are well known [30]; within a few percent, they are

$$f_{\frac{3}{2}} \approx \frac{2}{3} \tag{B.28}$$

$$f_{\frac{1}{2}} \approx \frac{1}{3} \tag{B.29}$$

If we apply the Wigner-Eckart theorem to Eqn.(B.27),

$$f_{j_i,j_f} = \frac{2m}{3\hbar}\frac{\omega_{fi}}{(2j_i+1)^2}|\langle j_i||r||j_f\rangle|^2 \sum_{m_f,m_i,q}|\langle j_f m_f|1q,j_i m_i\rangle|^2\delta(m_f = q+m_i) \tag{B.30}$$

where the delta function has been imposed by the dipole selection rules. With the help of the previously calculated CG coefficients,

$$f_{\frac{1}{2}} = \frac{2m}{3\hbar}\frac{\omega_{D1}}{4}|\langle S_{1/2}||r||P_{1/2}\rangle|^2\left(2\left(\frac{2}{3}+\frac{1}{3}+\frac{1}{2}\right)\right) \tag{B.31}$$

$$= \frac{m\omega_{D1}}{3\hbar}|\langle S_{1/2}||r||P_{1/2}\rangle|^2 \tag{B.32}$$

$$f_{\frac{3}{2}} = \frac{2m}{3\hbar}\frac{\omega_{D2}}{4}|\langle S_{1/2}||r||P_{3/2}\rangle|^2\left(2\left(\frac{1}{6}+\frac{1}{3}+\frac{1}{2}\right)\right) \tag{B.33}$$

$$= \frac{m\omega_{D2}}{3\hbar}|\langle S_{1/2}||r||P_{3/2}\rangle|^2. \tag{B.34}$$

Finally, we can invert to solve for the radial matrix element

$$|\langle S_{1/2}||r||P_{1/2}\rangle|^2 \;\; = \;\; \frac{\hbar}{m\omega_{D1}} \tag{B.35}$$

$$|\langle S_{1/2}||r||P_{3/2}\rangle|^2 \;\; = \;\; \frac{2\hbar}{m\omega_{D2}} \tag{B.36}$$

Appendix C

Optics

C.1 Waveplates

A waveplate is an object with different indices of refraction along two orthogonal axes. Because of the two different indices, one of the perpendicular components will travel through the waveplate slower and accumulate a phase (called the retardance).

Waveplates are described in terms of the Jones matrix, T. In particular, if a waveplate has its fast axis oreinted horizontally,

$$T = \begin{pmatrix} 1 & 0 \\ 0 & e^{-i\Gamma} \end{pmatrix},$$

where Γ is the retardance that is accumulated along the slow axis. Explicitly,

$$\Gamma = \delta k(t)l = \frac{2\pi l}{\lambda}\delta n. \tag{C.1}$$

If the polarization vector of the incident light is not parallel with the fast axis of the waveplate (see Fig. C.1), a coordinate rotation needs to be performed on the Jones matrix. For a waveplate oriented at an angle θ to the incident light, the following

rotation is performed,

$$T' = R(-\theta)TR(\theta) \tag{C.2}$$

where

$$R = \begin{pmatrix} \cos\theta & \sin\theta \\ -\sin\theta & \cos\theta \end{pmatrix}.$$
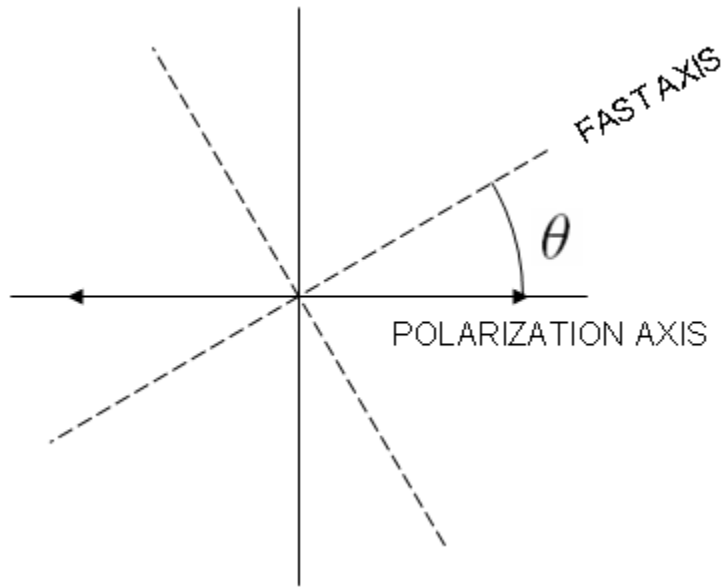
Figure C.1: Coordinate Rotation

C.1.1 Quarter-Wave Plate

A quarter-wave plate (QWP) has a retardance of $\frac{1}{4}(2\pi)$. When oreinted with its fast axis at $45°$ to the incident polarization axis, a QWP can convert linear light to circular and vice versa. The transformed Jones matrix for a QWP at $45°$ is

$$T' = \frac{1}{\sqrt{2}}e^{-i\pi/4}\begin{pmatrix} 1 & i \\ i & 1 \end{pmatrix}.$$

C.1.2   Half-Wave Plate

A half-wave plate (HWP) has a retardance of $\frac{1}{2}(2\pi)$. When oreinted with its fast axis at an angle θ to the incident polarization axis, the transformed Jones matrix is

$$T' = \begin{pmatrix} \cos(2\phi) & \sin(2\phi) \\ \sin(2\phi) & -\cos(2\phi) \end{pmatrix}.$$

A HWP at any angle will interchange left and right circular polarizations; additionally, it will mirror linear polarization about its fast axis (See Fig. C.2).
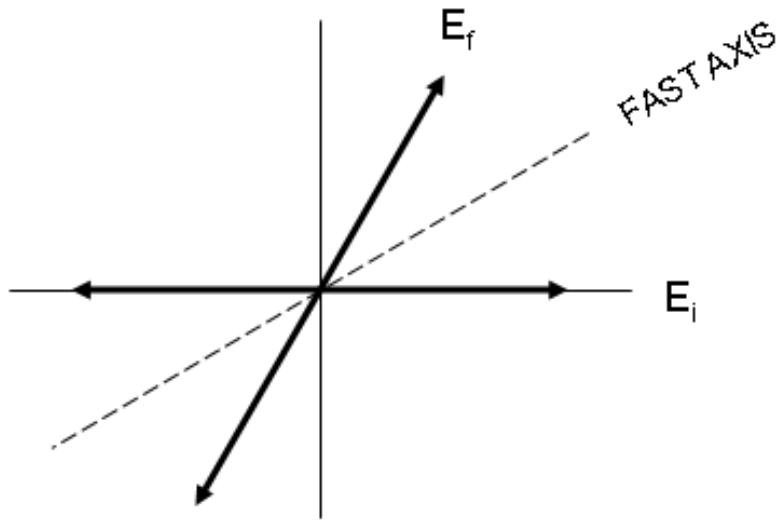
Figure C.2: Half-Wave Plate

C.2   Using a Half-Wave Plate to Cancel Unwanted Rotation

A half-wave performs the following rotation on light,

$$\begin{pmatrix} E_x^f \\ E_y^f \end{pmatrix} = \begin{pmatrix} \cos 2\phi_h & \sin 2\phi_h \\ \sin 2\phi_h & -\cos 2\phi_h \end{pmatrix} \begin{pmatrix} E_x^i \\ E_y^i \end{pmatrix}, \tag{C.3}$$

where ϕ_h refers to the angle the fast axis makes with the polarization vector. If the initial light is rotated at an angle

$$\phi_i = \phi_r + \phi_{misc}, \tag{C.4}$$

Eqn.(C.3) reads

$$\begin{pmatrix} E_x^f \\ E_y^f \end{pmatrix} = E_i \begin{pmatrix} \cos 2\phi_h & \sin 2\phi_h \\ \sin 2\phi_h & -\cos 2\phi_h \end{pmatrix} \begin{pmatrix} \cos \phi_i \\ \sin \phi_i \end{pmatrix} \tag{C.5}$$

$$= E_i \begin{pmatrix} \cos 2\phi_h \cos \phi_i + \sin 2\phi_h \sin \phi_i \\ \sin 2\phi_h \cos \phi_i - \cos 2\phi_h \sin \phi_i \end{pmatrix} \tag{C.6}$$

$$= E_i \begin{pmatrix} \cos (2\phi_h - \phi_i) \\ \sin (2\phi_h - \phi_i) \end{pmatrix} \tag{C.7}$$

$$= E_i \begin{pmatrix} \cos \Phi \\ \sin \Phi \end{pmatrix} \tag{C.8}$$

where

$$\Phi = 2\phi_h - \phi_{misc} - \phi_r. \tag{C.9}$$

Eq.Making the substituation $\phi_r \rightarrow \Phi$, Eq. 4.85 becomes

$$\frac{\Delta}{\Sigma} = \frac{\cos 2\Phi}{\cosh (2\beta_r)}. \tag{C.10}$$

C.3   Photoelastic Modulators

A Photoelastic Modulator (PEM) contains an optically transparent glass which is vibrated longitudinally by a piezoelectric transducer. The glass is stressed and consequently exhibits birefrengence via the photoelastic effect. The amount of birefrengence is directly proportional to the width of the glass (l) and the amplitude of the modulation. This modulation is given by the phase difference (Γ) of the orthogonal

states of polarization

$$\Gamma(t) = \delta k(t) l = \frac{2\pi l}{\lambda} \delta n \sin(\gamma t). \tag{C.11}$$

This phase difference is the retardance; a PEM set to $\frac{\pi}{2}$ retardance will act as a half-wave plate (See see Appendix C.1). We employ a Hinds Instruments PEM-90 Model I/FS50 that oscillates at a fixed frequency of $\gamma/2\pi = 50$ kHz and can provide a retardance over a range of $.013(2\pi)$ to $.65(2\pi)$ at 780nm. When used in conjunction

Transparent Glass   **Piezoelectric Transducer**

Modulator Fast Axis
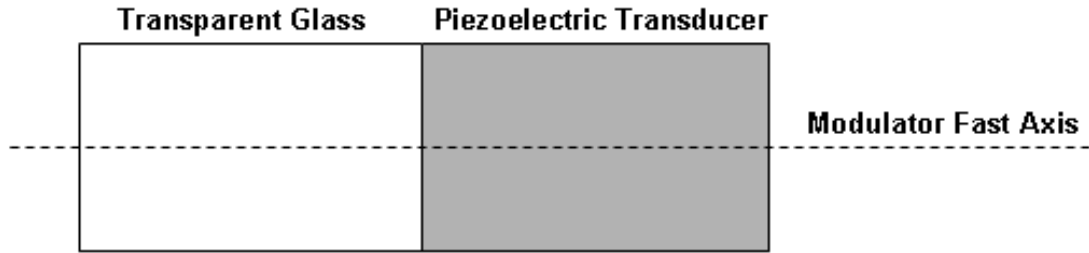
Figure C.3: Photoelastic Modulator

with a lock-in amplifier, a PEM is a powerful tool for isolating small signals.

C.3.1   Interaction with the Probe Beam

After passing through two linear polarizers (Fig. 4.2), the horizontally-polarized probe beam travels through a quarter-wave plate (see Appendix C.1), which is oreinted at $45°$ with respect to the polarizing cube. This setup typically yields circular polarizations in excess of 99%. Next the circularly polarized light travels through a PEM, which has its fast axis horizontal (and hence at $45°$ to the QWP's fast axis).

To solve for the light exiting the PEM, the following matrix operations are performed (see Appendix C.1):

$$E_f = R(-45°)T_{PEM}R(45°)R(-45°)T_{QWP}R(45°)E_i \tag{C.12}$$

$$E_f = R(-45°)T_{PEM}T_{QWP}R(45°)E_i. \tag{C.13}$$

where T is the Jones matrix of the optic under consideration and R is a rotation matrix (see Appendix C.1). For initially horizontally polarized light, matrix algebra yields

$$E_f = \frac{E_0}{2} \begin{pmatrix} 1 - ie^{-i\Gamma} \\ 1 + ie^{-i\Gamma} \end{pmatrix},$$

which simplifies to

$$E_f = \frac{E_0}{\sqrt{2}} e^{-i\Gamma/2} e^{i\pi/4} \begin{pmatrix} i(\sin(\frac{\Gamma}{2}) - \cos(\frac{\Gamma}{2})) \\ \sin(\frac{\Gamma}{2}) + \cos(\frac{\Gamma}{2}) \end{pmatrix},$$

or, more conveniently,

$$E_f = \frac{E_0}{\sqrt{2}} e^{-i\Gamma/2} e^{i\pi/4} \left[i \left(\sin(\frac{\Gamma}{2}) - \cos(\frac{\Gamma}{2}) \right) |x\rangle + \sin(\frac{\Gamma}{2}) + \cos(\frac{\Gamma}{2}) |y\rangle \right] \qquad (C.14)$$

Following the method developed in Section 4.1.1, the light must be projected onto the coordinates of the atomic vapor,

$$E_f = iE_0 e^{-i\Gamma/2} e^{i\pi/4} \left[-\cos(\frac{\Gamma}{2})|R\rangle + \sin(\frac{\Gamma}{2})|L\rangle \right]. \qquad (C.15)$$

After the cell, the two different circular polarizations will have evolved differently,

$$E_f = \underbrace{\frac{E_0}{\sqrt{2}} e^{-i\Gamma/2} e^{i\pi/4} e^{i\tilde{k}_R l} e^{i\delta\tilde{k}l/2}}_{\sqrt{2}E_0'} \left[-\cos(\frac{\Gamma}{2}) e^{-i\delta\tilde{k}l/2}|R\rangle + \sin(\frac{\Gamma}{2}) e^{i\delta\tilde{k}l/2}|L\rangle \right]. \qquad (C.16)$$

Note that for $\Gamma = 0$ (no PEM), only the right circular component exists. Finally, when project back onto the lab coordinates,

$$E_f = E_0' \left[E_x |x\rangle + E_y |y\rangle \right], \qquad (C.17)$$

where

$$E_x = -\cos(\frac{\Gamma}{2})e^{-i\phi_r}e^{\beta_r} + \sin(\frac{\Gamma}{2})e^{i\phi_r}e^{-\beta_r} \tag{C.18}$$

$$E_y = -i\left(\cos(\frac{\Gamma}{2})e^{-i\phi_r}e^{\beta_r} + \sin(\frac{\Gamma}{2})e^{i\phi_r}e^{-\beta_r}\right). \tag{C.19}$$

Finally we can rewrite Eq. 4.88 as

$$\frac{\Delta}{\Sigma} = \frac{\sin\Gamma(t)\cos 2\Phi}{\cosh 2\beta + \cos\Gamma(t)\sinh 2\beta}. \tag{C.20}$$

Appendix D

Tunability of Line-Narrowed Lasers

Although considerably higher optical-pumping rates can be achieved with narrowband lasers, we note that such lasers are not ideal for SEOP with both ^{3}He and ^{129}Xe. In particular, the Rb D1 pressure-broadened shift for ^{3}He and ^{129}Xe are in opposite directions [31]. The shift for a typical high-density ^{3}He target cell is about 67GHz; for a high-density Xe cell, the shift is about -36 GHz. This gives a difference of 103GHz, or about 0.22nm. This can be a serious issue because line-narrowed lasers have limited tunability (one of our line-narrowed laser has a tunability of about 0.15nm). It can therefore be difficult to tune a line-narrowed laser to pump both ^{3}He and ^{129}Xe.

Appendix E

Cell Data

Cell	Lasers	T_{pc}^{set}	P_{He}^{∞}	Γ_s^{-1}	$\langle\Gamma\rangle^{-1}$	T_{pc}	f_{pc}	P_A	D	[Rb]	m_{pc}
Sosa	2C1F	160	0.57(03)	16.7(09)	55.7(1.8)	190(7)	0.71(03)	1.00(03)	0	1.97(45)	0.0402(004)
	2C1F	170	0.61(03)	11.7(03)	55.5(2.0)	208(14)	0.71(03)	0.98(03)	0	-	-
	2C1F	180	0.55(03)	8.79(09)	55.2(2.2)	227(7)	0.70(02)	0.97(03)	0	4.30(89)	0.0764(008)
	2C1F	190	0.40(02)	6.39(22)	55.1(2.3)	238(20)	0.69(03)	-	0	-	-
	2C1F	200	0.26(01)	5.40(17)	55.0(2.4)	243(17)	0.69(03)	0.83(17)	0	5.02(2.42)	0.0680(007)
Alex	2C1F	235	0.59(03)	4.81(03)	26.8(2.0)	282(10)	0.58(02)	0.99(03)	1.37(08)	4.08(90)	0.158(017)
Stephanie	3C	235	0.71(04)	4.55(09)	37.0(2.3)	289(6)	0.54(02)	0.99(03)	1.39(11)	5.08(1.63)	-
Brady	3C	235	0.70(03)	5.30(01)	26.9(1.7)	274(7)	0.55(02)	0.99(03)	2.60(20)	2.87(81)	0.244(025)
	2C	235	0.68(03)	5.52(70)	27.0(1.7)	260(8)	0.56(02)	0.99(03)	-	-	-
	1C	235	0.62(03)	4.82(1.08)	27.1(1.6)	249(9)	0.56(02)	0.95(03)	-	-	-
Moss	1C1F	235	0.62(03)	5.35(04)	24.5(1.6)	264(8)	0.57(02)	0.95(09)	-	-	-
Tigger	1C1F	235	0.51(03)	4.89(05)	12.1(9)	258(9)	0.57(02)	0.95(09)	-	-	-
Samantha	3C	235	0.68(03)	4.63(03)	17.1(1.1)	256(10)	0.57(02)	0.99(03)	4.37(10)	1.80(20)	-
Maureen	3C	235	0.66(03)	5.42(12)	23.3(1.5)	267(12)	0.53(02)	0.97(09)	-	-	-
Astral Weeks	2C1F	235	0.69(03)	6.57(12)	34.9(2.3)	260(4)	0.54(02)	0.99(03)	7.09(55)	0.965(181)	0.186(019)

Table E.1: Hybrid Results. T_{pc}^{set} and T_{pc} have units of °C; Γ_s, $\langle\Gamma\rangle$, and m_{pc} have units of 1/hours; [Rb] has units of $10^{14}/\text{cm}^3$. In the 'Lasers' column, 'C' refers to line-narrowed Comet lasers and 'F' refers to broadband FAP lasers.

Bibliography

[1] Romalis, M. *Laser Polarized 3He Target Used for a Precision Measurement of the Neutron Spin Structure*. PhD thesis, Princeton University, (1997).

[2] Alcock, C., Itkin, V., and M.K, H. *Canadian Metallurgial Quarterly* **23 (3)**, 309 (1984).

[3] Team, N. A. Technical report, National Institute of Standards and Technology, Gaithersburg, MD, June (2008).

[4] Hammond, C. *Handbook of Chemistry and Physics*, chapter The Elements. CRC Press, 69 edition (1989).

[5] Singh, J. Technical Report 1.52, University of Virginia, (2008).

[6] Singh, J. *Thesis*. PhD thesis, University of Virginia, (2010).

[7] HAPPER, W. *Rev. Mod. Phys.* **44**(2), 169–249 Apr (1972).

[8] Walter, D. K., Griffith, W. M., and Happer, W. *Phys. Rev. Lett.* **88**(9), 093004 Feb (2002).

[9] Knize, R. J. *Phys. Rev. A* **40**(11), 6219–6222 Dec (1989).

[10] Larson, B., Häusser, O., Delheij, P. P. J., Whittal, D. M., and Thiessen, D. *Phys. Rev. A* **44**(5), 3108–3118 Sep (1991).

[11] Tscherbul, T. V., Zhang, P., Sadeghpour, H. R., and Dalgarno, A. *Phys. Rev. A* **79**(6), 062707 Jun (2009).

[12] Walker, T. G., Thywissen, J. H., and Happer, W. *Phys. Rev. A* **56**(3), 2090–2094 Sep (1997).

[13] Kadlecek, S. J. *Spin Relaxation in Alkali Vapors.* PhD thesis, University of Wisconsin-Madison, (1999).

[14] Kadlecek, S., Anderson, L. W., and Walker, T. *Nuclear Instruments and Methods in Physics Research Section A: Accelerators, Spectrometers, Detectors and Associated Equipment* **402**(2-3), 208 – 211 (1998). Proceedings of the 7th RCNP International Workshop on Polarized He Beams and Gas Targets and Their Application.

[15] Anthony, P. L., Arnold, R. G., Band, H. R., Borel, H., Bosted, P. E., Breton, V., Cates, G. D., Chupp, T. E., Dietrich, F. S., Dunne, J., Erbacher, R., Fellbaum, J., Fonvieille, H., Gearhart, R., Holmes, R., Hughes, E. W., Johnson, J. R., Kawall, D., Keppel, C., Kuhn, S. E., Lombard-Nelsen, R. M., Marroncle, J., Maruyama, T., Meyer, W., Meziani, Z.-E., Middleton, H., and Morgenstern, J. *Phys. Rev. Lett.* **71**(7), 959–962 Aug (1993).

[16] Riordan, S. *arXiv:1008.1738v2* .

[17] Coulter, K., McDonald, A., Happer, W., Chupp, T., and Wagshul, M. *Nuclear Instruments and Methods in Physics Research Section A: Accelerators, Spectrometers, Detectors and Associated Equipment* **270**(1), 90 – 94 (1988).

[18] Albert, M. S., Cates, G. D., Driehuys, B., Happer, W., Saam, B., Springer, C. S., and Wishnia, A. *Nature* **370**, 199–201 July (1994).

[19] Middleton, H., Black, R. D., Saam, B. T., Cates, G. D., Cofer, G. P., Guenther, R., Happer, W., Hedlund, L. W., Johnson, G. A., Juvan, K., and Swartz, J. *Magnetic Resonance in Medicine* **33**, 271–275 February (1995).

[20] Cates, G., Riordin, S., and Wojtsekhowski, B. January (2009). PAC34 Meeting at Jefferson Lab.

[21] Commission, U. S. N. R. http://www.nrc.gov/reading-rm/doc-collections/fact-sheets/tritium.pdf, (2005).

[22] of Representatives Committee on Science, U. H., on Investigations, T. S., and Oversight. http://democrats.science.house.gov/Media/File/Commdocs/hearings/2009/Oversig November (2009).

[23] Wang, C., Altes, T., Miller, G., de Lange, E., Ruppert, K., Mata, J., and Cates, G. Radiological Society of North America, (2007).

[24] Lauterbur, P. *Nature* **242**, 190–191 March (1973).

[25] Middleton, H., Black, R., Saam, B., Cates, G., Cofer, G., Guenther, R., Happer, W., Hedlund, L., Johnson, G., and Juvan, K. e. a. *Magnetic Resonance in Medicine* , 271–5 February (1995).

[26] Walker, T. G. and Happer, W. *Rev. Mod. Phys.* **69**(2), 629–642 Apr (1997).

[27] Happer, W. and Tam, A. *Phys. Rev. A* **16**, 1877–1891 (1977).

[28] Applet, S., Baranga, A. B.-A., Erickson, C., Romalis, M., Young, A., and Happer, W. *Phys. Rev. A* **58**, 1412–1439 (1998).

[29] Merzbacher, E. *Quantum Mechanics*. Wiley, 3 edition, (1998). Pages 490, 499.

[30] Hansen, W. *J. Phys. B At. Mol. Phys.* **17**, 4833–4850 (1984).

[31] Romalis, M., Miron, E., and Cates, G. *Phys. Rev. A* **56**, 4569 (1997).

[32] Singh, J. Technical Report 1.10, University of Virginia, (2006).

[33] Herman, R. M. *Phys. Rev.* **137**(4A), A1062–A1065 Feb (1965).

[34] Middleton, H. L. *The Spin Structure of the Neutron Determined Using a Polarized 3-He Target.* PhD thesis, Princeton University, (1994).

[35] Ben-Amar Baranga, A., Appelt, S., Romalis, M. V., Erickson, C. J., Young, A. R., Cates, G. D., and Happer, W. *Phys. Rev. Lett.* **80**(13), 2801–2804 Mar (1998).

[36] Babcock, E., Nelson, I., Kadlecek, S., Driehuys, B., Anderson, L. W., Hersman, F. W., and Walker, T. G. *Phys. Rev. Lett.* **91**(12), 123003 Sep (2003).

[37] Newbury, N. R., Barton, A. S., Cates, G. D., Happer, W., and Middleton, H. *Phys. Rev. A* **48**(6), 4411–4420 Dec (1993).

[38] Gamblin, R. L. and Carver, T. R. *Phys. Rev.* **138**(4A), A946–A960 May (1965).

[39] Schearer, L. D. and Walters, G. K. *Phys. Rev.* **139**(5A), A1398–A1402 Aug (1965).

[40] Cates, G. D., Schaefer, S. R., and Happer, W. *Phys. Rev. A* **37**(8), 2877–2885 Apr (1988).

[41] Heil, W., Humblot, H., Otten, E., Schafer, M., Sarkau, R., and Leduc, M. *Physics Letters A* **201**(4), 337 – 343 (1995).

[42] Jacob, R. E., Morgan, S. W., Saam, B., and Leawoods, J. C. *Phys. Rev. Lett.* **87**(14), 143004 Sep (2001).

[43] Barbe, R., Leduc, M., and Laloe, F. *J. Phys. France* **35**, 935–951 (1974).

[44] Jackson, J. *Classical Electrodynamics.* third edition.

[45] Fitzsimmons, W. A., Tankersley, L. L., and Walters, G. K. *Phys. Rev.* **179**(1), 156–165 Mar (1969).

[46] Hsu, M. F., Cates, G. D., Kominis, I., Aksay, I. A., and Dabbs, D. M. *Applied Physics Letters* **77**(13), 2069–2071 (2000).

[47] Babcock, E., Chann, B., Walker, T. G., Chen, W. C., and Gentile, T. R. *Physical Review Letters* **96**(8), 083003 (2006).

[48] Happer, W., Cates, G., Romalis, M., and Erikson., C. (2001).

[49] Babcock, E. D. *Spin-Exchange Optical Pumping with Alkali-Metal Vapors.* PhD thesis, University of Wisconsin-Madison, (2005).

[50] Zumdahl, S. *Chemical Principles.*

[51] Company, V. A.

[52] Abragam, A. *Principles of Nuclear Magnetism.* Oxford University Press, (1961).

[53] Cates, G. D., White, D. J., Chien, T.-R., Schaefer, S. R., and Happer, W. *Phys. Rev. A* **38**(10), 5092–5106 Nov (1988).

[54] Griffiths, D. J. *Introduction to Electrodynamics.* Prentice Hall, 3 edition, (1999). Pages 236-37, 264-65.

[55] Babcock, E., Nelson, I. A., Kadlecek, S., and Walker, T. G. *Phys. Rev. A* **71**(1), 013414 Jan (2005).

[56] Grover, B. C. *Phys. Rev. Lett.* **40**(6), 391–392 Feb (1978).

[57] Romalis, M. V. and Cates, G. D. *Phys. Rev. A* **58**(4), 3004–3011 Oct (1998).

[58] Schaefer, S. R., Cates, G. D., Chien, T.-R., Gonatas, D., Happer, W., and Walker, T. G. *Phys. Rev. A* **39**(11), 5613–5623 Jun (1989).

[59] Newbury, N. R., Barton, A. S., Bogorad, P., Cates, G. D., Gatzke, M., Mabuchi, H., and Saam, B. *Phys. Rev. A* **48**(1), 558–568 Jul (1993).

[60] Wu, Z., Kitano, M., Happer, W., Hou, M., and Daniels, J. *Appl. Opt.* **25**(23), 4483–4492 (1986).

[61] Boas, M. *Mathematical Methods in the Physical Science.* second edition, (1983).

[62] Young, A. R., Appelt, S., Ben-Amar Baranga, A., Erickson, C. J., and Happer, W. *Applied Physics Letters* **70**(23), 3081–3083 (1997).

[63] Anderson, L. W., Pipkin, F. M., and Baird, J. C. *Phys. Rev.* **116**(1), 87–98 Oct (1959).

[64] Chann, B., Babcock, E., Anderson, L. W., and Walker, T. G. *Phys. Rev. A* **66**(3), 032703 Sep (2002).

[65] Chupp, T. E., Loveman, R. A., Thompson, A. K., Bernstein, A. M., and Tieger, D. R. *Phys. Rev. C* **45**(3), 915–930 Mar (1992).

[66] Zheng, X. *Precision Measurement of Neutron Spin Asymmetry A1n at Large Xbj Using CEBAF at 5.7 GeV.* PhD thesis, (2002).

[67] Kestin, J., Knierim, K., Mason, E. A., Najafi, B., Ro, S. T., and Waldman, M. *J. Phys. Chem. Ref. Data* **13** (1984).

[68] Anthony, P. L., Arnold, R. G., Band, H. R., Borel, H., Bosted, P. E., Breton, V., Cates, G. D., Chupp, T. E., Dietrich, F. S., Dunne, J., Erbacher, R., Fellbaum, J., Fonvieille, H., Gearhart, R., Holmes, R., Hughes, E. W., Johnson, J. R., Kawall, D., Keppel, C., Kuhn, S. E., Lombard-Nelsen, R. M., Marroncle, J., Maruyama, T., Meyer, W., Meziani, Z. E., Middleton, H., and Morgenstern, J. *Phys. Rev. D* **54**(11), 6620–6650 Dec (1996).

[69] Dodge, R. and Thompson, M. *Fluid Mechanics*. McGraw-Hill Book Company, INC., (1937).

[70] Tritton, D. *Physical Fluid Dynamics*. Van Nostrand Reinhold Company, Ltd., (1977).

[71] Keller, W. E. *Phys. Rev.* **105**(1), 41–45 Jan (1957).

[72] Kestin, J., Knierim, K., Mason, E., Najafi, B., Ro, S., and Waldman, M. *J. Phys. Chem. Ref. Data* **13**(1), 229 (1984).

[73] Schiller, L. *Forschungsarbeiten Ver. deut. Ing.* **248** (1922).

[74] *Flow of fluids through valves, fittings, and pipe, Technical Paper 410*. Crane Company, (2009).

[75] Darby, R. *Chemical Engineering Fluid Mechanics*. Marcel Dekker, Inc., (2001).

[76] Singh, J. and Dolph, P. Technical report, (2009).

[77] Davis, S. J. and Balling, L. C. *Phys. Rev. A* **8**(2), 1136–1138 Aug (1973).

[78] Kadlecek, S., Anderson, L. W., and Walker, T. G. *Phys. Rev. Lett.* **80**(25), 5512–5515 Jun (1998).

[79] Borel, P. I., Søgaard, L. V., Svendsen, W. E., and Andersen, N. *Phys. Rev. A* **67**(6), 062705 Jun (2003).

[80] Wagshul, M. E. and Chupp, T. E. *Phys. Rev. A* **49**(5), 3854–3869 May (1994).

[81] Bhaskar, N. D., Pietras, J., Camparo, J., Happer, W., and Liran, J. *Phys. Rev. Lett.* **44**(14), 930–933 Apr (1980).

[82] Walker, T. G. *Phys. Rev. A* **40**(9), 4959–4964 Nov (1989).

[83] Walter, D. K., Happer, W., and Walker, T. G. *Phys. Rev. A* **58**(5), 3642–3653 Nov (1998).

[84] Wang, G. *Polarizing He-3 by spin exchange with potassium.* PhD thesis, California Institute of Technology, (2004).

[85] Franz, F. A. and Volk, C. *Phys. Rev. A* **26**(1), 85–92 Jul (1982).

[86] Chen, W. C., Gentile, T. R., Walker, T. G., and Babcock, E. *Phys. Rev. A* **75**(1), 013416 Jan (2007).

[87] Franz, F. A. and Sooriamoorthi, C. E. *Phys. Rev. A* **10**(1), 126–140 Jul (1974).

[88] Beverini, N., Minguzzi, P., and Strumia, F. *Phys. Rev. A* **4**(2), 550–555 Aug (1971).

[89] Franz, F. A. and Volk, C. *Phys. Rev. A* **14**(5), 1711–1728 Nov (1976).

[90] Walter, D. *Optical Probes of Angular Momentum and Energy Transport in Spin-Exchange Optical Pumping Systems.* PhD thesis, Princeton University, (2002).

[91] Vanier, J., Simard, J.-F., and Boulanger, J.-S. *Phys. Rev. A* **9**(3), 1031–1040 Mar (1974).

[92] Corney, A. *Atomic and Laser Spectroscopy.* Oxford:Clarendon Press, (1977). Ch 4.5-4.8.